QUENCHES ACROSS STRUCTURAL TRANSITIONS IN ION COULOMB CRYSTALS

Dynamics of Ion Coulomb Crystals in State-Dependent Potentials and their Characterization by Ramsey Interferometry

DISSERTATION

zur Erlangung des Grades des Doktors der Naturwissenschaften

der Naturwissenschaftlich-Technischen Fakultät
der UNIVERSITÄT DES SAARLANDES

von

JENS DOMAGOJ BALTRUSCH

Saarbrücken

2016

Tag des Kolloquiums:	14.07.2016
Dekan:	Prof. Dr. Guido Kickelbick
Mitglieder des Prüfungsausschusses:	Prof. Dr. Christoph Becher Prof. Dr. Giovanna Morigi Prof. Dr. Heiko Rieger Dr. Reza Shaebani

QUENCHES ACROSS STRUCTURAL TRANSITIONS IN ION COULOMB CRYSTALS

Dynamics of Ion Coulomb Crystals in State-Dependent Potentials and their Characterization by Ramsey Interferometry

Jens D. Baltrusch: *Quenches Across Structural Transitions in Ion Coulomb Crystals: Dynamics of Ion Coulomb Crystals in State-Dependent Potentials and their Characterization by Ramsey Interferometry.*

Dissertation zur Erlangung des Grades des Doktors der Naturwissenschaften
der Naturwissenschaftlich-Technischen Fakultät der Universität des Saarlandes.

Betreuerin: Prof. Dr. Giovanna Morigi.

– Plichtexemplar –

EIDESSTATTLICHE VERSICHERUNG

Hiermit versichere ich an Eides statt, dass ich die vorliegende Arbeit selbstständig und ohne Benutzung anderer als der angegebenen Hilfsmittel angefertigt habe. Die aus anderen Quellen oder indirekt übernommenen Daten und Konzepte sind unter Angabe der Quelle gekennzeichnet. Die Arbeit wurde bisher weder im In- noch im Ausland in gleicher oder ähnlicher Form in einem Verfahren zur Erlangung eines akademischen Grades vorgelegt.

Ulm, 27. Juni 2017

Jens Domagoj Baltrusch

ABSTRACT

This thesis theoretically discusses the dynamics of small Coulomb crystals of ions confined in state-dependent potentials following a sudden quench of the mechanical forces on a single ion embedded in the crystal. This dynamics is analysed using the principle of Ramsey interferometry, for which purpose the electronic state of the ion is put into a superposition, thereby entangling the ion's internal degrees of freedom with the crystal wavefunction due to the state-dependent dynamics. Measuring the electronic state after a time of free evolution and determining the interferometric visibility enables us to deduce information about the motional state of the crystal. We analyse the temporal variation of this visibility in dependence on the trap parameters, the crystal size, and the temperature close to a structural transition, which allows us to infer the equilibrium properties of the crystal close to criticality as well as the crystal's features as a non-Markovian bath.

ZUSAMMENFASSUNG

Diese theoretische Arbeit behandelt die Dynamik von kleinen Ionen-Coulomb-Kristallen in zustandsabhängigen Potentialen nach einer rasch erfolgten Änderung des Fallenpotentials für ein einzelnes Ion. Diese Dynamik analysieren wir mittels des Konzepts der Ramsey-Interferometrie indem wir den elektronischen Zustand in eine Überlagerung bringen, sodass sich dieser aufgrund der zustandsabhängigen Dynamik mit der Wellenfunktion des gesamten Kristalls verschränkt. Die Messung des elektronischen Zustands des Ions nach einer freien Zeitentwicklung und die Bestimmung des interferometrischen Kontrasts dieser Messung ermöglichen es uns, Rückschlüsse auf den Bewegungszustand des gesamten Kristalls zu ziehen. Wir analysieren die zeitliche Veränderung des Kontrasts für verschiedene Fallenparameter, Kristallgrößen und Temperaturen nahe eines strukturellen Überganges, worüber sich die Gleichgewichtseigenschaften des Kristalls nahe des kritischen Überganges sowie die Charakteristik des Kristalls als nicht-markovsches Bad ableiten lassen.

In memory of

Frederick William Ayer
(1941 – 2010)

CONTENTS

LIST OF FIGURES

LIST OF TABLES

INTRODUCTION

What comprises the border between the classical and the quantum world? This question puzzled the founders of quantum mechanics since the establishment of the theoretical framework in the 1920s, and it has kept on puzzling numerous scientists ever since (see Wheeler and Zurek 1983, for a comprehensive collection of milestone articles on the subject). On the theoretical side, much progress has been made within the so-called *decoherence program* (Paz and Zurek 2002; Joos et al. 2003; Zurek 2003; Schlosshauer 2005). In this framework the evident instability of macroscopic quantum mechanical superpositions is explained as resulting from entanglement, that is established via a quantum mechanical interaction between the physical system of interest and the surrounding physical systems, the latter being collectively termed *environment* or *bath*. Such entanglement leads to an apparent degradation of the system's quantum mechanical features such as the disappearance of interference, the presence of which is one manifestation of the quantum mechanical superposition principle. Despite the achievements of the decoherence program, several fundamental problems remain unsolved (Penrose 2005, Ch. 29, pp.782–815; Schlosshauer 2005). One question that is especially relevant to this thesis is the systematic development of a statistical mechanics framework allowing the description of the emergence of the classical world in a consistent manner and starting from the individual constituents. Such a framework would permit, amongst other things, the identification of the relevant physical properties that preserve or alternatively destroy quantum mechanical coherence. It would thus be instrumental for finding efficient ways to combat the loss of quantum coherence, which is the main obstacle to the development of deployable quantum technologies such as quantum computers, quantum metrology, and quantum sensors.

Some theoretical studies go beyond the typical approach of deriving Born-Markov master equations (Gardiner and Zoller 2000, Ch. 5, pp. 130ff.; Englert and Morigi 2002) for the description of the system-bath interaction; instead they consider, for instance, spin systems by analysing the dynamics of a single spin coupled to a spin environment (Khaetskii et al. 2002; Merkulov et al. 2002). Since these systems exhibit quantum critical behaviour, they constitute an ideal setting for analysing the emergence of thermalization after a sudden or slow quench of the external magnetic field crossing the critical value (Iglói

and Rieger 2011; Calabrese et al. 2011; Polkovnikov et al. 2011; Eisert et al. 2015). With this in mind, Porras and Cirac (2004) and Schneider, Porras et al. (2012) theoretically proposed to simulate the behaviour of spin chains by engineering the coupling of trapped ions with external fields.

As a matter of fact, cold trapped ions are well suited for an experimental setup addressing these open questions: Not only are they one of few quantum systems to possess outstanding controllability in almost all their degrees of freedom, they are also better separable from their surroundings than many other physical systems. Applications with trapped ions include high precision spectroscopy measurements of the g-factor of elementary particles and anti-particles (Brown and Gabrielse 1986), antecendent approaches for quantum computation (Häffner et al. 2008; Blatt and Wineland 2008),[1] realizations of quantum simulation of various physical model systems (Johanning et al. 2009; Schneider, Porras et al. 2012), and also atomic clocks (Riehle 2005) with higher accuracy than those currently in use to establish the common time standard. Because of the outstanding control over practically all degrees of freedom, trapped ions are ideally suited for the investigation of open questions in quantum mechanics. Take for instance the experimental creation of Schrödinger cat states of a single trapped ion (Monroe, Meekhof, King and Wineland 1996) and the experimentally verified fragility of such states when subjected to external noise (Myatt et al. 2000; Turchette et al. 2000).

One possible alternative to analysing the stability of such superposition states under the influence of external noise would be a combined arrangement under which one part is considered as the system and the remainder is regarded as an environment or bath. Many of the paradigmatic models have a collection of harmonic oscillators as the bath system, to which another quantum system is coupled, e. g. a central particle in a potential (Ford et al. 1965; Caldeira and Leggett 1983) or a two-level system (also called the spin-boson model, which is equivalent to a particle in a double well coupled to a bath of harmonic oscillators; Leggett et al. 1987; Weiss et al. 1987). Some of these paradigmatic models have been investigated theoretically for cold trapped ion Coulomb crystals (Porras, Marquardt et al. 2008). For the former system, recent studies have shown that even entanglement between distant particles in a harmonic chain can be generated (Audenaert et al. 2002; Paz and Roncaglia 2008; Wolf et al. 2011), and a feasible experimental verification can be implemented for ion Coulomb chains (Fogarty et al. 2013; Taketani et al. 2014).

1 However, due to a lack of scalability, trapped ions probably never mature beyond the current antetype status.

In this work, we investigate another approach under which the harmonic oscillators themselves become dependent on the state of a two-level system. This scheme can be implemented for trapped ion Coulomb crystals by the addition of a state-dependent potential on top of the regular trapping potential. We then examine how the coherence between two electronic levels of a single ion embedded inside such a crystal is affected by a local quantum quench of the external state-dependent potential. When we put the ion into a quantum superposition of its electronic levels such that the equilibrium positions become dependent on the electronic state, the system realizes a dynamical quantum superposition that simultaneously oscillates around equilibrium positions of different crystalline structures. This setup is then combined with a scheme of Ramsey interferometry, previously suggested by Poyatos, Cirac, Blatt et al. (1996) and De Chiara et al. (2008), in order to probe the motional state by monitoring the coherence between the two electronic levels. We identify the properties of various calculated instances of this visibility as a function of the time between the Ramsey pulses and provide an explanation rooted in the dynamics of the normal modes after the quench. When the temperature of the initial motional state is increased, we observe a quick drop of the visibility with certain periodically occurring "thermal revivals", which are absent at absolute zero temperature. These originate from the interplay of the dynamical phases of the initial and evolving thermally excited motional states of the ion Coulomb crystal. The result suggests that thermal dephasing of the environment can indeed have an important (and possibly underestimated) impact on the coherence of an embedded two-level system.

This thesis is composed of two parts: The first part is concerned with the creation of ion Coulomb crystals in state-dependent potentials and their properties. After reviewing the basic physics of trapped ions and of ion Coulomb crystals in Chapter 1, we exemplify how to implement such a state-dependent potential in Chapter 2, where we also discuss the possible state-dependent structures for a three-ion crystal. We then derive the necessary tools for analysing the dynamical evolution of such an ion Coulomb crystal in a state-dependent potential in Chapter 3.

In the second part of this thesis, we show that after a local quantum quench of an ion Coulomb crystal in a state-dependent potential, the coherence between two electronic levels of a single ion embedded in the crystal is determined by the dynamics of the motional state of the whole crystal. The coherence can be monitored by making use of the scheme of Ramsey interferometry, which we review for that purpose in Chapter 4; in particular, we show how this scheme allows the extraction of information about the motional degrees of freedom

by simply monitoring the visibility of the Ramsey interference fringes over time. In Chapters 5 and 6 we examine different characteristics of the visibility in dependence on the parameters of the quench, like the initial state preparation or the strength of the quench, and additionally on the temperature.

In the Conclusions we suggest possible extensions to the work presented here.

Part I

ION COULOMB CRYSTALS IN STATE-DEPENDENT POTENTIALS

In this part, we first review the physics of trapped ions and trapped ion Coulomb crystals. Then we discuss how to subject ion Coulomb crystals to a state-dependent potential and propose how to implement such a potential in an experiment. Finally, we discuss the equilibrium configurations of ion Coulomb crystals in such state-dependent potentials and develop the theoretical methods for analysing the dynamics of ion Coulomb crystals after a local quantum quench.

1

TRAPPED IONS AND ION COULOMB CRYSTALS

In this chapter we introduce the background for the system studied in this thesis, a small trapped ion Coulomb crystal. For this purpose we review first the basic principles of commonly used ion trapping apparatus in Section 1.1; then, we turn to a brief review of the physics of many trapped ions and the conditions for observing plasmas and crystals in Section 1.2; finally, we present an overview of the different crystalline structures and the possible structural transitions between them in Section 1.3, with particular emphasis on the linear–zigzag transition.

1.1 TRAPPING IONS

Why Trap Ions?

Before the advent of ion traps, all experiments involving the measurement of atomic properties, such as frequencies of spectral lines, were performed on ensembles of a large number of particles. Measurements on ensembles such as gaseous atoms in evacuated cells are affected primarily by two effects. First, interactions between the particles may change the measured properties; for example, the collisions between the atoms of a gas induce a *collisional broadening* of the measured spectral linewidths (Allen and Eberly 1987). Second and more profoundly, any measurement over an ensemble yields an averaged result (Paul 1990). In particular, an ensemble of atoms inside a gas cell has a certain velocity distribution; atoms with different velocities experience different Doppler shifts and thus have resonance curves which are centred at different frequencies. The measured curve is given by the superposition and hence the average of the resonance curves of the individual atoms; it is much broader than the individual resonance curves. Any measurement on a sample of atoms at non-zero temperature thus suffers from this so-called *inhomogeneous broadening* (Allen and Eberly 1987), limiting the precision of the measured results.

The achievement of laser cooling for trapped ions (Neuhauser et al. 1978; Wineland, Drullinger et al. 1978) allowed for the first observation

of a single trapped atomic ion (Neuhauser et al. 1980).[1] This milestone experiment paved the way for examining the pure interaction of a single atomic particle with the electromagnetic field, and thus for more precise spectroscopic measurements. Soon after, it was realized that a single trapped atomic ion could provide a new method for establishing a more accurate frequency standard (Dehmelt 1981): Laser cooling makes possible the elimination of the non-relativistic Doppler shift, and the electric field – and with it any Stark shifts – vanish at the centre of the trap (see Rosenband et al. 2008, Chou et al. 2010, King et al. 2012, Huntemann et al. 2012, and Madej, Dubé et al. 2012 for recent experiments, and Madej and Bernard 2001 or Riehle 2005, Ch. 10, pp. 315–352 for an overview on atomic clocks).

The successful demonstration of ground-state cooling of a single ion (Diedrich, Bergquist et al. 1989) gave the means to controlling and manipulating the motional state of a single trapped ion (Leibfried et al. 2003). These achievements led to a method allowing actual control over the motional state of a single or a small number of trapped ions (Meekhof et al. 1996), most striking result being the first demonstration of the basic constituents of a *quantum computer* (Cirac and Zoller 1995; Monroe, Meekhof, King, Jefferts et al. 1995; Schmidt-Kaler et al. 2003; Leibfried et al. 2003).[2]

Moreover, trapped ions are a promising platform for realizing certain instances of *quantum simulators* of complex problems, otherwise inaccessible with state-of-the-art computers; a number of different models are currently being explored (Johanning et al. 2009; Schneider, Porras et al. 2012; Blatt and Roos 2012; see Georgescu et al. 2014, for a review comparing the potential of trapped ions for quantum simulation with other physical systems). By and large, the presence of a regular lattice is advantageous for employing ion Coulomb crystals as quantum simulators, as many models considered for simulation are indeed defined on regular lattices. There a several different crystal structures occurring for ion Coulomb crystals (Dubin and O'Neil 1999), which we shall review later in this chapter. These structures are the focus of a number of interesting studies in the realms of quantum reservoir engineering (Poyatos, Cirac and Zoller 1996), quantum phase transitions (Islam et al. 2011; Bermudez and Plenio 2012; Shimshoni et al. 2011b), non-equilibrium statistical mechanics (Huber et al. 2008;

1 The trapping of a single electron had been achieved some years earlier by Wineland, Ekstrom et al. (1973).

2 In fact, trapped ions for demonstrating a useful quantum computer lacks one of the essential requirements listed by DiVincenzo (2000), namely the *scalability* of the system, i. e. the trapped ion quantum computer can be implemented only for a small number of trapped ions (Monz et al. 2011) but not for arbitrarily large numbers of ions. Hence, tremendous efforts are currently being spent in making the system scalable, e.g. by using micro-fabricated traps. For a review of quantum computation with trapped ions see Blatt and Wineland (2008); Häffner et al. (2008).

Dorner et al. 2013; Mazzola et al. 2013), and thermalization of many-body systems (Lin and Duan 2011). Before turning to the physics of ion Coulomb crystals in Section 1.2, though, we start by reviewing how a single ion is trapped.

1.1.1 *The Basic Principles of Trapping Ions*

A reasonable first attempt at trapping a charged particle would be to assemble a set of electrodes in such a way that they provide an electric field which would enclose the ion within a small spatial region from which it cannot escape. This is equivalent to creating a local minimum in the electric potential, as the force by which the charge is accelerated is proportional to the gradient of the potential. However, it turns out that this is impossible to achieve by an electrostatic potential alone. This conclusion goes by the name of *Earnshaw's theorem* (Earnshaw 1842), which states that an electric charge[3] cannot be trapped in all three spatial dimensions by an electrostatic potential only.[4] This stems from the mathematical properties of the solutions of Laplace's equation for the free electrostatic potential (Landau and Lifschitz 1971, Ch. 5, § 35, pp. 88). Hence, for trapping electric charges, we are left with basically two choices, which define the two main types of ion traps encountered in laboratories: either adding a magnetic field, or making the electric field time-dependent.

1.1.2 *Trapping with Electrostatic and Magnetic Fields: Penning Trap*

The first of these two methods employs a magnetic field superimposed on an electric quadrupole field. One realization with such a configuration is the cold-cathode ionization gauge, a manometer build by Penning (1937) to measure low gas pressures; Dehmelt (1968) adapted this device for the purpose of trapping electrons. the trapping mechanism of the so-called *Penning trap*, see Figure 1.1 for a sketch, has first been described by Pierce (1954; for a historical account see Holzscheiter 1995), works as follows: A cylindrically symmetric electric quadrupole potential confines the charged particles along one

3 It is possible to trap a dipole with nothing but static electric fields. This is actually in complete analogy to the trapping of particles with magnetic dipoles (Phillips 1998; Chu 1998) in static magnetic fields. Curiously, this mechanism allows trapping of diamagnetic objects in strong magnetic fields by inducing magnetic dipole moments, which has been demonstrated by having even *living frogs* levitating in a strong magnetic field (Berry and Geim 1997; Geim 1998).

4 More interestingly, in his original work Earnshaw (1842) concluded that the stability of particles subject to an attractive interaction with inverse-square forces (such as electromagnetic interactions) requires forces with a higher inverse power than two to achieve a stable equilibrium; see Scott (1959); Bassani (2006) for a discussion.

spatial dimension but it does not confine them in the other two spatial dimensions; choosing the confining direction along the z-direction, the potential is of the following form,

$$\Phi(x, y, z) = \frac{U_0}{d^2}(2z^2 - x^2 - y^2), \tag{1.1}$$

which conforms to Laplace's equation. Here, U_0 is the voltage applied between the ring electrodes and the endcaps, and d is a normalizing factor to fulfil the boundary conditions at the surface of the electrodes. Figure 1.2a shows how the confining part of the field traps the charged particles in x–y-plane, while the anti-confining part pushes them radially outward, away from the z-axis. Additionally, a strong uniform magnetic field is applied along the z-direction, $\mathbf{B}(x, y, z) = B_0\hat{\mathbf{z}}$. The resulting Lorentz force guides the charged particles onto circular trajectories, so-called *cyclotron orbits*. The anti-confining electric field is perpendicular to the magnetic field, so it accelerates and decelerates the particles on their orbits in such a way that they obtain a net azimuthal acceleration component perpendicular to both the magnetic and electric field. The centres of the cyclotron orbits undergo a circular $\mathbf{E} \times \mathbf{B}$-drift (Jackson 1999, Ch. 12.3, pp. 586ff.) around the trap centre; this drift is called *magnetron motion*.

Penning traps are used in many sophisticated experiments as, for instance, the measurement of the g-factors of the electron, positron and other elementary particles (Brown and Gabrielse 1986), and are among the experimental standard devices in the study of non-neutral plasmas (Dubin and O'Neil 1999; Davidson 2001). However, a Penning trap involves considerable technical overhead in the experimental realization as the magnetic fields, being in the order of several Tesla, require superconducting magnets; usually the whole trap together with the vacuum chamber is immersed inside a dilution refrigerator filled with liquid helium. Due to this, optical access, meaning the possibility for manipulating the ions inside the trap by electromagnet radiation, is much more limited than in the second kind of trap, which we are going to discuss next.

1.1.3 *Trapping with Time-Varying Electric Fields: Paul Trap*

The second way to trap charged particles uses time-dependent electrical fields. Paul and co-workers devised (Paul and Steinwedel 1953) and built (Paul and Raether 1955) an apparatus operating such fields for applications in mass spectroscopy (Paul, Reinhard et al. 1958; Paul 1990; March 2009). In the original version of this apparatus, henceforth named *Paul trap*, the electrodes are manufactured as for the Penning trap, such that their surfaces are exactly aligned along the equipotential surfaces of the potential of an ideal quadrupole located at the

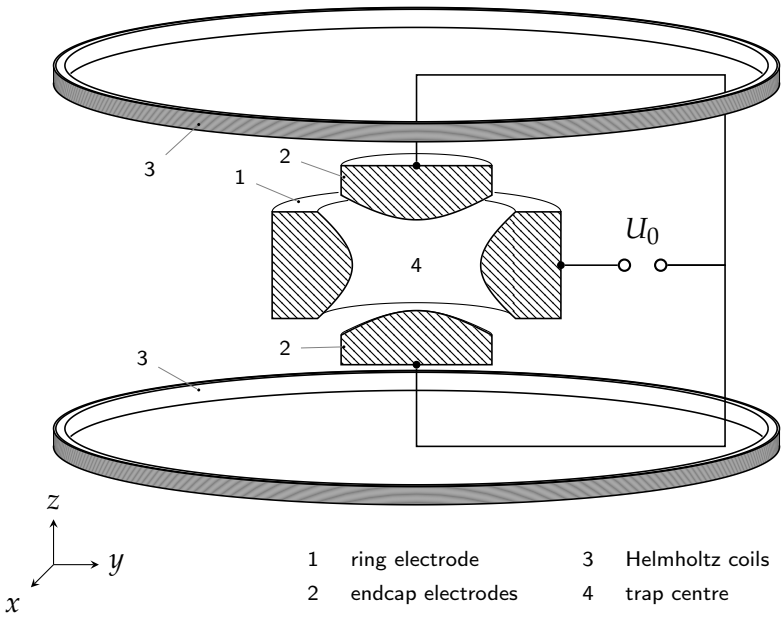

Figure 1.1: Sketch of a typical Penning trap; the electrodes are shown in cross-section. The inner surfaces of the electrodes are formed along one hyperboloid-shaped equipotential surface of an ideal quadrupole located at the trap centre. The voltage is chosen such that the potential of the two endcap electrodes is above that of the ring electrode. The Helmholtz coils provide a homogeneous magnetic field in the centre of the trap.

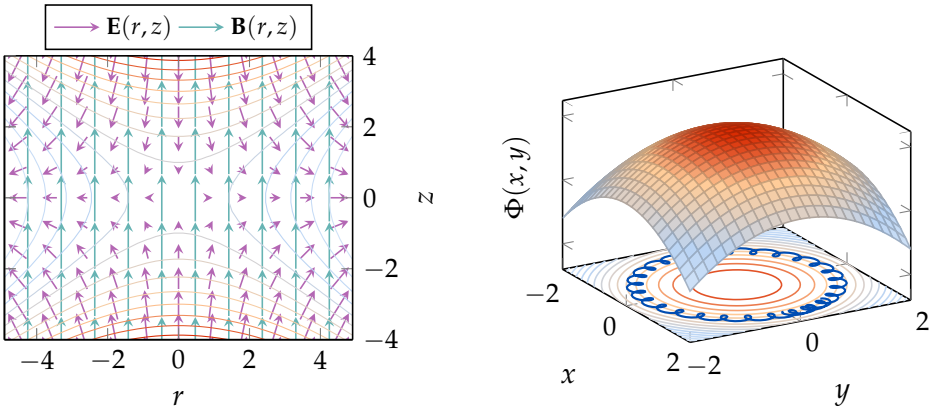

(a) (b)

Figure 1.2: (a) Electric (violet arrows) and magnetic field (green arrows) of an idealized Penning trap. The electric field confines a positively charged particle towards the x–y-plane ($z = 0$), but expels it outward in the radial direction. In the $z = 0$ plane the electric and magnetic fields are perpendicular to each other. The electrostatic equipotential lines are shown as straight lines. (b) In the x–y-plane the electrostatic potential $\Phi(x, y)$ (surface and contours) is anti-confining. Trapping is still possible as the conservation of angular momentum keeps a trapped particle moving on epitrochoidal orbits (blue line).

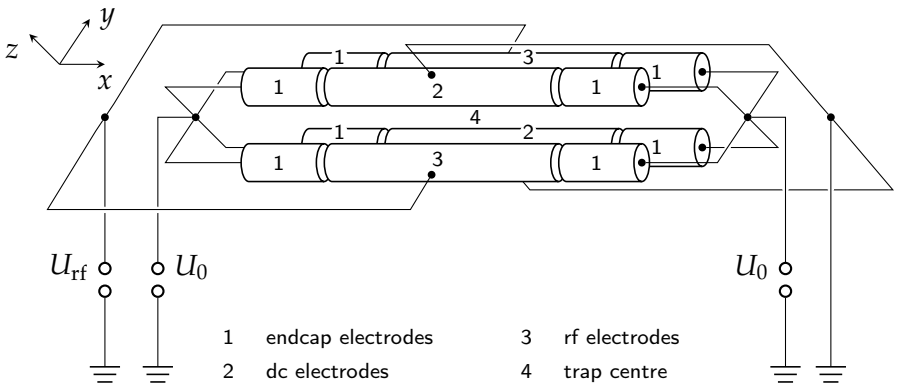

Figure 1.3: Sketch of a typical linear Paul trap. Maintaining a positive potential at the left and right endcap electrodes traps the ions along the x-direction. The four main rod electrodes consist of two pairs of opposing electrodes; one pair is grounded, while the other pair is connected to a potential oscillating at radiofrequency. These four electrodes provide a dynamical confinement in the y–z-plane (see Figure 1.4).

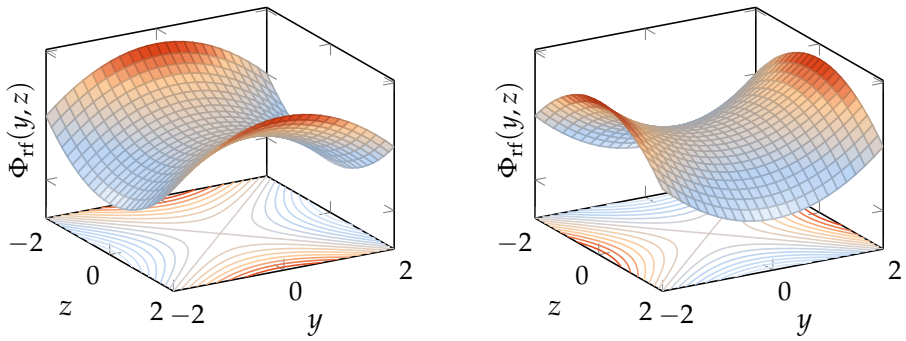

Figure 1.4: Time-dependent electric potential of a Paul trap. (a) At time $t = 0$ and at multiples of the rf-period $T_{rf} = 2\pi/\Omega_{rf}$ the electric potential is confining along the z-direction, but anti-confining along the y=direction. (b) After evolving for times that are half-integer multiples of the rf-period the confining and anti-confining directions are interchanged. The potential in the centre of the trap remains constant. Outside the trap centre, a charged particle experiences alternately an outward pushing and an inward pulling force. By switching between those two situations quickly the particle is effectively confined, though the particle undergoes a fast motion because of the driving.

centre. However, now instead of a static electric field a time-varying one is applied: The angular frequency of the time-varying field is typically in the radio-frequency (rf) domain, i. e. several hundred kHz up to some ten MHz for trapping ions. It turns out that for applications employing trapped linear ion Coulomb crystals there is another, more advantageous arrangement of electrodes (Beaty 1987; Prestage et al. 1989), consisting of four[5] main rod electrodes and endcap electrodes, see Figure 1.3. The endcap electrodes, which exist in many different realizations such as rings, tips, or as cut-off extensions of the main rods as shown in Figure 1.3, are kept on a positive potential which ensures a confinement along one direction (say along the x-direction); the electrostatic potential satisfies the boundary conditions given by the potentials on the electrodes. The potential has a saddle point in the centre of the trap and can therefore be approximated around the trap centre by the following quadrupole potential (Raizen et al. 1992),

$$\Phi_0(x, y, z) = \frac{U_0}{d_0^2}(2x^2 - y^2 - z^2)\,, \tag{1.2}$$

where U_0 is the applied voltage and d_0 is a factor depending on the distance between the endcap electrodes and also their geometry.[6] The main rod electrodes are connected pair-wise such that two diagonally opposing electrodes are grounded, and the other pair is connected to a time-varying rf-potential, which at the trap centre is of the following form (Raizen et al. 1992):

$$\Phi_{\mathrm{rf}}(x, y, z, t) = \frac{U_{\mathrm{rf}}}{2}\left(1 + \frac{y^2 - z^2}{d^2}\right)\cos(\Omega_{\mathrm{rf}} t)\,. \tag{1.3}$$

Each of the two potentials $\Phi_0(x, y, z)$ and $\Phi_{\mathrm{rf}}(x, y, z, t)$ – and thus also their sum – conforms to Laplace's equation. The static part confines the particle along the x-direction but anti-confines along the other two directions. Thus, in order to confine the particle in the remaining directions, we also need to overcome this anti-confining part.

Although no static confinement is possible along all three spatial dimensions, we could utilize time-dependent fields to achieve a situation which is called *dynamical stabilization*, similar to, e.g., the vertically

5 The modified set-up of the main rods bent to closed rings actually corresponds to a quadrupole storage ring (Church 1969). Choosing more than four rods results in higher multipole potentials in the centre, e.g. an octopole potential for using eight rod electrodes. In recent years, many experiments have been setup using micro-structured ion traps for realizing a scalable trapped ion quantum computer. In many cases, these have a two-dimensional electrode design such that the ions are trapped *above* the surface (Häffner et al. 2008; Wineland and Leibfried 2011).

6 d_0 is exactly equal to the distance if the endcap electrods are hyperboloids of two sheets. For other geometries a scale factor is necessary (Raizen et al. 1992), as the potential in Eq. (1.2) is only an approximation valid close to the trap centre, but which does not conform to the boundary conditions.

driven inverted pendulum (Stephenson 1908; Kapitza 1951d,a; Landau and Lifschitz 1969a, § 30, p. 95).

First let us look only at the time-varying potential in the y–z plane, which is shown for different points in time in Figure 1.4. At any instant of time, the potential is such that in one of the directions in the plane it is confining while in the other direction it is anti-confining, as illustrated in Figure 1.4a. The centre of the trap is an unstable saddle-point equilibrium, and for small deviations away from the centre along the anti-confining direction the forces on the particle are expelling it further outward. Now, the trick here is to quickly switch the anti-confining and confining directions, quite similar to balancing a long stick vertically on the palm of the hand. The forces along the direction which was expelling just an instant of time ago now becomes restoring and vice versa, such that the charge turns back to the origin. The charge then would escape along the originally confining direction, but the potential is quickly switched back again before it can do so. By keeping the switching fast enough the charged particle never departs far away from the centre of the trap.

From these qualitative arguments it is not obvious that the resulting trajectory is a closed one, or that the motion will be restricted to a small area around the unstable equilibrium point. In fact, the question of the stability of a trajectory depends on the actual driving, which for a sinusoidally varying voltage leads to equations of motion for the y-coordinate of the following form (Paul 1990; Leibfried et al. 2003),

$$\frac{\mathrm{d}^2 y}{\mathrm{d}t^2} + \left[a_y - 2q_y \cos(2t) y\right] = 0\,, \tag{1.4}$$

and to a similar equation for the z-coordinate. Here, $t = \Omega_{\mathrm{rf}} t/2$ is the time rescaled by half the driving period, and

$$a_y = -4QU_0/(m\Omega_{\mathrm{rf}}^2 d_0^2)\,, \tag{1.5a}$$

$$q_y = \quad 2QU_{\mathrm{rf}}/(m\Omega_{\mathrm{rf}}^2 d^2)\,, \tag{1.5b}$$

are dimensionless parameters, which both depend on the charge Q and mass m of the ion as well as the driving angular frequency Ω_{rf}, while a_y depends on the dc-voltage U_0 and q_y depends on the ac-voltage U_{rf} only (Paul 1990; Leibfried et al. 2003). Equation (1.4) is a *Mathieu differential equation* (McLachlan 1947) which describes a class of physical and mathematical problems such as the vibration of elliptic membranes, parametric resonances, and the propagation of waves in periodic potentials. The general solution of the Mathieu equation (1.4) is given by

$$y(t) = A \sum_{k=-\infty}^{+\infty} c_{2k} \cos[(2k+\beta_y)t] + B \sum_{k=-\infty}^{+\infty} c_{2k} \sin[(2k+\beta_y)t]\,, \tag{1.6}$$

where the coefficients c_{2k} and β_y are dependent on the parameters a_y and q_y and can be calculated by recursion methods (McLachlan 1947; Leibfried et al. 2003). The solution given by Eq. (1.6) is stable (i. e. not exponentially growing) for $0 < \beta_y < 1$; the regions in the parameter space spanned by a_y and q_y for which these inequalities hold are called *stability regions*.

The stability for trapping an ion depends also on the analogous Mathieu equation for the z-direction, for which the parameters a_z and q_z are not independent from a_y and q_y. In addition, the static trapping along the x-direction demands for $a_y, a_z < 0$ (Drewsen and Brøner 2000), so that the intersection of these stability regions for the different directions gives the overall stability diagram for the linear Paul trap (Paul 1990; Drewsen and Brøner 2000; Leibfried et al. 2003).

Most, if not all experiments with trapped ions cited in this thesis are operating in the lowest stability region for which $|a_y|, |q_y| \ll 1$, with the time-dependent field oscillating in the radio-frequency range of hundreds of kHz up to several MHz. In this region, one can assume that the higher terms in Eq. (1.6) are negligible, as the higher coefficients $c_{\pm 2k}$ vanish for small q values (Leibfried et al. 2003). Keeping just the lowest terms (Leibfried et al. 2003), the solution turns into the much simpler form

$$y(t) \approx A c_0 \cos(\beta_y t)\left[1 + \frac{c_2}{c_0}\cos(2t)\right]. \tag{1.7}$$

Approximating $\beta_y \approx \sqrt{a_y + q_y^2/2}$ (McLachlan 1947; Leibfried et al. 2003) and converting back to real units, the motion of the ion $y(t)$ can be decomposed into two parts by $y(t) = Y(t) + \zeta_y(t)$. The *secular motion* $Y(t)$ is a harmonic oscillation with angular frequency

$$\nu_y = \beta_y \Omega_{\mathrm{rf}}/2, \tag{1.8}$$

and $\zeta_y(t)$ is a superposed harmonic oscillation at the rf-frequency Ω_{rf}. The latter has an amplitude that is smaller by a factor of $q_y/2$ than the secular motion and is therefore called *micromotion*.[7]

The secular motion can also be obtained by replacing the time-dependent potential energy with an effective energy or *pseudopotential* (Landau and Lifschitz 1969a, Ch. V, § 30, pp. 93ff.; Dehmelt 1968). A charged particle oscillating in an inhomogeneous electric field experiences a net force over the average of a period; the mean position thus moves as if it were subjected to an effective (mechanical) potential, which is rewritten as a harmonic potential,

$$V(Y) = \frac{1}{2} m \nu_y^2 Y^2, \tag{1.9}$$

7 The advantage of the linear ion trap is the two-dimensional rf-potential, which causes the micromotion to vanish along the whole trapping axis, whereas in the original Paul trap the rf-potential extends along all three spatial dimensions and the micromotion only vanishes strictly at the centre of the trap

with the secular angular frequency ν_y given in Eq. (1.8).

As the micromotion can be considered a small correction for $\mathfrak{q}_y \ll 1$, we may neglect it within the so-called *pseudopotential approximation* by approximating the motion by the secular oscillation, $y(t) \approx Y(t)$, in the following.

Similar, by repeating the steps as above we obtain a pseudopotential along the z-direction, given by $V(z) = \frac{1}{2}m\nu_z^2 z^2$, where ν_z can be adjusted to a different value than ν_y by adding an appropriate offset voltage to the electrodes (which changes $\mathfrak{a}_y$ and $\mathfrak{a}_z$). The trapping along the axial x-direction is given by the dc-voltages on the endcaps, which can be written as a harmonic confinement with axial trap angular frequency

$$\nu_x = \sqrt{\frac{4QU_0}{md_0^2}}\,. \tag{1.10}$$

We are going to retain this approximation for the remainder of this thesis.

Since in the following chapters we are going to analyse the quantum properties of the ion motion, we need to justify the assumption that this approximation carries over to the quantized description. The quantum motion of a single ion inside a Paul trap has been discussed in several articles (Cook et al. 1985; Combescure 1986; Brown 1991; Stenholm 1992; Glauber 2007). Despite the fact that the total energy is not conserved – as the Hamiltonian is time-dependent –, it is still possible to define a basis of quasi-stationary states with a fixed excitation or quasi-energy[8] similar to the energy eigenstates of a harmonic oscillator. Further, it is possible to define creation and annihilation operators that connect these states of different quasi-energy just like for the harmonic oscillator in a static potential. What is more, the analogues to coherent states can be constructed as eigenstates of the annihilation operator. Astonishingly, the wave packets of these quasi-coherent states follow classical trajectories and their width does not spread out, but rather keeps pulsating or breathing periodically with the period $T_{\mathrm{rf}} = 2\pi/\Omega_{\mathrm{rf}}$ (Glauber 2007). Although the kinetic energy associated with the micromotion is of the same order as the energy of the secular motion (Berkeland et al. 1998), for high values of radio-frequency (compared to the secular angular frequency ν) it is sensible to average this breathing of the wavepacket width over one period of the rf-driving field (Cook et al. 1985) and to quantize only the motion resulting from the harmonic pseudopotential within the approximation described above.

8 These are in fact the quasi-energies of the Floquet formalism when applied to the Mathieu equation (Combescure 1986; Glauber 2007). The Floquet formalism is a commonly applied technique to solve the Schrödinger equation with a time-periodic Hamiltonian (Chu et al. 1985).

1.1.4 *Miscellaneous Requirements for Trapped Ion Experiments*

Besides trapping ions with fields, it is necessary to isolate them from the perturbations originating from the surroundings, such as interactions with other particles or fluctuating electromagnetic fields. In particular, by so-called background gas collisions with gas particles surrounding the trap, the momentum of such a gas particle can be transferred to an ion such that it gains enough kinetic energy to leave the trap. Another possible occurrence is the induction of a chemical reaction, caused by the collision of an atom or molecule with a trapped ion, forming a molecular ion which replaces the original ion in the trap. In order to avoid such collisions as much as possible, the ion trap is mounted inside a vacuum chamber operating in an ultra-high vacuum with typical pressures around 10^{-8} Pa, ensuring a low density of the residual gas inside the vacuum chamber.

For trapping ions of a desired element (or isotope), typically an oven filled with that element is mounted inside the vacuum chamber, which is usually heated to some hundred degrees Celsius such that atoms evaporate at a sufficiently high rate. Before reaching the trap centre these atoms are ionized e. g. by electron impact ionization or photo-ionization. Those ions with a kinetic energy below a certain threshold are eventually trapped. For further discussion of technological requirements see Ghosh (1995, Ch. 4) or Major et al. (2005, Ch. 5 and App. E).

Initially, the trapped ions form a hot cloud or plasma, where the individual particles follow complicated trajectories with a kinetic energy typically much larger than the energy of the Coulomb interaction between the ions. For the preparation of an ion Coulomb crystal, the temperature has to be reduced to a few mK by appropriate cooling methods (Itano, Bergquist et al. 1995; Ghosh 1995, Ch. 5; Major et al. 2005, Ch. 10–15).

1.2 PHYSICS OF TRAPPED IONS – PLASMAS AND CRYSTALS

We now turn to the physics of many trapped ions, in particular that of trapped plasmas and ion Coulomb crystals. For typical densities around $10^{10}\,\mathrm{cm}^{-3}$ and temperatures of several mK, quantum effects are unimportant for the thermodynamic properties of the system, so we shall first discuss the classical energy of the system.

1.2.1 *Classical Energy of the System*

The classical dynamics of the trapped ions is determined by the classical energy of the system. For this, we assume that N atomic ions of

equal mass m and equal charge Q are confined and sufficiently cold such that their trajectories remain close to the trap centre. We shall now label the ions by the index $n = 1, \ldots, N$, so that

$$\mathbf{r}_n = x_n \hat{\mathbf{x}} + y_n \hat{\mathbf{y}} + z_n \hat{\mathbf{z}} \,, \tag{1.11}$$

denotes the position vector from the coordinate origin to the nth, where $\hat{\mathbf{x}}$, $\hat{\mathbf{y}}$ and $\hat{\mathbf{z}}$ are the unit vectors in the x-, y- and z-direction, respectively.

Let us summarize the list of assumptions and approximations we are going to apply in order to have a simple and tractable description for the ions in the trap. The approximations are as follows:

1) We shall neglect the form of the electrodes and assume that the equipotential surfaces are perfect hyperboloids of revolution, so any effects originating from the form of the electrodes or from the finite size of the trapping apparatus are neglected.

2) In the case of the Paul trap we shall employ the *pseudopotential* approximation, i. e. we neglect any effects caused by the fast oscillation of the electric field leading to micromotion and substitute the actual time-dependent potential energy with a static harmonic potential. In the case of the Penning trap, we shall assume that the total classical[9] angular momentum of the ions is zero, which is the condition for not having a complicated interplay between cyclotron-like and magnetron motion (Major et al. 2005, Ch. 3). It is then possible to change into a coordinate frame that is rotating at half the cyclotron frequency (Landau and Lifschitz 1969a, Ch. VI, §39, pp. 128f.), in which the effective potential appears harmonic (Dubin and O'Neil 1999, p. 92).[10]

3) We also shall neglect the effect of the image charges induced at the surface of the electrodes, which can become important for large ion numbers. Further, any other effects originating from charges on the surface of the trap electrodes or the insulating material between them are neglected. Actually, these charges, called patch-charges, are suspected to be the origin of heating effects which can not be explained solely by temperature effects (Häffner et al. 2008, Sec. 3.2).

These approximations affect the potential energy of the trapping potential, which is now replaced in all three spatial dimensions by a pure

9 The total classical angular momentum is not taking the spin and orbital angular momenta of the electrons and the nuclei into account.

10 It is also possible to calculate the structures of Coulomb crystals and their dynamics in the case of non-zero total classical angular momentum and without the need for transformation into a special rotating frame (Baltrusch, Negretti et al. 2011; Wang et al. 2013).

harmonic potential energy. The angular frequencies of the pseudopotential depend on the mass and charge of the trapped ions. As we assume that all ions are of the same atomic isotope and are ionized by the same number of electrons, they all have the same mass and same charge. In that case, the pseudopotential takes the following simple harmonic form,

$$V_{\text{trap}}(\mathbf{r}_n) = \frac{m}{2}\left(\nu_x^2 x_n^2 + \nu_y^2 y_n^2 + \nu_z^2 z_n^2\right), \tag{1.12}$$

where the angular *trap frequencies* ν_x, ν_y and ν_z are along the axes x, y and z, respectively, and depend on the mass m and charge Q as well as on the rf-angular frequency Ω_{rf} applied to the electrodes, see Eqs. (1.5), (1.8) and (1.10).

The total potential energy is the sum of the trap potential, Eq. (1.12), and the unscreened[11] Coulomb interaction energy,

$$V_{\text{pot}} = V_{\text{trap}} + V_{\text{Coul}}\,. \tag{1.13}$$

The Coulomb interaction energy is summed up over the contribution of all mutual pairs of charges,

$$V_{\text{Coul}} = \frac{1}{2}\sum_{n=1}^{N}\sum_{\substack{k=1\\k\neq n}}^{N}\frac{Q^2}{4\pi\epsilon_0}\frac{1}{\|\mathbf{r}_n - \mathbf{r}_k\|}\,, \tag{1.14}$$

were ϵ_0 is the vacuum permittivity and $\|\cdot\|$ is the Euclidean norm in $\mathbb{R}^3$, specifying the distance between the ions.

Together with the kinetic energy of the ions, we can write down a Lagrangian function (Landau and Lifschitz 1969a, Ch. I, §5; Goldstein 1950, Ch. I, Sec. 1-4) for the system,

$$\mathcal{L} = T_{\text{kin}} - V_{\text{pot}}\,. \tag{1.15}$$

By following the standard procedure (Landau and Lifschitz 1969a, Ch. II, § 7 and Ch. VII, § 40; Goldstein 1950, Ch. VII, Sec. 7-1), we obtain the canonical momenta $\mathbf{p}_n$ for all $n = 1, \ldots, N$,

$$\mathbf{p}_n = \frac{\partial \mathcal{L}}{\partial \dot{\mathbf{r}}_\mathbf{n}}\,, \tag{1.16}$$

and derive the classical Hamiltonian function from the Lagrangian function. This consists of three parts

$$H = T_{\text{kin}} + V_{\text{Coul}} + V_{\text{trap}}\,, \tag{1.17}$$

11 In the field of plasma physics and for the classical theory of electrons in metals one usually takes a *screened* Coulomb interaction into account. In this case, a continuum theory with an uniform charge background is used, while the discrete size of the charge carriers is neglected. If an impurity charge is immersed under these conditions, the free charge carriers of the charge background move to shield the field so that the Coulomb interaction gets screened, which usually gives rise to an additional exponential damping factor in Eq. (2.2) as a function of the distance between two charges.

where the kinetic energy in terms of the canonical momenta (and in absence of magnetic fields) reads

$$T_{\text{kin}} = \sum_{n=1}^{N} \frac{\mathbf{p}_n^2}{2m}\,, \tag{1.18}$$

while the other two terms are identical to those given above in Eqs. (1.12) and (2.2). The equations of motion are then given by Hamilton's equation (Landau and Lifschitz 1969a, Ch. VII, § 40),

$$\dot{p}_{n,\nu} = -\,\partial H/\partial q_{n,\nu}\ , \qquad \dot{q}_{n,\nu} = \partial H/\partial p_{n,\nu}\ . \tag{1.19}$$

Dimensionless Hamiltonian

It is useful to recast the Hamiltonian function in a dimensionless form. Basically, this means rescaling all lengths, time scales, and masses by some characteristic length, time scale, and mass of the system. These characteristic scale units can be chosen arbitrarily for the independent base units, but need to be chosen consistently for all derived quantities. As we are interested in effects resulting from the interaction between the ions, a sensible choice for the scaling is such that the Coulomb interaction energy of two ions separated by the unit distance is scaled to unity.[12] For this, we introduce a length scale $\bar{l}$ by which we define new dimensionless position vectors $\mathbf{r}'_n = \mathbf{r}_n/\bar{l}$. Instead of using a time scale, we could alternatively use a frequency scale $\bar{f}$ such that the dimensionless frequencies are defined by $\nu'_k = 2\pi \times f'_k = 2\pi(f_k/\bar{f}) = \nu_k/\bar{\nu}$ (implying $\bar{f} = \bar{\nu}$, as all quantities with the same units transform by the same scale factor), where $\bar{\nu}$ is the scale quantity for angular frequencies which could be used equivalently. Finally,[13] the dimensionless masses are given by $m' = m/\bar{m}$, where $\bar{m}$ is the characteristic mass. Any other quantities can be rescaled in terms of these base units, e.g. the energy is rescaled by dividing it by a factor $\bar{m}\bar{l}^2\bar{\nu}^2$. With this, we can rewrite the total Hamiltonian function Eq. (1.17), where we choose the value of these scale factors such that we can eliminate most of the constants in front of the terms of the Hamiltonian. So, by choosing the length scale as

$$\bar{l} = Q^{2/3}/(4\pi\epsilon_0\bar{m}\bar{\nu}^2)^{1/3} \tag{1.20}$$

12 These could be any two ions at this distance, not necessarily neighbouring ones; yet, as we are going to see below, the distance between the ions in a crystal will be of the order of the unit distance for the scaling chosen.

13 There is no need to also transform the electrical charges, as one might expect initially, for the Ampere being defined as another basic unit in the international SI unit system. The reason for defining the Ampere as a basic unit is to avoid having non-integer exponents of basic units in the definition of other frequently used units. In other unit systems, charge is given in units of $(\text{Length})^{3/2}(\text{Mass})^{1/2}(\text{Time})^{-1}$, e. g. in the cgs-unit systems, the electric charge is given in Franklin ($1\text{Fr} = 1\,\text{g}^{1/2}\,\text{cm}^{3/2}\,\text{s}^{-1}$).

and rescaling the energy as stated above, we get rid of all constants in front of the Coulomb interaction term. We are then free to choose the remaining scaling quantities, e. g. such as

$$\bar{m} = m\,, \qquad\qquad \bar{\nu} = \nu_x\,. \tag{1.21}$$

Here, we arbitrarily took ν_x as the reference scale for the angular frequencies. It could have been any of the angular trap frequencies, or even some other (angular) frequency, but as we are assuming a fixed angular axial trap frequency in the following chapters, it is convenient for us to choose this quantity as the reference scale.

Using these scaled quantities, the dimensionless terms in the Hamiltonian read

$$T_{\text{kin}} = \frac{1}{2}\sum_{n=1}^{N} \mathbf{p}_n^2\,, \tag{1.22a}$$

$$V_{\text{trap}} = \frac{1}{2}\sum_{n=1}^{N} \left(\alpha_x x_n^2 + \alpha_y y_n^2 + \alpha_z z_n^2\right), \tag{1.22b}$$

$$V_{\text{Coul}} = \frac{1}{2}\sum_{n=1}^{N}\sum_{\substack{k=1\\k\neq n}}^{N} \frac{1}{\|\mathbf{r}_n - \mathbf{r}_k\|}\,, \tag{1.22c}$$

where we have replaced the unprimed quantities by the primed ones (not shown) and dropped the primes outright in order to keep the notation simple. An overview for all scale factors is given in Table 1.1. Further, in Eq. (1.22b) we have defined the dimensionless parameters α_x, α_y and α_z, given by

$$\alpha_x = \frac{\nu_x^2}{\bar{\nu}^2}\,, \qquad \alpha_y = \frac{\nu_y^2}{\bar{\nu}^2}\,, \qquad \alpha_z = \frac{\nu_z^2}{\bar{\nu}^2}\,. \tag{1.23a}$$

These are the *anisotropy parameters* in the y- and z-directions, which determine the shape of the cloud and crystals in the trap, as discussed in the following sections. Since we have already defined the scale parameter for the angular frequencies by $\bar{\nu} = \nu_x$, the anisotropy parameters are given by

$$\alpha_x = \frac{\nu_x^2}{\nu_x^2} = 1\,, \qquad \alpha_y = \frac{\nu_y^2}{\nu_x^2}\,, \qquad \alpha_z = \frac{\nu_z^2}{\nu_x^2}\,. \tag{1.23b}$$

1.2.2 *Plasmas and Crystals*

Consider now that a large number of ions is confined inside the trap apparatus, forming an ion cloud. At high temperatures, the ion cloud is not in the gas phase; a substance present in the gas phase consists

quantity	scale factor	value
length	$\bar{l}$	$Q^{2/3}/(4\pi\epsilon_0 m\nu_x^2)^{1/3}$
mass	$\bar{m}$	m
time	$1/\bar{\nu}$	$1/\nu_x$
frequency	$\bar{\nu}$	ν_x
angular frequency	$\bar{\nu}$	ν_x
energy	$\bar{m}\bar{\nu}^2\bar{l}^2$	$m\nu_x^2\bar{l}^2$

Table 1.1: Conversion table for dimensionless quantities

of neutral particles with a weak short-range interaction such as van-der-Waals forces. An ion cloud, of course, is composed of charged particles interacting via the long-ranged Coulomb interaction and thus is not in the gas phase but in the *plasma* phase. A plasma features a class of physical phenomena absent in real gases, for example oscillations of the charge density, called plasma oscillations, which have a frequency that is approximately independent of the wave length of the oscillation.[14]

Many of the plasmas that are observed in nature or in experiments emerge from a neutral gas where the neutral particles are ionized and separated into electrons and ions, which together compose a neutral two-component plasma. In the case of the trapped ion cloud we have a *non-neutral one-component plasma*. A one-component plasma consists only of one kind of charge carriers – ions or electrons –, hence it is non-neutral by definition. Unlike for neutral plasmas, recombination of charge carriers is not possible for a one-component plasma at cold temperatures due to the absence of any charge carriers of opposite charge. Also, non-neutral plasmas can be trapped by static fields and simultaneously stay in a thermal equilibrium state, which is not possible for neutral plasmas (the different sign of the charges prevents the two components from having the same Boltzmann distribution *and* being confined at the same time; see Dubin and O'Neil 1999, pp. 95f.).

Another specific feature of these plasmas is that in thermal equilibrium the density is nearly homogeneous over the whole sample. The sum of the external (effective) potential and of the interaction potential has to stay constant within the cloud at equilibrium. Evaluating the self-consistent Poisson equation gives a constant density for harmonic

14 This phenomenon is actually responsible for the reflection of electromagnetic radiation with frequencies below the plasma frequency of the electrons inside a metal, which happens for radio frequency up to optical frequencies (for higher frequencies, i. e. UV-light, X-ray and higher, the radiation is absorbed by the metal).

confinement (Dubin and O'Neil 1999, pp. 98–99). The density drops to zero close to the edges, within a distance of about the Debye length, $\lambda_D = (\epsilon_0 k_B T / nQ^2)$, which is of the order of milli- to micrometers or even smaller, depending on temperature and density.[15]

By cooling down the ionic plasma (for an overview of different cooling techniques see Major et al. 2005, Part V; Ghosh 1995, Ch. 5; Riehle 2005, Sec. 10.2.2), the kinetic energy of the ions decreases such that the cloud becomes denser, by which in turn the Coulomb interaction energy increases. By further cooling the ions, they condense first into a liquid-like phase and then eventually into a phase with long-range order, which is called an *ion Coulomb crystal*, first observed experimentally by Diedrich, Peik et al. (1987); Wineland, Bergquist et al. (1987). The transitions between these phases are characterised by the so-called *coupling parameter* Γ, which is defined as the ratio between the mean Coulomb interaction energy and the mean kinetic energy of the particles,

$$\Gamma = \frac{e^2}{4\pi\epsilon_0 a_{WS}} \frac{1}{k_B T} . \tag{1.24}$$

Here, k_B is the Boltzmann constant and T the temperature of the ion sample. The Wigner-Seitz radius a_{WS} is defined as the radius of a sphere of volume that equals the average volume occupied by one particle, i. e. $4\pi a_{WS}^3/3 \times n = 1$, where n is the average particle density.

For an infinite homogeneous system, calculations (Dubin and O'Neil 1999, pp. 113–115) predict the appearance of strong correlations around a value of $\Gamma \approx 2$ and that of long-range order for a value of $\Gamma > 174$, which is believed to be a first-order phase transition from a liquid-like state to a body-centered cubic (bcc) crystal for an isotropic confinement (meaning $\alpha_x = \alpha_y = \alpha_z$). The corresponding temperature at which this transition happens depends on the inter-particle density; for typical experimental realizations with ionic plasmas it occurs at around 1 to 10 mK (Bollinger et al. 1994).

Shapes

When the confinement is anisotropic, different structures may occur upon crystallization. In fact, the anisotropy parameters defined in Eq. (1.23a) determine the shape of the plasma cloud of ions or the crystal structure, respectively. The shape can vary from flat pancake-like two-dimensional over disc-shaped and spherical three-dimensional forms to elongated cigar-shaped and quasi-one-dimensional chain-like shapes. In the crystalline phase, these different shapes also have various crystalline structures, which we discuss in the next section.

15 This is apparently only true for plasmas for which the Debye length is much greater than the typical ion separation.

1.3 CRYSTALLINE STRUCTURES AND STRUCTURAL TRANSITIONS

Suppose that the ion cloud has been cooled down to such a low temperature that the ion cloud forms a crystal. The ions are then localized close to some fixed equilibrium positions around which they are oscillating.

The equilibrium positions are determined by the balance of forces coming from the trap potential and the mutual interaction between the ions. This condition can be written quantitatively by requiring that the gradient of the total potential with respect to every particle coordinate vanishes at equilibrium,

$$\boldsymbol{\nabla}_{\mathbf{r}_n} V(\mathbf{r}_1, \ldots, \mathbf{r}_N) = 0 \qquad \forall n = 1, \ldots, N\,. \tag{1.25}$$

The equilibrium positions of the ions $\{\mathbf{R}_n\}$ are found by the solution of these $3N$ equations. These are not spaced equidistantly because the ions farther outside experience a stronger force from the trapping potential, thus pressing the inner ions together to agglomerate more densely in the centre. Yet, for large crystals, the inner part of the crystal is described to a good approximation by a periodic lattice. The onset of long-range order can be analysed by e. g. a two-particle correlation function, which transforms from a smooth distribution for a plasma to one with clear distinct peaks (Dubin and O'Neil 1999, pp. 120–122) for a crystal. For small crystals, however, the equilibrium positions of the ions do not coincide with a regular lattice.

1.3.1 *Overview of Crystalline Structures*

Depending on the anisotropy parameters, the ion crystal takes different shapes and the ions arrange themselves inside the crystal in

anisotropy	dimensions	shape	crystal structures
$\alpha_x \gg \alpha_y \approx \alpha_z$	2	pancake-like	hexagonal
$\alpha_x > \alpha_y \approx \alpha_z$	3	oblate	multiple planes, shells
$\alpha_x \approx \alpha_y \approx \alpha_z$	3	spherical	shells
$\alpha_x < \alpha_y \approx \alpha_z$	3	prolate	shells, tubes
$\alpha_x \ll \alpha_y \approx \alpha_z$	3	chain	helical
	2	chain	zigzag
	1	chain	linear

Table 1.2: Overview of crystal shapes and lattice structures. Quantitative relations were obtained by Dubin (1993) and measured by Birkl et al. (1992).

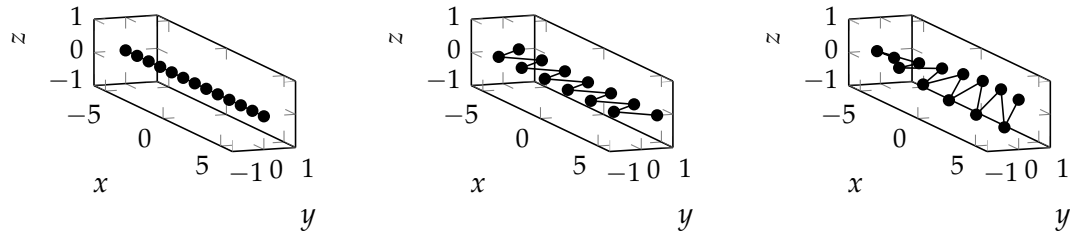

Figure 1.5: Schematic drawing of the crystal structures of Coulomb chains. The ions are spaced equidistantly along the x-axis, an arrangement found in the middle of large chains. (a) For strong confinement along the y and z-direction, the crystal is in a linear chain configuration. (b) For weaker transverse confinement, the ions align within a plane in a zigzag structure with alternating positions. (c) For even weaker transverse confinement the ions take a three-dimensional structure where the zigzag gets tilted into a helical structure.

different lattice structures. In the case of two anisotropy parameters being equal and one being much larger than the other two, e. g. $\alpha_x \gg \alpha_y \approx \alpha_z$, the shape of the crystal is pancake-like. In the most extreme case, the crystal is forms only a single layer with a hexagonal lattice as crystal structure. Decreasing the large anisotropy parameter causes the crystal to align in multiple planes, with different structures such as square or bcc lattices (Dubin and O'Neil 1999, pp. 140–146). Then, for real three-dimensional structures, shell structures appear with different crystal lattices within the shells.

On the other extreme, where one anisotropy parameter is much smaller than the other two, e. g. $\alpha_x \ll \alpha_y, \alpha_z$, the crystal forms a quasi-one-dimensional chain, i. e. its dimensions perpendicular to the axis with the smallest confinement are of the order of the mean-ion separation. The most extreme case of this is a *linear chain*, where all ions are arranged exactly on the axis next to each other; see Figure 1.5a for a schematic drawing. Reducing the inequality between the anistropy parameters $\alpha_x < \alpha_y, \alpha_z$, i. e. opening the trapping in the directions transverse to the chain, or equivalently increasing the trapping frequency along the chain, causes the linear chain to undergo a transition to a planar, so-called *zigzag structure*, see Figure 1.5b. In this configuration, the ions deviate away from the axis in alternating directions such that they minimize their interaction energy by increasing their mutual distance. We shall discuss these two structures and the transition between them in more detail in the next section. By further decreasing the anisotropy inequality, the zigzag gets twisted into a three-dimensional helical structure as shown in Figure 1.5c, and after that assumes even more complicated structures arranged in shells (Dubin and O'Neil 1999, p. 136).

In this thesis, we only discuss the linear chain and the zigzag chain and the transition between these two configurations.

1.3.2 *Linear and Zigzag Structures and the Linear–Zigzag Transition*

Linear Chain

In the case of high anisotropy, meaning one anisotropy parameter much smaller than the other two, the ions align in a linear chain where they are arrayed periodically along one axis. The distance between them is given by the lattice constant a and is constant along the axis (until boundary effects become important).

In the limit where the system can be regarded[16] as infinite and homogeneous, a solution of the eigenmodes and eigenfrequencies is feasible (Morigi and Fishman 2004). Experimentally, this situation is reached by putting the ions into a storage ring as realized by Birkl et al. (1992); Waki et al. (1992) and Schätz et al. (2001). That device is basically a linear Paul trap, only with the endcaps removed; instead the trap is elongated and bent with a large radius such that the electrodes form closed rings (Church 1969). If the radii of these ring electrodes are large enough, their curvature may be neglected. The ions then arrange themselves evenly spaced along the ring (with a equal to the mean circumference of the ring divided by the number of ions). This corresponds to the theoretical description of a crystal with periodic boundary conditions.

The symmetries of this crystal configuration are: (i) translation by a along the axis; (ii) reflection at planes perpendicular to the crystal axis containing an ion; (iii) reflection at planes perpendicular to the crystal axis in the middle of two ions, and (iv) all possible point group transformations in the plane perpendicular to the crystal axes, i. e. of the continuous symmetry group $O(2)$, which is called the orthogonal group. The latter symmetry transformation also contains the reflection at the axis; the result is the same as that of a π-rotation around the axis.

Zigzag Chain

If the ratio between the anisotropy parameters is reduced, the mutual Coulomb repulsion between the ions becomes stronger in comparison to the transverse trapping (by either increasing the confinement in axial direction or by releasing it in transverse direction). There exists a critical value for the ratio between the anisotropy parameters (or the trapping frequencies) for which the linear chain is still a stable configuration. If the ratio is reduced further, the ion is located at the equilibrium positions of the linear chain are still force-free but do not remain stable. Instead, another possible solution of equilibrium positions appears where the equilibrium positions are located away

16 The confinement along the chain has to vanish for the density to stay constant.

from the axis. The change of equilibrium positions is continuous, meaning that for an infinitesimal decrease of the anisotropy ratio below the critical one, there will be only an infinitesimal deviation of the equilibrium positions away from the axis. The new set of equilibrium positions has the property that all ions are arranged within a single plane going through the trap axis. The orientation of this plane is fixed if the anisotropy parameters in the directions perpendicular to the trap axis are different – either due to choosing intentionally different voltages on the electrodes or having a small difference in the field strengths because of alignment errors, unbalanced or fluctuating electric circuits, or other unwanted stray fields.

But even in the case of a perfectly symmetric device and carefully adjusted voltages on the electrodes, and despite the fact that the Hamiltonian of the system is invariant under rotations around the crystal axis, the crystal aligns itself spontaneously in a single plane.

Within the plane, the symmetries of the crystal configuration[17] are given by: (i) translation by a along the axis together with a reflection at the axis; (ii) reflection at planes perpendicular to the trap axis containing an ion, and (iii) point reflection in the middle of two ions.

The Linear–Zigzag Transition

In ion crystals, the linear–zigzag transition has been studied numerically by Molecular Dynamics simulations (Schiffer 1993), by Monte Carlo simulations (Piacente et al. 2004), and by density functional theory (Dubin 1997, see also Dubin and O'Neil 1999). For a long time it was suspected that this transition is a second-order phase transition in the thermodynamic limit. Fishman et al. (2008) have shown that in the classical limit the linear–zigzag transition is indeed a second-order phase transition described by the Landau model (Landau 1965, Ch. 29, pp. 193f., and Ch. 73, pp. 546f.; Landau and Lifschitz 1969b, Ch. XIV), and Shimshoni et al. (2011b,a) have shown that this transition at $T = 0$ is a *quantum phase transition* that, in two dimensions (in a plane), is of the same universality class as the Ising model in a transverse field (Huang 1987, Ch. 14). Additionally, Silvi et al. (2013) have confirmed this mapping by sophisticated numerical studies using a density matrix renormalization group algorithm.

For describing the structural phase transition in the thermodynamic limit, the phase in which the symmetry is still present is called the disordered phase, whereas the phase with the broken symmetry is denoted as the ordered phase. These phases are distinguished by a suitable order parameter, which is usually described by a continuous field; in our case, the order parameter is the displacement of the zigzag mode. In the disordered phase, the mean value of the order parameter

17 The symmetries of the Hamiltonian are unchanged with respect to the linear chain.

is zero (for one specific spatial point the order parameter takes a random value in the presence of thermal or quantum fluctuations, thus the term disordered phase), and it takes a finite value in the ordered phase. In general, in the symmetry-broken phase the order parameter has two or more equivalent possible values, attaining a specific value randomly. The main idea of Landau theory is to expand the relevant thermodynamic potential in terms of the order parameter around the critical point of the phase transition.

In the disordered phase, the *soft mode* – which is a term usually used in the realm of critical phenomena in statistical mechanics to denote the mode of vanishing excitation energies (in the case of a continuous broken symmetry this is just the appearing Goldstone mode) – is the zigzag mode. For this mode, the ions move in alternating direction in a single plane; here it is the transverse mode with the shortest wavelength, in contrast to the long wavelength modes associated with a phase transition in the case of ferroelectric crystals (Cochran 1960, 1961; Ginzburg 1987). The frequency of this mode vanishes at the critical point and attains an imaginary frequency below the critical point. Thus the equilibrium positions of the crystal in the disordered phase become unstable; however, there appears a new set of equilibrium positions, around which the zigzag configuration is build up.

Structural Defects

So far, we have discussed only the lowest energy configurations. Yet, meta-stable structural configurations are possible, too, which can be associated with *structural defects* of the crystal lattice; these kinds of defects typically result from a fast change of the trapping potential, a so-called *quench*, across the structural instability. Surprisingly,[18] the abundance of these defects in dependence upon the quench rate of the external potential can be predicted for quenches across any kind of phase transitions by a universal scaling law (see del Campo and Zurek 2014, and references cited therein). In the context of trapped ion Coulomb crystals, such defects have been studied theoretically (del Campo, De Chiara et al. 2010; Landa, Marcovitch et al. 2010) and have been observed experimentally (Mielenz et al. 2013; Keller et al. 2013; Ulm et al. 2013). Most interestingly, a recent theoretical proposal (Dziarmaga et al. 2011) suggested the superposition of structural defects in a quantum Ising chain, which could possibly be applied to structural defects in ion Coulomb crystals as well.

18 It is surprising in the sense that the scaling law describes a *non-equilibrium* response of a system across a phase transition by critical exponents which are derived in *thermodynamic equilibrium* (del Campo and Zurek 2014).

Spontaneous Symmetry Breaking

Even if the Hamiltonian (or equivalently the Lagrangian) of a system is invariant under a certain symmetry, its ground state or lowest-energy configuration does not need to preserve that symmetry: It might be that there is a set of two or more degenerate configurations (i. e. they have the same energy) that do not meet the symmetry individually, but which are transformed by the symmetry operation into each other. In the example of the zigzag chain locked in a plane, each of the two classical equilibrium configurations does not meet the reflection symmetry along the main crystal axis, but the two configurations transform into each other by reflecting their positions on the axis.

In quantum mechanics the ground state still preserves the symmetries of the Hamiltonian. For instance, consider the one-dimensional motion of a particle in a symmetric double well where the wells are sufficiently deep for the potential barrier to be much higher than the lowest energy levels. Naïvely, one could argue that the ground state is given by a wavefunction centred around one of the two potential minima as if the potential were locally approximated by its second-order Taylor expansion around the corresponding minima. One would then assume two equivalent "ground states", one for the left and right well respectively. However, the wavefunctions of the left and the right "ground states" extend across the potential barrier such that they have a non-zero overlap and thus a non-zero transition probability for tunnelling from one well to the other. Therefore, these "ground states" cannot be energy eigenstates of the system. The proper ground state is given by a wavefunction that is symmetric in both wells, which is approximately given by the *symmetric superposition* of the left and the right "ground states".[19]

Yet, in real physical systems the double well (or the system in general) is not isolated from its surrounding environment. Depending on the details of the environment, the type of the interaction between system and environment and the temperature of the environment, the state of the particle can become localized in one of the minima of the double well (Leggett et al. 1987). The origin of this localization may be understood as follows: Because of the entanglement of the particle with its surrounding environment we cannot describe the sub-state of the particle by a pure quantum state but need to represent it as

19 The left and right "ground states" are given by the sum and difference of the actual ground state and the first excited state, which has an anti-symmetric wavefunction. The energy difference between the ground state and the first excited state is commonly called *ground state splitting*, and it determines the tunnelling rate between the left and the right state. This energy splitting can be calculated approximately by the WKB-approximation (Landau and Lifschitz 1965, Ch. VII, § 50, Problem 3, p. 175; Bender and Orszag 1978, Ch. 10, Problem 10.45) or by the instanton method (Coleman 1979), yielding the same result (Garg 2000).

a mixed state, which is obtained from the total entangled state of system and environment by tracing out the degrees of freedom of the environment (Simonius 1978). The wavefunction of the particle thus becomes localized in the left or the right well with equal probability in the case of a symmetric double well.[20] This kind of processes, where the system attains a asymmetric state despite everything in the system including the Hamiltonian is symmetric, is called *spontaneous symmetry breaking*.

The theory of ferromagnetism (Heisenberg 1928) is maybe the most prominent representative of a system in which spontaneous symmetry breaking occurs. Exceeding the Curie temperature results in a disordering of the magnetic moments in the metal lattice so no preferred direction exists, meaning that the system is rotationally invariant (depending on the symmetries of the lattice). Below the Curie temperature, a macroscopic magnetization occurs in some specific but *random* direction. The magnetization thus is asymmetric although the Hamiltonian of the system perfectly fulfils the symmetry.

If the symmetry broken is a continuous symmetry, there is always a specific kind of excitation emerging in the system (Goldstone 1961; Goldstone et al. 1962), which is called a Nambu-Goldstone mode. This excitation, or mode, is now invariant with respect to the symmetry broken by the ground state. Moreover, this mode turns out to be gapless, i. e. in the dispersion relation the frequency is vanishing when the momentum approaches zero, $\omega(\mathbf{k}) \to 0$ for $\mathbf{k} \to 0$. In this mode, excitations can be created with infinitesimally small energy transfers to the system, and this mode connects the different ground states dynamically.

These kind of excitations are also responsible for the absence of ferromagnetic or antiferromagnetic order in the one- or two-dimensional isotropic Heisenberg models (Wagner 1966; Mermin and Wagner 1966; Hohenberg 1967), or generally for the absence of spontaneous symmetry breaking in two dimensions (Coleman 1973).

Although in this work we are not dealing with structural phase transitions in the thermodynamic limit but rather with small crystals composed of just a few ions, many of the phenomena discussed here turn up again in a related manner, as we are going to see in the following chapter.

20 Our reasoning does not rule out a mixed state in the eigenstate basis. The type of coupling plays a more crucial role here, as the type of system observable determines the type of steady states the system evolves to (Zurek 1981).

2

STATE-DEPENDENT STRUCTURES OF ION COULOMB CRYSTALS

The main goal of this chapter is to discuss the structures of ion Coulomb crystals in state-dependent potentials. We first review the crystal structures of small ion Coulomb crystals in absence of a state-dependent potential in Section 2.1. We present a proposal achieving a state-dependent trapping potential in Section 2.2. In Section 2.3, we discuss the observable structures for small ion Coulomb crystals in the presence of a state-dependent potential for different parameters, and analyse their stability regions.

2.1 SMALL ION COULOMB CRYSTALS IN HARMONIC POTENTIALS

In this section we review the features of a small ion Coulomb crystal homogeneously trapped in the potential of a standard trap.

2.1.1 *Setting the Stage*

In order to simplify the description, we adopt the approximations introduced in Section 1.2.1, which we summarize here:

1) We shall neglect the form of the electrodes and assume a perfect quadrupole potential with hyperboloids of revolution as equipotential surfaces.

2) We shall employ the *pseudopotential* approximation for the case of the Paul trap, i. e. replacing the time-dependent potential by an averaged harmonic potential. Equivalently, for the Penning trap we choose a crystal rotation where the coupling between momenta and coordinates vanishes.

3) We shall neglect the effect of image charges at the electrodes.

Hamiltonian of Trapped Ions

The potential energy of N trapped ions is composed of two parts, the potential energy originating from the trapping potential and the

potential energy originating from the mutual Coulomb interaction between the ions. The part originating from the trapping potential is given by the sum of the single-particle contributions,

$$V_{\text{trap}}(\mathbf{r}_1, \ldots, \mathbf{r}_N) = \sum_{n=1}^{N} \frac{m_n}{2} \left(\nu_{n,x}^2 x_n^2 + \nu_{n,y}^2 y_n^2 + \nu_{n,z}^2 z_n^2 \right), \tag{2.1}$$

where the mass of the ions might be different in general (see Home 2013 for a review of ion Coulomb crystals with different species). Eq. (2.1) takes into consideration that, in general, the trap frequencies are dependent on the mass and the charge of the ions, and thus may be different for different ion species. The potential energy originating from the mutual Coulomb interaction between the ions is given by

$$V_{\text{Coul}}(\mathbf{r}_1, \ldots, \mathbf{r}_N) = \frac{1}{2} \sum_{n=1}^{N} \sum_{\substack{l=1 \\ l \neq n}}^{N} \frac{Q_n Q_l}{4\pi\epsilon_0} \frac{1}{\|\mathbf{r}_n - \mathbf{r}_l\|}, \tag{2.2}$$

with ϵ_0 the vacuum permittivity and Q_n, Q_l the charges of the particles.[1] Together with the kinetic energy,

$$T_{\text{kin}}(\mathbf{p}_1, \ldots, \mathbf{p}_N) = \sum_{n=1}^{N} \frac{\mathbf{p}_n^2}{2m_n}, \tag{2.3}$$

we obtain the total classical Hamilton function of the system by the sum of the three terms,

$$H = T_{\text{kin}}(\mathbf{p}_1, \ldots, \mathbf{p}_N) + V_{\text{Coul}}(\mathbf{r}_1, \ldots, \mathbf{r}_N) + V_{\text{trap}}(\mathbf{r}_1, \ldots, \mathbf{r}_N). \tag{2.4}$$

Single Ion Species

Now let us assume that all ions have the same charge Q, which simplifies the Coulomb energy to

$$V_{\text{Coul}}(\mathbf{r}_1, \ldots, \mathbf{r}_N) = \frac{1}{2} \sum_{n=1}^{N} \sum_{\substack{l=1 \\ l \neq n}}^{N} \frac{Q^2}{4\pi\epsilon_0} \frac{1}{\|\mathbf{r}_n - \mathbf{r}_l\|}. \tag{2.5}$$

Similarly, we take it as given that all the ions have the same mass (they are of the same isotope), therefore the kinetic energy simplifies to

$$T_{\text{kin}}(\mathbf{p}_1, \ldots, \mathbf{p}_N) = \sum_{n=1}^{N} \frac{\mathbf{p}_n^2}{2m}. \tag{2.6}$$

Presupposing equal masses and charges, the pseudo-potential is the same for all ions, and we can assume that the potential is of the following form

$$V_{\text{trap}}(\mathbf{r}_1, \ldots, \mathbf{r}_N) = \frac{m}{2} \sum_{n=1}^{N} \left(\nu_x^2 x_n^2 + \nu_y^2 y_n^2 + \nu_z^2 z_n^2 \right), \tag{2.7}$$

1 For experiments with ion Coulomb crystals with differently charged ions, see Kwapień et al. (2007); Feldker, Pelzer et al. (2013).

with ν_x, ν_y and ν_z the angular trap frequencies along the axes x, y and z respectively. We refer to this situation where all ions experience the same trapping potential as *homogeneously trapped* ions.

Flat Land

We now employ an additional restriction by assuming that the confinement along one dimension is much stronger than that in the remaining two dimensions, e. g.

$$\nu_x, \nu_y \ll \nu_z \,, \tag{2.8}$$

with the z-direction being strongly confined. Further, we assume that the kinetic energy in the z-direction is negligibly small such that the motion along this direction can be considered as "frozen". For this to happen, the ion crystal needs to be laser cooled close to the motional ground state in the z-direction, such that

$$\langle n_{j,z} \rangle \ll 1 \quad \forall j \,, \tag{2.9}$$

where $\langle n_{j,z} \rangle$ are the quantum mechanical expectation values of the occupation numbers of the corresponding normal modes (labelled with j) in the z-direction. We shall apply this assumption throughout the remainder of the thesis with respect to the evaluated examples and numerical calculations while keeping the main discussion three-dimensional. For the dimensionless description along the lines of Eq. 1.2.1, only one anisotropy parameter is needed to describe the trap potential, so that we can write $\alpha_y = \alpha$ in the following.

Dimensionless Hamiltonian

For later convenience, we convert the Hamilton function into dimensionless variables just like in Section 1.2.1 on page 20f. The full Hamiltonian is given by

$$H = T_{\text{kin}}(\mathbf{p}_1, \ldots, \mathbf{p}_N) + V_{\text{trap}}(\mathbf{r}_1, \ldots, \mathbf{r}_N) + V_{\text{Coul}}(\mathbf{r}_1, \ldots, \mathbf{r}_N) \,. \tag{2.10}$$

Here, the dimensionless kinetic energy is given by

$$T_{\text{kin}}(\mathbf{p}_1, \ldots, \mathbf{p}_N) = \frac{1}{2} \sum_{n=1}^{N} \mathbf{p}_n^2 \,, \tag{2.11}$$

and the obtained dimensionless potentials are given by

$$V_{\text{trap}}(\mathbf{r}_1, \ldots, \mathbf{r}_N) = \frac{1}{2} \sum_{n=1}^{N} \left(x_n^2 + \alpha^2 y_n^2 \right) , \tag{2.12}$$

$$V_{\text{Coul}}(\mathbf{r}_1, \ldots, \mathbf{r}_N) = \frac{1}{2} \sum_{n=1}^{N} \sum_{\substack{l=1 \\ l \neq n}}^{N} \frac{1}{\|\mathbf{r}_n - \mathbf{r}_l\|} \,, \tag{2.13}$$

where we employ the same notation for the rescaled quantities as for the unscaled ones.

We will apply this dimensionless Hamiltonian for actual calculations, but keep the dimensions for the general derivations.

2.1.2 *Equilibrium Positions*

Let us first pay some attention to the classical trajectories of the ions. For Hamiltonian dynamics,[2] an *equilibrium state* is defined as a fix point of the dynamics in phase space spanned by the canonically conjugate variables. This means that the state of the system is not changing with time if its is initially prepared in the state at this fix point.

A fix point for Hamilton's equations is given when these all equate to zero,

$$\dot{q}_{n,\nu} = \frac{\partial H}{\partial p_{n,\nu}} = 0\,, \qquad \dot{p}_{n,\nu} = -\frac{\partial H}{\partial q_{n,\nu}} = 0\,. \tag{2.14}$$

When the kinetic energy depends only on the momenta and the potential energy depends only on the coordinates,[3] we find the following conditions:

i) The momenta should all be zero, $\mathbf{p}_n = 0 \quad \forall \quad n = 1, \ldots N$, such that all ions are at rest[4] and the kinetic energy is zero, $T_{\text{kin}} = 0$.

ii) All derivatives with respect to all coordinates of the potential energy need to vanish, so that we have to solve the following $3N$ equations:

$$\boldsymbol{\nabla}_{\mathbf{r}_n} V(\mathbf{r}_1, \ldots, \mathbf{r}_N) = 0 \qquad \forall n = 1, \ldots, N\,. \tag{2.15}$$

This is essentially the requirement that all the forces each ion experiences balance out, as a net residual force would lead to an acceleration and a dynamical evolution. The set[5] of positions fulfilling these equations are called *equilibrium positions*, denoted by $\{\mathbf{R}_1, \ldots, \mathbf{R}_N\}$, or $\{\mathbf{R}_n\}$ for short. We also might label them

2 For parametrically driven systems the more general concept of Lyapunov stability is applicable (Arnol'd 1980, Ch. 5, Sec. 25).

3 This is not the case for the Penning trap, in which the magnetic field couples momenta and coordinates such that they do not separate into kinetic and potential energy.

4 Actually, in the Paul trap the velocities of the ions are not zero because of the micromotion; for the full treatment of equilibrium states and their stability see Landa et al. (2012b,a).

5 The equilibrium positions constitute a set as the order of the equilibrium positions is not relevant for indistinguishable ions; the permutation of two positions leads to a completely equivalent physical situation. Also, the equilibrium positions of two ions cannot be identically for the divergence of the interaction energy, so each element can only appear once.

by an additional upper index, e. g. $\{\mathbf{R}_n^0\}, \{\mathbf{R}_n^1\}, \ldots$, if there is more than one possible set.

If the initial conditions are chosen to correspond exactly to the equilibrium positions with zero kinetic energy, the positions of the ions will remain stationary. However, small perturbations may change the positions by a tiny amount, which could lead the system to change its state to one very different from the initial state. So we need to additionally impose the concept of stability.

An equilibrium state is called *stable* if for any arbitrarily given region in phase space around that state one can find a subregion of initial conditions such that the dynamical evolution of the system remains bounded within the provided region for all times.

The stability of the equilibria is connected to the convexity of the energy of the system at the equilibrium state; the energy of the system increases if one moves away from the equilibrium in phase space, hence the equilibrium is a minimum of the energy. As the kinetic energy is convex, we find this condition to be equivalent to the potential energy having a strict minimum (Arnol'd 1980, Ch. 5, Sec. 22), such that around the equilibrium the particles experience forces which accelerate them back toward the positions of equilibrium.

Mathematically, this can be expressed by expanding the potential energy in a Taylor series around the equilibrium positions. At the point of equilibrium, the first order vanishes, so the first relevant term is of second order. Therefore, the stability is equivalent to checking the Hessian of the total potential evaluated at the equilibrium positions, given by

$$\mathscr{V}_{nl,\nu\lambda} = \frac{\partial^2}{\partial r_{n,\nu} \partial r_{l,\lambda}} \left[V_{\text{trap}}(\mathbf{r}_1, \ldots, \mathbf{r}_N) + V_{\text{Coul}}(\mathbf{r}_1, \ldots, \mathbf{r}_N) \right] \Big|_{\{\mathbf{R}_n\}} , \tag{2.16}$$

for positive-definiteness (the kinetic energy being positive-definite in any case):

$$\sum_{n,l,\nu,\lambda} \mathscr{V}_{nl,\nu,\lambda} \xi_{n\nu} \xi'_{l\lambda} > 0 \qquad \forall \quad \boldsymbol{\xi}, \boldsymbol{\xi}' \in \mathbb{R}^{3N} \setminus \{\mathbf{0}\} , \tag{2.17}$$

which is equivalent to all eigenvalues of matrix $\mathscr{V}$ being larger than zero.[6]

Let us summarize the two conditions for a stable equilibrium:

6 If a classical Goldstone mode exists, the Hessian would possess a zero eigenvalue, thus not fulfilling this strict requirement for stability. In fact, in this case motion is always allowed along the direction of the broken continuous symmetry, so the phase space for the coordinate belonging to the Goldstone mode would not be restricted. In the case of degeneracy of the two transverse trapping directions, this mode would be the rotation around the axial direction of the trap.

I) *The forces on the particles must balance out.*

II) *The eigenvalues of the Hessian matrix of the total potential evaluated at the equilibrium positions must be larger than zero.*

To find the stable equilibrium positions for a given set of parameters, we need to solve for Eq. (2.15) and evaluate the Hessian. Often, there is more than one possible set of equilibrium positions for a given set of parameters. But then, in most of the cases these sets are connected by the transformations leaving the symmetry of the Hamiltonian invariant. Yet, sometimes we also encounter situations where there is more than one type of solution for the equilibrium positions, a case usually referred to as *bistability* (see e. g. Cormick and Morigi 2012).

While in most cases it is necessary to solve the equations numerically, for three ions an analytical solution is feasible, as will be discussed in Section 2.1.4.

2.1.3 *Normal Modes*

We now restrict ourselves to an even smaller region of phase space than the stable region around the equilibrium point. We analyse the motion of the ions only for small deviations around their equilibria where we can linearise the forces acting upon them, thereby treating their dynamics similar to the mathematical pendulum in classical mechanics. We then decompose the position vectors of each ion $\mathbf{r}_n$ into the equilibrium position vector $\mathbf{R}_n$ and the deviation $\mathbf{q}_n$ away from it,

$$\mathbf{r}_n = \mathbf{R}_n + \mathbf{q}_n \,, \tag{2.18}$$

and perform a Taylor expansion of the potential energy around the equilibrium positions up to second order,

$$\begin{aligned} V(\mathbf{r}_1, \ldots, \mathbf{r}_N) = V(\mathbf{R}_1, \ldots, \mathbf{R}_N) + \sum_{n=1}^{N} \boldsymbol{\nabla}_{\mathbf{r}_n} V(\mathbf{R}_1, \ldots, \mathbf{R}_N) \cdot \mathbf{q}_n \\ + \frac{1}{2} \sum_{n,l=1}^{N} \sum_{\nu,\lambda=x,y,z} \frac{\partial^2}{\partial r_{n,\nu} \partial r_{l,\lambda}} V(\mathbf{R}_1, \ldots, \mathbf{R}_N)\; q_{n,\nu} q_{l,\lambda} + \mathcal{O}(q^3) \,. \end{aligned} \tag{2.19}$$

In this expansion, the first term is the energy of the equilibrium configuration, which does not affect the classical dynamics, so it will be dropped from now on. The second term is proportional to the gradient of the potential evaluated at the equilibrium positions, which is zero according to Eq. (2.15), i. e. the requirement of the equilibrium for all forces balancing out. The third term is the first relevant term for the dynamics. It is given by the Hessian defined in Eq. (2.16), which is evaluated at the equilibrium positions.

n	1	2	…	N	1	2	…	N	1	2	…	N
ν	1	1	…	1	2	2	…	2	3	3	…	3
j	1	2	…	N	$N+1$	$N+2$	…	$2N$	$2N+1$	$2N+2$	…	$3N$

Table 2.1: Mapping between different index notations. n labels the different ions, ν the spatial dimensions, i. e. $\nu = 1$ for the x-coordinate, etc. j is a combined index where we take the convention to number first all x-coordinates, then all y-coordinates, and finally all z-coordinates of the ions.

At this point it is convenient to replace the double index by a single index $j \equiv (n, \nu)$, e. g. by the mapping $j = n + (\nu - 1)N$, where all the x-coordinates are mapped to indices from 1 to N, the y-coordinates from $N + 1$ to $3N$, and so on (see Table 2.1).

The (non-dimensionless) Hamiltonian can then be approximated in a region around the equilibrium positions by the following expression,

$$H \approx H_{\text{quad}} = \sum_{j=1}^{3N} \frac{p_j^2}{2m} + \sum_{j,k}^{3N} \frac{m}{2} \mathscr{V}_{jk} q_j q_k \,. \tag{2.20}$$

There, the Hamilton function is now expressed as a quadratic form in the momenta and coordinates, neglecting the constant energy from the equilibrium positions.

The region for which the quadratic Hamiltonian (2.20) is a good approximation is generally smaller than the largest neighbourhood for which stable trajectories are guaranteed. It is also smaller than the convergence radius of the Taylor series. As a matter of fact, the Taylor series approximates the Coulomb interaction between the ions only for a small region (not containing the poles), whereas it diverges elsewhere. As a practical estimate, the range of where the Taylor expansion is expected to yield a faithful approximation should be considered to be much smaller than the typical ion distance in order to avoid the non-linearities of the Coulomb interaction between the ions, see for instance Morigi, Eschner, Cirac et al. (1999); Marquet et al. (2003).

We assume that we stay within this region, such that the dynamics determined by Eq. (2.20) is essentially described by a set of *coupled harmonic oscillators*. The Hamilton function of Eq. (2.20) can now be transformed into a set of uncoupled harmonic oscillators by defining a new set of coordinates, the so-called *normal modes*. Hamilton's equations for the normal mode coordinates are independent from each other, which enables us to solve them straightforwardly. This uncoupled form can be immediately seen when the Hamilton function is written as a quadratic form in the momenta and coordinates as in

Eq. (2.20); having uncoupled Hamilton's equations is then equivalent to the matrix describing the quadratic form to be diagonal.

The general procedure for obtaining the normal modes is to determine a *canonical transformation* (Landau and Lifschitz 1969a, Ch. VII, §45, pp.143ff.; Goldstein 1950, Ch. VIII; Fasano and Marmi 2006, Ch. 10) of the coordinates q_j, the momenta p_j, and of the Hamiltonian H to a new set of coordinates Q_j and momenta P_j, and a new Hamilton function $\tilde{H}$. This transformation is given by

$$\{q_j\} \mapsto \{Q_j(p_1, \ldots, p_{3N}, q_1, \ldots, q_{3N})\}\,, \tag{2.21a}$$

$$\{p_j\} \mapsto \{P_j(p_1, \ldots, p_{3N}, q_1, \ldots, q_{3N})\}\,, \tag{2.21b}$$

and

$$H(p_1, \ldots, p_{3N}, q_1, \ldots, q_{3N}) \mapsto \tilde{H}(P_1, \ldots, P_{3N}, Q_1, \ldots, Q_{3N})\,. \tag{2.21c}$$

A transformation is canonical if the equations of motion for Hamiltonian systems, Hamilton's equations, are left invariant. This is equivalent to the invariance of the Poisson brackets between all possible combinations of coordinates and momenta under this transformation. Mathematically, a canonical transformation is described by a *symplectic transformation* (Fasano and Marmi 2006, Ch. 10) of the combined vector of momenta and coordinates, which algebraically is represented by a $6N \times 6N$-matrix M that fulfils $\mathrm{M}^T \mathbb{J} \mathrm{M} = \mathbb{J}$, where M^T denotes the transpose of matrix M and $\mathbb{J}$ is the symplectic form (which reflects the inherent geometry of phase space for Hamiltonian dynamics),

$$\mathbb{J} = \begin{pmatrix} 0 & \mathbb{1} \\ -\mathbb{1} & 0 \end{pmatrix}\,, \tag{2.22}$$

with $\mathbb{1}$ denoting the $3N \times 3N$ identity matrix.

As the momenta are already diagonal in the Hamiltonian, and as there is no coupling between coordinates and momenta, the form of the transformation is much simpler, and it can be represented by a *simultaneous* orthogonal transformation of momenta and coordinates.[7]

The new momenta P_j and coordinates Q_j are then defined by

$$P_j = \sum_k M_{jk} p_k\,, \qquad\qquad Q_j = \sum_k M_{jk} q_k\,. \tag{2.23}$$

Here, M is the same orthogonal matrix in both equations, which is obtained by diagonalizing the Hessian, Eq. (2.16),

$$\mathscr{V}_{jk} = \sum_l M_{jl} \Omega_{ll} M_{kl}\,, \tag{2.24}$$

7 Since in a Penning trap the magnetic field couples the ions' momenta and coordinates, only a general symplectic transformation leads to normal mode coordinates. The representation of this transformation can be determined with the help of Williamson's theorem (Williamson 1936).

where Ω is a diagonal matrix, with positive entries $\Omega_{lk} = \delta_{lk}\omega_l^2$, which follows from the positive-definiteness of the Hessian. The matrix M is orthogonal because the Hessian is real and symmetric (Horn and Johnson 1985, Theorem 2.5.6, p. 104). These new collective coordinates and momenta are called *normal mode coordinates and momenta*. They are given by a linear combination of the original coordinates and momenta, with weights given by the entries in the kth row of the orthogonal matrix M. This allows us to identify the rows of the orthogonal matrix M directly with the normal modes, which is also evident from the inverse relations given by

$$p_j = \sum_k M_{kj} P_k \,, \qquad\qquad q_j = \sum_k M_{kj} Q_k \,. \tag{2.25}$$

Here we made use of the property of the inverse of an orthogonal matrix to be equal to the transpose of it.

Inserting this for the kinetic energy, we obtain

$$\begin{aligned} \frac{1}{2m}\sum_j p_j^2 &= \frac{1}{2m}\sum_j \Big(\sum_k M_{kj}P_k\Big)\Big(\sum_l M_{lj}P_l\Big) \\ &= \frac{1}{2m}\sum_j \sum_{lk} \underbrace{M_{kj}M_{lj}}_{=\delta_{kl}} P_k P_l = \frac{1}{2m}\sum_j P_j^2 \,, \end{aligned} \tag{2.26}$$

while the potential energy transforms to

$$\begin{aligned} \frac{m}{2}\sum_{jk} \mathscr{V}_{jk} q_j q_k &= \frac{m}{2}\sum_{jk} \mathscr{V}_{jk} \Big(\sum_i M_{ij} Q_i\Big)\Big(\sum_l M_{lk} Q_l\Big) \\ &= \frac{m}{2}\sum_{il} \underbrace{\sum_{jk} M_{ij}\mathscr{V}_{jk}M_{lk}}_{=m\omega_l^2\delta_{il}} Q_i Q_l = \frac{m}{2}\sum_j \omega_j^2 Q_j^2 \,. \end{aligned} \tag{2.27}$$

The Hamiltonian thus transforms to

$$H_{\text{quad}} = \frac{1}{2m}\sum_j P_j^2 + \frac{m}{2}\sum_j \omega_j^2 Q_j^2 \,, \tag{2.28}$$

which is a collection of $3N$ uncoupled harmonic oscillators, as anticipated above.

2.1.4 *Equilibrium Positions and Normal Modes for Three Ions*

As an illustration of the considerations of the previous sections we provide here the equilibrium positions and the normal modes for three ions, this being the smallest crystal where one may observe a zigzag structure. Under the assumptions stated before, we take the confinement along the y-direction to be stronger than the one in

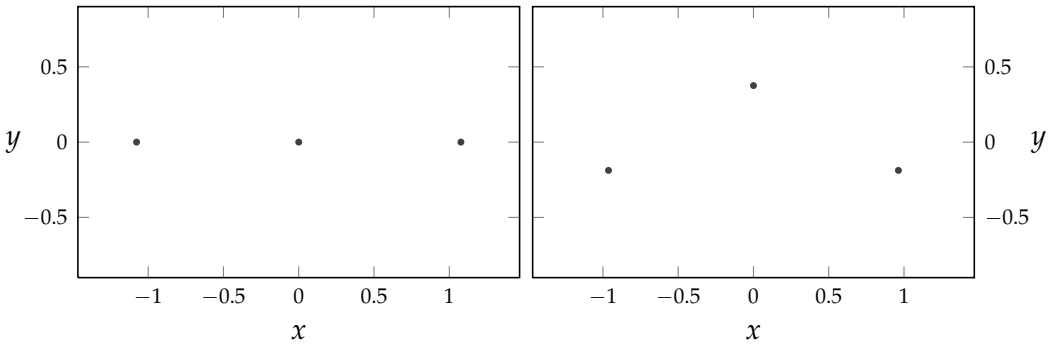

(a) linear (b) zigzag

Figure 2.1: Equilibrium positions for three ions in a potential which is homogeneous for all ions. (a) The linear chain is the stable configuration for $\alpha > \alpha_c = 12/5$. (b) The zigzag structure, here for $\alpha = 2$, is the stable configuration for $\alpha < \alpha_c$.

x-direction, so we have $\alpha > 1$ hereafter.[8] We shall refer to the direction of weaker confinement as the *axial* direction, and to the direction of stronger confinement as the *transverse* direction.

Under this assumption, there are only two distinct types of configurations, shown in Figure 2.1; the *linear chain*, where each ion is located on the x-axis, and a planar, so-called *zigzag* structure, where the ions form an isosceles triangle with the y-axis as symmetry axis. We review these configurations in the following sections.

Linear Configuration

The dimensionless equilibrium coordinates for the ions in the linear configuration are (Rafac et al. 1991):

$$X_1 = -\sqrt[3]{5/4}\,, \qquad Y_1 = 0\,, \tag{2.29a}$$

$$X_2 = \quad 0\,, \qquad Y_2 = 0\,, \tag{2.29b}$$

$$X_3 = \quad \sqrt[3]{5/4}\,, \qquad Y_3 = 0\,. \tag{2.29c}$$

This set of positions is always a solution to the condition of balanced forces, Eq. (2.15), but it does not necessarily fulfil the condition of stability, Eq. (2.17). Clearly, for $\alpha \to \infty$ we expect this to be the unique stable configuration.

The linear configuration becomes unstable when at least one of the eigenvalues of the Hessian turns negative and thus the corresponding angular normal mode frequency imaginary. For determining the eigenvalues, we diagonalize the Hessian via an orthogonal matrix; we find that the Hessian is already block-diagonal with blocks corresponding

8 We could also allow for $\alpha = 1$, but in this case the equilibrium positions will form an equilateral triangle which is free to rotate in the x–y-plane.

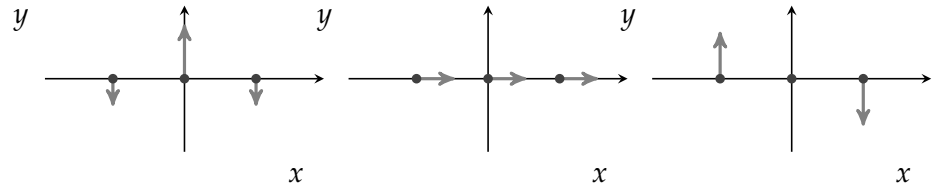

(a) zigzag (b) x-COM (c) rocking

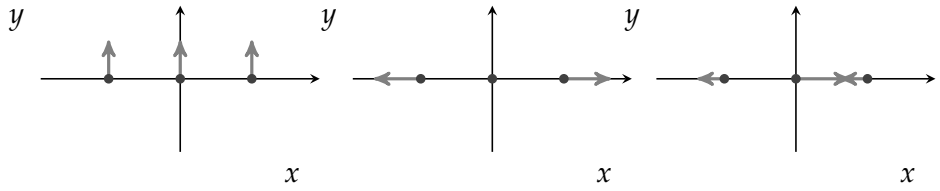

(d) y-COM (e) stretch (f) Egyptian

Figure 2.2: The normal modes of the linear chain configuration for three ions. Their dimensionless angular frequencies ω_j are given by (a) $\omega_1 = \sqrt{\alpha - 12/5}$ for the zigzag mode, (b) $\omega_2 = 1$ for the axial COM-mode, (c) $\omega_3 = \sqrt{\alpha - 1}$ for the rocking mode, (d) $\omega_4 = \sqrt{\alpha}$ for the transverse COM-mode, (e) $\omega_5 = \sqrt{3}$ for the stretch mode, and (f) $\omega_6 = \sqrt{29/5}$ for the Egyptian mode.

to the x- and y-coordinates. From this block-diagonal structure we can immediately conclude that the normal modes are grouped in axial modes, where all ions move collectively in the x-direction only, and transverse modes, where the ions move collectively in the y-direction.

Diagonalizing the block for the x-coordinates, we get the dimensionless angular eigenfrequencies along the axial direction, given by $(1, \sqrt{3}, \sqrt{29/5})$. The modes are depicted graphically in Figure 2.2. The axial modes (see also James 1998) and their frequencies depend only on the choice of the trapping potential in the axial direction, so in the dimensionless units chosen they are constant.

The angular frequencies of the normal modes in the transverse direction, however, depend all on the ratio between the transverse and axial trapping potential. The dimensionless angular frequencies in the transverse direction read $\sqrt{\alpha - \alpha_c}$ for the zigzag, $\sqrt{\alpha - 1}$ for the rocking, and $\sqrt{\alpha}$ for the COM-mode, where $\alpha_c = 12/5$ is called the *critical anisotropy parameter* that specifies the transition from the linear to the zigzag configuration (Rafac et al. 1991). As the linear structure is the configuration in the limit of large α, apparently the linear structure is stable from $\alpha \to \infty$ down to the value of α for which the first of the eigenfrequencies becomes negative. The mode for which this happen turns out to be the zigzag mode, whose eigenfrequency attains the

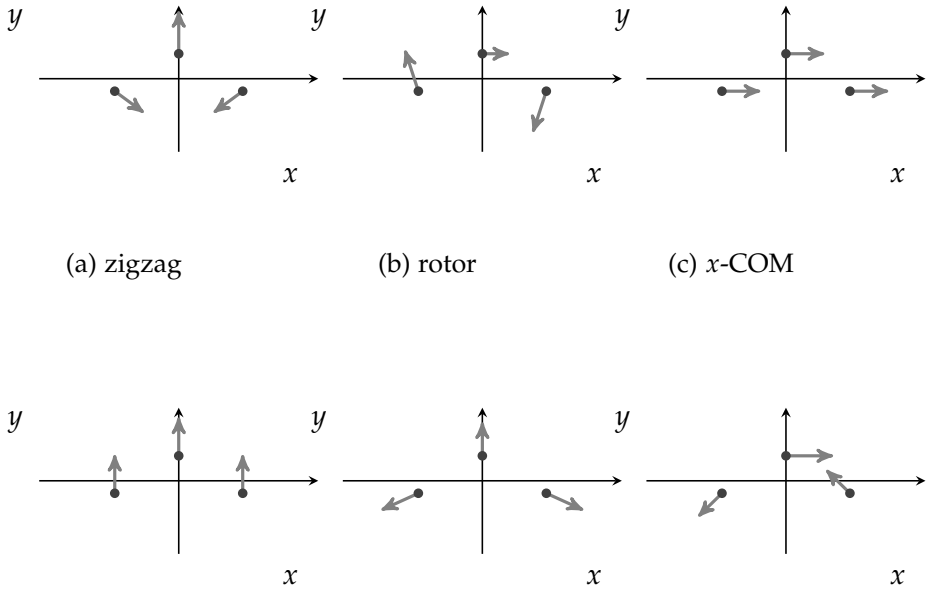

(a) zigzag (b) rotor (c) x-COM

(d) y-COM (e) breathing (f) twist

Figure 2.3: Normal modes of the zigzag chain configuration for three ions. The dimensionless angular eigenfrequencies of the two COM-modes are (c) $\omega_3 = 1$ for the COM-mode in x-direction, and (d) $\omega_4 = \sqrt{\alpha}$ for the COM-mode in y-direction. The other angular eigenfrequencies have no simple analytical form, thus they are more conveniently calculated numerically, see Figure 2.4.

value zero at $\alpha = \alpha_c$, and that turns imaginary for α being smaller. Thus $\alpha = \alpha_c$ is the lower stability boundary for the linear structure.

Zigzag Configuration

For $\alpha < \alpha_c$ (and $\alpha > 1$) a new set of equilibrium positions emerges, for which the forces caused by the trap potential and the Coulomb interaction get balanced out. This is the zigzag structure as shown in Figure 2.1b, where the dimensionless equilibrium positions are given by (Fishman et al. 2008)

$$X_1 = -\bar{X}\,, \qquad Y_1 = -\bar{Y}\,, \tag{2.30a}$$

$$X_2 = \quad 0\,, \qquad Y_2 = \ 2\bar{Y}\,, \tag{2.30b}$$

$$X_3 = \quad \bar{X}\,, \qquad Y_3 = -\bar{Y}\,. \tag{2.30c}$$

Here, we introduced the two dimensionless parameters $\bar{X}$ and $\bar{Y}$, which are determined analytically by (Fishman et al. 2008)

$$\bar{X} = \left[4\left(1 - \frac{\alpha}{3}\right)\right]^{-1/3}, \tag{2.31a}$$

$$\bar{Y} = \pm\frac{1}{3}\left[\left(\frac{3}{\alpha}\right)^{2/3} - \bar{X}^2\right]^{1/2}. \tag{2.31b}$$

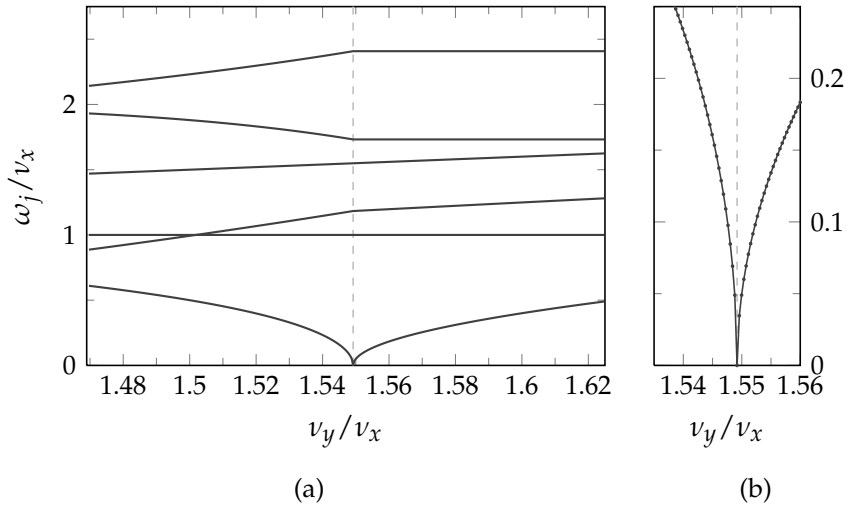

Figure 2.4: Dimensionless angular normal mode frequencies for three ions confined in a harmonic potential in units of the angular trap frequency ν_x, as a function of the ratio ν_y/ν_x, which is the square root of the anisotropy parameter $\alpha = \nu_y^2/\nu_x^2$. The dashed vertical line indicates the critical value $\sqrt{\alpha_c} \approx 1.5492$, separating the zigzag ($\alpha < \alpha_c$) from the linear configuration ($\alpha > \alpha_c$).

The angular normal mode frequencies could in principle be calculated analytically; we can reduce the characteristic polynomial from sixth order down to fourth order by "guessing" the eigenvalues 1 and α for the two COM-modes that are, of course, eigenmodes of the crystal. This fourth order polynomial can then be solved for the remaining four eigenvalues by the method of reducing it to a depressed quartic; hence one of the methods for solving depressed quartics can be applied, such as factorizing into two quadratics (Brookfield 2007) or the method of Ferrari, see Turnbull (1947, Ch. X, pp. 130f.). However, the general solution of such a quartic is quite intricate and therefore omitted here. For practical calculations it is convenient to resort to a numerical solution of the eigenvalues and eigenmodes. The angular normal mode frequencies as a function of the ratio between the angular trap frequencies ν_y/ν_x are plotted in Figure 2.4 for both, the linear and the zigzag regime.

Nevertheless, it is possible to analytically obtain the conditions for when the eigenvalues become imaginary in terms of the discriminant of the quartic. It turns out to be more practical to calculate the sign of the determinant of the Hessian for determining the stability of the structure instead. Of course, this procedure cannot detect regions where an even number of eigenvalues turns negative simultaneously, but this is not likely to occur at all. Therefore, finding the parameters for which the determinant equals to zero gives virtually all possible limits of stability.

Structures for Ion Crystals with More than Three Ions

For small ion Coulomb crystals up to 15 ions, typical linear and zigzag structures for odd ion numbers are shown in Figure 2.5. The transition between the two structures depends on the number of ions, and it shifts to higher values of the anisotropy parameter for increasing N (Schiffer 1993; Dubin 1993; Morigi and Fishman 2004). For larger N, one can recognize two effects: First, the ions in the centre are much closer together than those on the edges in both the zigzag and the linear structures. And second, for the zigzag configuration, the transverse displacements are decreasing quickly from the centre to the edges such that the ions on the edges experience just tiny displacements as compared to those in the centre of the crystal.

2.2 STRUCTURAL SUPERPOSITION STATES

In this thesis, we want to investigate the dynamical behaviour of the ions after a sudden *quantum quench* of the external potential. Generally, in a quantum quench the dynamics for one part of the system – called the *quenched system* – depends on the quantum state of another part of the system, which we call the *control system* (we shall return to a more detailed discussion of quantum quenches in Chapter 5.) Evidently, there has to be a part in the Hamiltonian which governs the dynamics of the quenched system in dependence on the state of the control system; mathematically, this is expressed by a sum of the projectors onto the eigenspaces of the control system. Assuming that the dynamical variables of the quenched system are described by a set of coordinates and momenta, and assuming further that the dynamics after the quench only affect the coordinates of the ions, this part in the Hamiltonian can be written in the form of a *state-dependent potential* as

$$\hat{\mathrm{V}}_{\mathrm{sdp}} = \sum_{\phi_j} |\phi_j\rangle\langle\phi_j| \, \hat{\mathrm{V}}_{\phi_j}(\mathbf{r}_1, \ldots, \mathbf{r}_N) \,, \tag{2.32}$$

where $|\phi_j\rangle$ are eigenstates of the control system and $\hat{\mathrm{V}}_{\phi_j}(\mathbf{r}_1, \ldots, \mathbf{r}_N)$ is the potential energy for the quenched system when the state of the control system is prepared in the eigenstate $|\phi_j\rangle$.

In our case, the control system is the electronic state of the ion in the centre of the crystal for which we assume the two-level approximation to hold (Allen and Eberly 1987, Ch. 2, pp.28 ff.). Denoting the two states by $|\uparrow\rangle$ and $|\downarrow\rangle$, the state-dependent potential has then the following form,

$$\hat{\mathrm{V}}_{\mathrm{sdp}} = |\downarrow\rangle\langle\downarrow| \, V_{\downarrow}(\mathbf{r}_1, \ldots, \mathbf{r}_N) + |\uparrow\rangle\langle\uparrow| \, V_{\uparrow}(\mathbf{r}_1, \ldots, \mathbf{r}_N) \,. \tag{2.33}$$

Here, we treat the potential for the motional degrees of the ions as classical, but assume that it depends on the electronic state of a spe-

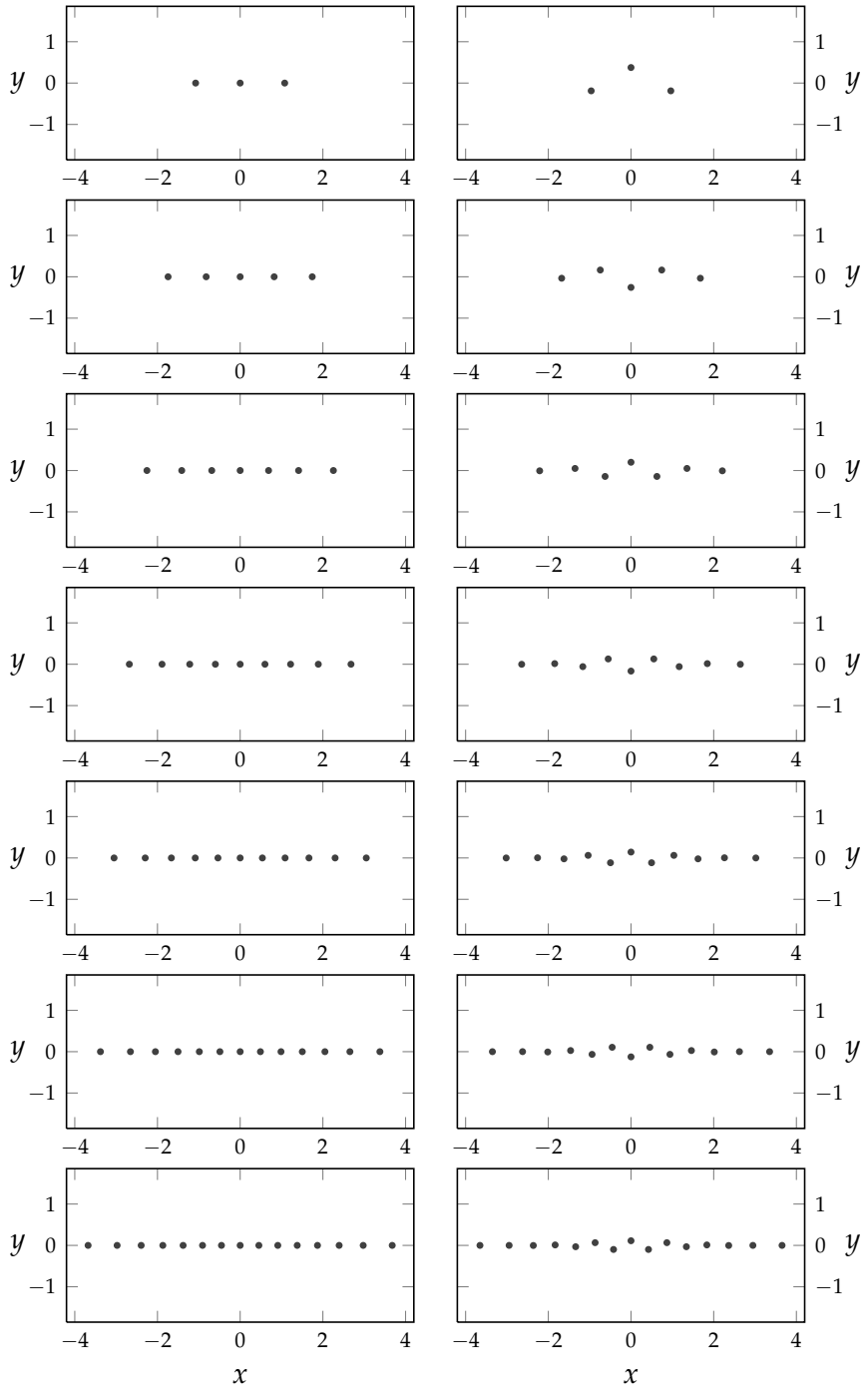

(a) linear (b) zigzag

Figure 2.5: Equilibrium positions for ion Coulomb crystals with up to 15 ions. As the value of the critical anisotropy parameter depends on N, the plots for the linear chain (left) are for the value of $\alpha = 1.02\,\alpha_c(N)$, while the zigzag structures (right) are plotted for $\alpha = 0.9\,\alpha_c(N)$, respectively.

cific ion. Later, when considering the dynamics of the ions, we are quantizing the vibrations of the ions around their classical equilibrium positions. Since we are considering single atoms at ultracold temperatures, we should in principle treat their motional state quantum mechanically by assigning to it a total wavefunction given in the tensor product space of the Hilbert spaces of the individual particles. In that case we would need to include the statistics of the ions under particle exchange. Yet, the distance between the ions, of the order of around ten µm, is usually much larger than the spread of the wavefunction of the individual ions, which is of the order of tens of nm or below (see Wineland, Monroe et al. 1998, e. g.). Therefore, we can treat the ions as practically distinguishable particles.

2.2.1 *Implementation of a State-Dependent Potential*

We shall now turn to the question of how such a potential as in Eq. (2.33) can be prepared. Generally, the potential has to have components which project onto subspaces of the control system. Any coupling between these subspaces is detrimental to the capability of controlling the quenched system, as then the dynamics would not evolve separately in distinct subspaces.

There are several possibilities for realizing such a state-dependent potential. One realization is implemented by the dispersive interaction of atoms with light within a so-called *optical dipole potential*. This experimental technique has been mastered in the field of ultracold atoms, where different types of traps employing light fields are in use. It utilizes the dispersive interaction of the light field with an electrical dipole, far-detuned from resonance. This results in the so-called dipole force, which can be described by a potential (Grimm et al. 2000). The dipole potential is used for trapping neutral atoms with light in focused beams, standing waves (so-called optical lattices), and other schemes that are reviewed in Grimm et al. (2000). Furthermore, this kind of interaction is at the heart of many proposals that attempt to devise a trapped ion quantum computer, in which fundamental two-qubit gate operations between the ions are mediated by state-dependent forces (see Blatt and Wineland 2008, for instance).

Another, but seemingly equivalent possibility uses magnetic fields that are coupled to an internal magnetic dipole. This alternative possibility has been demonstrated successfully for quantum computation (Mintert and Wunderlich 2001; Wunderlich 2002), too. Yet another proposal suggests to excite one ion into a Rydberg-excited state, where the dipole-ion interaction energy then shifts the potential energy in a state-dependent way (Li and Lesanovsky 2012; Feldker, Bachor et al. 2015). In this thesis, we shall restrict ourselves to discussing the former

scheme, which is reviewed in the upcoming section, with specific focus on the requirements for the implementation of a state-dependent potential.

Optical Dipole Potential

When light interacts with an atom it can induce an atomic dipole moment, which in turn affects and modifies the light field. The simplest understanding of the dipole force can then be gained by examining a classical oscillator model (Grimm et al. 2000, Sec. IIA). Here we focus on a more involved explanation of the dipole potential,[9] using the concept of *dressed states* (Cohen-Tannoudji 1998; Cohen-Tannoudji, Dupont-Roc et al. 1992, Ch. VI). These are the new eigenstates (the "bare" atomic states being "dressed" by the light field) of the Hamiltonian of the coupled system of atom and light field. We consider the case of a single atom interacting with the radiation field of a single laser mode. This mode is modelled in the following as a single ring cavity mode in order to derive the workings of the dipole force (Cohen-Tannoudji, Dupont-Roc et al. 1992, Ch. VI). Later, the specific parameters of the model will turn out to be unimportant for the mechanism of the dipole force in the limit of strong laser intensities, enabling us to replace the quantized electromagnetic field by its classical expression.

The Hamiltonian of the atom is given by

$$\hat{H}_A = \hbar\omega_{EG}|E\rangle\langle E|\,, \tag{2.34}$$

where ω_{EG} is the angular frequency of the dipole transition between the atomic eigenstates labelled $|G\rangle$ and $|E\rangle$. The Hamiltonian for the electromagnetic field of the laser mode is

$$\hat{H}_L = \hbar\omega_L\left(\hat{a}^\dagger\hat{a} + \frac{1}{2}\right), \tag{2.35}$$

where $\hat{a}^\dagger$ and $\hat{a}$ are the creation and annihilation operators of the laser mode with angular frequency ω_L.

The eigenstates of the Hamiltonian of the uncoupled system $\hat{H}_A + \hat{H}_L$ are denoted by $|G,\mathfrak{N}\rangle$ and $|E,\mathfrak{N}\rangle$, where $\mathfrak{N} = 0,1,2,\ldots$ is the number of photons in the laser mode. The difference between the angular frequency of the laser beam ω_L and the angular atomic transition frequency ω_{EG} is characterized by the *detuning*, given by

$$\Delta_L = \omega_L - \omega_{EG}\,. \tag{2.36}$$

The Hamiltonian of the interaction between the atomic dipole and the laser field is given in the electric dipole representation by

$$\hat{H}_{int} = -\hat{\mathbf{d}}\cdot\hat{\mathbf{E}}_\perp(\mathbf{r})\,, \tag{2.37}$$

9 The effect described here is often referred to as the ac-Stark effect.

where $\mathbf{r}$ is the COM-coordinate of the atom. Further, we introduced the atomic dipole operator $\hat{\mathbf{d}}$; assuming the matrix elements of the dipole operator for the transition between $|G\rangle$ and $|E\rangle$ to be real (and thus equal),

$$\mathbf{d}_{GE} = \langle G|\hat{\mathbf{d}}|E\rangle = \langle E|\hat{\mathbf{d}}|G\rangle\,, \tag{2.38}$$

we can re-express the dipole operator as

$$\hat{\mathbf{d}} = \mathbf{d}_{GE}(|G\rangle\langle E| + |E\rangle\langle G|)\,. \tag{2.39}$$

The second quantity in the interaction term Eq. (2.37) is the transverse electric field,

$$\hat{\mathbf{E}}_{\perp}(\mathbf{r}) = \sqrt{\frac{\hbar\omega_{\mathrm{L}}}{2\epsilon_0 V_{\mathrm{cav}}}}\mathbf{e}_{\mathrm{L}}(\hat{a} + \hat{a}^{\dagger})\,, \tag{2.40}$$

where ϵ_0 is the vacuum permittivity and $\mathbf{e}_{\mathrm{L}}$ is the unit polarization vector of the laser mode, and V is the volume of the cavity. The interaction can be rewritten as

$$\hat{\mathrm{H}}_{\mathrm{int}} = \mathfrak{g}\big(|G\rangle\langle E| + |E\rangle\langle G|\big)(\hat{a} + \hat{a}^{\dagger})\,, \tag{2.41}$$

where $\mathfrak{g}$ is the coupling constant

$$\mathfrak{g} = -\mathbf{e}_{\mathrm{L}} \cdot \mathbf{d}_{GE}\sqrt{\frac{\hbar\omega_{\mathrm{L}}}{2\epsilon_0 V_{\mathrm{cav}}}}\,. \tag{2.42}$$

In the case where the laser radiation is close to resonance of the atomic dipole transition, i. e. $|\Delta_{\mathrm{L}}| = |\omega_{EG} - \omega_{\mathrm{L}}| \ll \omega_{EG}$, the interaction $\hat{\mathrm{H}}_{\mathrm{int}}$ gives rise to a resonant coupling between the states $|G, \mathfrak{N}\rangle$ and $|E, \mathfrak{N} - 1\rangle$. Transitions to other states are non-resonant and can therefore be neglected.[10]

The matrix elements for the resonant transitions are given by

$$\langle E, \mathfrak{N} - 1|\hat{\mathrm{H}}_{\mathrm{int}}|G, \mathfrak{N}\rangle = \mathfrak{g}\sqrt{\mathfrak{N}} \approx \mathfrak{g}\sqrt{\langle\mathfrak{N}\rangle}\,, \tag{2.43}$$

where the approximation is justified by assuming that the cavity is initially prepared in a coherent state with a large mean photon number $\langle\mathfrak{N}\rangle$, such that

$$\langle\mathfrak{N}\rangle \gg \Delta\mathfrak{N} \gg 1\,, \tag{2.44}$$

with $\Delta\mathfrak{N}$ being the standard deviation of the photon number distribution. Consequently, for the laser mode being in a coherent state

10 These non-resonant couplings can become important for the interaction of atoms with radiation of lower frequencies such as rf-fields, which are leading to the so-called Bloch-Siegert shift of energy levels (Bloch and Siegert 1940).

that has a large photon number all matrix elements are approximately equal.

Evaluating the expectation value for the electric field operator in such a coherent state $|\alpha\, e^{-i\omega_L t}\rangle$, we obtain

$$\left\langle \alpha\, e^{-i\omega_L t} \middle| \hat{\mathbf{E}}_\perp(\mathbf{r}) \middle| \alpha\, e^{-i\omega_L t} \right\rangle = \boldsymbol{\mathcal{E}}_0(\mathbf{r}) \cos(\omega_L t)\,, \tag{2.45}$$

where the field amplitude is given by

$$\boldsymbol{\mathcal{E}}_0(\mathbf{r}) = 2\mathbf{e}_L \sqrt{\frac{\hbar\omega_L}{2\epsilon_0 V_{\text{cav}}}} \sqrt{\langle \mathfrak{N} \rangle}\,. \tag{2.46}$$

Henceforth, the electric field can be replaced by its expectation value corresponding to the classical value of the electric field in this limit.

Further, we define the *Rabi frequency* $\Omega_0(\mathbf{r})$, which we define as real and positive by

$$\Omega_0(\mathbf{r})\, e^{i\phi(\mathbf{r})} = -\mathbf{d}_{GE} \cdot \boldsymbol{\mathcal{E}}_0(\mathbf{r})/\hbar\,, \tag{2.47}$$

such that the matrix elements in Eq. (2.43) are given by

$$\langle E, \mathfrak{N}-1 | \hat{H}_{\text{int}}(\mathbf{r}) | G, \mathfrak{N} \rangle = \hbar\Omega_0(\mathbf{r})\, e^{i\phi(\mathbf{r})}/2\,. \tag{2.48}$$

Taking the interaction into account, the states $|G, \mathfrak{N}\rangle$ and $|E, \mathfrak{N}-1\rangle$ get coupled to new eigenstates (Dalibard and Cohen-Tannoudji 1985),

$$\begin{aligned} |1(\mathfrak{N})\rangle &= e^{-i\phi(\mathbf{r})/2} \sin[\theta(\mathbf{r})]\, |G, \mathfrak{N}\rangle + e^{i\phi(\mathbf{r})/2} \cos[\theta(\mathbf{r})]\, |E, \mathfrak{N}-1\rangle\,, \\ |2(\mathfrak{N})\rangle &= e^{-i\phi(\mathbf{r})/2} \cos[\theta(\mathbf{r})]\, |G, \mathfrak{N}\rangle - e^{i\phi(\mathbf{r})/2} \sin[\theta(\mathbf{r})]\, |E, \mathfrak{N}-1\rangle\,, \end{aligned} \tag{2.49}$$

where the dressed state "angle" θ is given by

$$\tan[2\theta(\mathbf{r})] = -\frac{\Omega_0(\mathbf{r})}{\Delta_L}\,, \qquad 0 \le \theta \le \pi/2\,. \tag{2.50}$$

The energies of the eigenstates get shifted apart from each other such that their energy difference is given by

$$\hbar\Omega(\mathbf{r}) = \hbar\sqrt{\Omega_0^2(\mathbf{r}) + \Delta_L^2}\,. \tag{2.51}$$

The interaction Eq. (2.37) thus "repels" the energy levels by displacing the higher bare energy level up to higher energy and moving the lower bare energy level energetically further down. In the limit of large detuning, $|\Delta_L| \gg \Omega_0(\mathbf{r})$, the dressed-state angle θ remains small so that the states $|1(\mathfrak{N})\rangle$ and $|2(\mathfrak{N})\rangle$ contain each a large and a small component of the states $|G, \mathfrak{N}\rangle$ and $|E, \mathfrak{N}-1\rangle$ (depending on the sign of the detuning Δ_L). The shift of the energy level of that state that contains mainly the atomic ground state can be approximated by

$$\Delta E(\mathbf{r}) \approx \hbar\Omega_0^2(\mathbf{r})/4\Delta_L\,. \tag{2.52}$$

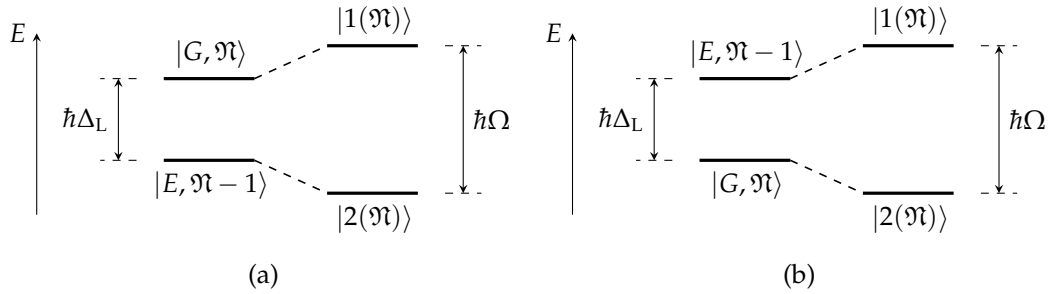

Figure 2.6: The interaction between atoms and the radiation field leads to new eigenstates, the dressed states $|1(\mathfrak{N})\rangle$ and $|2(\mathfrak{N})\rangle$, which are separated by an energy $\hbar\Omega$. The splitting is shown for (a) for $\Delta_L > 0$ (blue-detuning), and (b) for $\Delta_L < 0$ (red-detuning). The figure is adapted from Dalibard and Cohen-Tannoudji (1985).

Which of the atomic states is associated with the lower or the higher bare energy state depends on the detuning of the light field with respect to the atomic transition: If the detuning Δ_L is positive, the energy of the ground state dressed by $\mathfrak{N}$ photons is larger than the energy of the excited state dressed by $\mathfrak{N} - 1$ photons; this situation is called *blue-detuning*. In the case of *red-detuning*, $\Delta_L < 0$, the energy of the excited atomic state dressed by $\mathfrak{N} - 1$ photons is higher than the energy of the ground atomic state dressed by $\mathfrak{N}$ photons.

If now the intensity of the laser has a spatially varying profile, the potential energy depends on the position of the atom in the laser beam, as the square of the Rabi frequency is proportional to the intensity of the light field, see Figure 2.7. Therefore, the atom experiences a force whose direction depends on the detuning and on the gradient of the intensity; it attracts the atom into the direction of higher intensity for red-detuning, while it repels the atom away from the direction of higher intensity for blue-detuning.

These two situations lead to two families of possible optical dipole traps for red- and for blue-detuned light (Grimm et al. 2000, Sections IV and V), respectively. In the following, we will only discuss the case of red-detuning.

Besides the shift of the energy levels, we have also to consider the effect of the finite line width of the excited atomic state. As the dressed states are linear combinations of the bare states, meaning that they are a linear combination of the ground state with $\mathfrak{N}$ photons and the excited atomic state with $\mathfrak{N} - 1$ photons. Therefore, the lower dressed state now attains a finite line width, which is essentially the rate of absorption of a photon, while the line width of the upper state is reduced compared to the one of the bare excited state. The finite line width now causes unwanted transitions to the excited atomic state. Thus one has to analyse in detail how the broadening and the shift relate to the actual detuning of the laser from the atomic transition.

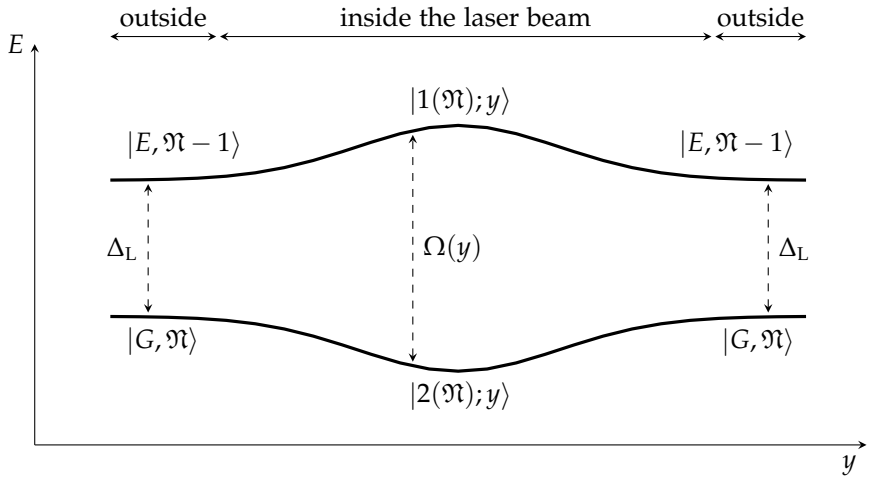

Figure 2.7: In an inhomogeneous laser beam, the energy splitting $\Omega(y)$ of the dressed states depends on the spatial variation (here shown for the y-direction) of the intensity of the laser beam, which is here taken as a Gaussian beam. The laser frequency is red-detuned ($\Delta_L = \omega_L - \omega_{EG}$) from the atomic transition. The figure is adapted from Dalibard and Cohen-Tannoudji (1985).

The shift and the broadening of the dressed states can be calculated in the limit of large detuning Δ_L (Cohen-Tannoudji 1998). The broadening of the ground state is given by

$$\Gamma_G = \Omega^2 \frac{\Gamma}{\Gamma^2 + 4\Delta_L^2}\,, \tag{2.53a}$$

and the energy shift by

$$\Delta E = \hbar\Omega^2 \frac{\Delta_L}{\Gamma^2 + 4\Delta_L^2}\,. \tag{2.53b}$$

The ground state broadening scales like $\sim 1/\Delta_L^2$ in the large detuning limit (i. e. for $|\Delta_L| \gg \Gamma, \Omega$), while the level shifts scale like $\sim 1/\Delta_L$. By keeping the detuning sufficiently large, it is possible to achieve considerable energy shifts by increasing the laser intensity while keeping the probability of exciting the atom below a chosen threshold.

If the detuning is not sufficiently large, there will be transitions between the dressed states and the dipole force will fluctuate around a mean value. As this leads to unwanted excitations of the atom, we exclude this case by restricting ourselves to the limits of the appropriate parameters. Even more, these unwanted excitations lead to heating of the atomic motion through the fluctuating forces. Surprisingly, and despite this difficulty, the first experimental demonstration of an all-optical trapping of a single ion has been achieved in precisely this regime (Schneider, Enderlein et al. 2010, and personal communication

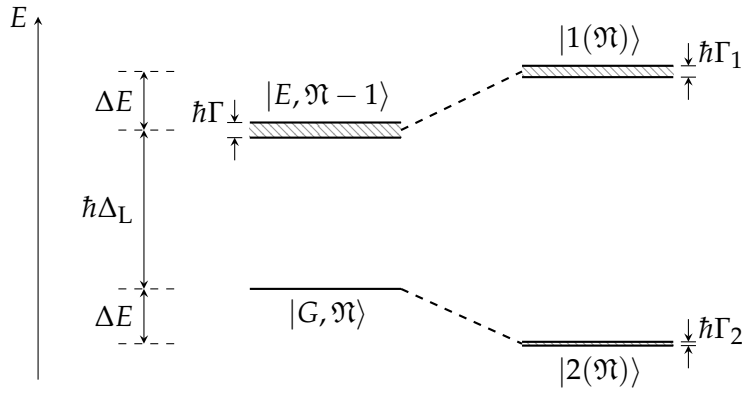

Figure 2.8: Linewidths of the dressed states. Of the two bare states only the excited atomic state exhibits a line width. Since the dressed states are a superposition of the bare states, now both dressed states obtain a finite line width. The figure is adapted from Cohen-Tannoudji (1998).

by Tobias Schätz), even though the detuning had to be chosen in such a way mainly because of technical reasons.[11]

Level Scheme for State-Dependent Potential

For the implementation of a state-dependent potential we need to choose two electronic levels that will lead to different potential energies. We have seen in this section how the interaction of an atom with a detuned light field can lead to a dipole potential. We now choose two electronic levels and the polarization of the laser field in such a way that only one of the two levels couples via the interaction with the light field to an additional auxiliary level. For the other level no upper electronic level is available with which the light field could interact with; therefore this level experiences no shift in energy.

Another equivalent possibility not discussed here is that both states couple to an upper auxiliary state, but experience different energy shifts.

Modelling of the Dipole Potential

Now we choose a specific experimental arrangement to draft a model of the dipole potential. Of course, other arrangements can be chosen and evaluated in a similar manner.

For this, we consider a laser beam propagating parallel to the axial direction of the trap. In order to achieve a sufficiently strong intensity gradient close to the centre of the trap, the beam is focused down to a waist with a size of the order of the inter-ion separation. Such a

11 The element used in this experiment – in the present case, Mg – has a transition frequency in the UV domain, where the commonly available lasers provide limited laser power only.

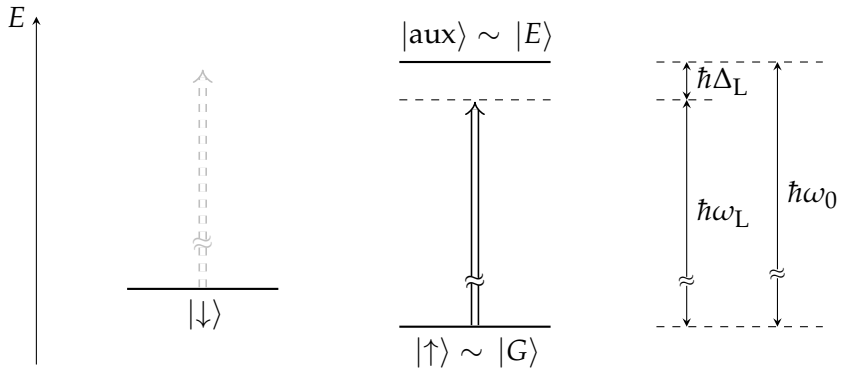

Figure 2.9: Level scheme and laser setup for dipole potential. The laser frequency and its polarization are chosen such that only the state $|E\rangle$ has an excited state partner to couple to via the interaction with the light field. Thus only the state $|E\rangle$ and its auxiliary counterpart become dressed states (denoted previously by $|G\rangle$ and $|E\rangle$) which lead to the dipole potential.

focused laser beam is well described by a Gaussian beam (Saleh and Teich 2007, Ch. 3, p. 79), which propagates along the x-direction with an intensity specified by

$$I(x,r) = I_0 \left(\frac{w_0}{w(x)}\right)^2 \mathrm{e}^{-2r^2/w(x)^2}, \tag{2.54}$$

where $r = \sqrt{y^2+z^2}$ is the radial distance away from the beam axis. The beam has a Gaussian profile in the directions transversal to the propagation direction, see Figure 2.10a for the profile at $x = 0$. The beam radius $w(x)$ defines the distance at which the intensity has dropped by $1/\mathrm{e}^2 \approx 0.135$ of the maximum intensity $I(x,0) = I_0$ within the corresponding cross-section. The beam radius has an axial dependency given by

$$w(x) = w_0 \sqrt{1 + \left(\frac{x}{x_0}\right)^2}, \tag{2.55}$$

where w_0 is the minimum beam radius or the *beam waist*. The dependence of the beam radius along the x-direction is depicted in Figure 2.10b. $x_0 = \pi w_0^2/\lambda$ is the so-called Rayleigh length that is dependent on the wavelength λ of the laser; the cross section area, when measured at a Rayleigh length's distance from the beam waist, is twice as large as the cross section area when measured at the beam waist. Integrating the intensity in Eq. (2.54) over the total transverse section yields the total beam power; this allows us to calculate the maximum intensity I_0 attained at $x = 0, r = 0$ (corresponding to the focal point for geometric optics).

Now let us assume that the length of the crystal is smaller than the waist and thus much smaller than the Rayleigh length, such

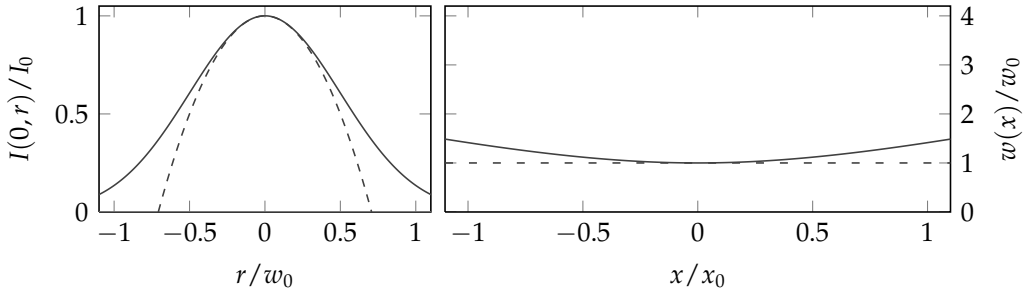

(a) (b)

Figure 2.10: Approximation of a Gaussian beam. (a) The radial dependence of the intensity $I(r,0)$ at the beam waist $x = 0$ is shown (straight line). Close to the centre of the beam for $r \ll w_0$ the beam profile can be approximated by a parabola. (b) The axial dependence of the beam radius $w(x)$ is shown (straight line). Here the beam is approximated by a constant intensity close to the beam waist for $x \ll x_0$.

that the beam radius $w(x)$ can be assumed to be constant over the crystal size, $w(x) \simeq w_0$, and there is no resulting intensity gradient along the x-direction. In the direction radially to the beam, we can expand the transverse profile in r/w_0, where r is the distance of the ion transversally to the trap axis. The exponential in Eq. (2.54) can be expanded up to second order, so that we obtain the following approximate intensity profile

$$I(r) \approx I_0 \left(1 - \frac{2r^2}{w_0^2}\right). \tag{2.56}$$

The dipole potential obtained is proportional to the intensity and has a parabolic shape with a minimum at $r = 0$ for red-detuning. Thus we can take the following expression for the dipole potential for the central ion, which is labelled by n_0,

$$V_{\text{dip}}(\mathbf{r}_{n_0}) = \left[-V_0 + \frac{m}{2}\nu_{\text{dip}}^2 \left(y_{n_0}^2 + z_{n_0}^2\right)\right] |\uparrow\rangle_{n_0}\langle\uparrow| \,. \tag{2.57}$$

The first term, $-V_0$, would be the trap depth if we would consider this as a particle trap in the spirit of the experiment of Schneider, Enderlein et al. (2010). The angular frequency ν_{dip} of this parabolic dipole potential can be calculated by Eqs. (2.47), (2.51), (2.53b) and (2.56) for given intensity and detuning. If we were to choose a blue-detuning, the second term in Eq. (2.57) would acquire a minus sign, as the sign of the detuning determines the direction of the dipole force.

With Eq. (2.57), we have now found an appropriate model for a state-dependent potential. We assume that the ion has two meta-stable electronic energy levels. These states, denoted by $|\downarrow\rangle$ and $|\uparrow\rangle$, can then be manipulated by further external laser pulses; in particular, by driving resonant transitions between them – e. g. a two-photon Raman

transition – one can control the probability to be in one of these two states between zero and one arbitrarily. If the central ion is in the state $|\downarrow\rangle$, it experiences only the potential arising from the trap. If the central ion is, however, in the state $|\uparrow\rangle$, it is additionally exposed to the dipole potential given by Eq. (2.57). This additional potential for the central ion might change the equilibrium positions of the whole crystal, provided the crystal is sufficiently small. This change in the structural configurations is examined in the next section.

2.3 STATE-DEPENDENT CRYSTALLINE STRUCTURES

In this section we discuss the state-dependent equilibrium configurations close to the linear–zigzag transition only. For a comprehensive discussion of the possible structural configurations, we refer to Appendix B. We start this section by discussing the changes in the Hamiltonian before we exemplify the change for a three-ion crystal close to the linear–zigzag transition.

2.3.1 *State-Dependent Potential Energy*

The Hamiltonian for the motional degrees of freedom, Eq. (2.4), depends on the electronic state of the excited ion labelled by n_0, which we always take to be the central one (except in Appendix B, where we also discuss a three-ion crystal with one of the outer ions excited).[12] The Hamiltonian now contains a state-dependent potential,

$$H = T_{\text{kin}}(\mathbf{p}_1, \ldots, \mathbf{p}_N) + V_{\text{Coul}}(\mathbf{r}_1, \ldots, \mathbf{r}_N) + V_{\text{sdp}}(\mathbf{r}_1, \ldots, \mathbf{r}_N)\,, \quad (2.58)$$

given by

$$V_{\text{sdp}} = \sum_{i=1}^{N} V_{\text{trap}}(\mathbf{r}_n) + V_{\text{dip}}(\mathbf{r}_{n_0})|\uparrow\rangle_{n_0}\langle\uparrow|\,, \quad (2.59)$$

with $V_{\text{trap}}(\mathbf{r}_n)$ and $V_{\text{dip}}(\mathbf{r}_{n_0})$ given by Eqs. (2.1) and (2.57), respectively. To highlight the state-dependency we added explicitly a projection operator in the above equation. The state-dependency becomes even more evident by the following decomposition,

$$V_{\text{sdp}} = |\downarrow\rangle_{n_0}\langle\downarrow|\, V_{\downarrow}(\mathbf{r}_1, \ldots, \mathbf{r}_N) + |\uparrow\rangle_{n_0}\langle\uparrow|\, V_{\uparrow}(\mathbf{r}_1, \ldots, \mathbf{r}_N)\,, \quad (2.60)$$

where the potentials in the subspaces of the projectors are given by

$$V_{\downarrow}(\mathbf{r}_1, \ldots, \mathbf{r}_N) = V_{\text{trap}}(\mathbf{r}_1, \ldots, \mathbf{r}_N)\,, \quad (2.61a)$$

$$V_{\uparrow}(\mathbf{r}_1, \ldots, \mathbf{r}_N) = V_{\text{trap}}(\mathbf{r}_1, \ldots, \mathbf{r}_N) + V_{\text{dip}}(\mathbf{r}_{n_0})\,. \quad (2.61b)$$

12 Alternatively, one can imagine to have more than one ion's electronic state manipulated, or to have even the electronic states of many ions entangled with each other.

In the same way it is possible to write the Hamiltonian in an explicit state-dependent form by

$$H = |\downarrow\rangle_{n_0}\langle\downarrow| H_\downarrow + |\uparrow\rangle_{n_0}\langle\uparrow| H_\uparrow , \tag{2.62}$$

where the state-dependent Hamiltonians are given by

$$H_\downarrow = T_{\text{kin}}(\mathbf{p}_1, \ldots, \mathbf{p}_N) + V_\downarrow(\mathbf{r}_1, \ldots, \mathbf{r}_N) + V_{\text{Coul}}(\mathbf{r}_1, \ldots, \mathbf{r}_N) , \tag{2.63a}$$

$$H_\uparrow = T_{\text{kin}}(\mathbf{p}_1, \ldots, \mathbf{p}_N) + V_\uparrow(\mathbf{r}_1, \ldots, \mathbf{r}_N) + V_{\text{Coul}}(\mathbf{r}_1, \ldots, \mathbf{r}_N) . \tag{2.63b}$$

Writing out the state-dependent parts of the potential explicitly, we can determine the relevant parameters for the further discussion:

$$V_\downarrow(\mathbf{r}_1, \ldots, \mathbf{r}_N) = \frac{m\nu_x^2}{2} \sum_{n=1}^{N} \left(x_n^2 + \alpha_y y_n^2 + \alpha_z z_n^2 \right) , \tag{2.64a}$$

$$V_\uparrow(\mathbf{r}_1, \ldots, \mathbf{r}_N) = \frac{m\nu_x^2}{2} \left[\sum_{n=1}^{N} \left(x_n^2 + \alpha_y y_n^2 + \alpha_z z_n^2 \right) + \alpha_{\text{dip}} \left(y_{n_0}^2 + z_{n_0}^2 \right) \right] , \tag{2.64b}$$

where we have rescaled the angular frequency of the dipole potential by the angular axial trapping frequency as

$$\alpha_{\text{dip}} = \frac{\nu_{\text{dip}}^2}{\nu_x^2} . \tag{2.65}$$

In the dimensionless form introduced in Eq. (1.22) the energies get divided by the scale factor $m\bar{l}^2\nu_x^2$; thus the parameters determining the crystal structure are the number of ions N, the anisotropy parameters α_y and α_z, and the additional anisotropy α_{dip} experienced by the central ion only.

2.3.2 *State-Dependent Crystalline Structures*

Now we discuss the effect of the state-dependent potential on a three-ion crystal close to the linear–zigzag transition. Dropping the dependency along the z-direction and restricting the discussion to two dimensions as before, the structures the crystal attains depend on the two parameters $\alpha_y = \alpha$ and α_{dip} only.

LINEAR CHAIN For the linear chain configuration, we obtain the equilibrium positions given in Eqs. (2.29), i. e. the same as before, as the forces at those positions have not changed. However, the

normal modes and their angular frequencies do change. Consider, for instance, the original COM-mode in y-direction: The central ion now experiences a steeper potential and thus can not move synchronously with the outer ions. The corresponding normal mode thus has a smaller mode vector for the central ion than for the outer ones.

The normal mode frequencies change too, now given by

$$\omega_1 = 1\,, \tag{2.66a}$$
$$\omega_2 = \sqrt{3}\,, \tag{2.66b}$$
$$\omega_3 = \sqrt{29/5}\,, \tag{2.66c}$$
$$\omega_4 = \sqrt{\alpha - 1}\,, \tag{2.66d}$$
$$\omega_5 = \sqrt{\alpha - 1 - \mu_1}\,, \tag{2.66e}$$
$$\omega_6 = \sqrt{\alpha - 1 - \mu_2}\,, \tag{2.66f}$$

where

$$\mu_{1,2} = \frac{-\alpha_{\text{dip}} + 2/5 \pm \sqrt{\alpha_{\text{dip}}^2 - 8\alpha_{\text{dip}}/5 + 144/25}}{2}\,. \tag{2.67}$$

Since the normal mode frequencies are real and positive only for stable equilibria, the roots of these equations determine the stability boundaries for the linear structure.

The stability boundary of the linear configuration is given by

$$\alpha_{\text{dip},c} = \left(\frac{8}{5\alpha - 4} - 1\right)\alpha \quad \text{for } \alpha > 1\,. \tag{2.68}$$

The linear configuration corresponds to the stable equilibrium positions for all values of $\alpha_{\text{dip}} > \alpha_{\text{dip},c}$, or implicitly all values of α such that the point in the parameter space is lying above or to the right of the curve shown in Figure 2.11.

ZIGZAG CHAIN For all values below and to the left of this curve (at least for $\alpha > 2$ as discussed below), the zigzag structure is the equilibrium configuration. The equilibrium positions are given by

$$X_1 = -\bar{X}, \qquad X_2 = 0, \qquad X_3 = \bar{X}, \tag{2.69a}$$
$$Y_1 = \bar{Y}, \qquad Y_2 = -2R\bar{Y}, \qquad Y_3 = \bar{Y}\,, \tag{2.69b}$$

where the coordinates of the outer ions are

$$\bar{X} = \left[4\left(1 - \frac{\alpha}{1+2R}\right)\right]^{-1/3}, \tag{2.70}$$
$$\bar{Y} = \pm\frac{1}{1+2R}\left[\left(\frac{1+2R}{\alpha}\right)^{2/3} - \bar{X}^2\right]^{1/2}. \tag{2.71}$$

Here we introduced the parameter R, defined as

$$R = \frac{\alpha}{\alpha + \alpha_{\text{dip}}}\,. \tag{2.72}$$

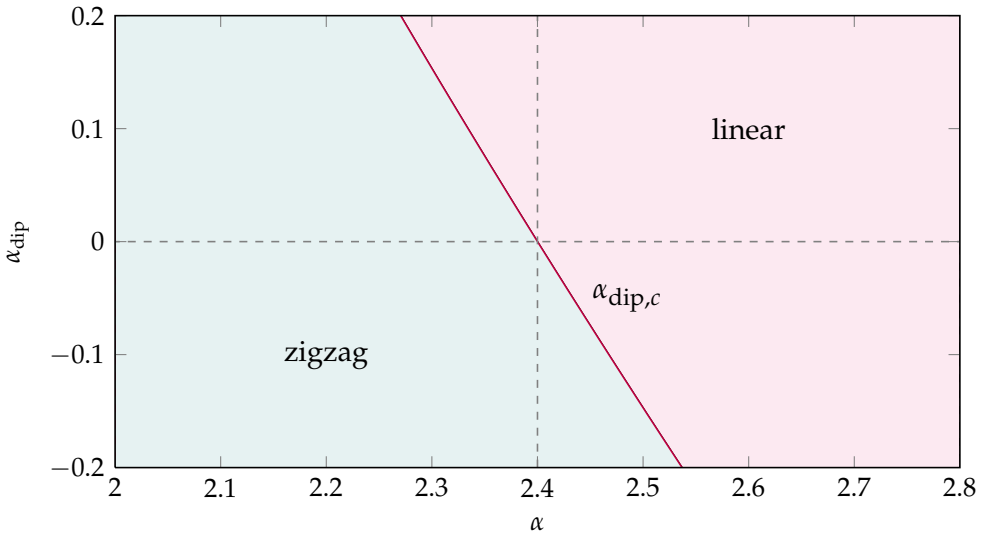

Figure 2.11: The linear–zigzag transition for three ions where the central ion is subjected to an additional potential. The outer ions experience a trapping potential that is characterized by the anisotropy parameters α, while the central ion experiences an additional potential α_{dip}. The boundary between the linear and the zigzag configurations is now a curve which can be characterized by $\alpha_{\mathrm{dip},c}$, given by Eq. (2.68).

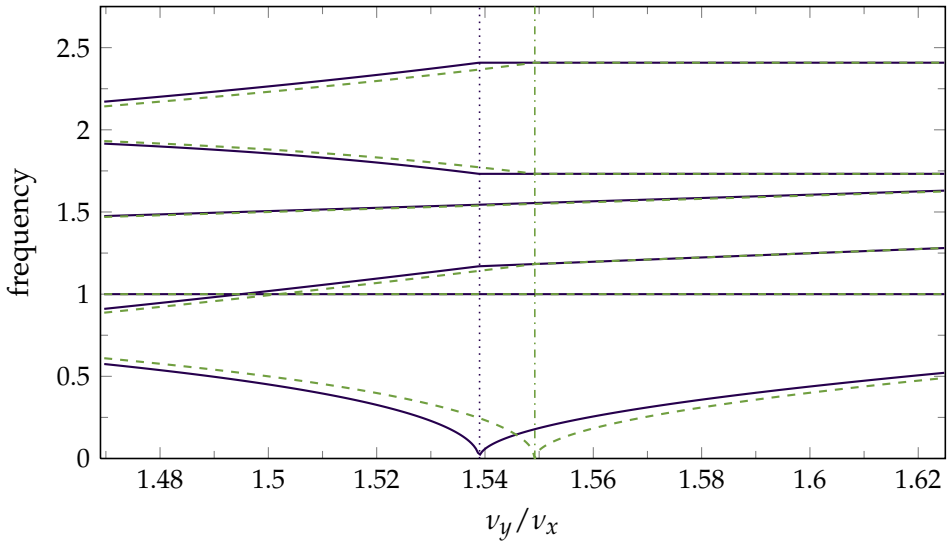

Figure 2.12: Normal mode frequencies for a three-ion crystal in which the central ion experiences a different potential (straight line) as a function of the trapping frequency ratio ν_y/ν_x compared to those of the homogeneously trapped crystal (dashed line), see Figure 2.4. The strength of the additional dipole potential is held constant. The inhomogeneous trapping potential is an additional harmonic potential in the transverse y-direction with a frequency $\nu_{\mathrm{dip}} \approx 0.219\,\nu_x$. The dash-dotted vertical line (light-blue) indicates the critical value $\alpha_c \approx 1.5492$ of the homogeneously trapped crystal.

By setting $\alpha_{\mathrm{dip}} = 0$ we recover the formulae for the homogeneous case.

The normal modes of the zigzag, again, are too involved to calculate analytically. In Figure 2.12 we show the normal mode frequencies for a three-ion Coulomb crystal in a state-dependent potential as a function of the ratio of the trapping frequencies.

The zigzag structure is the stable configuration for values of $\alpha_{\mathrm{dip}} < \alpha_{\mathrm{dip},c}$ for given α, or for values of α and α_{dip} that are to the left of and below the transition boundary given by Eq. (2.68) as shown in Figure 2.11. For lower values of α, however, other configurations are possible; since these are not at the focus of this thesis, they are discussed systematically in Appendix B. Yet we need to be sure to choose the parameter space for our considerations in such a way as to avoid any of these other possible configurations. The results of Appendix B show that by taking $\alpha > 2$ we can establish a safe lower boundary for our considerations. (The highest value of ν_y/ν_x for which a different configuration than the linear and the zigzag configurations becomes possible is around $\nu_y/\nu_x \approx 1.31$, which is well below $\nu_y/\nu_x = \sqrt{\alpha} = \sqrt{2}$, see Figure B.1.)

In this chapter we discussed how to implement a state-dependent potential in an ion trap, and we described the obtained state-dependent equilibrium positions of trapped ion Coulomb crystals. In the next chapter, we shall turn to the dynamics of ion Coulomb crystals in such state-dependent potentials.

3

DYNAMICS OF STATE-DEPENDENT ION COULOMB CRYSTALS

In this chapter we derive the necessary formalism for describing the dynamics of an ion Coulomb crystals confined by a state-dependent potential. First, in Section 3.1 we review the various levels of describing the dynamics of an ion Coulomb crystal as a set of coupled harmonic oscillators in the case of state-dependent equilibrium configurations. Then we discuss the transformations between the different descriptions of the dynamical variables such as coordinates and momenta, normal mode variables, and harmonic oscillator operators in Section 3.2. The main result of this chapter is then obtained in Section 3.3, where we derive the transformation between the quantum ground states belonging to different configurations of ion Coulomb crystals.

3.1 DYNAMICS OF STATE-DEPENDENT HARMONIC OSCILLATORS

We presuppose for now a state-dependent potential superimposed with the trap potential, as discussed in Chapter 2. Further, we discuss only the concrete case in which the electronic state of the central ion is manipulated for controlling the state-dependent potential.

As before, the position and momentum of the nth ion are denoted by $\mathbf{r}_n$ and $\mathbf{p}_n$, respectively. Since the equilibrium positions depend on the electronic state of the central ion, the equilibrium position of the nth ion is labelled by $\mathbf{R}_n^s$ with an additional upper index $s = \downarrow, \uparrow$ that indicates the electronic state the central ion is in. The ion coordinates are then expanded around the equilibrium positions by $\mathbf{r}_n = \mathbf{R}_n^s + \mathbf{q}_n^s$, and the potential energy can be approximated by a Taylor series up to second order in the deviations $\mathbf{q}_n^s$.

For convenience, we shall again switch to the single index notation (see also Table 2.1),

$$
\begin{aligned}
q_{n,x} &\mapsto q_j \qquad \text{with} \quad j = n\,, \\
q_{n,y} &\mapsto q_j \qquad \text{with} \quad j = N + n\,, \\
q_{n,z} &\mapsto q_j \qquad \text{with} \quad j = 2N + n\,.
\end{aligned}
$$

The Hamiltonian of the crystal, depending on whether the central ion is in state $s = \downarrow, \uparrow$, takes the in the approximations discussed the following form

$$H_s \approx \sum_{j=1}^{3N} \frac{p_j^2}{2m} + \sum_{j,k}^{3N} \frac{m}{2} \mathcal{V}_{jk}^s q_j^s q_k^s , \tag{3.1}$$

where the Hessian $\mathcal{V}^s$ is defined as

$$\mathcal{V}_{jk}^s = \frac{\partial^2}{\partial r_j \partial r_k} \left[V_s(r_1, \ldots, r_{3N}) + V_{\text{Coul}}(r_1, \ldots, r_{3N}) \right] \Big|_{\{r_j\}=\{R_j^s\}} \tag{3.2}$$

and $V_s(r_1, \ldots, r_{3N}) = \langle s | V_{\text{sdp}}(r_1, \ldots, r_{3N}) | s \rangle$.

Hamiltonian (3.1) is transformed into a set of uncoupled oscillators by an orthogonal matrix M^s such that

$$\sum_{ij} M_{ik}^s \mathcal{V}_{ij}^s M_{jl}^s = m \left(\omega_k^s\right)^2 \delta_{kl} , \tag{3.3}$$

where ω_k^s are the normal mode frequencies with $l = 1, \ldots, 3N$; the corresponding normal mode coordinates are related to the original displacements by the transformation $Q_l^s = \sum_k M_{kl}^s q_k^s$, with $l = 1, \ldots, 3N$.

The quantized Hamiltonian is obtained by the standard procedure by promoting the canonical coordinates and momenta to quantum mechanical operators,

$$Q_j^s \mapsto \hat{\mathrm{Q}}_j^s , \qquad P_j^s \mapsto \hat{\mathrm{P}}_j^s , \qquad \text{with} \quad [\hat{\mathrm{Q}}_j^s, \hat{\mathrm{P}}_k^s] = \mathrm{i}\hbar\delta_{jk} . \tag{3.4}$$

The commonly used harmonic oscillator form of the Hamiltonian,

$$\hat{\mathrm{H}}_s = \sum_{j=1}^{3N} \hbar\omega_j^s \left(\hat{\mathrm{b}}_j^{s\dagger} \hat{\mathrm{b}}_j^s + \frac{1}{2} \right) , \tag{3.5}$$

is obtained by introducing annihilation and creation operators, defined as linear combinations of the position and momentum operators,

$$\hat{\mathrm{b}}_j^s = \sqrt{\frac{m\omega_j^s}{2\hbar}} \left[\hat{\mathrm{Q}}_j^s + \frac{\mathrm{i}}{m\omega_j^s} \hat{\mathrm{P}}_j^s \right] , \tag{3.6a}$$

$$\hat{\mathrm{b}}_j^{s\dagger} = \sqrt{\frac{m\omega_j^s}{2\hbar}} \left[\hat{\mathrm{Q}}_j^s - \frac{\mathrm{i}}{m\omega_j^s} \hat{\mathrm{P}}_j^s \right] , \tag{3.6b}$$

with $[\hat{\mathrm{b}}_j^s, \hat{\mathrm{b}}_k^{s\dagger}] = \delta_{jk}$. The total Hamiltonian can then be written as

$$\hat{\mathrm{H}} = \sum_{s=\downarrow,\uparrow} |s\rangle\langle s| \hat{\mathrm{H}}_s , \tag{3.7}$$

where we left out the index labelling the central ion. Each of the two effective Hamiltonians $\hat{H}_s$ for $s = \uparrow, \downarrow$ possesses a complete and orthonormal basis of eigenstates, given by $\{ |n_1, \ldots, n_{3N}\rangle_s \}$ with

$$\hat{b}_j^{s\dagger} \hat{b}_j^s \, |n_1, \ldots, n_{3N}\rangle_s = n_j \, |n_1, \ldots, n_{3N}\rangle_s \qquad \text{for } n_j = 0, 1, 2, \ldots . \tag{3.8}$$

The eigenstates are constructed from the ground state by successive application of the creation operators on the ground state,

$$\frac{(\hat{b}_1^{s\dagger})^{n_1}}{\sqrt{n_1!}} \cdots \frac{(\hat{b}_j^{s\dagger})^{n_j}}{\sqrt{n_j!}} \cdots \frac{(\hat{b}_{3N}^{s\dagger})^{n_{3N}}}{\sqrt{n_{3N}!}} \, |0, \ldots, 0, \ldots, 0\rangle_s = |n_1, \ldots, n_j, \ldots, n_{3N}\rangle_s \, . \tag{3.9}$$

The motional ground state $|0, \ldots, 0\rangle_s$ is often written as $|0\rangle_s$ for short.

The eigenstates of $\hat{H}_\downarrow$ and $\hat{H}_\uparrow$ are related by a transformation that we derive in Section 3.3.

3.2 TRANSFORMATIONS BETWEEN DYNAMICAL VARIABLES

In this section we are going to discuss the transformation between the dynamical variables for classical mechanics, first in spatial coordinates, then in normal modes coordinates. As the discussion applies also for the quantized version of the dynamical variables, we conclude this section by reviewing the transformation between harmonic oscillator operators.

3.2.1 *Spatial Coordinates*

In this section we introduce the transformation between the spatial coordinates of the ions. The state of the crystal is specified by the coordinates r_j and their conjugate momenta p_j, cf. Eq. (1.16) in Section 1.2.1.

The coordinates are expanded around the equilibrium positions, which depend on the internal state of the central ion; thus there may exist more than one set of equilibrium positions. In the case of two different sets of equilibrium positions – provided the harmonic approximation holds for both sets *simultaneously* – we may take this expansion equivalently around both sets, finding the following two equations:

$$r_j = R_j^\downarrow + q_j^\downarrow \tag{3.10a}$$

$$r_j = R_j^\uparrow + q_j^\uparrow \tag{3.10b}$$

Here, $R_j^{\downarrow}$ is the equilibrium value of the coordinate labelled by j when the probed ion, labelled by n_0, is in the state $|\downarrow\rangle$, and accordingly for $R_j^{\uparrow}$. The dynamical variables are now the deviations from the equilibrium positions, $q_j^{\downarrow}$ and $q_j^{\uparrow}$, and we need to determine the transformation between them. By setting the expressions (3.10a) and (3.10b) equal (both specify the same coordinate but in different expansions),

$$R_j^{\downarrow} + q_j^{\downarrow} = r_j = R_j^{\uparrow} + q_j^{\uparrow}\,, \tag{3.11}$$

and by introducing the displacement vectors $d_j^{\downarrow\uparrow}$ and $d_j^{\uparrow\downarrow} = -d_j^{\downarrow\uparrow}$ between both sets of equilibrium positions for each ion,

$$d_j^{\downarrow\uparrow} = R_j^{\downarrow} - R_j^{\uparrow}\,, \tag{3.12a}$$

$$d_j^{\uparrow\downarrow} = R_j^{\uparrow} - R_j^{\downarrow}\,, \tag{3.12b}$$

we can relate them in the following way:

$$q_j^{\downarrow} = q_j^{\uparrow} - d_j^{\downarrow\uparrow}\,, \tag{3.13a}$$

$$q_j^{\uparrow} = q_j^{\uparrow} - d_j^{\uparrow\downarrow}\,. \tag{3.13b}$$

In order to completely describe the system classically, we need also to specify how the momenta transform. They are independent of the choice of equilibrium positions, just as they do not dependent on the choice of the coordinate origin. Therefore, the transformation between the canonical momenta is just the identity operation,

$$p_j^{\downarrow} = p_j^{\uparrow}\,. \tag{3.14}$$

Starting from Eqs. (3.13) and (3.14) we turn towards the transformation between the normal mode coordinates.

3.2.2 *Normal Mode Coordinates*

As discussed in Chapter 2, the concept of normal modes is essentially just a change in the basis representation; each normal mode coordinate is given by a linear combination of several ion coordinates, and accordingly each conjugate normal mode momentum is given by a linear combination of several momenta conjugated to the ion coordinates. The key point is that in these new coordinates the up-to-second-order expanded Hamiltonian is written in a diagonal representation, meaning that the equation of motion for each normal mode coordinate does only depend on itself and on its conjugate momentum, but not on other coordinates and momenta.

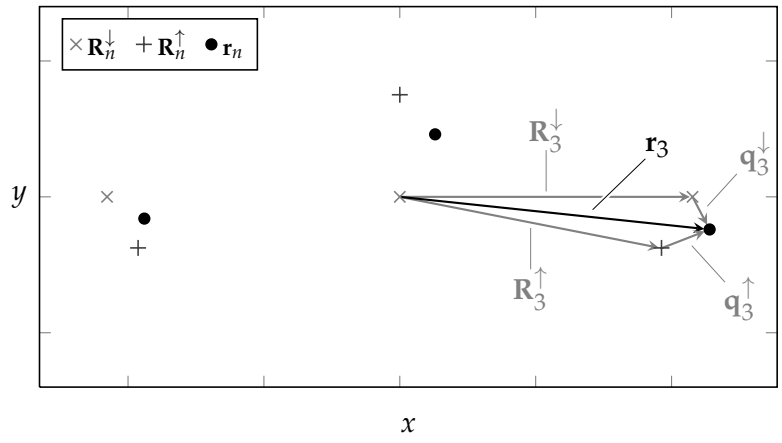

Figure 3.1: Expansion of the position vector around different equilibrium positions. The actual positions of the ions are marked by the black dots, while the equilibrium positions are marked by crosses, dependent on the electronic state of the central ion. A position vector, here $\mathbf{r}_3$, can be equivalently expanded around the two different equilibrium positions, either as the deviations $\mathbf{q}_3^{\downarrow}$ around the equilibrium positions $\mathbf{R}_3^{\downarrow}$, or as the deviations $\mathbf{q}_3^{\uparrow}$ around the equilibrium positions $\mathbf{R}_3^{\uparrow}$.

As we recall the discussion in Chapter 2, the definitions of the normal mode coordinates for both realizations are given by

$$Q_j^{\downarrow} = \sum_k M_{kj}^{\downarrow} q_k^{\downarrow}\,, \tag{3.15a}$$

$$Q_j^{\uparrow} = \sum_k M_{kj}^{\uparrow} q_k^{\uparrow}\,. \tag{3.15b}$$

Inserting Eqs. (3.13a) and (3.13b) into Eqs. (3.15a) and (3.15b), we obtain the relations

$$Q_j^{\downarrow} = \sum_k M_{kj}^{\downarrow} (q_k^{\uparrow} - d_k^{\downarrow\uparrow}) \tag{3.16a}$$

and

$$Q_j^{\uparrow} = \sum_k M_{kj}^{\uparrow} (q_k^{\downarrow} - d_k^{\uparrow\downarrow})\,. \tag{3.16b}$$

Now we use the relations inverse to Eq. (3.15), given by

$$q_j^{\downarrow} = \sum_k M_{jk}^{\downarrow} Q_k^{\downarrow}\,, \tag{3.17a}$$

$$q_j^{\uparrow} = \sum_k M_{jk}^{\uparrow} Q_k^{\uparrow}\,, \tag{3.17b}$$

and insert Eq. (3.17b) into Eq. (3.16a), respectively Eq. (3.17a) into Eq. (3.16b), to arrive at the following equations:

$$Q_j^{\downarrow} = \sum_k M_{kj}^{\downarrow} \Big(\sum_l M_{kl}^{\uparrow} Q_l^{\uparrow} - d_k^{\downarrow\uparrow} \Big) = \sum_k T_{jk} Q_k^{\uparrow} - D_j^{\downarrow\uparrow}\,, \tag{3.18a}$$

$$Q_j^{\uparrow} = \sum_k M_{kj}^{\uparrow} \Big(\sum_l M_{kl}^{\downarrow} Q_l^{\downarrow} - d_k^{\uparrow\downarrow} \Big) = \sum_k T_{kj} Q_k^{\downarrow} - D_j^{\uparrow\downarrow}\,. \tag{3.18b}$$

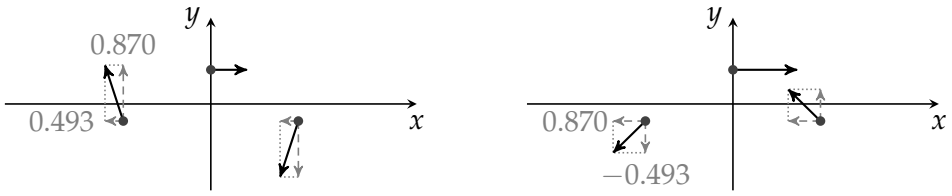

Figure 3.2: The modes of the zigzag structure can be written as the sum of the normal modes of the linear structure, here demonstrated for the transformation between $\alpha = 2.16$ and $\alpha = 2.64$. (a) The rotor mode of the zigzag structure is composed of 0.493 times the Egyptian mode and 0.870 times the rocking mode. (b) The twist mode of the zigzag structure is given by 0.870 times the Egyptian mode minus 0.493 times the rocking mode.

In the last step, we have combined the two orthogonal normal mode transformations into the product T,

$$T_{jl} = \sum_k M^{\downarrow}_{kj} M^{\uparrow}_{kl}\,, \tag{3.19}$$

which is orthogonal too, following from the orthogonality of the normal mode matrices $\mathrm{M}^{\uparrow}$ and $\mathrm{M}^{\downarrow}$ and the group properties of orthogonal matrices. The matrix T is the *transformation matrix* for the change of representation from one normal mode basis to the other; we can directly observe the mixing of the modes from its entries. The columns of the matrices $\mathrm{M}^{\downarrow}$ and $\mathrm{M}^{\uparrow}$ can be regarded as the normal modes, since any entry T_{jl} is obtained as the projection of the mode j of the configuration $\downarrow$ onto the mode l of configuration $\uparrow$. As the matrix T is orthogonal, its inverse is just equal to its transpose. The transformed modes are calculated by the matrix product of the transformation matrix with the initial modes: A transformed mode labelled by the index j is therefore given by a linear combination of the old modes with the entries along the jth row of the transformation matrix T as weights; an old mode labelled by l is decomposed into a linear combination of new modes with entries along the lth column of the transformation matrix as weights. So a mode that is invariant under a change of the Hamiltonian leads to zeros everywhere in the jth row and the lth column except for an entry equal to 1 for the element T_{jl} where the row and the column intersect.

In Eq. (3.18), we have also defined the *normal mode displacements*,

$$D^{\downarrow\uparrow}_j = \sum_k M^{\downarrow}_{kj} d^{\downarrow\uparrow}_k, \tag{3.20a}$$

$$D^{\uparrow\downarrow}_j = \sum_k M^{\uparrow}_{kj} d^{\uparrow\downarrow}_k. \tag{3.20b}$$

Here, the information about the displacement between the equilibrium positions of the two configurations is contained: The normal

mode displacement tells us how far any mode of one configuration is displaced when having the other mode as an initial condition. The two different mode displacements are transformed into each other by

$$D_j^{\downarrow\uparrow} = \sum_l T_{jl} D_l^{\uparrow\downarrow}, \tag{3.21}$$

which is directly derived from their definitions (3.20) and the relation between the displacements in coordinate space, Eq. (3.12).

For the transformation of the normal mode momenta we perform similar steps as for the normal mode coordinates. The normal mode momenta are defined as

$$P_j^{\downarrow} = \sum_k M_{kj}^{\downarrow} p_k^{\downarrow}, \tag{3.22a}$$

$$P_j^{\uparrow} = \sum_k M_{kj}^{\uparrow} p_k^{\uparrow}, \tag{3.22b}$$

However, as the particle momenta do not change, according to Eq. (3.14), the momenta are consequently just mapped into each other by the transformation matrix T,

$$P_j^{\downarrow} = \sum_k T_{jk} P_k^{\uparrow}, \tag{3.23a}$$

$$P_j^{\uparrow} = \sum_k T_{kj} P_k^{\downarrow}. \tag{3.23b}$$

without any mode displacement, as the change of equilibrium positions does not influence the momenta.

In order to illustrate the transformation between the normal mode coordinates, we write out explicitly the transition matrix T for the transformation between the homogeneously trapped structures with the values for $\alpha = 2.16$ to $\alpha = 2.64$, that is between a linear and a zigzag configuration (the linear–zigzag transition is at $\alpha_c = 2.4$). The transition matrix for these parameters is given approximately by

$$\mathrm{T} = \begin{pmatrix} 0.786 & 0 & 0 & 0 & -0.618 & 0 \\ 0 & 0 & 0.870 & 0 & 0 & 0.493 \\ 0 & 1 & 0 & 0 & 0 & 0 \\ 0 & 0 & 0 & 1 & 0 & 0 \\ 0.618 & 0 & 0 & 0 & 0.786 & 0 \\ 0 & 0 & -0.493 & 0 & 0 & 0.870 \end{pmatrix}. \tag{3.24}$$

Modes that are common to both configurations show up here as one in a diagonal entry, with the row and column filled up with zeros. The other modes are transformed into linear combinations of normal modes in the new normal mode coordinate basis. A few examples of such a transformation are illustrated in Figure 3.2.

So far, we have derived the transformation between the classical normal mode momenta and positions. The same transformation holds for the quantized normal mode momentum and position operators, as the transformation given by Eq. (3.19) is linear and involves no cross-terms between momenta and coordinates. Now we can turn to the transformation of the harmonic oscillator creation and annihilation operators in the following section.

3.2.3 *Harmonic Oscillator Operators*

The transformation between the harmonic oscillator operators is commonly called a *Bogoliubov transformation*, and it is a standard tool used in quantum field theory (Fetter and Walecka 1971, Ch. 35; Abrikosov et al. 1965, Ch. 4) and in the theory of ultracold atomic gases (Pitaevskii and Stringari 2003, Ch. 4). A Bogoliubov transformation is a linear transformation of harmonic creation and annihilation operators, and it is canonical if the commutation relations are preserved by the transformation. It is generally given in the form of the following Hermitian conjugated equations:

$$\hat{b}_j^{\downarrow} = \sum_k U_{jk} \hat{b}_k^{\uparrow} - \sum_k V_{jk} \hat{b}_k^{\uparrow\dagger} - \beta_j^{\downarrow}, \tag{3.25a}$$

$$\hat{b}_j^{\downarrow\dagger} = \sum_k U_{kj}^* \hat{b}_k^{\uparrow\dagger} - \sum_k V_{kj}^* \hat{b}_k^{\uparrow} - \beta_j^{\downarrow *}, \tag{3.25b}$$

where the transformed annihilation and creation operators inherit the commutation relations of harmonic oscillator operators,

$$\left[\hat{b}_j^{\uparrow}, \hat{b}_k^{\uparrow\dagger}\right] = \delta_{jk}, \qquad \left[\hat{b}_j^{\uparrow}, \hat{b}_k^{\uparrow}\right] = 0, \qquad \left[\hat{b}_j^{\uparrow\dagger}, \hat{b}_k^{\uparrow\dagger}\right] = 0, \tag{3.26a}$$

provided that the untransformed operators fulfil these kind of commutation relations a priori,

$$\left[\hat{b}_j^{\downarrow}, \hat{b}_k^{\downarrow\dagger}\right] = \delta_{jk}, \qquad \left[\hat{b}_j^{\downarrow}, \hat{b}_k^{\downarrow}\right] = 0, \qquad \left[\hat{b}_j^{\downarrow\dagger}, \hat{b}_k^{\downarrow\dagger}\right] = 0. \tag{3.26b}$$

Essentially, this is a restatement of the requirement for the transformation to be canonical, which sets certain conditions on the coefficients, U_{jk} and V_{jk}, and the displacements, $\beta_j^{\downarrow}$, which we discuss in the following paragraphs.[1] The transformation (3.25) is derived by inserting Eqs. (3.18) and (3.23) into the definition of the annihilation operators,

$$\hat{b}_l^{\downarrow} = \sqrt{\frac{m\omega_l^{\downarrow}}{2\hbar}} \left[\hat{Q}_l^{\downarrow} + \frac{\mathrm{i}}{m\omega_l^{\downarrow}} \hat{P}_l^{\downarrow}\right]$$

1 The terms of the displacements $\beta^{\downarrow}$ in Eq. (3.25) are usually absent in the commonly used Bogoliubov transformation; these originate from a possible change in the equilibrium positions. This generalized form of transformation is discussed in Bogoliubov and Bogoliubov Jr. (2010, Part III, Ch. 2, Sec. 1. g).

$$= \sqrt{\frac{m\omega_l^{\downarrow}}{2\hbar}} \left[\sum_k T_{lk} \hat{Q}_k^{\uparrow} - D_l^{\downarrow\uparrow} + \frac{\mathrm{i}}{m\omega_l^{\downarrow}} \sum_k T_{lk} \hat{P}_k^{\uparrow} \right] . \tag{3.27}$$

By using the expansion of the canonical momentum and position operators in terms of the corresponding creation and annihilation operators,

$$\hat{Q}_k^{\uparrow} = \sqrt{\frac{\hbar}{2m\omega_k^{\uparrow}}} \left(\hat{b}_k^{\uparrow\dagger} + \hat{b}_k^{\uparrow} \right) , \quad \hat{P}_k^{\uparrow} = \mathrm{i} \sqrt{\frac{\hbar m \omega_k^{\uparrow}}{2}} \left(\hat{b}_k^{\uparrow\dagger} - \hat{b}_k^{\uparrow} \right) , \tag{3.28}$$

we arrive at Eq. (3.25) after a regrouping of the terms. By this, we simultaneously determine the relations for the Bogoliubov coefficients U_{jk} and V_{jk},

$$U_{lk} = \frac{T_{lk}}{2} \left[\sqrt{\frac{\omega_k^{\uparrow}}{\omega_l^{\downarrow}}} + \sqrt{\frac{\omega_l^{\downarrow}}{\omega_k^{\uparrow}}} \right] , \tag{3.29a}$$

$$V_{lk} = \frac{T_{lk}}{2} \left[\sqrt{\frac{\omega_k^{\uparrow}}{\omega_l^{\downarrow}}} - \sqrt{\frac{\omega_l^{\downarrow}}{\omega_k^{\uparrow}}} \right] , \tag{3.29b}$$

which are real and dimensionless. At the same time we obtain the relation for the displacements,

$$\beta_j^{\downarrow} = \sqrt{m\omega_j^{\downarrow}/2\hbar}\, D_j^{\downarrow} , \tag{3.30}$$

which are real since we only have a shift in the position coordinates (a shift in momentum would result in a complex-valued displacement).

In order to comply with Eqs. (3.26), the Bogoliubov coefficients have to fulfil the following relations,

$$\sum_k \left(U_{jk} U_{lk} - V_{jk} V_{lk} \right) = \delta_{jl} , \tag{3.31a}$$

$$\sum_k \left(U_{jk} V_{lk} - V_{jk} U_{lk} \right) = 0 \quad \forall j, l . \tag{3.31b}$$

These are derived by inserting Eqs. (3.29) and making use of the orthogonality of the transformation matrix T. We can also obtain the inverse relations, either by using the just derived properties after multiplying Eqs. (3.25) by the Bogoliubov coefficients and adding them together, or by employing the inverse Bogoliubov transformation by starting from the definition of $\hat{b}_j^{\uparrow}$ instead. In either way, the result is given by

$$\hat{b}_j^{\uparrow} = \sum_k U_{kj} \hat{b}_j^{\downarrow} - \sum_k V_{kj} \hat{b}_k^{\downarrow\dagger} - \beta_j^{\uparrow} , \tag{3.32a}$$

$$\hat{b}_j^{\uparrow\dagger} = \sum_k U_{kj} b_k^{\downarrow\dagger} - \sum_k V_{kj} \hat{b}_k^{\downarrow} - \beta_j^{\uparrow} . \tag{3.32b}$$

Having gathered these relations, we can now re-express any operator compound of the harmonic oscillator operators of one basis as a decomposition in the other basis. For ease of calculation, it is desirable to have also a transformation relating the phase space displacements, which can be obtained by Eqs. (3.31),

$$\beta_l^{\uparrow} = \sum_k \sqrt{\frac{\omega_l^{\uparrow}}{\omega_k^{\downarrow}}} T_{kl} \beta_k^{\downarrow} = \sum_k (U_{kl} + V_{kl}) \beta_k^{\downarrow} , \tag{3.33a}$$

$$\beta_l^{\downarrow} = \sum_k \sqrt{\frac{\omega_l^{\downarrow}}{\omega_k^{\uparrow}}} T_{lk} \beta_k^{\uparrow} = \sum_k (U_{lk} - V_{lk}) \beta_k^{\uparrow} . \tag{3.33b}$$

With this, we conclude the discussion of the transformation of the operators and turn now to the transformation of the motional quantum states.

3.3 TRANSFORMATIONS BETWEEN QUANTUM STATES

3.3.1 *Motional Ground States*

Before moving on to the transformation of arbitrary motional states in Section 3.3.2, we will discuss in this section the transformation between the ground states. The reader, familiar with the concept of unitary transformations in quantum mechanics, might wonder why we distinguish here between a transformation of ground states and one of arbitrary states. After all, any quantum state can be transformed from one basis into another one by a specific unitary operation, which does not depend on the state on which the transformation is applied to. What is then the point of having a different transformation for the ground state that turns out to even be non-unitary? The answer is simply that it is much easier for us to first find the transformation which can be applied only onto the ground states and then advance it to the full unitary transformation. The derivation of this simpler transformation, based on a work by Fetter (1972), is the subject of this section.

Replacing a Unitary by a Non-Unitary Transformation

Let us now start with the derivation of this non-unitary transformation. For this, first consider the general unitary transformation connecting two arbitrary quantum states,

$$|\psi\rangle_{\downarrow} = \hat{U} |\psi\rangle_{\uparrow} . \tag{3.34}$$

In general, unitary transformations generated by up to quadratic bosonic operators are made up of four different building blocks (Ferraro et al. 2005, Ch. 1.4; Olivares 2012, Sec. 4), consisting of the operations of:

1. harmonic oscillation,

$$\hat{\mathrm{O}}_{\uparrow}(\varphi) = \exp\Big\{-\mathrm{i}\sum_j \varphi_j^{\uparrow}\hat{\mathrm{b}}_j^{\uparrow\dagger}\hat{\mathrm{b}}_j^{\uparrow}\Big\}\,, \tag{3.35a}$$

2. displacement,

$$\hat{\mathrm{D}}_{\uparrow}(\gamma) = \exp\Big\{\sum_j (\gamma_j\hat{\mathrm{b}}_j^{\uparrow\dagger} - \gamma_j^*\hat{\mathrm{b}}_j^{\uparrow})\Big\}\,, \tag{3.35b}$$

3. one- (for $j = k$) and two-mode (for $j \neq k$) squeezing,

$$\hat{\mathrm{S}}_{\uparrow}(\xi) = \exp\Big\{\frac{1}{2}\sum_{jk} (\xi_{jk}\hat{\mathrm{b}}_j^{\uparrow\dagger}\hat{\mathrm{b}}_k^{\uparrow\dagger} - \xi_{jk}^*\hat{\mathrm{b}}_j^{\uparrow}\hat{\mathrm{b}}_k^{\uparrow})\Big\}\,, \tag{3.35c}$$

4. and two-mode mixing (also called beam-splitter operation),

$$\hat{\mathrm{M}}_{\uparrow}(\zeta) = \exp\Big\{\sum_{\substack{jk\\ j\neq k}} (\zeta_{jk}\hat{\mathrm{b}}_j^{\uparrow\dagger}\hat{\mathrm{b}}_k^{\uparrow} + \zeta_{jk}^*\hat{\mathrm{b}}_j^{\uparrow}\hat{\mathrm{b}}_k^{\uparrow\dagger})\Big\}\,. \tag{3.35d}$$

Thus, the most general transformation is given by the product of these building-blocks,

$$\hat{\mathrm{U}} = \hat{\mathrm{D}}_{\uparrow}(\gamma)\,\hat{\mathrm{S}}_{\uparrow}(\xi)\,\hat{\mathrm{O}}_{\uparrow}(\varphi)\,\hat{\mathrm{M}}_{\uparrow}(\zeta)\,, \tag{3.36}$$

where the order of the transformations is arbitrary, but not interchangeable.[2] This transformation is between Hamiltonians of up to quadratic order in the annihilation and creation operators; thus we need to make sure that the local harmonic approximation of the potential is still valid. We are going to discuss the aspect of the validity domain in more detail in Chapter 5.

As already mentioned, we now want to find a simpler transformation connecting only the ground states, assuming the following ansatz (Fetter 1972):

$$|0\rangle_{\downarrow} = \hat{\mathrm{W}}\,|0\rangle_{\uparrow}\,. \tag{3.37}$$

2 The different possibilities for the ordering correspond to different parametrizations of the Lie group generated by the Lie algebra of the bosonic operators. These different parametrizations are then related by specific disentangling formulae, see Gilmore (2008, Ch. 7.4, pp. 110ff.) and Appendix C. Changing the order thus leads to other parameters γ, ξ, ζ, ϕ.

We can further assume the following identity, only valid for the mapping between the ground states,

$$\hat{U}\,|0\rangle_{\uparrow} = \hat{W}\,|0\rangle_{\uparrow}\,, \tag{3.38}$$

where both transformations lead to the same result when applied onto the ground state, but generally yield different outcomes when applied onto other states. The relation (3.38) between the transformations is going to help us find the full transformation in Section 3.3.2, and it also enables us to determine the form of the non-unitary transformation $\hat{W}$ based on the ansatz of the unitary transformation $\hat{U}$ of Eq. (3.36). For this, we evaluate the operators in Eq. (3.36) onto the ground state and replace them in two steps by their simpler counterparts, which conform to Eq. (3.37).

First, we make use of the choice of the order of the operators in Eq. (3.36). The first and the second operators (counting from right to left), i. e. the two-mode mixing and the harmonic oscillation operators, yield just the identity operation when applied onto the ground state. (This can be seen by expanding the exponentials and realizing that all terms from the first order expansion on contain annihilation operators to their very right, which, when applied on the ground state, all vanish. So only the zeroth order expansion remains, which is just the identity operation.)

Second, we apply the *disentangling theorem* (cf. Appendix C) onto the squeezing operator to split it up into separate factors as

$$\hat{S}_e = Z\,e^{\hat{A}}\,e^{\hat{B}}\,e^{-\hat{A}^\dagger}\,. \tag{3.39}$$

The operators in the exponents are given by the disentangling theorem, see Eqs. (C.29a) and (C.29b), and have the following form,

$$\hat{A} = \frac{1}{2}\sum_{jk} A_{jk}\hat{b}_j^{\uparrow\dagger}\hat{b}_k^{\uparrow\dagger}\,, \tag{3.40a}$$

$$\hat{B} = -\sum_{jk} B_{jk}\,\hat{b}_j^{\uparrow\dagger}\hat{b}_j^{\uparrow}\,, \tag{3.40b}$$

where the matrices A and B are real[3] and can be chosen symmetric, as the creation operators belonging to different modes commute. The factor Z is a normalization constant which we determine later.

It is instructive to analyse the effect of this operator when it is applied to the ground state. The utmost right operator contains only annihilation operators in the exponential, thus, when applying it to the ground state and expanding the exponential, only the zeroth order gives a non-zero contribution,

$$e^{-\hat{A}^\dagger}\,|0\rangle_e = |0\rangle_e\,,$$

3 They could have an imaginary part if the momentum had changed between both structures, which is not the case here.

which is just the identity. For the second operator, we find that, by the same reasoning, only the zeroth order contributes,

$$\mathrm{e}^{\hat{\mathrm{B}}} \left|0\right\rangle_e = \left|0\right\rangle_e ,$$

resulting in the identity operation when applied on the ground state. Thus, for the last two operators, only the terms of zeroth order survive – whereas all orders of the first term remain. Therefore, we have the following identity

$$Z\,\mathrm{e}^{\hat{\mathrm{A}}}\,\mathrm{e}^{\hat{\mathrm{B}}}\,\mathrm{e}^{-\hat{\mathrm{A}}^\dagger} \left|0\right\rangle_\uparrow = Z\,\mathrm{e}^{\hat{\mathrm{A}}} \left|0\right\rangle_\uparrow , \tag{3.41}$$

which justifies the ansatz (3.38). Thus, applied to the ground state $\left|0\right\rangle_e$, the transformation $\hat{\mathrm{U}}$ is just given by the first two terms of Eq. (3.36), effectively. By this we have found a form of the non-unitary transformation $\hat{\mathrm{W}}$, which mimics the effect of the unitary $\hat{\mathrm{U}}$ transformation for the application to the motional ground state. As already mentioned, this substitution of the unitary transformation has been previously introduced by Fetter (1972), whose approach we follow here. The non-unitary transformation thus is given by

$$\hat{\mathrm{W}} = Z\,\hat{\mathrm{D}}_\uparrow(\gamma_1, \ldots, \gamma_{3N})\,\mathrm{e}^{\hat{\mathrm{A}}} , \tag{3.42}$$

which is invertible. It can now be employed as the transformation between the ground states, Eq. (3.37).

Before we make use of this transformation, we still need a method for relating the actual coefficients γ_j, the matrix elements A_{jk}, and the normalization constant Z to the results of the discussion in the previous sections.

Calculating the Parameters of the Transformation

The general idea for calculating the coefficients A_{jk} of the operator $\hat{\mathrm{A}}$ and the displacements γ_j in Eq. (3.42) is to make use of specific properties of the transformed ground state. One such property is that any annihilation operator $\hat{\mathrm{b}}_j^\downarrow$, applied to the ground state, yields zero,

$$\hat{\mathrm{b}}_j^\downarrow \left|0\right\rangle_\downarrow = 0 \quad \forall j . \tag{3.43}$$

In this equation we replace the ground state by its transformed version using Eq. (3.37), and map the annihilation operator with the help of the Bogoliubov transformation Eq. (3.25) to a sum of creation and annihilation operators for the other harmonic oscillator basis, arriving at

$$0 = \hat{\mathrm{b}}_j^\downarrow \left|0\right\rangle_\downarrow = \left[\sum_k \left(U_{jk}\hat{\mathrm{b}}_k^\uparrow - V_{jk}\hat{\mathrm{b}}_k^{\uparrow\dagger}\right) - \beta_j^\downarrow\right] \hat{\mathrm{W}} \left|0\right\rangle_\uparrow . \tag{3.44}$$

We can expand the bracket such that the transformation $\hat{W}$ is right next to each of the harmonic oscillator operators, and we then insert the identity operator, $\mathbb{1} = \hat{W}\hat{W}^{-1}$, directly to the left of them. By this, we obtain the following terms

$$\hat{W}^{-1}\,\hat{b}_k^{\uparrow}\,\hat{W} = e^{-\hat{A}}\hat{D}_{\uparrow}^{\dagger}(\gamma_1,\ldots,\gamma_{3N})\,\hat{b}_k^{\uparrow}\,\hat{D}_{\uparrow}(\gamma_1,\ldots,\gamma_{3N})\,e^{\hat{A}}\,, \tag{3.45a}$$

$$\hat{W}^{-1}\,\hat{b}_k^{\uparrow\dagger}\,\hat{W} = e^{-\hat{A}}\hat{D}_{\uparrow}^{\dagger}(\gamma_1,\ldots,\gamma_{3N})\,\hat{b}_k^{\uparrow\dagger}\,\hat{D}_{\uparrow}(\gamma_1,\ldots,\gamma_{3N})\,e^{\hat{A}}\,, \tag{3.45b}$$

which are evaluated with the help of the Baker-Campbell-Hausdorff identity (BCH)-identity (Mandel and Wolf 1995, p.519 f.),

$$e^{\hat{X}}\hat{Y}\,e^{-\hat{X}} = \hat{Y} + [\hat{X},\hat{Y}] + \frac{1}{2!}\Big[\hat{X},[\hat{X},\hat{Y}]\Big] + \frac{1}{3!}\Big[\hat{X},\Big[\hat{X},[\hat{X},\hat{Y}]\Big]\Big] + \cdots\,. \tag{3.46}$$

This identity is applied twice to Eqs. (3.45); first evaluating the unitary displacement operators mode-by-mode, we find that the BCH-series terminates, yielding

$$\hat{D}_{\uparrow}^{\dagger}(\gamma_k)\,\hat{b}_j^{\uparrow}\,\hat{D}_{\uparrow}(\gamma_k) = \hat{b}_j^{\uparrow} + \gamma_k\delta_{jk}\,, \tag{3.47a}$$

$$\hat{D}_{\uparrow}^{\dagger}(\gamma_k)\,\hat{b}_j^{\uparrow\dagger}\,\hat{D}_{\uparrow}(\gamma_k) = \hat{b}_j^{\uparrow\dagger} + \gamma_k\delta_{jk}\,. \tag{3.47b}$$

Applying the identity to the exponential operators and employing the commutation relations $[\hat{A},\hat{b}_k^{\uparrow}]$ and $[\hat{A},\hat{b}_k^{\uparrow\dagger}]$, we find that the non-trivial terms terminate, [4] too, resulting in

$$e^{-\hat{A}}\hat{b}_j^{\uparrow}\,e^{\hat{A}} = \hat{b}_j^{\uparrow} + \sum_l A_{kl}\hat{b}_j^{\uparrow\dagger}\,, \tag{3.48a}$$

$$e^{-\hat{A}}\hat{b}_j^{\uparrow\dagger}\,e^{\hat{A}} = \hat{b}_j^{\uparrow\dagger}\,, \tag{3.48b}$$

The identities for the transformation $\hat{W}$ are summarized by

$$\hat{W}^{-1}\hat{b}_k^{\uparrow}\hat{W} = \hat{b}_j^{\uparrow} + \sum_l A_{kl}\hat{b}_j^{\uparrow\dagger} + \gamma_k\delta_{jk}\,, \tag{3.49a}$$

$$\hat{W}^{-1}\hat{b}_k^{\uparrow\dagger}\hat{W} = \hat{b}_j^{\uparrow\dagger} + \gamma_k\delta_{jk}\,. \tag{3.49b}$$

Using the results of these identities in Eq. (3.44), we can evaluate all annihilation operators by applying them to the ground state $|0\rangle_e$, such that we obtain the following equation:

$$0 = \hat{W}\Bigg\{\sum_k\Bigg[U_{jk}\Big(\sum_l A_{kl}\hat{b}_l^{\uparrow\dagger}\Big) - V_{jk}\hat{b}_k^{\uparrow\dagger}\Bigg] + \Bigg[\sum_k\Big(U_{jk} - V_{jk}\Big)\gamma_k - \beta_j^{\downarrow}\Bigg]\Bigg\}\,|0\rangle_{\uparrow}\,. \tag{3.50}$$

4 If we had used the not-disentangled squeezing operator instead, the last identity would yield infinite series instead of the closed expressions.

By multiplying both sides by $\hat{W}^{-1}$, we first remove the transformation $\hat{W}$ on the right-hand-side, leaving two terms in the braces on the right-hand side. The first one contains only a sum of creation operators – and no annihilation operators – belonging to different modes, which are applied to a state vector. When a creation operator is applied to the ground state vector, it will yield a state vector with a single excitation; altogether, it leads to a sum of linearly independent state vectors, each one weighted by a certain coefficient. In the second term, there are just numbers, so the whole term is proportional to the ground state $|0\rangle_{\uparrow}$. Consequently, there are two terms on the right-hand side: a sum of states with one excitation each and the ground state, each with given coefficients. For this equation to be valid, each of these coefficients needs to vanish separately.

For the coefficients in front of the singly excited states, we obtain for each of the $3N$ modes a set of $3N$ equations, totalling $(3N)^2$ equations, all of which can be summarized in the following matrix equation,

$$\sum_k U_{jk} A_{kl} - V_{jl} = 0 \quad \forall j, l\,. \tag{3.51}$$

This equation relates the coefficients A_{jk} to the presumably already known matrices U and V; it is well defined as U is non-singular, which is warranted by Eq. (3.29a). We can solve for the matrix A by inverting U,

$$A_{jk} = \sum_l (\mathrm{U}^{-1})_{jl} V_{lk}\,. \tag{3.52}$$

Since U and V are real-valued, cf. Eqs. (3.29), it follows immediately that A is real as well.

For the coefficients in front of the ground state, we obtain the following set of equations for the γ_j's,

$$\sum_k (U_{jk} - V_{jk})\gamma_k - \beta_j^{\downarrow} = 0 \quad \forall j\,. \tag{3.53}$$

We can solve these equations to obtain the displacements γ_j for each mode, which turn out, not surprisingly, to be just the inverse phase space displacements $\beta_j^{\uparrow}$ introduced in Eq. (3.33). This is not surprising when we recall that the operation of the displacement operator onto a Gaussian wavepacket just shifts it centre.

Calculating the Normalization Constant Z

Finally, we need to evaluate the value of the constant Z. The evaluation makes use of a variant of a *linked cluster expansion* (also known as Mayer cluster expansion), which is a known technique in statistical physics, (Huang 1987, Sec.10.1, 10.2, pp. 213ff.; Feynman 1972, Sec. 4.3,

pp. 105ff.; see Domb 1974, for a historical account). For this, we start by checking whether the normalization condition of the states is fulfilled,

$$1 = {}_{\downarrow}\langle 0|0\rangle_{\downarrow} = {}_{\uparrow}\langle 0|\hat{W}^{\dagger}\hat{W}|0\rangle_{\uparrow}\,. \tag{3.54}$$

The normalization for the right expression is not trivially guaranteed, since $\hat{W}$ is not a unitary operator; its Hermitian conjugate is *not* equal to its inverse, $\hat{W}^{\dagger} \neq \hat{W}^{-1}$, so that we cannot replace the product by the identity. However, by inserting the definition of $\hat{W}$, the displacement operators cancel each other out as they are unitary,

$$1 = |Z|^2\, {}_{\uparrow}\langle 0|\, e^{\hat{A}^{\dagger}} \hat{D}^{\dagger}_{\uparrow}(\gamma)\hat{D}_{\uparrow}(\gamma)\, e^{\hat{A}}|0\rangle_{\uparrow} = |Z|^2\, {}_{\uparrow}\langle 0|\, e^{\hat{A}^{\dagger}} e^{\hat{A}}|0\rangle_{\uparrow}\,, \tag{3.55}$$

while the non-unitary exponential operators do not.[5] We then expand the exponential functions of the operators $\hat{A}$ and $\hat{A}^{\dagger}$,

$$1 = |Z|^2\, {}_{\uparrow}\langle 0|\left(\sum_{n=0}^{\infty}\sum_{m=0}^{\infty}\frac{\hat{A}^{\dagger n}\hat{A}^{m}}{n!\,m!}\right)|0\rangle_{\uparrow}\,. \tag{3.56}$$

First, we inspect an arbitrary summand for which we have $n \neq m$. As $\hat{A}$ is a sum containing two creation operators in each summand, and likewise $\hat{A}^{\dagger}$ involves only summands containing two annihilation operators each, we know that there are $2m$ creation operators and $2n$ annihilation operators in such a term. For $n \neq m$ there are either more creation or more annihilation operators in any summand. But for any expression containing an unequal number of creation and annihilation operators, the expectation value for the ground state vanishes. Therefore, all terms in the sum of Eq. (3.56) with $n \neq m$ are zero and only one sum remains,

$$|Z|^{-2} = {}_{\uparrow}\langle 0|\left(\sum_{n=0}^{\infty}\frac{\hat{A}^{\dagger n}\hat{A}^{n}}{(n!)^2}\right)|0\rangle_{\uparrow} = \sum_{n=0}^{\infty}\frac{{}_{\uparrow}\langle 0|\hat{A}^{\dagger n}\hat{A}^{n}|0\rangle_{\uparrow}}{(n!)^2} = \sum_{n=0}^{\infty} W_n\,. \tag{3.57}$$

Here, we introduced W_n as a short-hand notation for the nth summand. Inserting the definition of the operator $\hat{A}$, we arrive at the following expression for W_n,

$$W_n = \frac{1}{(2^n n!)^2}\sum_{\substack{j_1,\ldots,j_{2n}\\ k_1,\ldots,k_{2n}}} A_{j_1 j_2}\cdots A_{j_{2n-1}j_{2n}} A_{k_1 k_2}\cdots A_{k_{2n-1}k_{2n}} \\ {}_{\uparrow}\langle 0|\hat{b}^{\uparrow}_{j_1}\hat{b}^{\uparrow}_{j_2}\cdots\hat{b}^{\uparrow}_{j_{2n-1}}\hat{b}^{\uparrow}_{j_{2n}}\hat{b}^{\uparrow\dagger}_{k_1}\hat{b}^{\uparrow\dagger}_{k_2}\cdots\hat{b}^{\uparrow\dagger}_{k_{2n-1}}\hat{b}^{\uparrow\dagger}_{k_{2n}}|0\rangle_{\uparrow} \tag{3.58}$$

5 Clearly, the normalization constant Z will be only determined up to a phase factor by this method.

where any of the indices $j_1, j_2, \ldots, k_1, k_2, \ldots$ runs from 1 to $3N$, the number of modes.

Let us inspect a summand in W_n a bit closer. Inside the matrix element, we are allowed to commute any two operators as long as they are of the same types, i. e. two creation operators or two annihilation operators. Thus we may rewrite Eq. (3.58) with the operators in any arbitrary order as long as all the annihilation operators remain to the left of the creation operators. For the evaluation of any matrix element in Eq. (3.58), therefore, only the unordered *multisets*[6] of indices $\{j_1, \ldots, j_{2n}\}$ and $\{k_1, \ldots, k_{2n}\}$ are important, and not the $2n$-tuples $(j_1, \ldots, j_{2n})$ and $(k_1, \ldots, k_{2n})$. If in a matrix element a mode index is not occurring as often in one of the multisets as in the other one, then for that mode the quantity of creation and annihilation operators in the matrix element is unequal, so the matrix element vanishes. Hence, any summand in Eq. (3.58) is non-zero only if the two multisets of indices $\{j_1, \ldots, j_{2n}\}$ and $\{k_1, \ldots, k_{2n}\}$ are *identical*.

Let us check these considerations for the first few terms. The term W_0 is trivially given by $W_0 = 1$. The next term W_1 is then given by

$$W_1 = \frac{1}{2^2} \sum_{\substack{j_1 j_2 \\ k_1 k_2}} A_{j_1 j_2} A_{k_1 k_2} \, {}_\uparrow\langle 0 | \hat{b}^\uparrow_{j_1} \hat{b}^\uparrow_{j_2} \hat{b}^{\uparrow\dagger}_{k_1} \hat{b}^{\uparrow\dagger}_{k_2} | 0 \rangle_\uparrow \,. \tag{3.59}$$

We can evaluate the matrix element by commuting all annihilation operators to the right, making use of the commutation relations, Eqs. (3.26),

$$\begin{aligned} {}_\uparrow\langle 0 | \hat{b}^\uparrow_{j_1} \hat{b}^\uparrow_{j_2} \hat{b}^{\uparrow\dagger}_{k_1} \hat{b}^{\uparrow\dagger}_{k_2} | 0 \rangle_\uparrow &= {}_\uparrow\langle 0 | \hat{b}^\uparrow_{j_1} \left(\hat{b}^{\uparrow\dagger}_{k_1} \hat{b}^\uparrow_{j_2} + \left[\hat{b}^\uparrow_{j_2}, \hat{b}^{\uparrow\dagger}_{k_1} \right] \right) \hat{b}^{\uparrow\dagger}_{k_2} | 0 \rangle_\uparrow \\ &= {}_\uparrow\langle 0 | \hat{b}^\uparrow_{j_1} \hat{b}^{\uparrow\dagger}_{k_1} \hat{b}^\uparrow_{j_2} \hat{b}^{\uparrow\dagger}_{k_2} | 0 \rangle_\uparrow + {}_\uparrow\langle 0 | \hat{b}^\uparrow_{j_1} \hat{b}^{\uparrow\dagger}_{k_2} | 0 \rangle_\uparrow \, \delta_{j_2 k_1} \,, \end{aligned} \tag{3.60}$$

where the second term on the right contains now only two operators. We can simplify it further by commuting the remaining operators,

$$\begin{aligned} {}_\uparrow\langle 0 | \hat{b}^\uparrow_{j_1} \hat{b}^{\uparrow\dagger}_{k_2} | 0 \rangle_\uparrow \, \delta_{j_2 k_1} &= {}_\uparrow\langle 0 | \left(\hat{b}^{\uparrow\dagger}_{k_2} \hat{b}^\uparrow_{j_1} + \left[\hat{b}^\uparrow_{j_1}, \hat{b}^{\uparrow\dagger}_{k_2} \right] \right) | 0 \rangle_\uparrow \, \delta_{j_2 k_1} \\ &= \underbrace{{}_\uparrow\langle 0 | \hat{b}^{\uparrow\dagger}_{k_2} \hat{b}^\uparrow_{j_1} | 0 \rangle_\uparrow}_{=0} \, \delta_{j_2 k_1} + \delta_{j_1 k_2} \delta_{j_2 k_1} = \delta_{j_1 k_2} \delta_{j_2 k_1} \,, \end{aligned} \tag{3.61}$$

obtaining a product of two Kronecker-δ symbols.

6 A multiset is similar to a set, but the elements may appear more than once. The order of the elements is irrelevant, in contrast to tuples.

We can evaluate the first term in Eq. (3.60) in the same manner,

$$\begin{aligned}
{}_\uparrow\langle 0|\hat{b}^\uparrow_{j_1}\hat{b}^{\uparrow\dagger}_{k_1}\hat{b}^\uparrow_{j_2}\hat{b}^{\uparrow\dagger}_{k_2}|0\rangle_\uparrow &= {}_\uparrow\langle 0|\hat{b}^\uparrow_{j_1}\hat{b}^{\uparrow\dagger}_{k_1}\left(\hat{b}^{\uparrow\dagger}_{k_2}\hat{b}^\uparrow_{j_2}+\left[\hat{b}^\uparrow_{j_2},\hat{b}^{\uparrow\dagger}_{k_2}\right]\right)|0\rangle_\uparrow \\
&= {}_\uparrow\langle 0|\,\hat{b}^\uparrow_{j_1}\hat{b}^{\uparrow\dagger}_{k_1}\hat{b}^{\uparrow\dagger}_{k_2}\underbrace{\hat{b}^\uparrow_{j_2}|0\rangle_\uparrow}_{=0} + {}_\uparrow\langle 0|\hat{b}^\uparrow_{j_1}\hat{b}^{\uparrow\dagger}_{k_1}|0\rangle_\uparrow\,\delta_{j_2k_2} \\
&= {}_\uparrow\langle 0|\left(\hat{b}^{\uparrow\dagger}_{k_1}\hat{b}^\uparrow_{j_1}+\left[\hat{b}^\uparrow_{j_1},\hat{b}^{\uparrow\dagger}_{k_1}\right]\right)|0\rangle_\uparrow\,\delta_{j_2k_2} \\
&= {}_\uparrow\langle 0|\,\hat{b}^{\uparrow\dagger}_{k_1}\underbrace{\hat{b}^\uparrow_{j_1}|0\rangle_\uparrow}_{=0}\,\delta_{j_2k_2}+\delta_{j_1k_1}\delta_{j_2k_2} = \delta_{j_1k_1}\delta_{j_2k_2}\,.
\end{aligned} \tag{3.62}$$

In summary, we obtain the following expression for W_1,

$$W_1 = \frac{1}{2^2}\sum_{\substack{j_1j_2\\k_1k_2}} A_{j_1j_2}A_{k_1k_2}\left\{\delta_{j_1k_1}\delta_{j_2k_2}+\delta_{j_1k_2}\delta_{j_2k_1}\right\} = \frac{1}{2}\,\mathrm{Tr}\{\mathrm{A}^2\}\,, \tag{3.63}$$

where we used the symmetry of A to evaluate the summations in the last step.

The term W_2, when evaluated in the same manner, has 24 summands, each of which containing four Kronecker-δ symbols,

$$\begin{aligned}
W_2 = \frac{1}{(2^2\,2!)^2}\sum_{\substack{j_1j_2j_3j_4\\k_1k_2k_3k_4}} A_{j_1j_2}A_{j_3j_4}A_{k_1k_2}A_{k_3k_4}\Big\{&\delta_{j_1k_1}\delta_{j_2k_2}\delta_{j_3k_3}\delta_{j_4k_4}+ \\
&+\delta_{j_1k_1}\delta_{j_2k_2}\delta_{j_3k_4}\delta_{j_4k_3}+\cdots+\delta_{j_1k_4}\delta_{j_2k_3}\delta_{j_3k_2}\delta_{j_4k_1}\Big\}\,.
\end{aligned} \tag{3.64}$$

When carrying out the summations over $j_1, k_1, j_2, k_2, \ldots$, we find two different kind of results for the summands. We exemplify the calculation for two of such terms; for the term $\delta_{j_1k_4}\delta_{j_2k_1}\delta_{j_3k_2}\delta_{j_4k_1}$ we obtain

$$\sum_{\substack{j_1j_2j_3j_4\\k_1k_2k_3k_4}} A_{j_1j_2}A_{j_3j_4}A_{k_1k_2}A_{k_3k_4}\delta_{j_1k_4}\delta_{j_2k_1}\delta_{j_3k_2}\delta_{j_4k_1} = \mathrm{Tr}\{\mathrm{A}^4\}\,, \tag{3.65}$$

while the term $\delta_{j_1k_1}\delta_{j_2k_2}\delta_{j_3k_4}\delta_{j_4k_3}$ can be factorized into two subterms,

$$\begin{aligned}
&\sum_{\substack{j_1j_2j_3j_4\\k_1k_2k_3k_4}} A_{j_1j_2}A_{j_3j_4}A_{k_1k_2}A_{k_3k_4}\delta_{j_1k_1}\delta_{j_2k_2}\delta_{j_3k_4}\delta_{j_4k_3} \\
=&\left(\sum_{j_1j_2} A_{j_1j_2}A_{j_1j_2}\right)\cdot\left(\sum_{j_3j_4} A_{j_3j_4}A_{j_4j_3}\right) = \left[\mathrm{Tr}\{\mathrm{A}^2\}\right]^2.
\end{aligned} \tag{3.66}$$

So the value of any term depends on the specific combination of mode indices into linked pairs, which appear as arguments of the Kronecker-δ symbols.

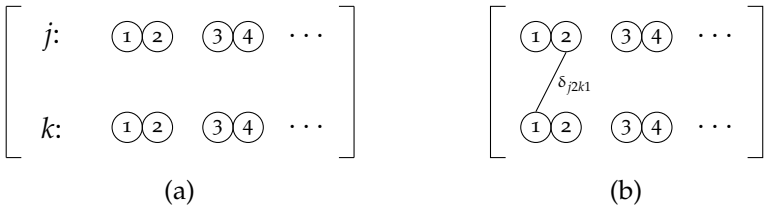

Figure 3.3: Principles for the graphical representation of index contraction. (a) Graphical representation for the indices of the A matrices appearing in Eq. (3.58). (b) The contraction by $\delta_{j_2 k_1}$ between the two indices j_2 and k_1, e. g., is graphically represented by a straight line between the corresponding circles.

We can evaluate the 24 terms of the second order all by hand, but for the third order term, W_3, we get already 720 summands with six Kronecker-δ symbols each. For arbitrary W_n the number of summands is $(2n)!$ with $2n$ Kronecker-δ symbols each.

It is obvious that we need a more systematic treatment for the evaluation of the terms W_n, which we are going to base on the presentation in (Huang 1987, Sec.10.1, pp. 213ff.). We introduce a symbolic notation for the calculations, which is displayed in Figure 3.3. We represent the indices of each matrix A appearing in Eq. (3.58) by two adjacent circles and write all pairs of circles containing the j-indices next to each other in a row. Inside each circle we write the subscript of the index, i. e. for j_1 we write just 1, for j_2 we write 2, etc. The remaining pairs containing all the k-indices are drawn in a row below the other circles, with the numbers filled in in the same way. The two types of indices are now only distinguished by their position in the upper or lower row. The order of the pairs is not important at all, so we keep them in the natural sequence of the positive integers to avoid unnecessary difficulties.

The evaluation of the Kronecker-δ symbols via summation over half of the indices, say over the j's, is a common tensor contraction, which means for any $\delta_{j_m k_l}$ the index j_m is replaced by the index k_l if a sum over the former one is evaluated. We can graphically illustrate this by connecting the two corresponding circles by a straight line. For each Kronecker-δ we need to connect the corresponding two circles by such a line. It follows that each circle must be connected with one other circle, and that there is a total of $2n$ lines. Thus each circle has exactly *one* line attached. We call each such representation of a summand in W_n a *n-graph*.

For the evaluation of each graph associated with W_1, as shown in Figure 3.4, there is no point for this graphical representation, as both possible terms yield the same result. However, when displaying all terms of W_2, we see two different types of graphs in Figure 3.5: the corresponding summands for the graphs (1), (2), (7), (8), (17), (18),

(21), and (22) all yield the result $[\mathrm{Tr}\{A^2\}]^2$, while the remaining ones have the value of $\mathrm{Tr}\{A^4\}$.

By close inspection we find the following: For the graphs yielding the result of $[\mathrm{Tr}\{A^2\}]^2$, each pair is only connected to one other pair by the lines, whereas for all remaining graphs, each pair is connected to two other pairs. To put it another way, for the latter graphs one could follow the lines connecting the pairs visiting all pairs in the graph, while for the former graphs one would be stuck in just a part of the full graph. Those graphs where we could connect all pairs by such a procedure we call a *fully connected graph*; other graphs can be decomposed into several fully connected subgraphs which we call *clusters*. In particular, we want to specify how many pairs are connected in such a cluster; therefore we call those clusters where one pair of j-indices is connected only with one pair of k-indices a 1-cluster, those with two pairs of j- and k-indices each a 2-cluster, etc.

As each line of a cluster corresponds to a tensor contraction, we can quickly identify the previous calculations by the following: For each line connecting a pair to a new pair, the contraction yields only a matrix multiplication; for the last line, which is closing the l-cluster, the contraction yields the trace operation. Therefore, the evaluation of a 1-cluster always yields the result $\mathrm{Tr}\{A^2\}$, of a 2-cluster always $\mathrm{Tr}\{A^4\}$, and of a l-cluster $\mathrm{Tr}\{A^{2l}\}$, in general. For the evaluation of W_n we now have to determine how to decompose any arbitrary n-graph into l-clusters.

A 2-graph is either composed of two 1-clusters or of one 2-cluster. Correspondingly, an arbitrary n-graph can be decomposed into a product of m_1 1-clusters, m_2 2-clusters, ..., and m_n n-clusters, where the numbers m_l have to fulfil the equation

$$\sum_{l=1}^{n} m_l \, l = n \,, \tag{3.67}$$

as there are in total n columns of pairs in an n-graph. The sum over all possible 2-graphs can be decomposed into a sum over all 2-graphs composed of two 1-clusters plus the sum over all 2-graphs composed

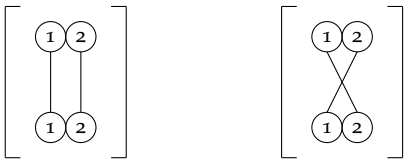

(1) (2)

Figure 3.4: All graphs associated with W_1.

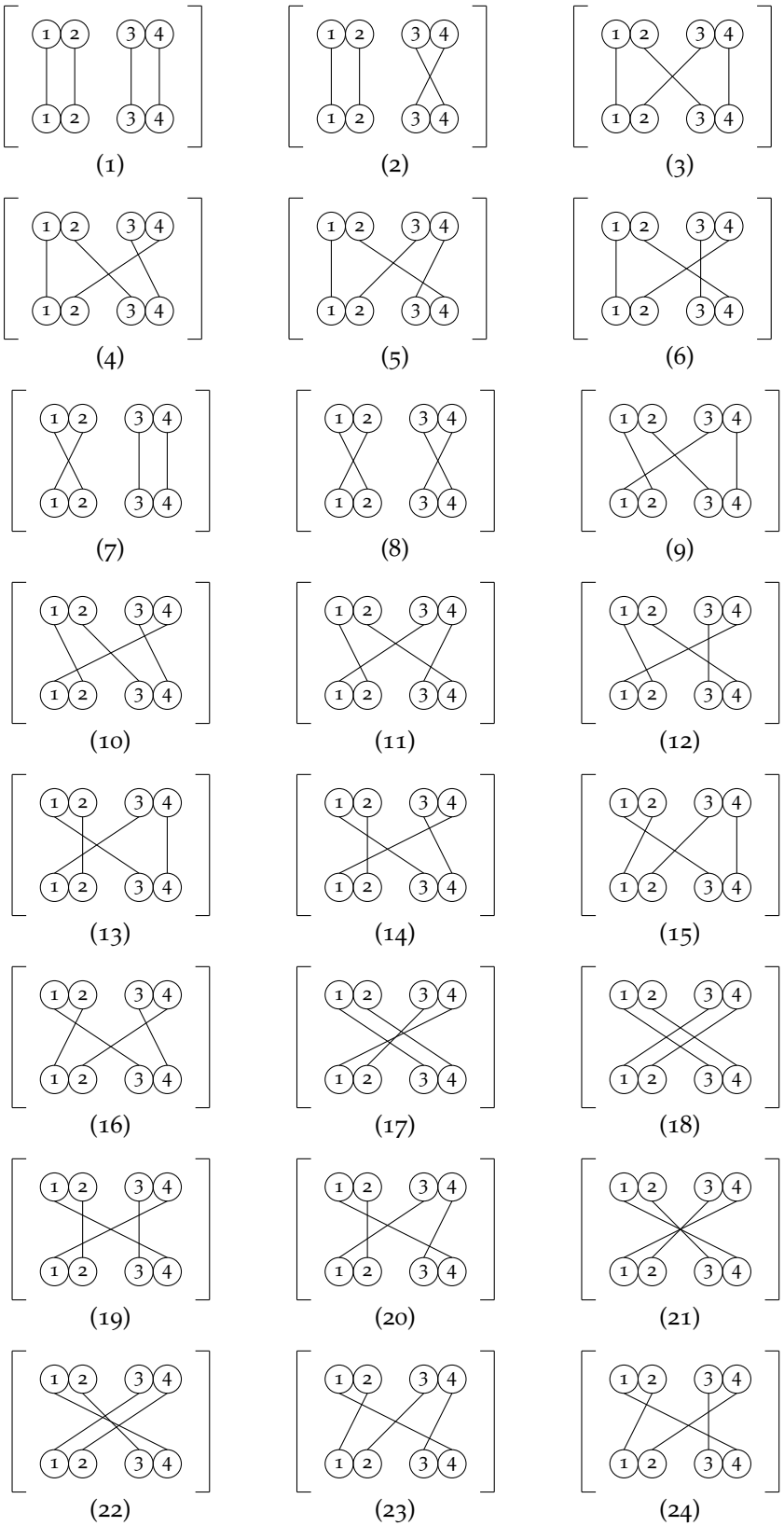

Figure 3.5: All graphs associated with W_2.

of a single 2-cluster. In general, the evaluation of W_n can then be written as follows,

$$\begin{aligned} W_n &= \frac{1}{(2^n n!)^2} \cdot (\text{sum of all possible n-graphs}) \\ &= \frac{1}{(2^n n!)^2} \sum_{(m_1,m_2,\dots)}{}' \mathcal{S}\{(m_1, m_2, \dots)\}, \end{aligned} \tag{3.68}$$

where the primed sum denotes a summation over all possiple n-tupels $(m_1, m_2, \dots, m_n)$, which are restricted by Eq. (3.67). The term $\mathcal{S}\{(m_1, m_2, \dots)\}$ is the sum over all n-graphs which are decomposed into m_1 1-clusters, m_2 2-clusters, etc., as specified by the n-tupel. In the sum $\mathcal{S}\{(m_1, m_2, \dots)\}$, the total multisets of indices $\{j_1, \dots, j_{2n}\}$ and $\{k_1, \dots, k_{2n}\}$ are then distributed in all possible partitions into several sub-multisets, in particular into m_1 sub-multisets containing two indices, m_2 sub-multisets containing four indices, and for arbitrary l there are m_l sub-multisets containing $2l$ indices each.

We now want to find a way to evaluate the value of such an l-cluster for any sub-multisets of indices $\{j_{i_1}, \dots, j_{i_{2l}}\}$ and $\{k_{i_1}, \dots, k_{i_{2l}}\}$ assigned to it beforehand. First, we determine the number of ways to draw such an l-cluster independently of the assigned subset of indices. Then, we draw the pairs of circles again in two lines, but now without filling in any indices as they are not yet determined. We can count the ways to draw fully connected graphs as follows: For having a fully connected graph, we need to connect all pairs, so we first count the number of distinct possibilities of drawing lines between pairs. To this end, we need to choose some convention for the counting; we may draw the 'outgoing' lines emerging from the right circle of the pair and attach the 'incoming' lines to the left circle. Without loss of generality, we start at the first pair in the top left corner. From there, we need to draw a line to one of the pairs in the lower row, giving us l possibilities to connect the first two pairs, cf. Figure 3.6a. The next line then must go again to an arbitrary pair of the upper row *excluding* the first upper pair, giving us $l - 1$ possibilities, cf. Figure 3.6b. Going down, there are again $l - 1$ possibilities, as we have to exclude the pair in the lower row chosen in the first connection. When we keep connecting the pairs like that, the last pair in the lower line then must be connected to first pair of the upper row to close the graph, and we obtain in total $l!\ (l-1)!$ possibilities of connecting the pairs, cf. Figure 3.6c.

Then, we get a new graph for exchanging the two circles in each pair, thereby intertwining the graph. When we are intertwining *all* pairs, though, we do not get a new graph, hence we have to omit this possibility from the count, giving us a total factor of $2^l 2^{l-1}$ we have to include, cf. Figure 3.6d. An example for this can be seen by inspecting Figure 3.5: the basic two graphs which are obtained by counting the

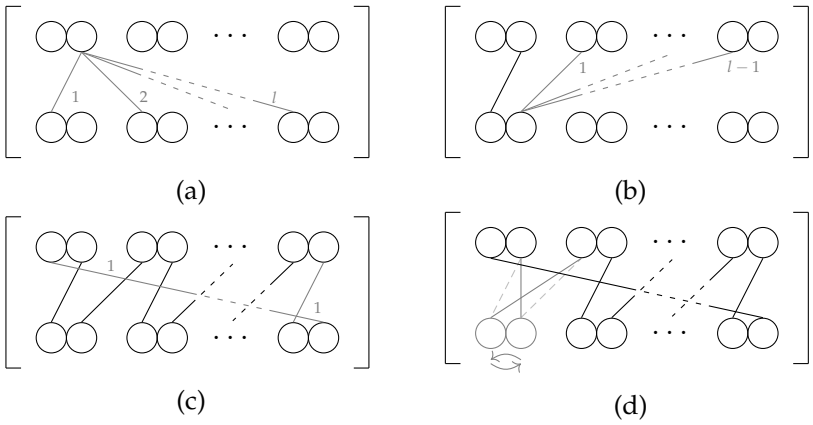

Figure 3.6: Counting of the possibilities drawing an l-cluster. (a) There are l possibilities of connecting the first pair of indices in the upper left corner to a pair in the lower row. (b) For the next connection, there are $l-1$ possibilities. (c) For the last connections from up to down and from down to up there is only one possibility left each. (d) We get a doubling of possibilities for each intertwining of a pair (dashed light grey links before and grey links after the intertwining), keeping the first upper pair fixed.

possibilities of linking pairs for the 2-clusters are graphs (10) and (14); by combining all possibilities for intertwining while skipping the pair (j_1, j_2), we obtain the graphs (3) to (6) and (9) to (12) from graph (10); the remaining graphs, (13) to (16), (19), (20), (23) and (24), are obtained by successive exchange of pairs starting from graph (14). However, by intertwining all pairs, we just transform graph (10) into (14). The 1-cluster and 2-clusters are kind of exceptional in the way that all graphs can be obtained by intertwining only, but for higher l-clusters this is not the case anymore since there are more than two possible pairs for the first connection.

To summarize, there are $2^l\, l!\, 2^{l-1}(l-1)!$ ways to draw a l-cluster. Now we can evaluate the matrix elements belonging to each l-cluster, defining the *l-cluster integral* (also called Mayer's cluster integral) as the sum of all possible clusters for l pairs of circles in each row, which is given by

$$b_l = 2^l\, l!\, 2^{l-1}(l-1)!\, \mathrm{Tr}(\mathrm{A}^{2l})\,. \tag{3.69}$$

The first four terms are given by $b_0 = 1$, $b_1 = 2\,\mathrm{Tr}(\mathrm{A}^2)$, $b_2 = 16\,\mathrm{Tr}(\mathrm{A}^4)$ and $b_3 = 384\,\mathrm{Tr}(\mathrm{A}^6)$.

Now we can formulate how to write the sum

$$\mathcal{S}\{(m_1, \ldots, m_l)\} = \sum_{\mathcal{P}} b_1^{m_1} b_2^{m_2} \cdots\,, \tag{3.70}$$

where the summation over $\mathcal{P}$ extends over all possible ways of distributing the n pairs of indices $\{(j_1; j_2), \ldots, (j_{2n-1}; j_{2n})\}$ into the circles in the upper row and the n index pairs $\{(k_1; k_2), \ldots, (k_{2n-1}; k_{2n})\}$ into those in the lower row, with the aim of obtaining only distinct graphs.

The summands do not depend on the distribution of indices, thus each of the summands gives the same contribution; we can simply count the number of summands and multiply the summand by this number. There are $n!$ ways of distributing n pairs (the ordering of a pair is already contained inside the cluster integral), which yields a factor $(n!)^2$ for the upper and lower row. But we have already counted some of the possibilities by counting the number of graphs. A permutation of two l-clusters with the same l does not give a new graph; there are m_l l-clusters with $m_l!$ possible ways to exchange them. Hence, we need to divide by the factor $\prod_l (m_l!)$. Moreover, we have also accounted for the permutation of pairs inside a cluster integral, so this leads to no new graphs; there are $l!$ ways to permute the upper and lower pairs each, and there are m_l clusters such that we have to take this to the m_l'th power. Therefore we divide by $\prod_l (l!)^{2m_l}$ to remove these doubly counted graphs. Equation (3.70) is then given by

$$\mathcal{S}\{(m_i, \ldots, m_l)\} = (n!)^2 \prod_{l=1}^{n} \frac{b_l^{m_l}}{m_l!(l!)^{2m_l}}. \tag{3.71}$$

For the full evaluation for the terms W_n we obtain

$$W_n = \frac{1}{(2^n n!)^2} {\sum_{\{m_l\}}}' (n!)^2 \prod_{l=1}^{n} \frac{b_l^{m_l}}{m_l!(l!)^{2m_l}} = \frac{1}{2^{2n}} {\sum_{\{m_l\}}}' \prod_{l=1}^{n} \frac{1}{m_l!} \left(\frac{b_l}{(l!)^2} \right)^{m_l}, \tag{3.72}$$

where we can pull the factor 2^{2n} into the restricted sum by making use of Eq. (3.67),

$$\begin{aligned} W_n &= {\sum_{\{m_l\}}}' \frac{1}{2^{2(m_1 1 + m_2 2 + \cdots)}} \prod_{l=1}^{n} \frac{1}{m_l!} \left(\frac{b_l}{(l!)^2} \right)^{m_l} \\ &= {\sum_{\{m_l\}}}' \prod_{l=1}^{n} \frac{1}{m_l!} \left(\frac{b_l}{(2^l l!)^2} \right)^{m_l}. \end{aligned} \tag{3.73}$$

By summing over all W_n we obtain

$$Z^{-2} = \sum_{n=0}^{\infty} {\sum_{m_l}}' \prod_{l=1}^{n} \frac{1}{m_l!} \left(\frac{b_l}{(2^l l!)^2} \right)^{m_l}. \tag{3.74}$$

Summing over all combinations of $\{(m_1, \ldots, m_l)\}$ followed by a summation over all n is equivalent to summing over all $m_1, m_2, \ldots$ from 0 to ∞ separately, so we can replace the restricted sum,

$$Z^{-2} = \sum_{m_1=0}^{\infty} \sum_{m_2=0}^{\infty} \cdots \prod_{l=1}^{\infty} \frac{1}{m_l!} \left(\frac{b_l}{(2^l l!)^2} \right)^{m_l} \tag{3.75}$$

$$= \prod_{l=1}^{\infty} \left[\sum_{m_l=0}^{\infty} \frac{1}{m_l!} \left(\frac{b_l}{(2^l l!)^2} \right)^{m_l} \right], \tag{3.76}$$

where we exchanged the summation with the product in the last line. The obtained result is in the form of the exponential series, so we get

$$Z^{-2} = \prod_{l=1}^{\infty} \exp\left[\frac{b_l}{(2^l l!)^2}\right] = \exp\left[\sum_{l=1}^{\infty} \frac{b_l}{(2^l l!)^2}\right]. \tag{3.77}$$

Now we can insert the value of the l-cluster integral to finally obtain

$$Z^{-2} = \exp\left[\sum_{l=1}^{\infty} \frac{\mathrm{Tr}(\mathrm{A}^{2l})}{2l}\right] = \exp\left(\frac{1}{2}\,\mathrm{Tr}\left[-\sum_{l=1}^{\infty} -\frac{(\mathrm{A}^{2l})}{l}\right]\right). \tag{3.78}$$

In the square brackets we recognize the power series expansion of the logarithm, $\ln(1-x) = -\sum_{k=1}^{\infty} \frac{x^k}{k}$, which allows us to reformulate the result as

$$Z^{-2} = \exp\left(\frac{1}{2}\,\mathrm{Tr}\left[\ln\frac{1}{1-\mathrm{A}^2}\right]\right), \tag{3.79}$$

provided that $1 - \mathrm{A}^2$ is non-singular.

Now we are going to prove the non-singularity of $1 - \mathrm{A}^2$ by finding a matrix norm $\|\cdot\|$ for which $\|\mathrm{A}\|$ is smaller than unity. The eigenvalues of a matrix A have the property to be located inside a circle bounded by any matrix norm (Horn and Johnson 1985, Theorem 5.6.9, p. 297). Therefore, if the absolute value of all the eigenvalues of A is smaller than one, none of the eigenvalues of $1 - \mathrm{A}$ can be zero. Using the spectral norm[7] $\|\cdot\|_2$, the orthogonal decomposition form $\mathrm{A} = \Lambda\chi\Lambda^T$ derived in Eq. (C.29a), and the submultiplicativity of the matrix norm, we obtain the following inequality,

$$\|\mathrm{A}\|_2 \leq \|\Lambda\|_2 \|\tanh\chi\|_2 \|\Lambda^T\|_2 = \|\tanh\chi\|_2 \tag{3.80}$$

where the equality follows from the fact that the spectral norm of the orthogonal matrices Λ is unity. Because of the decomposition Eq. (C.29a) we find that χ is diagonal, real, and positive, thus the spectral norm is equal to the tangent hyperbolicus of the largest eigenvalue of χ. It follows that $\|\mathrm{A}\|_2 < 1$ as the tangent hyperbolicus is smaller than one in its full domain.

So we find for Z the following form,

$$Z = \exp\left(-\frac{1}{4}\,\mathrm{Tr}\left[\ln\frac{1}{1-\mathrm{A}^2}\right]\right), \tag{3.81}$$

which can be further simplified, using the identity for the determinant of the matrix exponential, $\exp\{\mathrm{Tr}\,\mathrm{X}\} = \det\{\exp\mathrm{X}\}$,

$$Z = \det\left[(1-\mathrm{A}^2))^{1/4}\right]. \tag{3.82}$$

7 For a quadratic matrix A the spectral norm $\|\cdot\|_2$ is defined by $\|A\|_2 = \max\{\sqrt{\lambda} : \lambda \text{ is an eigenvalue of } \mathrm{A}^{\dagger}\mathrm{A}\}$, see Horn and Johnson (1985, Def. 5.6.6, p. 295).

Now we have established all the necessary relations of the coefficients of the transformation (3.37) with the normal mode transformations.

By determining the A_{jk}'s, the $\beta_j^{\uparrow}$'s, and Z via Eqs. (3.30), (3.52) and (3.82), we can directly calculate the overlap between the two different ground states, given by

$$\begin{aligned}\mathcal{G} &= {}_{\uparrow}\langle 0|0\rangle_{\downarrow} = Z\,{}_{\uparrow}\langle 0|\hat{D}_{\uparrow}(\beta^{\uparrow})\,e^{A}|0\rangle_{\uparrow} \\ &= Z\exp\Big\{\frac{1}{2}\sum_{jk}A_{jk}\beta_j^{\uparrow}\beta_k^{\uparrow}\Big\}\exp\Big\{-\frac{1}{2}\sum_{j}|\beta_j^{\uparrow}|^2\Big\}\,. \end{aligned} \tag{3.83}$$

3.3.2 *Arbitrary Motional States*

The transformation between arbitrary motional states makes use of the representation of the annihilation and creation operators in both bases, as these can be used to connect any state with the ground state.

Additionally, we can also determine the squeezing parameters ξ_{jk} of the general transformation (3.34) by using the results of the disentangling theorem in Appendix C. We find

$$\xi_{jk} = \sum_{l}\Lambda_{jl}\chi_l\Lambda_{kl}\,, \tag{3.84}$$

where the χ_l are given by $\chi_l = \operatorname{arctanh} a_l$. Λ_{jl} is the orthogonal transformation which diagonalizes A, Eq. (C.29a), where the a_l are the resulting eigenvalues. As A is real and symmetric, we find straight away that the ξ_{jk} are all real and positive.

Part II

RAMSEY INTERFEROMETRY

In this part, we discuss the use of Ramsey interferometry as a tool for probing the motional state of an ion Coulomb crystal. We show that the visibility of such a Ramsey interferometer has unique characteristics across the linear–zigzag transition and that it can therefore be employed as an indicator for this structural transition.

4

RAMSEY INTERFEROMETRY WITH ION COULOMB CRYSTALS

In this chapter, we discuss how Ramsey interferometry can be used to extract information about the motional state of an ion Coulomb crystal after a state-dependent quench of the trapping potential for a specific ion. First, in Section 4.1, we review the general principle of Ramsey interferometry and introduce the basic method for extracting information about the motional state after the quench. Poyatos, Cirac, Blatt et al. (1996) proposed to use a Ramsey interferometry scheme for a single trapped ion to determine the position of an ion, which could be used, for example, to measure magnetic field gradients more precisely. This proposal has been developed further by De Chiara et al. (2008) for application in an ion Coulomb crystal, where the impact of the photon recoil on the linear ion crystal close to the linear–zigzag transition could be revealed in the time-dependence of the visibility. For the presentation of the basic principle of the scheme in Section 4.2 we neglect many of the practical details of how to implement this for an ion Coulomb crystal, which are then presented in Section 4.3 for relevant experimental setups. Finally, in Section 4.4 we derive the formula for obtaining the visibility of the Ramsey interferometer, including the effects of the photon recoil as well as an initial thermal occupation of the motional state, thereby providing a more realistic description of the system.

4.1 THE PRINCIPLE OF RAMSEY INTERFEROMETRY

The original proposal by Ramsey was conceived as an improvement of the so-called magnetic resonance method that had been introduced earlier by Rabi, Zacharias et al. (1938); Rabi, Millman et al. (1939). The magnetic resonance method allows the measuring of the Larmor precession and hence the nuclear magnetic moment of molecules by letting a beam of hot molecules pass through a region of a rotating magnetic field (see Ramsey 1956, Ch. V, pp.115ff.). It is the foundation of nuclear magnetic resonance (NMR)-method introduced by Bloch, Hansen et al. (1946) and Purcell et al. (1946) with a multitude of applic-

ations in solid state physics (Kittel 2005, Ch. 13,), chemistry (Warren et al. 1993), and in particular in medicine, where it forms the basis of the magnetic resonance imaging (MRI) technique used for medical diagnosis (Bethge et al. 2004, Ch. 7, pp. 101ff.). The method subsequently developed by Ramsey (Ramsey 1949, 1950; Ramsey 1956, Ch. V.4, pp.124ff.) allowed the measuring of the Larmor precession with much greater accuracy. It has also been applied to electronic transitions in atoms, leading to a new frequency and time standard by using a certain stable atomic transition for atomic clocks (Ramsey 1956, Ch. IX.11, pp.282ff.; Ramsey 1983; Itano and Ramsey 1993; Diddams et al. 2004), providing the definition of the second ever since.

Magnetic Resonance

We first review the magnetic resonance method for a classical magnetic moment $\mathbf{m}$ driven by magnetic fields in a rather qualitative way in order to get a first intuitive understanding of the involved physics. Before we turn to the Ramsey method we are going to review the basics of the magnetic resonance method.

To this purpose, consider a particle with a magnetic moment $\mathbf{m} = \gamma\mathbf{j}$ that is proportional to its angular momentum $\mathbf{j}$; the proportionality constant γ is called the *gyromagnetic ratio* of the particle under consideration. Now let this particle be subjected to a static magnetic field $\mathbf{B}_0 = B_0\hat{\mathbf{z}}$ pointing along the positive z-direction, as shown in the top left corner in Figure 4.1a. The potential energy of an ideal magnetic moment in a magnetic field is given by $V_{\mathrm{mm}} = -\mathbf{m}\cdot\mathbf{B}_0$; the force on the magnetic moment is $\mathbf{F} = \boldsymbol{\nabla}(\mathbf{m}\cdot\mathbf{B}_0)$; and the torque on it is $\mathrm{d}\mathbf{j}/\mathrm{d}t = \mathbf{m}\times\mathbf{B}_0$ (Jackson 1999, Sect. 5.7, pp. 188ff.). The solution to the equation of motion for the angular momentum is such that the magnetic moment is gyrating around an axis parallel to the magnetic field, the so-called *Larmor precession* (Cohen-Tannoudji, Diu et al. 1997, Complement $\mathrm{F_{IV}}$, pp. 443ff.); the angular frequency $\omega_L = -\gamma|\mathbf{B}_0|$ of this gyration is called *Larmor frequency*, and it depends on the product of the gyromagnetic ratio with the magnetic field strength.

Next, a second magnetic field $\mathbf{B}_R(t)$ is applied which is perpendicular and rotating[1] with a certain frequency ω_R around the axis of the static field, see Figure 4.1b. If this second field were not rotating

1 According to the so-called rotating-wave approximation (RWA) (Allen and Eberly 1987, Ch. 2.4, pp. 41f.), an oscillating field is approximately equivalent to a rotating field. Bloch and Siegert first considered the case for a non-rotating field (Bloch and Siegert 1940), which gives rise to a shift of the resonance frequency which depends on the ratio $B_R^2/(16B_0^2)$. This shift is negligible for appropriately chosen magnetic field strengths $B_R \ll B_0$ for magnetic resonance experiments as well as for quantum optical experiments in which the condition is $\Omega \ll \omega_{\mathrm{L}}$, i. e., that the Rabi frequency is much lower than the frequency of the driving laser field.

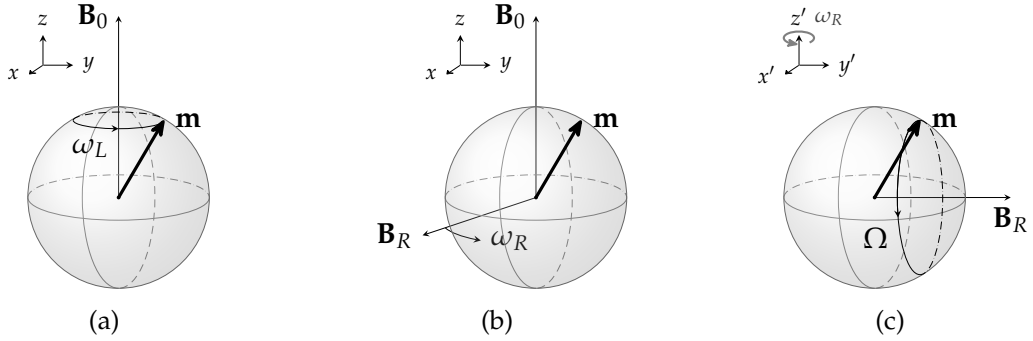

Figure 4.1: The principle of magnetic resonance. (a) The Bloch sphere of a spin pointing along **m** is shown in the case of a static magnetic field $\mathbf{B}_0$ in z-direction. The magnetic moment **m** gyrates around the axis of the magnetic field. (b) A weak second magnetic field $\mathbf{B}_R$ is applied that is perpendicular to $\mathbf{B}_0$, but rotating in the x–y-plane with angular frequency ω_R. (c) The resulting dynamics is best described in a coordinate frame rotating with ω_R. In this frame, the field $\mathbf{B}_R$ appears to be static, whereas the static field apparently vanishes if the rotating field is on resonance with the Larmor frequency, $\omega_R = \omega_L$.

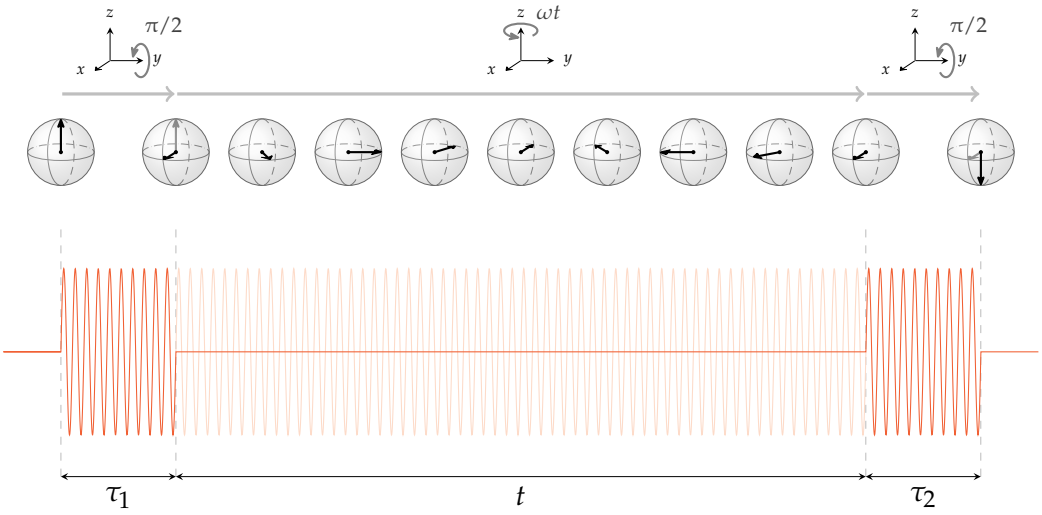

Figure 4.2: Sequence of Ramsey's method of separated oscillatory fields. The illustration shows the direction of the magnetic moment of a spin system at the top, while at the bottom the y-component of an rotating (or oscillating) magnetic field is shown. First, to the very left, the spin is polarized along the positive z-direction and the rotating field is off. Then, the rotating field is switched on for a duration τ_1, such that the spin rotates into the x–y-plane. The rotating field is switched off again and the spin precesses freely around the z-axis. After time t_R the rotating field is switched on again for a time τ_2 while keeping the phase of the rotation. Only if the frequencies of the rotating field and the precessing spin are equal will the second field pulse turn the spin in the negative z-direction. In all other cases, the phases of the two fields do not match and the second pulse will rotate the spin only partially toward the negative z-axis or even into the other direction (see Figure 4.3).

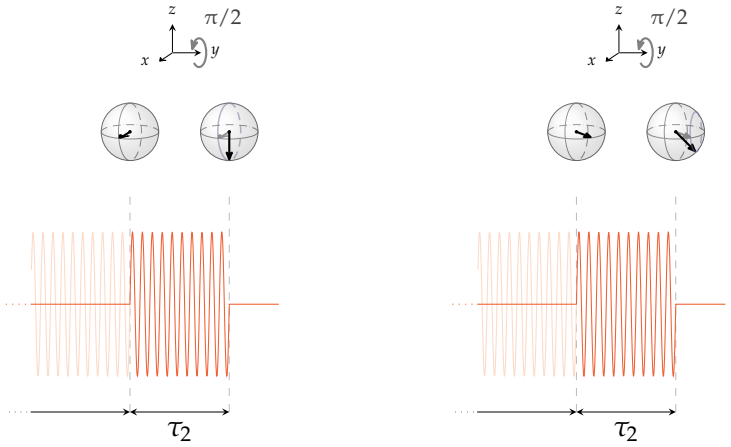

(a) Spin and field in phase (b) Spin and field out of phase

Figure 4.3: Effect of the second Ramsey pulse dependent on the phase between spin and field. (a) If spin precession and rotating field are in phase when the second pulse sets in, the spin is rotated toward the negative z-direction. (b) If spin precession and rotating field are out of phase before the second pulse, the spin rotates on a smaller circle parallel to the x–z-plane, thus not having a maximal z-component.

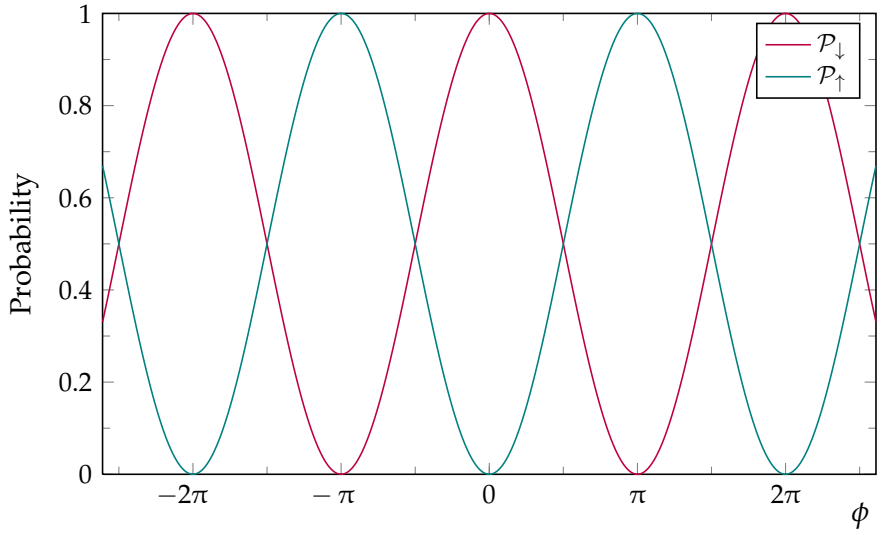

Figure 4.4: Illustration of the Ramsey fringes. Theoretically calculated probabilities $\mathcal{P}_\uparrow$ and $\mathcal{P}_\downarrow$ for measuring the different spin orientations $\uparrow$ and $\downarrow$ of the magnetic moment in the final measurement of the Ramsey interferometer scheme as a function of the phase shift ϕ between the spin and the rotating field.

but fixed, the magnetic moment would precess around the resulting vector of the sum of both fields; yet, as the second field rotates in the x–y-plane, the resulting vector does so, too. Therefore, the magnetic moment is revolving around a rotating axis.

The situation can be described much simpler in a coordinate frame $(\hat{\mathbf{x}}', \hat{\mathbf{y}}', \hat{\mathbf{z}}')$ that is rotating around the z-axis at just exactly the rotation frequency ω_R of the second field (Rabi, Ramsey et al. 1954). The effect of such a coordinate transformation $(\hat{\mathbf{x}}, \hat{\mathbf{y}}, \hat{\mathbf{z}}) \mapsto (\hat{\mathbf{x}}', \hat{\mathbf{y}}', \hat{\mathbf{z}}')$ is that Coriolis forces are appearing in the new coordinate frame that have the same mathematical structure as a magnetic field along the z-axis; therefore, the net effect of the rotating coordinate frame is to change the apparent magnitude of the magnetic field $\mathbf{B}_0$ (besides that the rotating field $\mathbf{B}_R(t)$ revolves with a different angular frequency). The resulting magnetic field is given by

$$\mathbf{B} = (B_0 + \omega_R/\gamma)\hat{\mathbf{z}}' + B_R\hat{\mathbf{x}}' \,. \tag{4.1}$$

If the rotation of the field is *in resonance* with the Larmor frequency of the static field,

$$\omega_R = -\gamma B_0 \equiv \omega_L \,, \tag{4.2}$$

the first term in Eq. (4.1) vanishes and only the term $B_R\hat{\mathbf{x}}'$ remains as a static field in this frame. Hence, the total dynamics in the rotating frame is given by a Larmor precession around the $\hat{\mathbf{x}}'$-axis with Larmor frequency $\Omega = -\gamma B_R$. As this basic idea of magnetic resonance was introduced by Rabi, Zacharias et al., the precession of the magnetic moment around the rotating magnetic field is usually called *Rabi oscillation* and the angular frequency Ω of the precession is called *Rabi frequency*, accordingly.

Ramsey's Method of Separated Oscillatory Fields

Now we turn to Ramsey's method, which we have illustrated in Figure 4.2. Suppose the magnetic moment $\mathbf{m}$ is initially pointing along the positive z-direction. Then, a rotating field $\mathbf{B}_R$ is applied with a definite strength and for a specific duration such that the magnetic moment is rotated by 90° into the x–y-plane. After the field has been switched off, the magnetic moment keeps precessing in the x–y-plane until, at some later time, the rotating field is switched on again in such a way that it points into the direction it would have had if it had been kept on all the time. A rotating field with this property is called *phase-coherent*. If now the phase of the field $\mathbf{B}_R$ and the phase of the Larmor precession match, the rotating field remains perpendicular to the magnetic moment in such a way that the magnetic moment precesses further around the axis of the rotating field. If the

strength and duration are chosen as for the first pulse, the magnetic moment will afterwards point in the direction of the negative z-axis, see Figure 4.3a. If, however, the phases of the Larmor precession and the field are not equal, this second field rotates the magnetic moment only partially into the negative z-direction, see Figure 4.3b, or it turns it into the positive z-direction (if it has a phase shift of π it turns until it points again along the initial direction). In the rotating frame, this mismatch of the phases means that the magnetic moment and the field $\mathbf{B}_R$ are not perpendicular anymore, hence the precession is such as if only the perpendicular component of the magnetic moment revolved around the magnetic field axis. The origin of the phase mismatch may be either that the frequencies are not exactly in resonance, or it may be a deliberately introduced phase shift.

The final step in the Ramsey method is to measure the direction of the magnetic moment; in a quantum mechanical description, the result of this measurement for a single particle is not deterministic, hence the experiment needs to be repeated in an identical way for a certain number of times in order to obtain the relative frequencies of the possible measurement outcomes. As the first experiments of this kind were performed with beams of molecules flying through different spatial zones, they provided a continuous flow of particles, such that the current of particles with the right final magnetic moment could simply be maximized by matching the frequency of the rotating field to that of the Larmor precession. The measured probability for obtaining a full turn of the magnetic moment is dependent on the phase shift, see Figure 4.4. When the phase shift originates from a detuning away from the resonance condition, one obtains an oscillating pattern in frequency space with a sharp resonance for $\omega_R = \omega_L$, the so-called *Ramsey fringes*.[2]

In summary, the Ramsey interferometer compares the precession of a magnetic moment with an external frequency. This method is sensitive to any phase shifts the magnetic moment experiences between the two applied fields. Also, it is applicable to many other systems, in particular any two-level system, where it measures the coherence i. e. phase relation between the two levels.

One important application used in numerous physical systems containing spins or spin-similar systems is to measure the rate with which the coherence between different quantum states is lost due to external noise or coupling to the environment. These processes are described

2 The usage of the term "fringes" originates from the analogy with the interference pattern of a double-slit experiment. Here, the two slits are separated in time instead of in space, and the interference pattern is in frequency space instead of in momentum space. In the original experiments with molecular beams, the final magnetic moment was detected by a spatial deflection in an inhomogeneous magnetic field resulting in fringes on a screen similar to those of a common interference experiment.

by introducing two relaxation rates in the equations of motion for the magnetic moment, the so-called *Bloch equations* (Bloch 1946): First, the longitudinal relaxation time T_1, which denotes the time from which a fully polarized state – meaning a magnetic moment parallel to the $\hat{\mathbf{z}}$-axis – relaxes back to a thermal equilibrium distribution. And second, the transversal relaxation time or spin-spin relaxation time T_2, which appears when the magnetic moment is subjected to a transverse relaxation process or dephasing process. That is, instead of pointing in a discrete direction, the magnetic moment is smeared out into a continuous distribution of the azimuthal phase angle, so that the total magnetization is given by the integral over the phase, which in general is smaller in amplitude than the initial value. The T_2 time is then defined as the time scale after which the total magnetization decays to $1/\mathrm{e}$ of its original value. The method of Ramsey interferometry is capable of detecting the loss of a fixed phase relation between the two spin states arising from such dephasing processes. The origin of the T_2-dephasing in NMR is commonly explained by the interaction between different spins in the sample which have random phases; the spin-spin coupling then leads to an averaging of the individual spins. In real-world experiments, another quantity, namely the T_2^* time, is of practical importance. It includes the effect of spatially inhomogeneous magnetic fields, which are another possible cause of dephasing for samples with a considerable spatial extent or particles moving along drawn-out trajectories.[3]

In an experiment T_2 and T_2^* could be distinguished by the *spin-echo* technique (Hahn 1950), which can undo the effects of stationary field inhomogeneities by reversing the precession direction of the spins, whereas the spin-spin relaxation is still present because of quasi-random fast fluctuations of the spins induced by the coupling among them.[4]

In the examples provided here, Ramsey interferometry is applied to ensembles either with a Maxwellian velocity distribution as in the case of molecular and atomic beams, or in macroscopically large samples where single spins cannot be resolved. In the following, we are going to examine the opposite case, in which Ramsey interferometry is applied to single atoms or ions close to their motional ground state.

3 The latter was actually the initial motivation for Ramsey to replace the single region of an oscillatory field with two separate ones, see Interview with Dr. Norman Ramsey by Ursula Pavlish at his office in Lyman Hall, Harvard University, December 4, 2006. Transcript by Center for History of Physics of the American Institute of Physics.

4 This is actually the basis for many applications in MRI (Bethge et al. 2004, Ch. 7, pp. 101ff.), in which a magnetic gradient is used in combination with the spin-echo technique or other advanced pulse sequences such as, e. g., the Carr-Purcell sequence (Carr and Purcell 1954; Slichter 1980, Ch. 8), to image organic tissue with different T_2 or T_2^* times in a spatial dependent way. Actually, all three phenomenological decay rates T_1, T_2 and T_2^* are used for the imaging of different tissues.

Of course, the technique has been in use for a long time in most if not all of the fields and subfields of atomic and molecular physics, and in particular it is among the standard tools used in trapped ion experiments.

Next we present a detailed theoretical description of Ramsey interferometry applied to a single quantum system, as already discussed by Ramsey (Ramsey 1950) himself, and show how this technique can also be used as a probe for a coupled system.

4.2 RAMSEY INTERFEROMETRY AS A PROBE

4.2.1 *Degrees of Freedom, Hilbert Space and States*

Now consider having a quantum system for which the degrees of freedom split into a two distinct sets, that we call internal and external degrees of freedom. Let further the internal degrees of freedom be described by a two-level system, while the external degrees of freedom can be arbitrary and even continuous. In our case, we take a single atom within the two-level approximation, where two electronic states form a basis of a two-dimensional Hilbert space; the external degrees of freedom are described by the wavefunction of the COM-coordinate of the atom.

The total Hilbert space of the system thus is given by tensor product space,

$$\mathscr{H} = \mathscr{H}_{\mathrm{TLS}} \otimes \mathscr{H}_{\mathrm{ext}} \,. \tag{4.3}$$

The Hilbert space $\mathscr{H}_{\mathrm{TLS}}$ of the two-level system is two-dimensional, and it is spanned by the orthonormal basis $\{ |\downarrow\rangle , |\uparrow\rangle \}$, with $\downarrow$ standing for ground state and $\uparrow$ for excited state. The naming scheme is arbitrary and should not exclude the possibility of degenerate states. Specifically, we assume the states $|\downarrow\rangle$ and $|\uparrow\rangle$ to be a meta-stable states, meaning that there is no spontaneous decay channel from one state to the other, at least not within the timespan of the experiment.

With that, any pure state may be written as[5]

$$|s\rangle = c_{\downarrow} |\downarrow\rangle + c_{\uparrow} |\uparrow\rangle \,, \tag{4.4}$$

with $|c_{\downarrow}|^2 + |c_{\uparrow}|^2 = 1$ for normalization. The complex coefficients $c_{\uparrow}$ and $c_{\downarrow}$ uniquely determine the state $|s\rangle$ for the two-level system.

5 Any state of a two-level system may also be expressed by the density matrix $\rho_{\mathrm{TLS}} = \frac{1}{2}(1 + \boldsymbol{\sigma} \cdot \mathbf{s})$, where $\boldsymbol{\sigma} = \sigma_x \mathbf{e}_x + \sigma_y \mathbf{e}_y + \sigma_z \mathbf{e}_z$ is the vector of Pauli matrices and $\mathbf{s}$ is the Bloch vector, obtained by $\mathbf{s} = \mathrm{Tr}[\boldsymbol{\sigma} \rho_{\mathrm{TLS}}]$; for a spin-1/2 system it is parallel to the magnetic moment of the spin. Thus one is motivated to use the analogy of a two-level system with the direction of the magnetization of a spin, in particular in the graphical representation of a Bloch sphere, which is essentially equivalent to the sphere shown in Figure 4.1.

The Hilbert space of the external degrees of freedom can take many different forms, but let us assume for simplicity's sake that it could be spanned by a single variable. In the case of a continuous basis $\{ |\phi(\eta)\rangle \}$, we can then write any arbitrary pure quantum state $|\phi\rangle$ as

$$|\phi\rangle = \int \mathrm{d}\eta \, c(\eta) \, |\phi(\eta)\rangle \ . \tag{4.5a}$$

For a countable basis $\{ |\phi_n\rangle \}$, we have similarly

$$|\phi\rangle = \sum_n c_n \, |\phi_n\rangle \ , \tag{4.5b}$$

where the basis is orthonormal $\langle \phi_n | \phi_{n'} \rangle = \delta_{nn'}$ (from which we find for the coefficients $\sum_n |c_n|^2 = 1$). The continuous basis is not necessarily orthonormal, and it can be also overcomplete as in the example of the coherent states basis (Le Bellac 2006, p. 366). The state $|\phi\rangle$ is uniquely determined by the function $c(\eta)$ of the continuous parameter η or by the coefficients c_n with $n = 0, 1, 2, \ldots$, respectively. The generalization to more than one variable is straightforward.

In general, the combined state of the system may then be written as

$$|\psi\rangle = \int \mathrm{d}\eta \left[c_\uparrow(\eta) \, |\uparrow\rangle \otimes |\phi(\eta)\rangle + c_\downarrow(\eta) \, |\downarrow\rangle \otimes |\phi(\eta)\rangle \right] , \tag{4.6a}$$

or

$$|\psi\rangle = \sum_n \left[c_{\uparrow,n} \, |\uparrow\rangle \otimes |\phi_n\rangle + c_{\downarrow,n} \, |\downarrow\rangle \otimes |\phi_n\rangle \right] . \tag{4.6b}$$

We may rewrite any arbitrary state vector always in the following form,

$$|\psi\rangle = c_\downarrow \, |\downarrow\rangle \otimes |\phi_\downarrow\rangle + c_\uparrow \, |\uparrow\rangle \otimes |\phi_\uparrow\rangle \ , \tag{4.7}$$

where we merged the expansion into basis states of the external degrees of freedom into two wavepackets,

$$|\phi_\downarrow\rangle = c_\downarrow^{-1} \int \mathrm{d}\eta \, c_\downarrow(\eta) \, |\phi(\eta)\rangle \ , \tag{4.8a}$$

$$|\phi_\uparrow\rangle = c_\uparrow^{-1} \int \mathrm{d}\eta \, c_\uparrow(\eta) \, |\phi(\eta)\rangle \ , \tag{4.8b}$$

for the continuous case, and

$$|\phi_\downarrow\rangle = c_\downarrow^{-1} \sum_n c_{\downarrow,n} \, |\phi_n\rangle \ , \tag{4.8c}$$

$$|\phi_\uparrow\rangle = c_\uparrow^{-1} \sum_n c_{\uparrow,n} \, |\phi_n\rangle \ , \tag{4.8d}$$

for the countable basis. In the following we are going to leave the "$\otimes$"-symbol out when writing a state of the form of Eq. (4.7).

Next, we are going to analyse the effect of the Ramsey interferometry scheme on the total quantum state.

4.2.2 *Description of the Sequence*

The Ramsey sequence then consists of the following steps:

1. INITIALIZATION,
2. FIRST RAMSEY PULSE,
3. FREE EVOLUTION,
4. SECOND RAMSEY PULSE,
5. MEASUREMENT.

We are now going to describe these steps for the ideal implementation. In Section 4.3 we describe the implementation in trapped ion experiments and also discuss the limitations before we present a more realistic theoretical description in Section 4.4.

1. INITIALIZATION. The two-level system is prepared in one of its eigenstates, say $|\downarrow\rangle$. The state of the quantum system after the initialization at time t_0 is given by

$$|\psi(t_0)\rangle = |\downarrow\rangle\ |\phi_\downarrow(t_0)\rangle\,. \tag{4.9}$$

In that way we do not have to synchronize the phase of the internal state with the phase of the applied pulses. Moreover, there is no initial entanglement between internal and external degrees of freedom.

2. FIRST RAMSEY PULSE. A pulse of radiation resonant with the transition between the two levels is applied for a duration $\tau_1 > 0$ such that the state of the two-level system afterwards is in an equal superposition between both eigenstates of the two-level system. The time evolution operator for such an interaction reads (we are discussing this in more detail in Section 4.3)

$$\hat{U}_{\pi/2} = \frac{1}{\sqrt{2}}\Big(|\uparrow\rangle\langle\uparrow| + |\uparrow\rangle\langle\downarrow| - |\downarrow\rangle\langle\uparrow| + |\downarrow\rangle\langle\downarrow|\Big)\,. \tag{4.10}$$

The state at time $t_1 = t_0 + \tau_1$ is given by

$$\begin{aligned}|\psi(t_1)\rangle &= \frac{1}{\sqrt{2}}\Big(\ |\uparrow\rangle\ |\phi_\uparrow(t_1)\rangle + |\downarrow\rangle\ |\phi_\downarrow(t_1)\rangle\Big) \\ &= \frac{1}{\sqrt{2}}\Big(\ |\uparrow\rangle + |\downarrow\rangle\Big)\,|\phi_\downarrow(t_0)\rangle\ .\end{aligned} \tag{4.11}$$

Here we are assuming that there is no evolution for the external degrees of freedom, i. e., $|\phi_\uparrow(t_1)\rangle = |\phi_\downarrow(t_0)\rangle$ and $|\phi_\downarrow(t_1)\rangle = |\phi_\downarrow(t_0)\rangle$, and that the state at the end of the pulse is still separable.

3. FREE EVOLUTION. After the pulse, the external degrees of freedom are undergoing a *state-dependent* time-evolution for a time t_R,

$$\hat{U}(t_R) = |\uparrow\rangle\langle\uparrow|\hat{U}_\uparrow(t_R) + |\downarrow\rangle\langle\downarrow|\hat{U}_\downarrow(t_R)\,, \tag{4.12}$$

with the state-dependent time-evolution given by the unitary operators acting on $\mathscr{H}_{\text{ext}}$,

$$\hat{U}_\uparrow(t_R) = \exp\left[-i\hat{H}_\uparrow t_R/\hbar\right], \tag{4.13a}$$

$$\hat{U}_\downarrow(t_R) = \exp\left[-i\hat{H}_\downarrow t_R/\hbar\right]. \tag{4.13b}$$

Here we assume that the free Hamiltonian of the system can be decomposed into two state-dependent parts,

$$\hat{H}_{\text{free}} = |\uparrow\rangle\langle\uparrow|\hat{H}_{\text{free}}|\uparrow\rangle\langle\uparrow| + |\downarrow\rangle\langle\downarrow|\hat{H}_{\text{free}}|\downarrow\rangle\langle\downarrow| = \hat{H}_\uparrow|\uparrow\rangle\langle\uparrow| + \hat{H}_\downarrow|\downarrow\rangle\langle\downarrow|\,, \tag{4.14}$$

where the Hamiltonians $\hat{H}_\uparrow = \langle\uparrow|\hat{H}_{\text{free}}|\uparrow\rangle$ and $\hat{H}_\downarrow = \langle\downarrow|\hat{H}_{\text{free}}|\downarrow\rangle$ are operators on the Hilbert space of the external degrees of freedom $\mathscr{H}_{\text{ext}}$ only. We further assume that the free Hamiltonian $\hat{H}_{\text{free}}$ is time-independent during the interval of the evolution.

The state at time $t_2 = t_1 + t_R$ is given by

$$|\psi(t_2)\rangle = \frac{1}{\sqrt{2}}\Big(\,|\uparrow\rangle\;|\phi_\uparrow(t_2)\rangle + \,|\downarrow\rangle\;|\phi_\downarrow(t_2)\rangle\Big)\,, \tag{4.15}$$

with

$$|\phi_\uparrow(t_2)\rangle = \hat{U}_\uparrow(t_R)\,|\phi_\downarrow(t_0)\rangle\,, \tag{4.16a}$$

$$|\phi_\downarrow(t_2)\rangle = \hat{U}_\downarrow(t_R)\,|\phi_\downarrow(t_0)\rangle\,. \tag{4.16b}$$

If the unitary operators $\hat{U}_\uparrow$ and $\hat{U}_\downarrow$ give rise to different dynamics, the internal and motional degrees of freedom for the state in Eq. (4.15) become entangled as a matter of course.

4. SECOND RAMSEY PULSE. After the free evolution, a second pulse of radiation resonant with the transition is applied such that if this pulse is directly applied after the first one, the state after the pulse is one of the two eigenstates of the two-level system. Consequently, there are two possibilities: Either the same unitary operation of a $\pi/2$-pulse is applied and the internal state is mapped to $|\uparrow\rangle$ (as the two pulses immediately combined together form a π-pulse); or the inverse unitary operation brings the internal state back to the state $|\downarrow\rangle$ by a $-\pi/2$-pulse (which is the identity upon the combination of the two pulses). We shall choose the latter possibility in the following, so that the evolution operator is given by

$$\hat{U}_{-\pi/2} = \frac{1}{\sqrt{2}}\Big(|\uparrow\rangle\langle\uparrow| - |\uparrow\rangle\langle\downarrow| + |\downarrow\rangle\langle\uparrow| + |\downarrow\rangle\langle\downarrow|\Big)\,. \tag{4.17}$$

This pulse should be phase coherent with the first pulse, but allow a controlled *phase shift* with respect to the first pulse. The effect of this phase shift is expressed by the following unitary,[6] which is applied right before the unitary of the second pulse, Eq. (4.54),

$$\hat{U}_{\phi} = e^{i\phi}|\uparrow\rangle\langle\uparrow| + |\downarrow\rangle\langle\downarrow| . \tag{4.18}$$

The two unitary operators can be combined into a single one,

$$\hat{U}_{-\pi/2,\phi} = \frac{1}{\sqrt{2}}\Big(e^{i\phi}|\uparrow\rangle\langle\uparrow| - |\uparrow\rangle\langle\downarrow| + e^{i\phi}|\downarrow\rangle\langle\uparrow| + |\downarrow\rangle\langle\downarrow|\Big) . \tag{4.19}$$

Denoting the duration of this pulse by τ_2, the state at time $t_3 = t_2 + \tau_2$ reads

$$|\psi(t_3)\rangle = \frac{1}{\sqrt{2}}\Big\{ |\uparrow\rangle\ |\phi_{\uparrow}(t_3)\rangle + |\downarrow\rangle\ |\phi_{\downarrow}(t_3)\rangle\Big\} , \tag{4.20}$$

with

$$|\phi_{\uparrow}(t_3)\rangle = \frac{1}{\sqrt{2}}\Big(- |\phi_{\downarrow}(t_2)\rangle + e^{i\phi}\,|\phi_{\uparrow}(t_2)\rangle\Big) , \tag{4.21a}$$

$$|\phi_{\downarrow}(t_3)\rangle = \frac{1}{\sqrt{2}}\Big(\quad |\phi_{\downarrow}(t_2)\rangle + e^{i\phi}\,|\phi_{\uparrow}(t_2)\rangle\Big), \tag{4.21b}$$

which are, using the previous results of Eqs. (4.16),

$$|\phi_{\uparrow}(t_3)\rangle = \frac{1}{\sqrt{2}}\Big(-\hat{U}_{\downarrow}(t_R)\,|\phi_{\downarrow}(t_0)\rangle + e^{i\phi}\hat{U}_{\uparrow}(t_R)\,|\phi_{\downarrow}(t_0)\rangle\Big) , \tag{4.22a}$$

$$|\phi_{\downarrow}(t_3)\rangle = \frac{1}{\sqrt{2}}\Big(\quad \hat{U}_{\downarrow}(t_R)\,|\phi_{\downarrow}(t_0)\rangle + e^{i\phi}\hat{U}_{\uparrow}(t_R)\,|\phi_{\downarrow}(t_0)\rangle\Big) . \tag{4.22b}$$

5. Measurement. At the end of the sequence the state of the two-level system is measured by a projective measurement, and the relative frequencies of observing the two-level system in one of its eigenstates are recorded. These relative frequencies or probabilities are given by

$$\mathcal{P}_{\uparrow}(\phi) = \langle\psi(t_3)|\uparrow\rangle\langle\uparrow|\psi(t_3)\rangle = \frac{1}{2}\Big\{1 - \mathrm{Re}\Big(e^{i\phi}\mathcal{O}(t_R)\Big)\Big\} , \tag{4.23a}$$

$$\mathcal{P}_{\downarrow}(\phi) = \langle\psi(t_3)|\downarrow\rangle\langle\downarrow|\psi(t_3)\rangle = \frac{1}{2}\Big\{1 + \mathrm{Re}\Big(e^{i\phi}\mathcal{O}(t_R)\Big)\Big\} . \tag{4.23b}$$

These probabilities depend directly on the phase with which the second pulse is applied as well as on the *complex contrast factor* (Englert 1996):

$$\mathcal{O}(t_R) = \langle\phi_{\downarrow}(t_0)|\hat{U}^{\dagger}_{\downarrow}(t_R)\hat{U}_{\uparrow}(t_R)|\phi_{\downarrow}(t_0)\rangle . \tag{4.24}$$

6 Here, we neglect a global phase shift and a phase that does not change the following result.

The complex contrast factor is actually identical to the *overlap* between the differently evolved motional wavefunctions, and it depends therefore on the time t_R elapsed in between the two Ramsey pulses.

Another way of looking at the complex contrast factor or overlap is to consider it as the scalar product between the initial state $|\phi(t_0)\rangle_\downarrow$ itself and an evolved version of it that is subjected to two consequent time evolution operators: First, it is evolved with $\hat{U}_\uparrow(t_R)$, which is the usual time evolution operator evolving the initial state forward in time. Then, in a second step, the so-obtained state is evolved with the unitary operator $\hat{U}_\downarrow^\dagger(t_R)$, which can also be regarded as a (hypothetical) time evolution by $\hat{U}_\downarrow(t_R)$ backward in time due to the time-reversibility of unitary dynamics. Thus, the overlap can serve as a measure of how good the time-evolution of $\hat{U}_\uparrow(t_R)$ can be "reversed" by $\hat{U}_\downarrow^\dagger(t_R)$. A more common version of such a measure is obtained by taking the modulus-square of the overlap, which is the so-called *quantum Loschmidt*[7] *echo* (Peres 1984; Jalabert and Pastawski 2001; Gorin et al. 2006). It is employed as a useful method in various fields such as quantum chaos (Peres 1984; Jacquod et al. 2001), decoherence (Cucchietti et al. 2003; Casabone et al. 2010), and quantum criticality (Quan et al. 2006; Zanardi and Paunković 2006) in many-body systems.

In Eq. (4.23), the sum of the probabilities always adds up to unity, $\mathcal{P}_\downarrow(\phi) + \mathcal{P}_\uparrow(\phi) = 1$, of course. As we vary the phase ϕ continuously, however, we observe oscillations in the probabilities (4.23), as sketched in Figure 4.4; these oscillations appear with a certain contrast or *visibility*,

$$\mathcal{V} = \frac{\max \mathcal{P}_\downarrow - \min \mathcal{P}_\downarrow}{\max \mathcal{P}_\downarrow + \min \mathcal{P}_\downarrow}, \qquad \text{with } 0 \leq \mathcal{V} \leq 1\,, \tag{4.25}$$

which is given by the absolute value of the complex contrast factor,

$$\mathcal{V}(t_R) = |\mathcal{O}(t_R)|\,. \tag{4.26}$$

For the theoretical treatment in the following, the visibility is given by the simpler formula $\mathcal{V} = \max \mathcal{P}_\downarrow - \min \mathcal{P}_\downarrow$, as, in theory, the sum of $\max \mathcal{P}_\downarrow + \min \mathcal{P}_\downarrow = 1$ always. In actual experiments, this sum may deviate from unity because of statistical and systematic measurement errors, so it is necessary to draw upon Eq. (4.25) for the evaluation of the visibility.

In the following chapters, our analysis concentrates on the visibility as the main quantity used to characterize the motional state of an ion

7 In a famous debate with Ludwig Boltzmann about entropy, Joseph Loschmidt based his claims on the time-reversal invariance of classical mechanics. The naming of the Loschmidt echo refers to him, though this argument of sudden time-reversal, or equivalently the reversal of the velocities of all molecules, has been put forward earlier by Thomson (1875).

Coulomb crystal. As we have seen by its definition via Eqs. (4.25) and (4.26), the visibility is given by the overlap of the motional states, and thus its temporal behaviour can give us some information about the actual dynamics of the motional state. Specifically, any change in the visibility is directly related to a change of the overlap of the wavefunctions of the two differently evolving parts of the motional states. If we now assume that the dynamics of one branch of the motional state is already known, it can serve us as a *probe* for the other state.

A simple case is realized for one of the branches remaining in its motional ground state, where the ions are located around their classical equilibrium positions. Assuming that there will be no significant spread in the wavefunctions, we will find the following: The visibility will decrease when the centre of the wavefunction of the second branch departs from these equilibrium positions, and it will grow when the centre of the wavefunction returns back. We are going to analyse this particular case in the next chapter. As the overlap can be used to characterize the "distance" between two quantum states, this statement can be generalized; in fact, as the overlap is just the scalar product between the two differently evolved states, the norm follows naturally from the scalar product. In that sense, the visibility is zero for orthogonal quantum states of the motional degrees of freedom, and almost zero for quasi-orthogonal states.

Another realization might use the known evolution of a coherent state or squeezed motional state; these states exhibit the minimum uncertainty allowed by the Heisenberg-Robertson relation (just like the ground state) and they follow the trajectories of the classical equations of motion. Most importantly, the spread in the wavefunction does not disperse for coherent states and it oscillates periodically for squeezed states. The positions and spreads of their wavefunctions are thus known and could be employed as a dynamical probe.

This overlap is taken between the two separately evolved motional states at time t_2 just before the application of the second Ramsey pulse, $\mathcal{O}(t_R) = \langle \phi_\downarrow(t_2) | \phi_\uparrow(t_2) \rangle$. Assume the evolution of one initial state is already known; the other component may now evolve dynamically, and we can extract some information directly by looking at the overlap – or even at the visibility. For instance, the deviation of the wavepacket of the excited component away from the initial state will result in a reduced overlap. Depending on the form of the evolution, the wavepacket may also return back to the initial state, thereby being the cause of *revivals* in the visibility. These simple arguments already hint at the fact that a certain amount of information about the motional state of the excited component can be extracted. We present in the

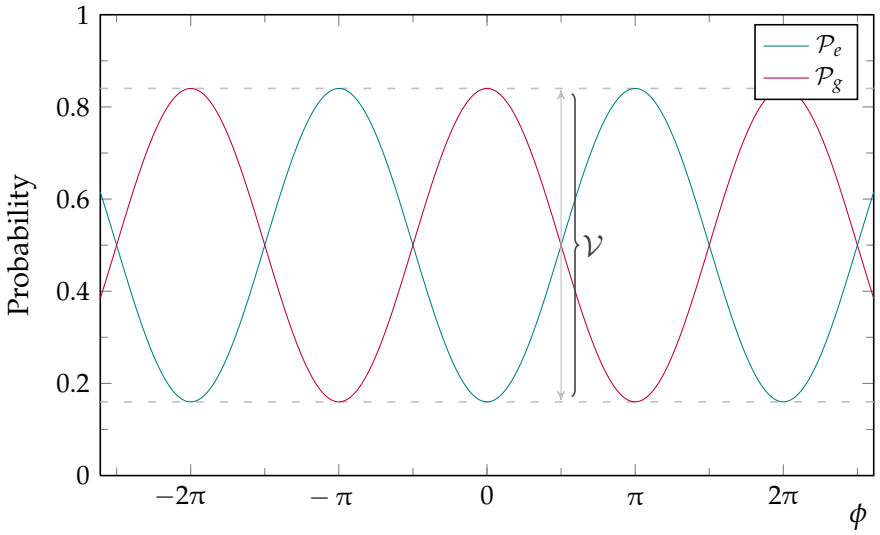

Figure 4.5: The visibility of the Ramsey fringes is given by $\mathcal{V} = (\max \mathcal{P}_\downarrow - \min \mathcal{P}_\downarrow)/(\max \mathcal{P}_\downarrow + \min \mathcal{P}_\downarrow)$, which is $\mathcal{V} \approx 0.68$ in this example.

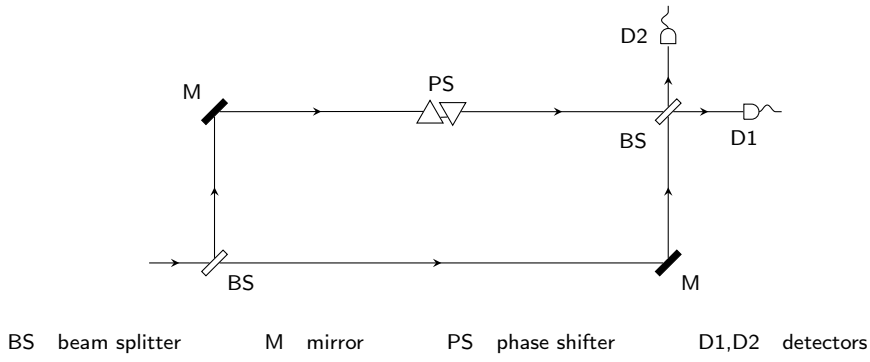

(a) Mach-Zender interferometer

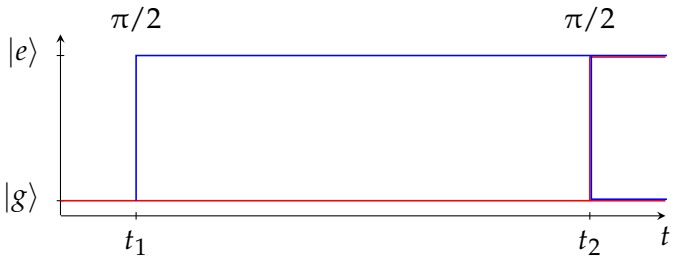

(b) Ramsey interferometer

Figure 4.6: In a Mach-Zender interferometer (a), a low intensity light pulse is split by a 50/50 beam splitter into two paths and recombined again. The measured intensities on the detectors depend on the phase shift induced in one arm of the interferometer. In a Ramsey interferometer (b), pulses split up the quantum state in Hilbert space and recombine it later. (b) is adopted from Cohen-Tannoudji and Guéry-Odelin (2011, Fig. 2.5, p. 28)

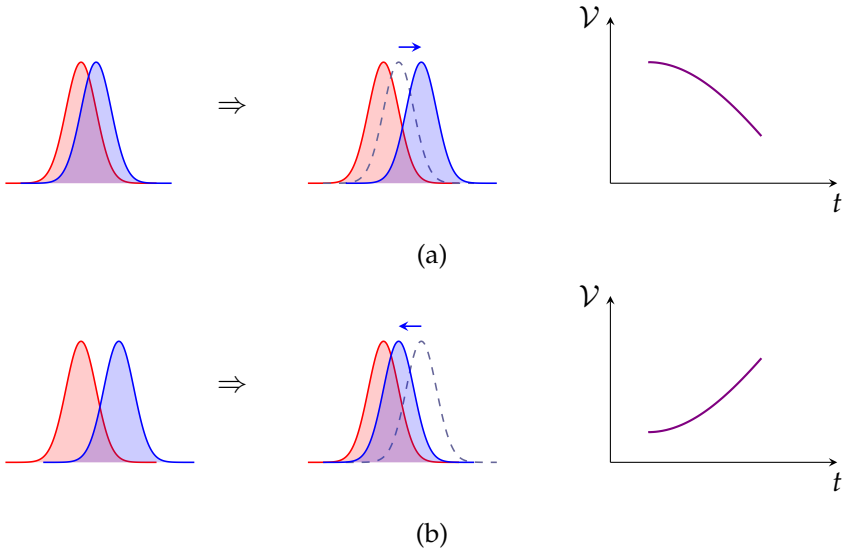

Figure 4.7: The visibility depends on the overlap of the wavefunctions via Equations (4.25) and (4.26). (a) A time-evolution that decreases the overlap leads to a falling visibility. (b) An increasing overlap results in a rise of the visibility.

later chapters a detailed analysis for these scenarios for the case of ion Coulomb crystals in state-dependent potentials.

Equivalence to a Mach-Zender-Interferometer

In order to improve our understanding of the Ramsey interferometry scheme we draw on an analogy with an interferometer in a common Mach-Zender setup. All the steps described in the previous section find their analogue in such an interferometer.

In a Mach-Zender interferometer, see Figure 4.6a, an incoming light beam is split up by a 50/50 beam splitter into two paths. With mirrors, the two paths are reflected onto a second beam splitter where they interfere. The interference can be controlled by introducing a phase shift into one arm of the interferometer, so that one can see a varying intensity at the output. The interference is also valid if instead of continuous light beams just short pulses are sent into the interferometer, even if each pulse contains only a single photon excitation.

In the Ramsey interferometer, Figure 4.6b, the beam splitters correspond to the $\pm\pi/2$ pulses; the free propagation along each path of the Mach-Zender interferometer is analogous to the free time evolution between the pulses. Thus, the phase shift and the measurement of the probabilities are equivalent in both cases. The difference is that in a Mach-Zender interferometer, the light beams are split spatially whereas in the Ramsey interferometer the initial state is put into a

superposition. Yet, in the Mach-Zender interferometer, one can also regard the field along the different paths as a superpositions state, in which the two arms correspond to two different field modes. Moreover, the spatial separation of the beam splitters can also be regarded as a temporal separation via the group velocity of the light fields.

In that sense, both interferometers are equivalent and can be described in the same framework, in which quantum mechanical probability amplitudes interfere at the "output" of the interferometer. In fact, this is also true for other two-way interferometers such as the Young's double-slit experiment, e. g., which could be compared with the Ramsey interferometer in a similar way.

Visibility and Which-Way Information

The time variation of the visibility allows us to extract some information about the motional dynamics. In Young's double slit experiment with single photons, the visibility of the interference at the output vanishes if the path of the photon is determined by any means. The explanation of this phenomenon dates back to the Bohr-Einstein debate (Wheeler and Zurek 1983, pp. 3ff.), in which Niels Bohr explained the vanishing of the interference fringes via the Heisenberg-Robertson uncertainty relation: The determination of the position leads to an uncertainty in the momentum of the scattered photon large enough to wash out the interference pattern. Another famous discussion can be found in *The Feynman Lectures on Physics*, where electrons are diffracted by a double slit and monitored by a light source placed behind the slits to determine which slit the electron took (Feynman et al. 1965b, Sections 1-6 and 3-2, pp. 1-6ff. and 3-5ff.). The uncertainty principle has been employed to explain this observation also for other proposed setups that try to determine the which-way information in two-way interferometers with single particles, such as schemes trying to employ the Aharonov-Bohm effect to determine the path of the particle (Furry and Ramsey 1960). It has been pointed out that this is an inherent feature of the complementarity of quantum mechanics, which is necessary for the consistency of the theory.

By analysing the double-slit experiment in which one is about to obtain only partial which-way information, Wootters and Zurek (1979) quantified the obtainable amount of information and showed that it is maximal for a pure state. This work was extended in the following by Bartell (1980); Tan and Walls (1993), and Greenberger and Yasin (1988), the latter deriving a first inequality between "wave versus particle knowledge". This notion was put on a firmer footing by the introduction of an inequality between the interferometric *visibility* and the *distinguishability*, derived by Jaeger et al. (1995) and independently

by Englert (1996). They assumed that the which-way information, which is connected with the distinguishability, is obtained by a second "which-way marker" particle that is entangled with the particle in the interferometer. The distinguishability $\mathcal{D} = \frac{1}{2}\,\mathrm{tr}(|\rho_{\uparrow\uparrow} - \rho_{\downarrow\downarrow}|\,)$ is defined as the trace distance between the two density matrices of the which-way marker particle that correspond to the detection of the two paths denoted by $\uparrow$ and $\downarrow$. In the pure state case, the density matrices are simply given by $\rho_{\uparrow\uparrow} = |\phi_\uparrow(t_3)\rangle\langle\phi_\uparrow(t_3)|$ and $\rho_{\downarrow\downarrow} = |\phi_\downarrow(t_3)\rangle\langle\phi_\downarrow(t_3)|$; the case of mixed states is treated in Section 4.4. In other words, the distinguishability measures the distances between the states or their orthogonality. The inequality between the distinguishability and the visibility of the interference fringes is given by (we take the notation of Englert)

$$\mathcal{D}^2 + \mathcal{V}^2 \leq 1\,. \tag{4.27}$$

It is worth emphasizing that the derivation of this inequality does not employ any kind of Heisenberg-Robertson uncertainty relation, but rather takes advantage of the mathematical properties of the total entangled state. The loss of the interferometric visibility by detection of the path taken by the particle is commonly explained in terms of random momentum kicks enforced by the uncertainty relation that result in a blurring of the phase. Yet, the analysis of a proposed experiment by Scully, Englert and Walther (1991) shows that a which-path detection without a momentum transfer is possible but still leads to a loss of coherence (Scully, Englert and Schwinger 1989) that follows from the entanglement of the interfering particle with the which-way marker. This work triggered a vivid debate whether complementarity is independent or derived from uncertainty relations (Storey et al. 1994; Englert et al. 1995; Storey et al. 1995; Wiseman and Harrison 1995; Wiseman, Harrison et al. 1997; Luis and Sánchez-Soto 1998; Englert et al. 2000; Björk et al. 1999; Dürr and Rempe 2000). The possibility of "erasing" the which-way information and thereby regaining the full visibility of the interference in the so-called *quantum eraser* (Scully and Drühl 1982), which could moreover be performed as a *delayed-choice* experiment (Wheeler 1983), showed the connection between complementarity and entanglement in a quite striking way (Mohrhoff 1996; Englert et al. 1999; Mohrhoff 1999). Nevertheless, other studies concluded that a hidden momentum transfer (Drezet et al. 2006), which could possibly be revealed by a weak measurement (Aharonov et al. 1988; Wiseman 2003; Garretson et al. 2004; Mir et al. 2007), is present in any which-way experiment.

The present status of the debate is probably best summarized by Busch and Shilladay:

> [...] it seems indeed moot to try and establish a hierarchy of principles of uncertainty, complementarity, or entanglement

> *within* quantum mechanics. As seen from within this theory, these features are linked with each other but cannot be claimed to be reducible to one another. They are not logically independent, nor simply consequences of each other. (Busch and Shilladay 2006, italics in original)

Irrespective of these considerations, the relation between the path distinguishability and the fringe visibility has been verified in various experiments (Mittelstaedt et al. 1987; Summhammer et al. 1987; Zou et al. 1991; Kwiat et al. 1992; Eichmann et al. 1993; Pfau et al. 1994; Chapman et al. 1995; Buks et al. 1998; Dürr et al. 1998b,a; Schwindt et al. 1999; Bertet et al. 2001; Braig et al. 2003; Jacques, Lai et al. 2008; Jacques, Wu et al. 2008; Barbieri et al. 2009; Liu et al. 2012; Kaiser et al. 2012; Ma et al. 2013; Tang et al. 2013; Banaszek et al. 2013), including experiments on delayed-choice and the quantum eraser. Currently, there are no experimental results that are in contradiction with inequality (4.27), despite the claims of a recent proposal (Afshar 2005; Afshar et al. 2007; see also Steuernagel 2007; Flores 2008; Kastner 2009; Flores and Tata 2010).

In a Ramsey interferometer with trapped ions, the which-way information is given by how far the wavepackets of the ions separate from each other and thereby decrease their overlap. A possible measure is given by the orthogonality between the state vectors corresponding to the wavepackets; if the states were orthogonal, we could perfectly distinguish them. So any time the visibility is low, the wavepackets separate from each other, and theoretically it might be possible to determine to which "path" the wavepacket belongs. In turn, a high visibility occurs only for those times when the two wavepackets overlap almost perfectly. Thus we can infer something from the change of the visibility as a function of the time, namely how close or how far separated the motional wavepackets are.

4.3 IMPLEMENTATION OF RAMSEY INTERFEROMETRY WITH TRAPPED IONS

We now turn to a short discussion of our assumptions and of the requirements for the implementation of the Ramsey interferometry protocol for experiments with ion Coulomb crystals. The discussion here then guides the theoretical description of a more realistic Ramsey interferometry setup presented in Section 4.4.

Electronic States and Transitions Between them

Since the scheme of Ramsey interferometry is based on the notion of a two-level system, we focus on the case where the electronic excitation

can only occupy two *meta-stable states*, denoted by $|\downarrow\rangle$ and $|\uparrow\rangle$, out of the entire level structure of the atom. For this, we need to assume that the frequency and polarization of the light field is chosen such that from all possible transitions between the levels of the whole manifold only a single transition is resonant and allowed by atomic selection rules (Allen and Eberly 1987, Ch. 2, pp.28ff.). This does not necessarily mean that the two levels are connected by a dipole-allowed transition; the two levels could also be connected by an electrical quadrupole transition driven by a laser field with sufficient intensity.

Further, we require that the electronic excitation does not decay out of any of these electronic levels by spontaneous emission of a photon, such that the excitation rather stays in the state in which it was prepared – at least with a high probability – for the typical time-intervals of the experiment. As the lifetime of dipole allowed transitions is typically of the order of 1×10^{-8} s (Kramida et al. 2014), none of the two levels should be connected to any lower level by such a transition. One possibility is to choose different Zeeman or hyperfine sublevels of the ground-state manifold, as has been done in experiments with $^{9}Be^{+}$ ions for the former and with $^{43}Ca^{+}$ or $^{171}Yb^{+}$ ions for the latter. Both realizations would potentially require an additional magnetic field to lift the degeneracy between the states. For electric quadrupole or magnetic dipole transitions, the lifetime can be of the order of seconds, and as the time scale of experiments is usually shorter than this, we can also allow meta-stable levels decaying via such transitions. In such a scheme, the two levels are chosen to be the S and D manifolds as in $^{40}Ca^{+}$ ions, e. g., as used in many trapped ion laboratories.

In any case, we assume that there are two well-defined levels which are denoted by $|\downarrow\rangle$ and $|\uparrow\rangle$. The Hamiltonian of the electronic degrees of freedom can be written as

$$\begin{aligned}\hat{\mathrm{H}}_{\mathrm{atom}} &\sim \hbar\omega_{\uparrow}|\uparrow\rangle\langle\uparrow| + \hbar\omega_{\downarrow}|\downarrow\rangle\langle\downarrow| \\ &\sim \hbar\omega_{\uparrow\downarrow}|\uparrow\rangle\langle\uparrow| \sim \frac{\hbar\omega_{\uparrow\downarrow}}{2}\Big(|\uparrow\rangle\langle\uparrow| - |\downarrow\rangle\langle\downarrow|\Big)\,, \quad (4.28)\end{aligned}$$

where the equivalence relation links the Hamiltonians by unitary transformations; the effect of these transformations is a shift of the zero-point energy to $\hbar\omega_{\downarrow}$, respectively to $(\omega_{\uparrow} + \omega_{\downarrow})/2$ afterwards, and a new definition of the angular frequency $\omega_{\uparrow\downarrow} = \omega_{\uparrow} - \omega_{\downarrow}$ is defined by the difference between the two atomic angular frequencies.

Apart from well-defined and (meta-)stable states, we also need to have full control over the initialization of a certain state, e. g. by means of optical pumping techniques (Kastler 1950, 1967). We also assume that it is possible to deterministically change the electronic state by coupling the ion to incident light or radio-frequency fields.

Addressing a Single Ion

The sequence of Ramsey interferometry is made up of a series of pulses of electromagnetic radiation. Each of these Ramsey pulses manipulates the electronic state of just a single ion while avoiding excitation of the electronic states of the other ions.

There are several possibilities of implementing this in an experiment. One is by tightly focussing a laser beam such that only the probed ion is illuminated and the other ions are not excited by the laser. This usually means that the laser beam is directed roughly perpendicularly to the symmetry axis of the crystal and is focused by an optical system to a beam waist of just a few µm width.

Another possibility of implementing single ion addressing is adding a magnetic field gradient, in which the Zeeman effect shifts certain electronic states in energy depending on the ion's positions (Johanning et al. 2009). Then the frequency of the incident radiation is in resonance with the atomic transition at just one particular spatial position. If the probed ion now sits exactly at this point, it is in resonance with the radiation field, while the other ions are at other spatial positions where they are not resonant.

A third possibility is to choose different electronic levels for the other ions such that the choice of the frequency and polarization of the laser does not allow exciting them in accordance with the atomic selection rules.

Finally, one could also choose different ion species, meaning different isotopes of the same atomic element, e. g. $^{40}Ca^{+}$ and $^{44}Ca^{+}$ as used in experiments in Innsbruck (Hempel et al. 2013), or even different atomic elements with a larger mass difference as $^{9}Be^{+}$ and $^{24}Mg^{+}$ as used in National Institute of Standards and Technology-experiments in Boulder (Jost et al. 2009). Different isotopes usually have different nuclear spins leading to different level structures and different atomic frequencies. Hence one can prepare the ions of one isotope in a state which is resonant to the incoming radiation, while for the other isotope the transition is non-resonant. However, different isotopes have different atomic masses, which complicates the description of the motional dynamics of the ions. As we want to expand on our discussion of state-dependent structures and normal modes in Chapter 2, we shall not consider this option (see Home 2013 for a review on mixed-species ion Coulomb crystals). Still, it might lead to interesting and rich physics and might be a motivation to generalize the findings of Chapter 2 and apply them to the case of crystals consisting of ions with different masses.

Manipulating the Electronic State of an Ion

The manipulation of the electronic states depends on the nature of the chosen levels. For the case of different Zeeman sublevels or hyperfine states of a single manifold, the transition between the states $|\downarrow\rangle$ and $|\uparrow\rangle$ is either driven by two-photon Raman transitions or driven directly by strong microwave or radio-frequency fields. In the case of having different manifolds, the transition between the states is a dipole-forbidden transition such as a quadrupole transition, which can be driven by using a laser with sufficient high intensity.

All three types can be described theoretically as if they were a dipole transition, as shown by Leibfried et al. (2003, Appendix), where an effective transition frequency ω_L, an effective wave vector k, and a Rabi frequency Ω for the Raman and quadrupole transitions are introduced. Hence, for the theoretical description of the interaction induced by the Ramsey pulses, we can treat the transition as a dipole-allowed transition.

Hamiltonian of the Ramsey Pulses

For the Ramsey pulses, the ion is addressed by pulses of a travelling wave laser beam, which is modelled as a classical electrical field. The Hamiltonian for the interaction of the two-level system with the classical electromagnetic field is given by Allen and Eberly (1987, Ch. 2, pp. 34f.),

$$\hat{\mathrm{H}}_1 = \hat{\mathrm{H}}_{\mathrm{atom}} + \hat{\mathrm{H}}_{\mathrm{pulse}} = \frac{\hbar\omega_{\uparrow\downarrow}}{2}\left(|\uparrow\rangle\langle\uparrow| - |\downarrow\rangle\langle\downarrow|\right) - \hat{\mathbf{d}} \cdot \mathbf{E}(\mathbf{r}, t)\,, \quad (4.29)$$

where $\hbar\omega_{\uparrow\downarrow}$ is the energy difference between the electronic states $|\uparrow\rangle$ and $|\downarrow\rangle$, and $\mathbf{d}$ is the atomic dipole operator. It is given by

$$\begin{aligned}\hat{\mathbf{d}} &= \mathbf{d}_{\uparrow\downarrow}|\uparrow\rangle\langle\downarrow| + \mathbf{d}_{\downarrow\uparrow}|\downarrow\rangle\langle\uparrow| \\ &= \mathrm{Re}\,\mathbf{d}_{\uparrow\downarrow}\Big(|\uparrow\rangle\langle\downarrow| + |\downarrow\rangle\langle\uparrow|\Big) + \mathrm{i}\,\mathrm{Im}\,\mathbf{d}_{\uparrow\downarrow}\Big(|\uparrow\rangle\langle\downarrow| - |\downarrow\rangle\langle\uparrow|\Big)\,, \quad (4.30)\end{aligned}$$

where we assume that the dipole moment is real, $\mathbf{d}_{\uparrow\downarrow} = \mathbf{d}^*_{\downarrow\uparrow} = \mathbf{d}_{\downarrow\uparrow}$, and given by $\mathbf{d}_{\downarrow\uparrow} = \langle\downarrow|\hat{\mathbf{d}}|\uparrow\rangle$. The electromagnetic field is given by a monochromatic plane wave propagating transverse to the trap axis,

$$\mathbf{E}(\mathbf{r}, t) = \mathcal{E}_0 \mathbf{e}_L \sin(\omega_L t - \mathbf{k}_L \cdot \mathbf{r} + \phi)\,. \quad (4.31)$$

The field is evaluated at the position of the ion $\mathbf{r} = \mathbf{r}(t)$ (we are taking the dipole approximation for the atom-field interaction, so this is the COM-position of the nucleus and all electrons). Here, ω_L is the frequency of the laser field and $\mathbf{k}_L$ the corresponding wavevector pointing in the direction of propagation, and $\mathbf{e}_L$ the polarization

vector perpendicular to $\mathbf{k}_L$; for simplicity's sake, we assume the dipole transition is excited by radiation with linear polarization. The field amplitude $\mathcal{E}_0$ may be assumed to be constant during the duration of the pulses and zero at other times. The phase ϕ is explicitly included in Eq. (4.31) as it will be varied for the two pulses.

By transformation into a suitable interaction picture and applying the RWA (Allen and Eberly 1987, Ch. 2, pp. 41ff.), the Hamiltonian (4.29) is rewritten as

$$\begin{aligned}\hat{\mathrm{H}}_1' = &-\frac{\hbar\delta_L}{2}\left(|\uparrow\rangle\langle\uparrow| - |\downarrow\rangle\langle\downarrow|\right) \\ &+ \frac{\mathrm{i}\hbar\Omega(t)}{2}\left(|\uparrow\rangle\langle\downarrow|\,\mathrm{e}^{\mathrm{i}\mathbf{k}_L\cdot\mathbf{r}-\mathrm{i}\phi} - |\downarrow\rangle\langle\uparrow|\,\mathrm{e}^{-\mathrm{i}\mathbf{k}_L\cdot\mathbf{r}+\mathrm{i}\phi}\right), \quad (4.32)\end{aligned}$$

where we introduced the detuning $\delta_L = \omega_L - \omega_{\uparrow\downarrow}$ of the laser frequency ω_L from the atomic transition frequency $\omega_{\uparrow\downarrow}$, and $\Omega(t) = \mathcal{E}_0\mathbf{e}_L \cdot \mathbf{d}_{\uparrow\downarrow}/\hbar$ is the *Rabi frequency*, which depends on the projection of the field polarization onto the atomic dipole moment, $\mathbf{e}_L \cdot \mathbf{d}_{\uparrow\downarrow}$, and on the field amplitude $\mathcal{E}_0$ of the laser beam.

Choosing the laser frequency on resonance, i. e., $\omega_L = \omega_{\uparrow\downarrow}$, the first term in Eq. (4.32) vanishes. If we are taking the motional degrees of freedom in harmonic approximation into account, the full Hamiltonian is given by

$$\hat{\mathrm{H}} = \hat{\mathrm{H}}_{\mathrm{mot}} + \hat{\mathrm{H}}_{\mathrm{atom}} + \hat{\mathrm{H}}_{\mathrm{pulse}}, \quad (4.33)$$

with $\hat{\mathrm{H}}_{\mathrm{mot}}$ given by Eq. (3.1). When changing to the interaction picture, we need to transform the motional Hamiltonian $\hat{\mathrm{H}}_{\mathrm{mot}}$ too, since the photon recoil operators depend on the position operator of the probed ion. The various terms appearing in the transformed Hamiltonian can be compared with each other (Poyatos, Cirac, Blatt et al. 1996). If we assume to be in the *strong-excitation regime*, in which the Rabi frequency is much larger than the motional normal mode frequencies, $\Omega \gg \omega_1, \ldots, \omega_{3N}$, it turns out that the terms originating from the transformation of the motional Hamiltonian $\hat{\mathrm{H}}_{\mathrm{mot}}$ can be neglected for sufficiently short times.

Another way of seeing this is to compare the typical time scales of each of the different Hamiltonians separately; if there are terms that are evolving much faster than others, the slow terms may be safely neglected within the *sudden approximation* (Gottfried and Yan 2003, Sec. 4.1, pp. 168f.). As long as the interaction is in effect for a sufficient short time period, as it is the case for one period of the Rabi oscillation or shorter, we may consider the motional dynamics as frozen.[8] This

8 It is worth mentioning that this approximation does not necessarily rely on the trapped ions being in the Lamb-Dicke regime; if the Lamb-Dicke parameter is larger than one, it may still be possible to fulfil the inequality.

means we definitely[9] need a sufficiently strong interaction $\hat{H}_{\text{pulse}}$ in order to drive the state significantly out of $|\downarrow\rangle$. Without this requirement, the motional state would change during the interaction in a continuous way into a non-trivial state as any pumped population will instantly start evolving because of the state-dependent potential.

A experimental setup capable of using such fast pulses has been realized in the group in Maryland, for which Rabi oscillations have been achieved within 50 ps (Campbell et al. 2010; Mizrahi, Senko et al. 2013; Mizrahi, Neyenhuis et al. 2014) by employing a high-power frequency-comb laser system (Hayes et al. 2010) with ultrafast pulses.

Neglecting the motional Hamiltonian during the duration of the pulses, the unitary evolution operator for this Hamiltonian is

$$\hat{U}'(t) = \exp(-i\hat{H}'_1 t/\hbar)\,, \tag{4.34}$$

which can be worked out by expanding the exponential function of the operator. The result is surprisingly simple,

$$\begin{aligned}\hat{U}'(t) = \cos[\Omega(t)t/2]\Big(|\uparrow\rangle\langle\uparrow| + |\downarrow\rangle\langle\downarrow|\Big) \\ + \sin[\Omega(t)t/2]\Big(|\uparrow\rangle\langle\downarrow|\hat{R}_{\mathbf{k}}\,e^{-i\phi} - |\downarrow\rangle\langle\uparrow|\hat{R}^{\dagger}_{\mathbf{k}}\,e^{i\phi}\Big)\,,\end{aligned} \tag{4.35}$$

where we introduced the *recoil operator*

$$\hat{R}_{\mathbf{k}} = e^{i\mathbf{k}_L\cdot\mathbf{r}}\,. \tag{4.36}$$

Here, $\mathbf{r} = \mathbf{r}(t)$ is the position of the ion that is affected by the pulse, which need not coincide with the trap centre. For the zigzag structure, the ion is initially away from the trap axis, resulting in a phase shift dependent on the equilibrium position of the ions. After the first pulse, due to the state-dependent potential, a part of the wavefunction of the ion starts evolving dynamically. The position of the probed ion at the time of the second pulse thus depends on the actual dynamics of all ions. This leads to a dynamical phase shift in the wavefunction that depends on the parameters of the motional Hamiltonian and the time elapsed before the second pulse is applied. This phase shift has no actual influence on the visibility, though, if it can be kept constant for a certain number of repetitions of experimental cycles with the same initial conditions and the same waiting time between the pulses,

9 In Baltrusch, Cormick and Morigi (2013, Endnote 28) it was claimed that alternatively one could assume that the dipole laser is switched off during the pulse duration such that a weak driving field for the $\pi/2$-pulses could be used instead. After the pulse, the dipole laser is switched on again. It was claimed that the proposal would equivalently work if the switching times for the laser are much shorter than the typical time scales of the motional dynamics. However, this is only true for the first pulse. During the second pulse, the crystal is already in motion, and switching off the dipole potential does not "freeze" the motion; even worse, it changes the dynamics completely.

as it only shifts the origin of the Ramsey fringes. We shall include the effect of the position at the time of the second pulse in the theoretical description later in this chapter.

State Measurement and Initialization

By illuminating the ion with a different laser, which couples one of the two levels $|\downarrow\rangle$ and $|\uparrow\rangle$ to another auxiliary level $|\text{aux}\rangle$ by a dipole transition, the state can be measured and initialized by the so-called *electron shelving method* (Dehmelt 1975; Nagourney et al. 1986). This electronic state needs to have an extremely short lifetime, usually ns or less, and it should decay with certainty back to only one of the two states. This second requirement is usually fulfilled by choosing this auxiliary state such that the only decay allowed by atomic selection rules is the one from $|\text{aux}\rangle \to |\downarrow\rangle$ (or equivalently $|\text{aux}\rangle \to |\uparrow\rangle$). If the electronic state of the ion is excited to $|\text{aux}\rangle$ by the laser, it rapidly decays back to the state $|\downarrow\rangle$ by spontaneously emitting a photon in a random direction. Then it is excited again, emits another photon, and so on. This cycle is repeated continuously with the emitted photons collected by a lens and focused onto a CCD-camera such that the fluorescent light is visible. If the ion is in state $|\uparrow\rangle$, no photons are emitted. Thus, on a CCD-camera with sufficient resolution and sensitivity it is possible to determine if a certain ion is fluorescing or not, which directly determines the electronic state of the ion. The effect of this measurement can be described by the projectors $\hat{P}_{\downarrow} = |\downarrow\rangle\langle\downarrow|$ and $\mathbb{1} - \hat{P}_{\downarrow} = \hat{P}_{\uparrow} = |\uparrow\rangle\langle\uparrow|$, assuming that $|\downarrow\rangle$ is the fluorescent level. During this measurement, the motional state experiences a heating since the fluorescing photons are radiated in random spatial directions and thus give random momentum kicks to the corresponding ion. Yet, this change in the motional state is irrelevant to us since we only need to measure the relative frequencies of finding the probed ion in state $|\uparrow\rangle$ and $|\downarrow\rangle$, respectively.

4.4 RAMSEY INTERFEROMETRY WITH ION COULOMB CRYSTALS AT FINITE TEMPERATURES

In this section we describe in detail the principle of using Ramsey interferometry as a probe, including all the physical constraints discussed in the previous section. For this we employ the density matrix formalism for the motional states, which allows us to treat all cases in one general calculation. In particular, we can apply this immediately to the case of thermal states at a given temperature T to which the crystal has been cooled before the experiment. We are going to use the results obtained in this section for the analysis of quantum

quenches for which the ion Coulomb crystal has been prepared at a finite temperature, which is the subject of Chapter 6.

Preparation

We assume that the electronic state can be prepared with certainty via the techniques discussed before in one of the two states, say $|\downarrow\rangle$, which reads as $|\downarrow\rangle\langle\downarrow|$ when written as a density matrix. The initial motional state of the ion crystal can generally be described by a density matrix $\rho_0 = \rho(t = 0)$. The total initial state ϱ_0 is then, assuming no initial entanglement between electronic and motional degrees of freedom, given by

$$\varrho_0 = |\downarrow\rangle\langle\downarrow| \otimes \rho_0 \,. \tag{4.37}$$

The motional states is either given by

$$\rho_0 = |\phi\rangle_\downarrow\langle\phi| \tag{4.38}$$

for a pure state $|\phi\rangle_\downarrow$, or by

$$\rho_0 = \frac{1}{\mathcal{Z}} \exp\left\{-\frac{\hat{\mathrm{H}}_\downarrow}{k_\mathrm{B}T}\right\} \tag{4.39}$$

for a thermal state (Cohen-Tannoudji, Diu et al. 1997, Complement $\mathrm{E_{III}}$, pp. 304). Here, k_B is the Boltzmann constant, T is the temperature of the thermal state, and

$$\mathcal{Z} = \mathrm{Tr}\left\{\mathrm{e}^{-\hat{\mathrm{H}}_\downarrow/(k_\mathrm{B}T)}\right\} \tag{4.40}$$

is the partition function for the canonical ensemble (Huang 1987, Ch. 7).

Actually, this state is the description for the equilibrium state of the crystal at any temperature T as it is reached through the coupling to a thermal bath, which for laser cooling, e. g., is the vacuum field of all modes of the electromagnetic field. After applying Doppler cooling (Neuhauser et al. 1978; Wineland, Drullinger et al. 1978) to the crystal, it attains a temperature of around 1 to 10 mK (Itano, Bergquist et al. 1995) at the so-called Doppler-cooling limit. For lower temperatures, other cooling techniques must be used (Eschner et al. 2003), such as motional sideband cooling (Diedrich, Bergquist et al. 1989; Monroe, Meekhof, King, Jefferts et al. 1995) or electromagnetically induced transparency-cooling (Morigi, Eschner and Keitel 2000; Roos et al. 2000; Lin, Gaebler et al. 2013), which reach a thermal distribution close to the motional ground state.

In order to describe the operations in the following, we introduce a matrix notation in the basis of the two-level system as follows:

$$\begin{aligned} |\uparrow\rangle\langle\uparrow| &= \begin{pmatrix} 1 & 0 \\ 0 & 0 \end{pmatrix}, \quad |\uparrow\rangle\langle\downarrow| = \begin{pmatrix} 0 & 1 \\ 0 & 0 \end{pmatrix}, \\ |\downarrow\rangle\langle\uparrow| &= \begin{pmatrix} 0 & 0 \\ 1 & 0 \end{pmatrix}, \quad |\downarrow\rangle\langle\downarrow| = \begin{pmatrix} 0 & 0 \\ 0 & 1 \end{pmatrix}. \end{aligned} \tag{4.41}$$

The density matrices of the motional states then can be written as simple elements of that matrix, e. g. the initial state is written as

$$\varrho_0 = |\downarrow\rangle\langle\downarrow| \otimes \rho_0 = \begin{pmatrix} 0 & 0 \\ 0 & 1 \end{pmatrix} \otimes \rho_0 \equiv \begin{pmatrix} 0 & 0 \\ 0 & \rho_0 \end{pmatrix}. \tag{4.42}$$

First Pulse

A laser pulse applied for a time τ_1 resonantly drives the transition $|\downarrow\rangle \rightarrow |\uparrow\rangle$ of the central ion, which we label by n_0. The absorption and emission of a photon by the ion introduces, via the photon recoil, a coupling between motional and electronic degrees of freedom, which is described by the operators $\hat{R}_{\mathbf{k}}$ and $\hat{R}_{\mathbf{k}'}$ in Eq. 6.1. The impact on the probed ion then affects the whole crystal motion via the long-range Coulomb interaction. Immediately after the absorption or emission event, the electronic state and the motional state of the crystal turn from a separable into an entangled state. This entanglement allows us to reveal partial information about the crystal motion by just measuring the electronic degrees of freedom. In fact, this is at the heart of the proposal by De Chiara et al. (2008), in which the crystal is probed by the photon recoil. Here we have an additional cause generating entanglement – the state-dependent evolution after the pulse. In this thesis we focus on the latter, but also provide a comparison in Section 6.2.

The operation of the pulse on the total density matrix is described by multiplying the unitary operator (which is a generalization to Eq. (4.10))

$$\hat{U}_{\pi/2}(\tau_1) = \frac{1}{\sqrt{2}}\Big(|\uparrow\rangle_{n_0}\langle\uparrow| + |\downarrow\rangle_{n_0}\langle\downarrow| + \hat{R}_{\mathbf{k}}|\uparrow\rangle_{n_0}\langle\downarrow| - \hat{R}^{\dagger}_{\mathbf{k}}|\downarrow\rangle_{n_0}\langle\uparrow|\Big) \tag{4.43}$$

from left and right onto the initial density matrix,

$$\varrho_1(t_1) = \hat{U}_{\pi/2}(\tau_1)\varrho_0(t_0)\hat{U}^{\dagger}_{\pi/2}(\tau_1), \tag{4.44}$$

where the operator $\hat{R}_{\mathbf{k}} \equiv \hat{R}_{\mathbf{k}}(\mathbf{r}_{n_0}) = e^{i\mathbf{k}\cdot\mathbf{r}_{n_0}}$ is again describing the mechanical effect of an absorption event of a laser photon. In terms of

the matrix notation introduced, the unitary $\hat{\mathrm{U}}(\tau_1)$ has the following form,

$$\hat{\mathrm{U}}_{\pi/2}(\tau_1) = \frac{1}{\sqrt{2}} \begin{pmatrix} \hat{1} & \hat{\mathrm{R}}_{\mathbf{k}} \\ -\hat{\mathrm{R}}_{\mathbf{k}}^{\dagger} & \hat{1} \end{pmatrix}, \tag{4.45}$$

and the result of equation (4.44) is computed by simple matrix multiplication,

$$\varrho_1 = \frac{1}{2} \begin{pmatrix} \hat{\mathrm{R}}_{\mathbf{k}} \rho_0 \hat{\mathrm{R}}_{\mathbf{k}}^{\dagger} & \hat{\mathrm{R}}_{\mathbf{k}} \rho_0 \\ \rho_0 \hat{\mathrm{R}}_{\mathbf{k}}^{\dagger} & \rho_0 \end{pmatrix}, \tag{4.46}$$

where we dropped the time arguments for clarity. From this form, we can acknowledge the effect of the first pulse: Neglecting the recoil operators for a second, we see that the pulse distributed the initial population of the state $|\downarrow\rangle\langle\downarrow|$ equally onto all elements of the new density matrix. If, after the evolution, all elements are still equal, the density matrix can be perfectly mapped back to the initial electronic state. If they are not equal, this mapping can be achieved partially at most. Therefore, including the recoil, this is already an entangled state in general.

Free Evolution

After this first pulse, the system evolves freely for a duration t_R, with the dynamics given by the following unitary time-evolution operator,

$$\hat{\mathrm{U}}(t, t_0) = |\downarrow\rangle\langle\downarrow| \otimes \mathrm{e}^{-\mathrm{i}\hat{\mathrm{H}}_{\downarrow}(t-t_0)/\hbar} + |\uparrow\rangle\langle\uparrow| \otimes \mathrm{e}^{-\mathrm{i}\hat{\mathrm{H}}_{\uparrow}(t-t_0)/\hbar} \tag{4.47}$$

where we assumed that the Hamiltonians $\hat{\mathrm{H}}_{\downarrow}, \hat{\mathrm{H}}_{\uparrow}$ are time-independent. These state-dependent Hamiltonians for the motional degrees of freedom $\hat{\mathrm{H}}_{\downarrow} = \langle\downarrow|\hat{\mathrm{H}}|\downarrow\rangle$ and $\hat{\mathrm{H}}_{\uparrow} = \langle\uparrow|\hat{\mathrm{H}}|\uparrow\rangle$ are obtained by projecting from left and right to the subspaces of the electronic degrees of freedom,

$$\hat{\mathrm{H}} = (|\uparrow\rangle\langle\uparrow| + |\downarrow\rangle\langle\downarrow|)\hat{\mathrm{H}}(|\uparrow\rangle\langle\uparrow| + |\downarrow\rangle\langle\downarrow|) = \hat{\mathrm{H}}_{\downarrow}|\downarrow\rangle\langle\downarrow| + \hat{\mathrm{H}}_{\uparrow}|\uparrow\rangle\langle\uparrow|, \tag{4.48}$$

as the Hamiltonian (3.7) is diagonal. It is important to avoid any *off-diagonal* terms at the present step, as these would lead to continuous Rabi oscillations between the electronic states. Instead, we want the evolution to entangle the electronic and motional degrees of freedom by providing different dynamics for the motional states depending on the electronic state.

The unitary operator for the free evolution from t_1 to $t_2 = t_1 + t_R$ is given by the following expression,

$$\hat{\mathrm{U}}(t_2, t_1) = \begin{pmatrix} \hat{\mathrm{U}}_{\uparrow}(t_2, t_1) & 0 \\ 0 & \hat{\mathrm{U}}_{\downarrow}(t_2, t_1) \end{pmatrix}, \tag{4.49}$$

where

$$\hat{U}_s(t_2, t_1) = \exp(-i\hat{H}_s(t_2 - t_1)/\hbar)\,. \tag{4.50}$$

The density matrix after a time t elapses, i. e. at time $t_2 = t_1 + t$, reads

$$\varrho_2(t_2) = \begin{pmatrix} \rho_{\uparrow\uparrow}(t_2) & \rho_{\uparrow\downarrow}(t_2) \\ \rho_{\downarrow\uparrow}(t_2) & \rho_{\downarrow\downarrow}(t_2) \end{pmatrix}, \tag{4.51}$$

where the entries are given by

$$\rho_{\uparrow\uparrow}(t_2) = \frac{1}{2}\left(\hat{U}_\uparrow(t)\hat{R}_{\mathbf{k}}\rho_0\hat{R}^\dagger_{\mathbf{k}}\hat{U}^\dagger_\uparrow(t)\right), \tag{4.52a}$$

$$\rho_{\uparrow\downarrow}(t_2) = \frac{1}{2}\left(\hat{U}_\uparrow(t)\hat{R}_{\mathbf{k}}\rho_0\hat{U}^\dagger_\downarrow(t)\right), \tag{4.52b}$$

$$\rho_{\downarrow\uparrow}(t_2) = \frac{1}{2}\left(\hat{U}_\downarrow(t)\hat{R}_{\mathbf{k}}\rho_0\hat{U}^\dagger_\uparrow(t)\right), \tag{4.52c}$$

$$\rho_{\downarrow\downarrow}(t_2) = \frac{1}{2}\left(\hat{U}_\downarrow(t)\rho_0\hat{U}^\dagger_\downarrow(t)\right). \tag{4.52d}$$

For $\hat{U}_\downarrow \neq \hat{U}_\uparrow$, atomic motion and internal degrees of freedom are now entangled by the state-dependent evolution in general even if the recoil is neglected.

Second Pulse

After the free evolution, the second pulse is applied. In the recoil operator, the position vector may be replaced by the expansion into the equilibrium position and the deviation from it. As the equilibrium positions depend on the internal state (see Section 2.3), we can expand around both of them; it is convenient, however, to express the recoil operators in the same basis, e. g. the one related to the state $|\uparrow\rangle$. Then, we can account for a phase shift of the equilibrium positions, as the displacement of the central between the two equilibrium structures is of the same order of magnitude as the typical laser wavelength. We have

$$e^{\pm i\mathbf{k}_L\cdot\mathbf{r}_{n_0}} = e^{\pm i\mathbf{k}_L\cdot(\mathbf{R}^\uparrow_{n_0}+\mathbf{q}^\uparrow_{n_0})} = e^{i\phi_0}e^{\pm i\mathbf{k}_L\cdot\mathbf{q}^\uparrow_{n_0}}, \tag{4.53}$$

where $\phi_0 = \mathbf{k}_L \cdot \mathbf{R}^\uparrow_{n_0}$ is the phase of the laser at the equilibrium position $\mathbf{R}^\uparrow_{n_0}$ of the illuminated ion. Its matrix representation is given by

$$\hat{U}_{-\pi/2;\phi}(\tau_2) = \begin{pmatrix} \hat{1} & \hat{R}_{\mathbf{k}'} \\ -\hat{R}^\dagger_{\mathbf{k}'} & \hat{1} \end{pmatrix} \begin{pmatrix} e^{i\phi} & 0 \\ 0 & 1 \end{pmatrix}, \tag{4.54}$$

where first (to the right) the state-dependent phase shift is applied, and then the inverse of the unitary operation given by Eq. (4.43). The state after this pulse at time $t_3 = t_2 + \tau_2$ is given by

$$\varrho(t_3) = \begin{pmatrix} \varrho_{\uparrow\uparrow}(t_3) & \varrho_{\uparrow\downarrow}(t_3) \\ \varrho_{\downarrow\uparrow}(t_3) & \varrho_{\downarrow\downarrow}(t_3) \end{pmatrix}, \tag{4.55}$$

with

$$\begin{aligned} \varrho_{\uparrow\uparrow}(t_3) = \frac{1}{2}\Big(&\varrho_{\uparrow\uparrow}(t_2) - \mathrm{e}^{-\mathrm{i}\phi}\hat{\mathrm{R}}_{\mathbf{k}'}\varrho_{\downarrow\uparrow}(t_2) \\ &- \mathrm{e}^{\mathrm{i}\phi}\varrho_{\uparrow\downarrow}(t_2)\hat{\mathrm{R}}^\dagger_{\mathbf{k}'} + \hat{\mathrm{R}}_{\mathbf{k}'}\varrho_{\downarrow\downarrow}(t_2)\hat{\mathrm{R}}^\dagger_{\mathbf{k}'}\Big), \end{aligned} \tag{4.56a}$$

$$\begin{aligned} \varrho_{\uparrow\downarrow}(t_3) = \frac{\mathrm{e}^{\mathrm{i}\phi}}{2}\Big(&\varrho_{\uparrow\uparrow}(t_2)R_{\mathbf{k}'} - \mathrm{e}^{-\mathrm{i}\phi}R_{\mathbf{k}'}\varrho_{\downarrow\uparrow}(t_2)R_{\mathbf{k}'} \\ &+ \mathrm{e}^{\mathrm{i}\phi}\varrho_{\uparrow\downarrow}(t_2) - R_{\mathbf{k}'}\varrho_{\downarrow\downarrow}(t_2)\Big), \end{aligned} \tag{4.56b}$$

$$\begin{aligned} \varrho_{\downarrow\uparrow}(t_3) = \frac{\mathrm{e}^{-\mathrm{i}\phi}}{2}\Big(&R^\dagger_{\mathbf{k}'}\varrho_{\uparrow\uparrow}(t_2) - \mathrm{e}^{\mathrm{i}\phi}R^\dagger_{\mathbf{k}'}\varrho_{\uparrow\downarrow}(t_2)R^\dagger_{\mathbf{k}'} \\ &+ \mathrm{e}^{-\mathrm{i}\phi}\varrho_{\downarrow\uparrow}(t_2) + \varrho_{\downarrow\downarrow}(t_2)R^\dagger_{\mathbf{k}'}\Big), \end{aligned} \tag{4.56c}$$

$$\begin{aligned} \varrho_{\downarrow\downarrow}(t_3) = \frac{1}{2}\Big(&R^\dagger_{\mathbf{k}'}\varrho_{\uparrow\uparrow}(t_2)R_{\mathbf{k}'} + \mathrm{e}^{-\mathrm{i}\phi}\varrho_{\downarrow\uparrow}(t_2)R_{\mathbf{k}'} \\ &+ \mathrm{e}^{\mathrm{i}\phi}R^\dagger_{\mathbf{k}'}\varrho_{\uparrow\downarrow}(t_2) + \varrho_{\downarrow\downarrow}(t_2)\Big). \end{aligned} \tag{4.56d}$$

Measuring the Populations

Immediately after the second pulse, the populations are measured at time $t_f = t_3 + \tau_2$. They are obtained by taking the trace over the corresponding projection operators,

$$\mathcal{P}_\downarrow(\phi, t_f) = \mathrm{Tr}\{\varrho_f|\downarrow\rangle_{n_0}\langle\downarrow|\} = \mathrm{Tr}\{\rho_{f,\downarrow\downarrow}(t_f)\}, \tag{4.57a}$$

$$\mathcal{P}_\uparrow(\phi, t_f) = \mathrm{Tr}\{\varrho_f|\uparrow\rangle_{n_0}\langle\uparrow|\} = \mathrm{Tr}\{\rho_{f,\uparrow\uparrow}(t_f)\}\,. \tag{4.57b}$$

Here, we arrived at the last expression in each line by first evaluating the partial trace over the electronic degrees of freedom. The probabilities are thus calculated by taking the remaining trace over the density matrices $\rho_{\uparrow\uparrow}$ and $\rho_{\downarrow\downarrow}$ of the motional degrees of freedom respectively. Using Eqs. (4.56), these motional density matrices are, fully written out,

$$\begin{aligned} \varrho_{\uparrow\uparrow}(t_f) = \frac{1}{4}\Big(&\hat{\mathrm{U}}_\uparrow\hat{\mathrm{R}}_{\mathbf{k}}\rho_0\hat{\mathrm{R}}^\dagger_{\mathbf{k}}\hat{\mathrm{U}}^\dagger_\uparrow - \mathrm{e}^{\mathrm{i}\phi}\hat{\mathrm{U}}_\uparrow\hat{\mathrm{R}}_{\mathbf{k}}\rho_0\hat{\mathrm{U}}^\dagger_\downarrow\hat{\mathrm{R}}^\dagger_{\mathbf{k}'} \\ &- \mathrm{e}^{-\mathrm{i}\phi}\hat{\mathrm{R}}_{\mathbf{k}'}\hat{\mathrm{U}}_\downarrow\rho_0\hat{\mathrm{R}}^\dagger_{\mathbf{k}}\hat{\mathrm{U}}^\dagger_\uparrow + \hat{\mathrm{R}}_{\mathbf{k}'}\hat{\mathrm{U}}_\downarrow\rho_0\hat{\mathrm{U}}^\dagger_\downarrow\hat{\mathrm{R}}^\dagger_{\mathbf{k}'}\Big) \end{aligned} \tag{4.58a}$$

and

$$\varrho_{\downarrow\downarrow}(t_f) = \frac{1}{4}\Big(\hat{R}^\dagger_{\mathbf{k}'}\hat{U}_\uparrow\hat{R}_{\mathbf{k}}\rho_0\hat{R}^\dagger_{\mathbf{k}}\hat{U}^\dagger_\uparrow\hat{R}_{\mathbf{k}'} + e^{i\phi}\hat{R}^\dagger_{\mathbf{k}'}\hat{U}_\uparrow\hat{R}_{\mathbf{k}}\rho_0\hat{U}^\dagger_\downarrow + e^{-i\phi}\hat{U}_\downarrow\rho_0\hat{R}^\dagger_{\mathbf{k}}\hat{U}^\dagger_\uparrow\hat{R}_{\mathbf{k}'} + \hat{U}_\downarrow\rho_0\hat{U}^\dagger_\downarrow\Big). \tag{4.58b}$$

Taking the trace over these expressions, the first and the last term each result in 1, as each of them is a density matrix.[10] The phase is attached to the middle terms, which are Hermitian conjugates of each other. Thus, taking the trace, we can exploit the following relation,

$$\mathrm{Tr}\,\hat{A}^\dagger = (\mathrm{Tr}\,\hat{A})^*,$$

which then is taking the trace of one term summed to its conjugate complex, giving twice the real part of that term. Therefore, we can write the probabilities in the following form,

$$\mathcal{P}_\downarrow(\phi, t) = \frac{1}{2}\Big(1 + \mathrm{Re}\big[e^{i\phi}\mathcal{O}(t)\big]\Big), \tag{4.59a}$$

$$\mathcal{P}_\uparrow(\phi, t) = \frac{1}{2}\Big(1 - \mathrm{Re}\big[e^{i\phi}\mathcal{O}(t)\big]\Big), \tag{4.59b}$$

where $\mathcal{O}(t)$ is the overlap between the differently evolving motional components, given by

$$\mathcal{O}(t) = \mathrm{Tr}\Big\{\hat{R}^\dagger_{\mathbf{k}'}\hat{U}_\uparrow\hat{R}_{\mathbf{k}}\rho_0\hat{U}^\dagger_\downarrow\Big\}. \tag{4.60}$$

The visibility $\mathcal{V}$ of the Ramsey signal is then again determined through the relation $\mathcal{V} = |\mathcal{O}|$.

With this, we have all the necessary tools to apply the principle of Ramsey interferometry on the dynamics of ion Coulomb crystals.

10 In fact, they are both just the initial density matrix unitarily transformed.

5

QUANTUM QUENCHES AT THE LINEAR–ZIGZAG TRANSITION – GROUND STATE PREPARATION

In this chapter we theoretically analyse the visibility of a Ramsey interferometer experiment with an ion Coulomb crystal in a state-dependent potential as discussed in Chapter 4. First, in Section 5.1, we discuss the proposal of the experiment, which involves inducing a transition between the electronic states of a single ion and thereby activating the dipole potential for that ion. Then, in Section 5.2, we derive the analytical formula for obtaining the visibility of such a Ramsey interferometer experiment as a function of the time between the Ramsey pulses. Finally, in Section 5.3, we turn to the numerical analysis of the visibility for various settings. Both, the analytical formula and the analysis are thereby subject to simplifications, some of which are dropped later in Chapter 6.

5.1 QUANTUM QUENCHES IN ION COULOMB CRYSTALS

5.1.1 *Quantum Quenches*

Consider a physical system that has some unique lowest energy state depending on one or more externally controllable parameters, like the magnetic field strength in a spin system. A *quench* of this system may be defined as an abrupt temporal change of these external parameters that leads to a dynamical response. The term originates from material sciences, where a rapid cooling of a material probe may bring it into a thermodynamic phase which would not be accessible by adiabatic processes alone. A typical example is that of quench hardening of steel.

Even if only a single parameter is changed, the behaviour of the quench can depend on other system parameters too. In order to completely describe a quench it is necessary to specify the functional changes of *all* parameters even if they remain constant during the quench. For the changing parameters, a common choice in many theoretical and experimental works is that of a linear ramp, which means that the final value is approached by a constant rate of change

for the varying parameter. In this thesis, we consider the case where the change of one parameter is *sudden*, i. e. on a much shorter time scale than that of the dynamics of the system,[1] so that the quench only depends on the initial and final values of the control parameters.

There are many different ways to perform such a quench for a trapped ion Coulomb crystal. One possibility is the change of one of the trapping frequencies by controlling the voltages on the electrodes, thus inducing a global quench on the crystal. This can lead to the creation of structural defects (Landa, Marcovitch et al. 2010; del Campo, De Chiara et al. 2010; Mielenz et al. 2013) for the case when the initial and final values of the trap frequencies lie on different sides of the linear–zigzag instability.[2] We focus here on the case where the state-dependent dipole potential of only one ion of the crystal is changed. This different potential for the single ion can be considered as an impurity, which also affects the dynamics of the other ions (recall Chapter 2). Since the dynamics of cold trapped ions need to be described by quantum mechanics, we might regard this situation as a *local quantum quench*.

One realization of such state-dependent quantum dynamics in a related approach is the analysis of quenches in central-spin models (Quan et al. 2006), where all degrees of freedom are typically described by spin-1/2-variables only. The central spin can then trigger a quantum phase transition in the state of the remaining spins in dependence on the parameters like the spin-spin interaction and the coupling to a transverse magnetic field.

For an ion Coulomb crystal in a state-dependent potential, in this thesis modelled as a two-level-system (or spin) coupled to a chain of harmonic oscillators, the quench dynamics is induced by a sudden change of the electronic state of the central ion. By putting one ion into a quantum superposition of its electronic levels instead, the crystal becomes entangled with the electronic degrees of freedom via the quench in the state-dependent potential and the Coulomb interaction. Following this step, salient features of this dynamics can be extracted by the method of Ramsey interferometry as discussed in Chapter 4.

5.1.2 *Symmetric Quenches*

As described in Chapter 1, we consider here an ion Coulomb crystal trapped in a combined potential. This potential consists of the static homogeneous trapping potential, which confines all the ions in the

1 See the discussion in Section 4.3 for the validity of this assertion.

2 In particular, the density of the created defects is correlated to the change rate of the involved parameter via the so-called Kibble-Żurek scaling, see Zurek (1996); Kibble (2007); del Campo, De Chiara et al. (2010)

same way, and of the dipole potential, which affects only the central ion and which can be controlled by the manipulation of that ion's electronic state. In the following, we choose to restrict the change of the dipole potential in such a way that the symmetries of the system are preserved, simplifying the analysis considerably. While examining local quenches close to and across the linear–zigzag transition (cf. Chapter 1), we need to respect the symmetries which are inherent in both the linear and the zigzag configurations: The only symmetries that are actually present in both structural configurations are the mirror symmetry on the y–z-plane, $x \mapsto -x$ for crystals containing an odd number of ions, and the inversion symmetry $\mathbf{r} \mapsto -\mathbf{r}$ for crystals with an even number of ions. Since the potential is changed for a single ion only, this ion should therefore be the central one of an ion Coulomb crystal containing an odd number of ions, and the equilibrium positions of the central ion should lie in the y–z-plane. We therefore require the dipole potential to have the same symmetries as the trapping potential. By these restrictions, a quench can only excite modes that respect these symmetries.

5.1.3 *Characterization of the Quench Parameters*

Recalling the discussion of Chapters 1 and 2 and the approximations made there, the ion trap and the dipole potential can both be described by harmonic potentials. Now we want to reduce the trap frequencies characterizing these potentials to a minimal set of dimensionless parameters. As mentioned above, the frequencies of the trapping potential are held fixed while only that of the dipole potential is changed. Nevertheless, the value of the trapping frequencies can play an important role: The change in the dipole potential can make a bigger or smaller change in the configuration of the crystal, depending on whether we are close or far away from the linear–zigzag transition (cf. Chapter 2). Using the assumptions made in Chapter 2, namely that the axial potential along the x-direction is held fixed, we only need to give the aspect ratio, which is the squared ratio of the transverse to the axial frequency, $\alpha = \nu_y^2/\nu_x^2$, to fully characterize the structural configuration of the crystal.

In order to compare quenches for crystals composed of different numbers of ions, we use the transverse trapping frequency normalized to the critical frequency of the linear–zigzag transition, since this is rising with the number of ions (Morigi and Fishman 2004), or equivalently, the aspect ratio to the critical aspect ratio. As only the distance to the transition point is of interest, it is sensible to define the

following dimensionless parameter describing the chosen values of the trapping potential:

$$g = \frac{\nu_y^2 - \nu_{y,c}^2}{\nu_{y,c}^2} = \frac{\alpha - \alpha_c}{\alpha_c} \,. \tag{5.1}$$

Subsequently, we shall call this new parameter the *trapping strength*. In the absence of an additional dipole potential (see Chapter 1) it equivalently describes the linear–zigzag transition: It is positive for $\nu_y > \nu_{y,c}$ (or $\alpha > \alpha_c$), which means that the transverse trapping frequency is above the critical trapping frequency and the crystal is in a linear configuration. For $\nu_y < \nu_{y,c}$ (or $\alpha < \alpha_c$) it is negative and the crystal is in a zigzag configuration.

As discussed in Chapter 2, the dipole potential can change the configuration of equilibrium positions for a small classical crystal because of the long-range nature of the Coulomb interaction. The requirement for the crystal to be small originates from the fact that a single ion cannot appreciably perturb the structure of an infinitely large crystal. The thermodynamic quantity which describes how far a localized perturbation has an effect is the *correlation length* (Fishman et al. 2008), which is determined by thermal or, at $T \to 0$, by quantum fluctuations. As long as the size of the crystal is smaller than the correlation length, we can assume that the change of the potential on the central ion can affect the whole crystal. Conversely, for crystals much larger than the correlation length, the change of the potential for a single ion will merely be a local perturbation, leading to the formation of a defect in the crystal.

For convenience, we also introduce the *dipole potential strength* by[3]

$$\Delta = \frac{\nu_{\mathrm{dip}}^2}{\nu_{y,c}^2} = \frac{\alpha_{\mathrm{dip}}}{\alpha_c} \,. \tag{5.2}$$

The parameters g and Δ are sufficient to describe the equilibrium positions of the crystal before and after the quench. They do not suffice, however, to describe *dynamical* properties, as the equations of motion contain the masses of the ions. Instead of specifying directly the masses of the ions, which are assumed to be equal for all the ions of the crystal, we want to introduce some dimensionless quantity which describes the effect of the mass. It is also advantageous for numerical calculations to use dimensionless units rather than SI-units. In Section 1.2.1, we already introduced a dimensionless length scaling l that is of the order of the inter-ion distance of the equilibrium

3 The squares of the trapping frequencies are given by ν_y^2 for no dipole potential present, and by $\nu_y^2 + \nu_{\mathrm{dip}}^2$ with dipole potential. We can rewrite them with the new parameters defined as $\nu_y^2 = \nu_{y,c}^2(1+g)$ and $\nu_y^2 + \nu_{\mathrm{dip}}^2 = \nu_{y,c}^2(1+g+\Delta)$.

	$^{9}Be^{+}$	$^{24}Mg^{+}$	$^{40}Ca^{+}$	$^{138}Ba^{+}$	$^{173}Yb^{+}$
$2\pi\times100\,\mathrm{kHz}$	2.2073	1.8750	1.7221	1.4009	1.3516
$2\pi\times1\,\mathrm{MHz}$	3.2398	2.7521	2.5276	2.0562	1.9839
$2\pi\times10\,\mathrm{MHz}$	4.7554	4.0396	3.7101	3.0181	2.9129

Table 5.1: Comparison of the values for $\zeta_0 \times 10^3$ for different masses and axial trapping frequencies.

configuration. Another possible way of defining a length scale is to look at the ground state properties of the crystal wavefunction. For this, we can simply take the ground state spread of the COM-mode along the x-direction, which is equal to the ground state spread of just a single ion trapped at the same frequency. This parameter, given by $\sqrt{\hbar/(2m\nu_x)}$, provides a different way of looking at the scaling of the spatial coordinates than the one given by l. As the former depends on the mass, but the latter does not, we can simply take their ratio to incorporate the mass of the ions by introducing a new parameter,

$$\zeta_0 \equiv \sqrt{\frac{\hbar}{2m\nu_x l^2}} = \sqrt{\frac{\hbar}{2}} \sqrt[3]{\frac{4\pi\epsilon_0}{q^2}} \left(\frac{\nu_x}{m}\right)^{\frac{1}{6}}. \tag{5.3}$$

This parameter essentially compares the *typical quantum length scale* of the ion Coulomb crystal, the ground state width of the COM-mode, with the *typical classical length scale*, which is of the order of the inter-ion separation. In that sense, it will characterize the "quantumness" of the probed system. Table 5.1 shows values of ζ_0 for various ion species and for different axial trapping frequencies for comparison.

This parameter only appears in a single quantity when changing to dimensionless variables, in the phase space displacements $\beta_k^{\downarrow}$'s (or via Eq. (3.33) the $\beta_k^{\uparrow}$'s), which read

$$\beta_k^{\downarrow} = \frac{1}{2\zeta_0} \sqrt{\frac{\omega_k^{\downarrow}}{\nu_x}} \frac{D_k^{\downarrow}}{l}, \tag{5.4}$$

where $\omega_k^{\downarrow}/\nu_x$ is the kth eigenfrequency normalized by the axial trapping frequency, and $D_k^{\downarrow}/l$ is the dimensionless displacement of the kth as calculated by Eqs. (3.11), (3.12) and (3.20).

Specifications of the Parameters

In the last section we have seen that a sudden quench is characterized by the initial and final values of the parameters (g_i, Δ_i) and (g_f, Δ_f). In the following we introduce further restrictions: As discussed in Chapter 4, the quench is performed by suddenly exciting the electronic

state of the central ion. As the trapping potential is not changed by this kind of quench, this leaves the initial value g_i constant, $g_f = g_i$. Moreover, the initial value of the dipole trapping strength is set to zero, $\Delta_i = 0$. In the following, we analyse quenches in which just the values of g_i and Δ_f are varied, as shown in Figure 5.2. For simplicity of notation and as there is no risk of confusion, we shall drop from now on the indices in the set of parameters, $(g_i, \Delta_i; g_f, \Delta_f) = (g_i, 0; g_i, \Delta_f) \equiv (g, \Delta)$.

As discussed in Chapter 2, the linear and zigzag crystal configurations are separated by a curve $\Gamma(\alpha, \alpha_{\text{dip}})$ in the parameter space spanned by α and α_{dip}, as shown in Figure 2.11. Equivalently, this curve can be represented in the parameter space spanned by g and Δ, which is represented in Figure 5.2. The curve $\Gamma g, \Delta$ can be represented by the equation for the critical value $\Delta_c(g)$ of the dipole potential strength as a function of the trapping strength g, derived from Eq. (2.68),

$$\Delta_c(g) = \left(\frac{8}{5\alpha_c(1+g) - 4} - 1 \right)(1+g)\alpha_c \,. \tag{5.5}$$

As we are restricting ourselves in the description of the dynamics to the second-order expanded Hamiltonian Eq. (2.28), we need to carefully choose the parameters in accordance with the harmonic approximation, which we show schematically in Figure 5.3. Close to the linear–zigzag transition the approximation of simple harmonic oscillators is not valid any more. Close to the transition, the higher-order terms in the expansion of the Hamiltonian become of the same order of magnitude for typical deviations away from the equilibrium positions, and we cannot simply neglect them in the description. In particular, the potential expanded in terms of the normal modes gives rise to a "Mexican hat"-potential for the zigzag eigenmode (Fishman et al. 2008), or it allows tunnelling between two different realizations of the zigzag configuration (Retzker et al. 2008). Neither the initial nor the final set of parameters should therefore be too close to the separation curve in Figure 5.2, as shown there by the cases (3) and (5).

Additionally, the dynamics after the quench need to be restricted as well. If the amplitude of the oscillation excited after the quench becomes of the order of the validity range of the harmonic approximation, which is of the order of the convergence radius of the Taylor series performed around the equilibrium positions, the description by simple harmonic oscillators breaks down (cf. Chapter 2). This puts an upper bound on the absolute value of Δ chosen. We therefore do not consider quenches as that of case (1) in Figure 5.3.

Further, there exists the special case when the parameters before the quench are chosen such that the crystal is a linear chain close to the transition. A sufficient large negative value of Δ results in new

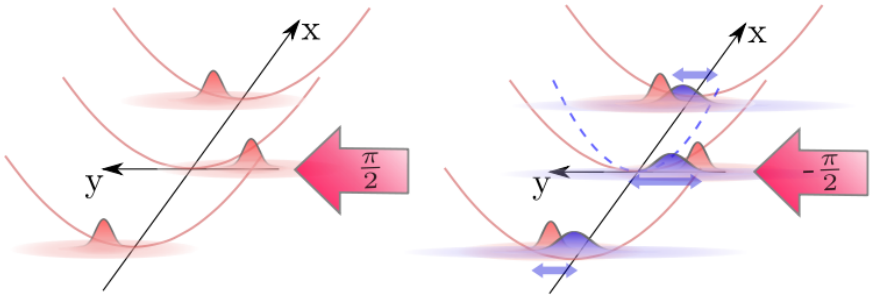

Figure 5.1 Quantum quench for an ion Coulomb crystal. (Left) The ion crystal is initially prepared in the ground state of one structural configuration. An ultra-fast pulse of electromagnetic radiation changes the electronic state of the central ion. (Right) In the new electronic state the central ion is subjected to a different potential, which also changes the motional ground state of the crystal. The motional state after the quench is therefore dynamically evolving, which affects the whole crystal via the Coulomb interaction between the ions. (Figure taken from Baltrusch, Cormick and Morigi (2013) © held by American Physical Society)

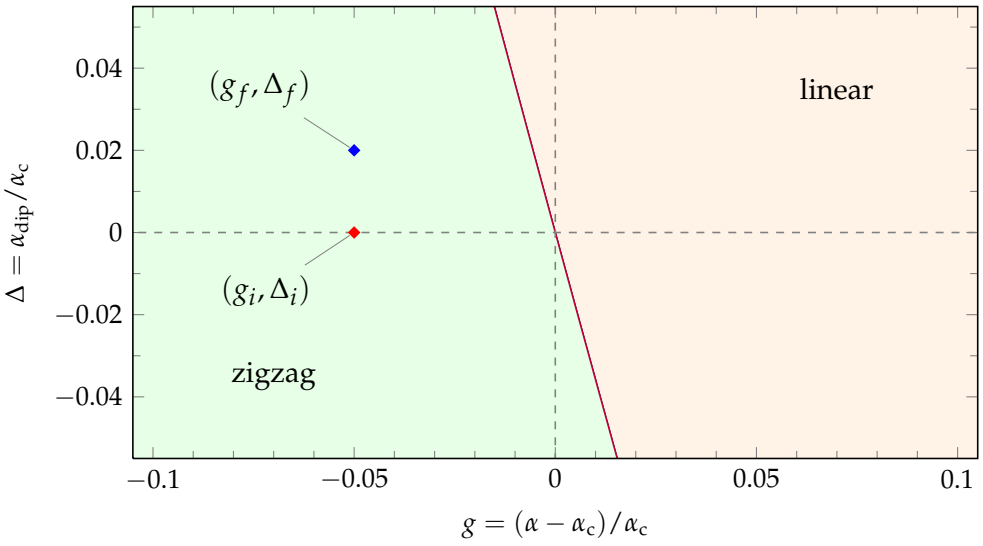

Figure 5.2 The parameter space for a quench of an ion Coulomb crystal is the structural diagram of Chapter 2, redrawn for the dimensionless parameters g and Δ. The solid red line separates the parameter regions where the ions form a zigzag (bottom left) or a linear chain (top right) for a three-ion crystal. The crystalline structure corresponding to the initial electronic state is at $\Delta = 0$. Henceforth, quenches are restricted to $g_f = g_i$ and $\Delta_i = 0$, such that a quench is described by the values of $g_i \equiv g$ and $\Delta_f \equiv \Delta$, which corresponds to the scheme discussed in Figure 5.1.

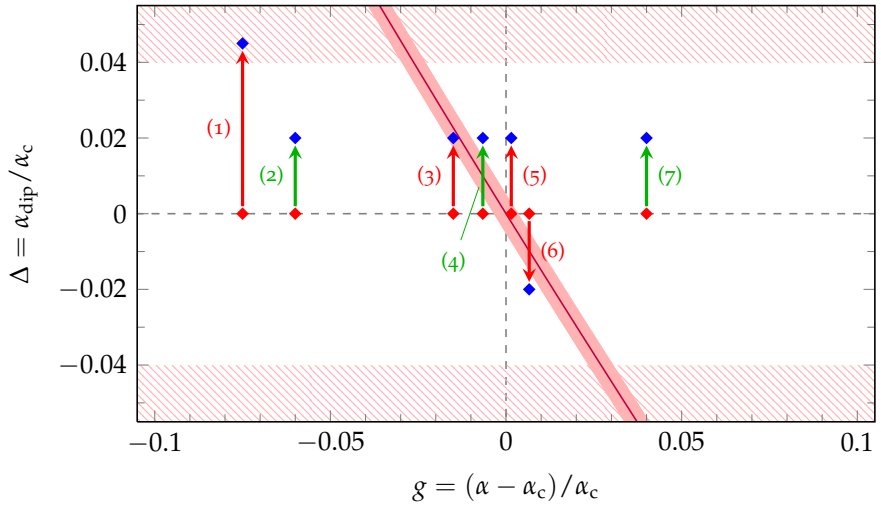

Figure 5.3: The validity region for applying a harmonic approximation approach to the quenches discussed in Figure 5.2 (schematic only). For case (1) the difference between the two equilibrium structures is too big to be able to describe the state immediately after the quench within the harmonic approximation. For (3) and (5) either the initial or the final equilibrium configuration is too close to the linear–zigzag instability (red stripe), which defies a harmonic description. For (6) the state immediately after the quench is in between two symmetric equilibrium positions and cannot be described in a harmonic framework. Subsequently only the cases (2), (4) and (7) are considered.

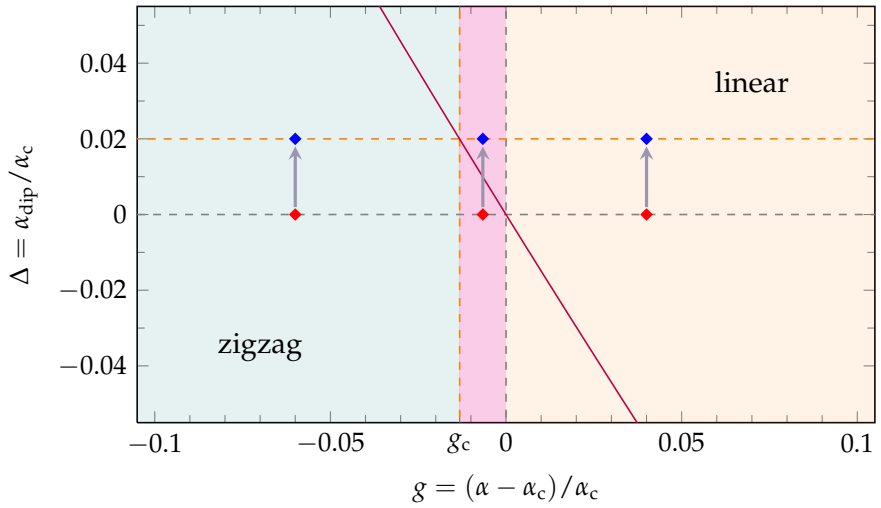

Figure 5.4: For quenches with ion Coulomb crystals in a state-dependent potential with a fixed dipole strength as described in Figure 5.2, we consider three regimes that are governed by the parameters of the states before and after the quench: (i) for $g < g_{\mathrm{c}}$, the equilibrium configuration for both initial and final parameters is a zigzag structure, (ii) for $g > 0$, the equilibrium configurations are both linear, while (iii) for $g_{\mathrm{c}} < g < 0$, the initial equilibrium configuration is the zigzag and the final configuration is the linear chain.

equilibrium positions with a zigzag structure, as shown in case (6) of Figure 5.3. But this situation does not specify the preferred alignment of this zigzag, whether the central ion is at positive or negative values with the other ions arranged in an alternating pattern. In that case, the quench actually simulates the same spontaneous symmetry breaking that is associated with the structural transition (Fishman et al. 2008). This is an interesting subject to study theoretically and experimentally, yet, in order to facilitate a theoretical description which is easy and feasible, we do not address that situation here, but rather restrict the discussion for positive values of Δ close to the transition.

Different Regimes for the Quenches

With these restrictions, we are left to examine three different scenarios for quenching the ion Coulomb crystal, as shown in Figure 5.4: First, we choose the value of the trapping strength g such that the crystal aligns as a linear chain. As we want to study quenches close to the linear–zigzag transition, the value of the trapping strength should remain sufficiently close the transition; in particular, we want the lowest eigenfrequency, which is attained by the zigzag eigenmode, to be well below the other eigenfrequencies (compare Figure 2.4). As we are restricting ourselves to positive values of Δ, the quench does not change the equilibrium positions – we have a linear chain before the quench and a linear chain afterwards. The quench only suddenly tightens the transverse trapping potential for the central ion. Classically, this situation would not induce any dynamics at all, as the ions of the crystal, which are described as point-particles, are resting at their equilibrium positions that are unchanged during the quench. However, quantum mechanically, the wavefunctions have a finite spread because of the uncertainty relation, therefore the wavefunctions will be affected by a change in the steepness of the potential. We expect for such a quantum quench to induce the dynamics of *squeezed states*, as we shall see in the following sections.

Second, we analyse quenches in which the trapping potential is such that the crystal configurations before and after are both in a zigzag structure. In that case, the equilibrium positions change and we expect a quasi-classical harmonic oscillation of the ions around their new positions, as given by the time-evolution of *coherent states*. Of course, there is also an effect of the different steepness of the trapping potential, but for the parameters we are employing in this chapter, the effect due to squeezing will be minor compared to the that of the oscillation. This can be estimated quantitatively by comparing the spread of the single ion wavefunctions with the shift between the two equilibrium positions.

Finally, in the third situation the trapping strength is smaller but close to the structural transition while still obeying the restrictions given above, i. e. being sufficiently far away from the transition to avoid any anharmonic corrections that are becoming significantly close to it. Before the quench, the crystal is in a zigzag structure, but after the quench the equilibrium positions are aligning in a linear chain configuration. The dynamics after the quench results in oscillations around the new equilibrium positions that are superimposed with a more dominant squeezing than in the case in which the quench is initiated in the region of the zigzag configuration.

In all three cases the initial state of the crystal is the motional ground state for all the normal modes. As discussed in Chapter 4, the ground state can be prepared via sub-Doppler cooling (cf. Section 4.4).[4] In order to evaluate the visibility of the Ramsey interferometry sequence discussed in Chapter 4, we apply the results from Chapter 3 for the transformation of the ground states via Eq. (3.37), trying to find an analytical expression, which we carry out in the next section.

5.2 ANALYTICAL FORMULA FOR THE VISIBILITY FOR QUENCHES OUT OF THE GROUND STATE

In this section we want to find an analytical expression for the visibility of the Ramsey experiment in which the Ramsey pulse triggers a quench of the trap frequency as described in the previous section. The formula for the visibility is evaluated by determining the absolute value of the overlap Eq. (4.24) between the initial ground state and the evolving state after the quench, which is given by

$$\mathcal{V}(t_R) = |\langle\phi_\downarrow(t_0)|\hat{U}_\downarrow^\dagger(t_R)\hat{U}_\uparrow(t_R)|\phi_\uparrow(t_0)\rangle| = |\mathcal{O}(t)|\,. \tag{5.6}$$

For the evaluation, we take the motional ground state as the initial motional state, $|\phi_\downarrow(t_0)\rangle = |0\rangle_\downarrow$.

Evaluation of the Overlap

With the help of the results from Chapter 3 we can express the initial ground state in the eigenbasis of the Hamiltonian after the quench. By doing so, the dynamics induced by the unitary operator $\hat{U}_\uparrow$ are calculated straightforwardly. Hence, using Eq. (3.37) to substitute the expressions for the ground states in the overlap matrix element, we can write the overlap as follows:

$$\mathcal{O}(t) = Z^2\,{}_\uparrow\langle 0|\,e^{\hat{A}^\dagger}\hat{D}_\uparrow^\dagger(\beta^\uparrow)\hat{U}_\uparrow(t)\hat{D}_\uparrow(\beta^\uparrow)\,e^{\hat{A}}|0\rangle_\uparrow\,. \tag{5.7}$$

4 Actually, this preparation leads to a thermal state at a very low temperature which approximately resembles the ground state, i. e. it has an overlap with the ground state close to unity.

Here we already evaluated the time evolution operator acting on the bra-vector on the left, yielding a dynamical phase which, however, we are going to omit in the following equations (as we take the absolute value in the end anyway). For evaluating this expression we first commute the displacement and exponential operators via the relation

$$\hat{\mathrm{D}}_{\uparrow}(\beta^{\uparrow})\,\mathrm{e}^{\hat{\mathrm{A}}} = \mathrm{e}^{\hat{\mathrm{A}}'(\beta^{\uparrow})}\hat{\mathrm{D}}_{\uparrow}(\beta^{\uparrow})\,, \tag{5.8}$$

where we defined the displaced $\hat{\mathrm{A}}$-operators by

$$\hat{\mathrm{A}}'(\beta) = \frac{1}{2}\sum_{jk} A_{jk}(\hat{\mathrm{b}}_j^{e\dagger} - \beta_j^*)(\hat{\mathrm{b}}_k^{e\dagger} - \beta_k^*)\,. \tag{5.9}$$

As $\hat{\mathrm{A}} = \hat{\mathrm{A}}'(0)$, we can leave the prime that labels the displaced operator out and introduce a generalized $\hat{\mathrm{A}}(\beta)$-operator defined by Eq. (5.9). When the displacement operators are applied to the ground states, we obtain coherent states $\hat{\mathrm{D}}_{\uparrow}(\beta^{\uparrow})\,|0\rangle_{\uparrow} = |\beta^{\uparrow}\rangle_{\uparrow}$ and arrive at the following expression for the overlap,

$$\mathcal{O}(t) = Z^2\,{}_{\uparrow}\Big\langle \beta^{\uparrow}\Big|\,\mathrm{e}^{\hat{\mathrm{A}}^{\dagger}(\beta^{\uparrow})}\hat{\mathrm{U}}_{\uparrow}(t)\,\mathrm{e}^{\hat{\mathrm{A}}(\beta^{\uparrow})}\Big|\beta^{\uparrow}\Big\rangle_{\uparrow}\,. \tag{5.10}$$

The evaluation of the unitary time evolution operator $\hat{\mathrm{U}}_{\uparrow}(t)$ can be simplified by inserting the representation of the identity operator in the overcomplete coherent state basis,

$$\mathbb{1} = \frac{1}{\pi^{3N}}\int \mathrm{d}^2\alpha_1 \ldots \mathrm{d}^2\alpha_{3N}\,|\alpha\rangle_{\uparrow}\langle\alpha|\,, \tag{5.11}$$

into Eq. (5.10),

$$\mathcal{O}(t) = \frac{Z^2}{\pi^{3N}}\int \mathrm{d}^2\alpha_1 \ldots \mathrm{d}^2\alpha_{3N}\;{}_{\uparrow}\langle\beta^{\uparrow}|\,\mathrm{e}^{\hat{\mathrm{A}}^{\dagger}(\beta^{\uparrow})}\hat{\mathrm{U}}_{\uparrow}(t)|\alpha\rangle_{\uparrow}\langle\alpha|\,\mathrm{e}^{\hat{\mathrm{A}}(\beta^{\uparrow})}|\beta^{\uparrow}\rangle_{\uparrow}\,, \tag{5.12}$$

which allows us to evaluate the remaining time evolution operator for the coherent state by

$$\hat{\mathrm{U}}_{\uparrow}(t)\,|\alpha_j\rangle_{\uparrow} = |\alpha_j \exp\{-\mathrm{i}\omega_j^{\uparrow} t\}\rangle_{\uparrow} =: |\alpha_j(t)\rangle_{\uparrow}\,. \tag{5.13}$$

We evaluate the two matrix elements in the integral (5.12), which yield

$$\begin{aligned}{}_{\uparrow}\langle\beta^{\uparrow}|\,\mathrm{e}^{\hat{\mathrm{A}}^{\dagger}(\beta^{\uparrow})}|\alpha(t)\rangle_{\uparrow} = \\ \exp\left\{\frac{1}{2}\sum_{jk} A_{jk}\left(\alpha_j(t) - \beta_j^{\uparrow}\right)\left(\alpha_k(t) - \beta_k^{\uparrow}\right)\right\}\;{}_{\uparrow}\langle\beta^{\uparrow}|\alpha(t)\rangle_{\uparrow}\end{aligned} \tag{5.14}$$

for the first matrix element, and

$${}_{\uparrow}\langle\alpha|\,\mathrm{e}^{\hat{\mathrm{A}}(\beta^{\uparrow})}|\beta^{\uparrow}\rangle_{\uparrow} = \exp\left\{\frac{1}{2}\sum_{jk} A_{jk}\left(\alpha_j^* - \beta_j^{\uparrow *}\right)\left(\alpha_k^* - \beta_k^{\uparrow *}\right)\right\}\;{}_{\uparrow}\langle\alpha|\beta^{\uparrow}\rangle_{\uparrow}$$

(5.15)

for the second one. Here we made use of the coherent states being eigenstates to the annihilation operator. Comparing these expressions with the diagonal matrix elements, i. e., the expectation values $\langle \cdot \rangle_\alpha =: {}_\uparrow\langle\alpha| \cdot |\alpha\rangle_\uparrow$ with respect to the coherent state $|\alpha\rangle_\uparrow$,

$$\begin{aligned}\langle \mathrm{e}^{\hat{\mathrm{A}}(\beta^\uparrow)} \rangle_\alpha &= {}_\uparrow\langle\alpha| \mathrm{e}^{\hat{\mathrm{A}}(\beta^\uparrow)} |\alpha\rangle_\uparrow \\ &= \exp\left\{ \frac{1}{2} \sum_{jk} A_{jk} (\alpha_j^* - \beta_j^{\uparrow *})(\alpha_k^* - \beta_k^{\uparrow *}) \right\}, \end{aligned} \tag{5.16a}$$

and the one with respect to the coherent state $|\alpha(t)\rangle_\uparrow$,

$$\begin{aligned}\langle \mathrm{e}^{\hat{\mathrm{A}}^\dagger(\beta^\uparrow)} \rangle_{\alpha(t)} &= {}_\uparrow\langle\alpha(t)| \mathrm{e}^{\hat{\mathrm{A}}^\dagger(\beta^\uparrow)} |\alpha(t)\rangle_\uparrow \\ &= \exp\left\{ \frac{1}{2} \sum_{jk} A_{jk} (\alpha_j(t) - \beta_j^\uparrow)(\alpha_k(t) - \beta_k^\uparrow) \right\}, \end{aligned} \tag{5.16b}$$

we can rewrite the overlap in the following form:

$$\begin{aligned}\mathcal{O}(t) = \frac{Z^2}{\pi^{3N}} \int \mathrm{d}^2\alpha_1 \ldots \mathrm{d}^2\alpha_{3N} \\ \langle \mathrm{e}^{\hat{\mathrm{A}}(\beta^\uparrow)} \rangle^*_{\alpha(t)} \, {}_\uparrow\langle\alpha(t)|\beta^\uparrow\rangle_\uparrow{}^* \, \langle \mathrm{e}^{\hat{\mathrm{A}}(\beta^\uparrow)} \rangle_\alpha \, {}_\uparrow\langle\alpha|\beta^\uparrow\rangle_\uparrow \,. \end{aligned} \tag{5.17}$$

The overlaps between the multimode coherent states yield

$${}_\uparrow\langle\alpha|\beta^\uparrow\rangle_\uparrow = \exp\Big\{ \sum_j \Big[-\frac{1}{2}|\alpha_j|^2 - \frac{1}{2}|\beta_j^\uparrow|^2 + \alpha_j^* \beta_j^\uparrow \Big] \Big\}, \tag{5.18a}$$

$${}_\uparrow\langle\beta^\uparrow|\alpha(t)\rangle_\uparrow = \exp\Big\{ \sum_j \Big[-\frac{1}{2}|\beta_j^\uparrow|^2 - \frac{1}{2}|\alpha_j(t)|^2 + \beta_j^{\uparrow *} \alpha_j(t) \Big] \Big\}, \tag{5.18b}$$

such that in Eq. (5.17) all operator expressions are now evaluated and the remaining calculation for the overlap is just a complex-valued integral in two times $3N$ dimensions.

Calculation of the Complex-Valued Integral in Eq. (5.17)

Before we can calculate the integral in Eq. (5.17) in the integration variables α_j, we first need to remove the time-dependent phase factors $\mathrm{e}^{-\mathrm{i}\omega_j t}$ from of the $\alpha_j(t)$'s in expressions (5.16) by shifting them to the coefficients A_{jk}, thereby defining

$$A_{jk}(t) \coloneqq A_{jk} \, \mathrm{e}^{-\mathrm{i}(\omega_j + \omega_k)t} \,. \tag{5.19}$$

The integrand of Eq. (5.17) contains four exponentials in the integration variables α_j and α_j^*; by merging them into a single one (now there

are only numbers in the exponents, so there is no need to employ the BCH formula), we can sort the terms inside the exponential by orders of α_j's,

$$\mathcal{O}(t) = \frac{Z^2}{\pi^{3N}} \int \mathrm{d}^2\alpha_1 \dots \mathrm{d}^2\alpha_{3N} \exp\{I_0 + I_1 + I_2\} . \tag{5.20}$$

The terms inside the exponent are

$$I_2 = \frac{1}{2} \sum_{jk} \begin{pmatrix} \alpha_j \\ \alpha_j^* \end{pmatrix}^T \begin{pmatrix} A_{jk}(t) & -\delta_{jk} \\ -\delta_{jk} & A_{jk} \end{pmatrix} \begin{pmatrix} \alpha_k \\ \alpha_k^* \end{pmatrix} , \tag{5.21a}$$

$$I_1 = -\sum_j S_j[\beta^*]\alpha_j^* - \sum_j S_j[\beta]\, \mathrm{e}^{-\mathrm{i}\omega_j t}\alpha_j , \tag{5.21b}$$

$$I_0 = G^*(\beta) + G(\beta) , \tag{5.21c}$$

where we defined the shorthands

$$S_j[\beta] = \sum_k A_{jk}\beta_k - \beta_j^* , \tag{5.22}$$

and

$$G(\beta) = \sum_{jk} \frac{A_{jk}}{2}\beta_j^*\beta_k^* - \sum_j \frac{|\beta_j|^2}{2} . \tag{5.23}$$

For the integration, we change to real and imaginary parts of the integration variables, $\alpha_j = u_j + \mathrm{i}v_j$ and $\alpha_j^* = u_j - \mathrm{i}v_j$. Reordering the terms according to this representation, the quadratic terms read

$$I_2 = -\sum_{jk} \begin{pmatrix} u_j \\ v_j \end{pmatrix}^T \begin{pmatrix} \delta_{jk} - \Lambda_{jk}^+ & -\mathrm{i}\Lambda_{jk}^- \\ -\mathrm{i}\Lambda_{jk}^- & \delta_{jk} + \Lambda_{jk}^+ \end{pmatrix} \begin{pmatrix} u_k \\ v_k \end{pmatrix} , \tag{5.24a}$$

with complex symmetric $3N \times 3N$-matrices defined by

$$\Lambda_{jk}^{\pm} = \frac{1}{2}\big(A_{jk}(t) \pm A_{jk}(0)\big) . \tag{5.24b}$$

The linear term in the new integration variables u_j and v_j has the form

$$I_1 = -\sum_j \left[S_j^+ u_j - \mathrm{i}S_j^- v_j\right] , \tag{5.25a}$$

with

$$S_j^{\pm} = S_j[\beta^*] \pm S_j[\beta]\, \mathrm{e}^{-\mathrm{i}\omega_j t} . \tag{5.25b}$$

By combining all integration variables into the $6N$-dimensional vector $\mathbf{w}^T = (\mathbf{u}^T, \mathbf{v}^T)$, with $\mathbf{u}^T = (u_1, \dots, u_{3N})$ and $\mathbf{v}^T = (v_1, \dots, v_{3N})$, the overlap integral is written in the following compact form,

$$\mathcal{O}(t) = \frac{Z^2}{\pi^{3N}}\, \mathrm{e}^{G^*(\beta)} e^{G(\beta)} \int \mathrm{d}\mathbf{w}\ \mathrm{e}^{-\mathbf{w}\cdot\mathbf{s} - \mathbf{w}^T\Omega\mathbf{w}} , \tag{5.26a}$$

with

$$\mathbf{s} = \begin{pmatrix} \mathbf{S}^{+} \\ -\mathrm{i}\mathbf{S}^{-} \end{pmatrix}, \qquad \Omega = \begin{pmatrix} 1-\Lambda^{+} & -\mathrm{i}\Lambda^{-} \\ -\mathrm{i}\Lambda^{-} & 1+\Lambda^{+} \end{pmatrix}. \tag{5.26b}$$

The result of this Gaussian integral for the complex symmetric matrix Ω is given by (cf. Appendix D)

$$\int \mathrm{d}\mathbf{w}\, \mathrm{e}^{-\mathbf{w}\cdot\mathbf{s}-\mathbf{w}^{T}\Omega\mathbf{w}} = \sqrt{\frac{\pi^{6N}}{\det\Omega}}\, \mathrm{e}^{\frac{1}{4}\mathbf{s}^{T}\Omega^{-1}\mathbf{s}}, \tag{5.27}$$

such that we can write the final result as

$$\mathcal{O}(t) = \frac{Z^{2}}{\sqrt{\det\Omega}}\, \mathrm{e}^{2\,\mathrm{Re}\{G(\beta)\}}\, \mathrm{e}^{\frac{1}{4}\mathbf{s}^{T}\Omega^{-1}\mathbf{s}}. \tag{5.28}$$

This allows us to analytically calculate the visibility for any given value and time.

Convergence of the Integral

While evaluating the Gaussian integral in Eq. (5.27), we implicitly assumed that it is converging. To justify this, we need to show that the real parts of the eigenvalues of the matrix Ω are all greater than zero. As we can write the matrix Ω as $\Omega = 1 - \mathrm{B}$, with

$$\mathrm{B} = \begin{pmatrix} \Lambda^{+} & \mathrm{i}\Lambda^{-} \\ \mathrm{i}\Lambda^{-} & -\Lambda^{+} \end{pmatrix}, \tag{5.29}$$

we see that it is equivalent to showing that the eigenvalues of the matrix B are bounded by one. To this end we consider the spectral radius of the matrix B, given by

$$\rho(\mathrm{B}) = \max_{\{\lambda_B\}}\{|\lambda_{\mathrm{B}}|\}, \tag{5.30}$$

where $\{\lambda_{\mathrm{B}}\}$ is the set of eigenvalues of B. The spectral radius fulfils the following inequality

$$\rho(\mathrm{B}) \leq \|\mathrm{B}\|, \tag{5.31}$$

for *any* matrix norm $\|\cdot\|$ (Horn and Johnson 1985, Theorem 5.6.9, p. 297). So if we have $\|\mathrm{B}\| < 1$, we know that all eigenvalues of B are confined inside a circle centred around zero with a radius of $\rho(\mathrm{B}) < 1$. As B is complex symmetric in its blocks, we can use Takagi's factorization (Horn and Johnson 1985, Corollary 4.4.4, pp. 204f.) to bring it to a block-diagonal form using an unitary matrix U_{B},

$$\mathrm{B} = \frac{1}{2}\begin{pmatrix} 1 & 1 \\ \mathrm{i} & -\mathrm{i} \end{pmatrix}\begin{pmatrix} \mathrm{A}(t) & 0 \\ 0 & \mathrm{A} \end{pmatrix}\begin{pmatrix} 1 & \mathrm{i} \\ 1 & -\mathrm{i} \end{pmatrix} = \mathrm{U}_{\mathrm{B}}\mathrm{D}_{\mathrm{B}}\mathrm{U}_{\mathrm{B}}^{T}, \tag{5.32}$$

and use the sub-multiplicativity property of matrix norms (Horn and Johnson 1985, Sec. 5.6, p. 290),

$$\|B\| = \|U_B D_B U_B^T\| \leq \|U_B\| \, \|D_B\| \, \|U_B^T\| \, . \tag{5.33}$$

As we are free to use any matrix norm for the inequality (5.31), we can use the spectral norm for convenience, defined by

$$\|A\|_2 := \max\{\sqrt{\lambda} : \lambda \text{ is an eigenvalue of } A^\dagger A\} \, . \tag{5.34}$$

Since unitary matrices generally have a spectral norm of 1, the spectral norm of B is bounded by the spectral norm of D_B by virtue of inequality (5.33). As D_B is block-diagonal, the spectral norm of D_B is given by the maximum of the spectral norm of the two block matrices A and $A(t)$,

$$\|D_B\|_2 = \max\{\|A(t)\|_2, \|A\|_2\} \, . \tag{5.35}$$

The spectral norm of $\|B\|_2$ is bounded from above by the spectral norm of the matrix $\|A\|_2$, since the spectral norm of the two matrices is equal, $\|A(t)\|_2 = \|A\|_2$.

In order to show the convergence of the integral in Eq. (5.27) we need to show that the spectral norm of A is bounded by 1, which is guaranteed by the results from Appendix C.

5.3 ANALYSIS OF QUENCHES OUT OF THE GROUND STATE

In this section we analyse the properties of the visibility of the Ramsey fringes after the quench with the crystal motion initially prepared in the motional ground state. We first describe the kind of visibility one would expect for the different parameters in Section 5.3.1. Then we take a closer look at the different properties of the visibility, such as the time of the first revival, the short-time decay, the behaviour for long times, and the Fourier properties of the visibility.

Numerical Evaluation

The visibility is given by the analytical formula derived in Section 5.2, which is in the following evaluated via the scientific programming environment MATLAB. The numerical evaluation is necessary since the analytical form of the eigenmodes for a three-ion crystal in the zigzag configuration is, though analytically feasible, too involved to be practical for further analytical processing as demanded by the formula of the visibility, Eq. (5.28). For bigger ion crystals an analytical formula for the eigenmodes is not feasible anyway, so that we determine the eigenmodes numerically and evaluate Eq. (5.28) by including the formula directly into the code of the algorithm. All of the plots in this chapter are generated by this procedure.

5.3.1 *General Form of the Visibility Close to the Linear–Zigzag Transition*

We want to determine the dependence on the initial crystal configuration, so we examine the visibility for different trapping strengths g (see Section 5.1.3 and the discussion in Chapter 2). As discussed before, there are three different regimes in which we can analyse the quench: First the linear regime, in which the value of the trapping strength is $g > 0$, the crystal is in a linear chain configuration both before and after the quench. Second the zigzag regime, with $g < g_c(\Delta, N)$ such that the initial and final equilibrium configurations are both a zigzag configuration. And the third regime in which the initial equilibrium configuration of the crystal is in a zigzag structure and the final configuration is a linear chain, i. e. $g_c < g < 0$.

As we shall see in the plots of the evaluation, for a domain of the zigzag regime which is very close to the linear–zigzag instability the visibility will have a very similar form to that of the third regime. Thus we restrict the zigzag regime to values of g just below $g_c - \epsilon$, with $\epsilon > 0$ some constant, and add this interval to the third regime and treat these cases together. A reasonable estimate for ϵ is the absolute value of $g_c < 0$, so that this regime is bounded by $g < 2g_c$. Therefore we define the third regime, which is close to the instability, as lying in the interval $2g_c < g < 0$. We shall therefore analyse the following three regimes:

(a) the linear regime for $g > 0$,

(b) the zigzag regime for $g < 2g_c$,

(c) the regime close to the transition for $2g_c < g < 0$.

The behaviour of the visibility in these regimes is discussed in the next sections.

Linear Regime

In the linear regime for $g > 0$ the central ion is always trapped *more tightly* after the quench; this is due to the restriction to positive values of the dipole potential $\Delta > 0$ only. Therefore, the structure after the quench remains a linear chain, more specifically, the equilibrium positions before and after the quench are *perfectly identical*. The only parameter changing is the transverse confinement of the central ion. Thus, in the case of classical dynamics we would not expect any motion to be excited at all. Yet, in a quantum mechanical description we anticipate a dynamical evolution because of the sudden tightening of the potential. The ground state wavefunction of the initial state is not the ground state for the new parameters any more, and we expect the spread of the wavefunction to be evolving in time.

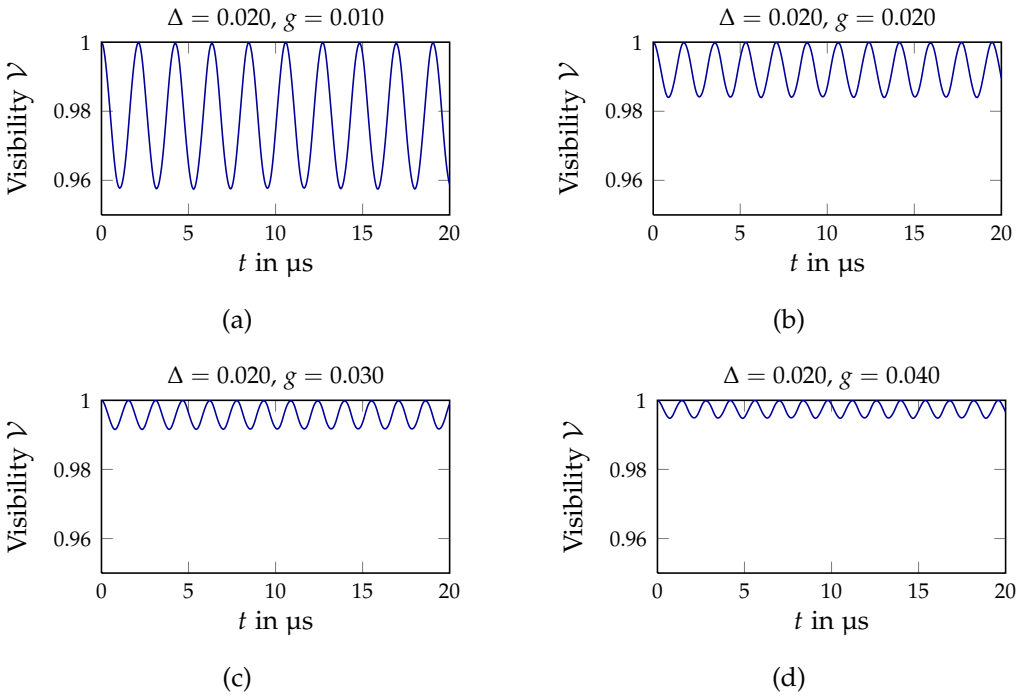

Figure 5.5: Visibility as a function of the time t between the two Ramsey pulses for three $^9Be^+$ ions, where the axial trapping frequency is given by $2\pi \times 1\,\mathrm{MHz}$. In all plots the crystal is prepared in a linear chain configuration before the quench, and the dipole strength is chosen to be $\Delta = 0.020$ while the transverse trapping strength g is varied.

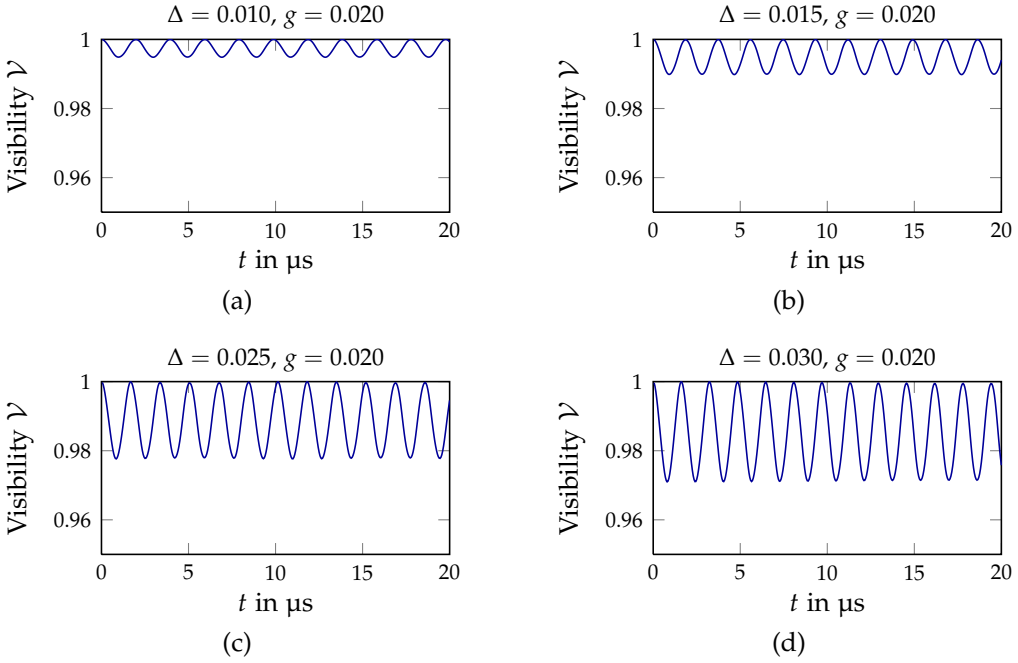

Figure 5.6: Visibility as a function of time between the Ramsey pulses for varied dipole strength Δ. The transverse trapping strength is held fixed at $g = 0.020$, while the other parameters are chosen identical to those in Figure 5.5.

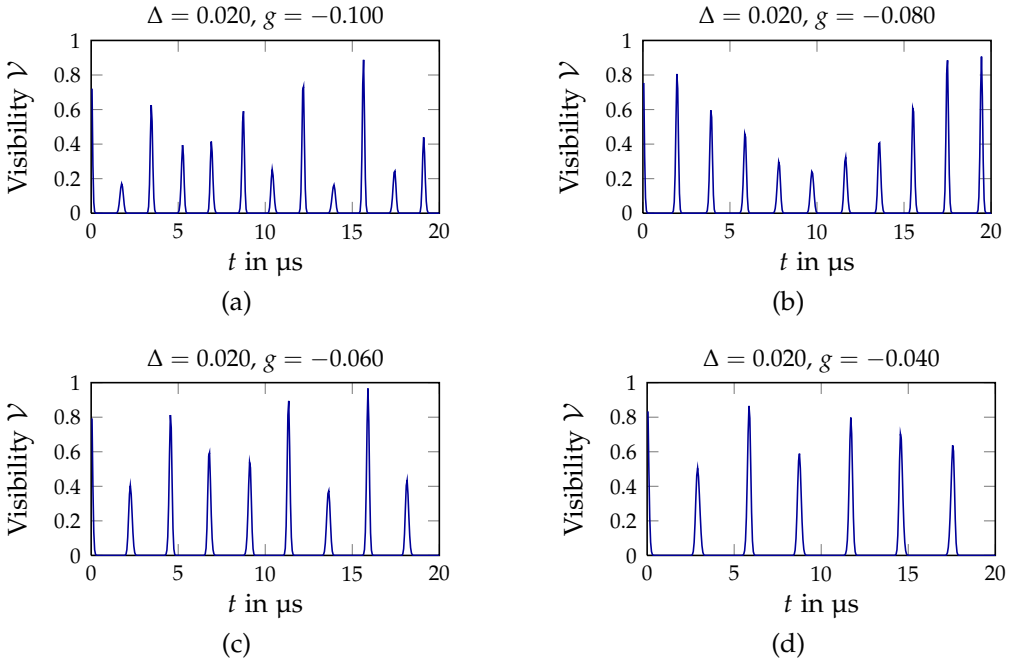

Figure 5.7: Visibility between the pulses for varied g as in Figure 5.5, but now the crystal state is initially prepared in a zigzag configuration.

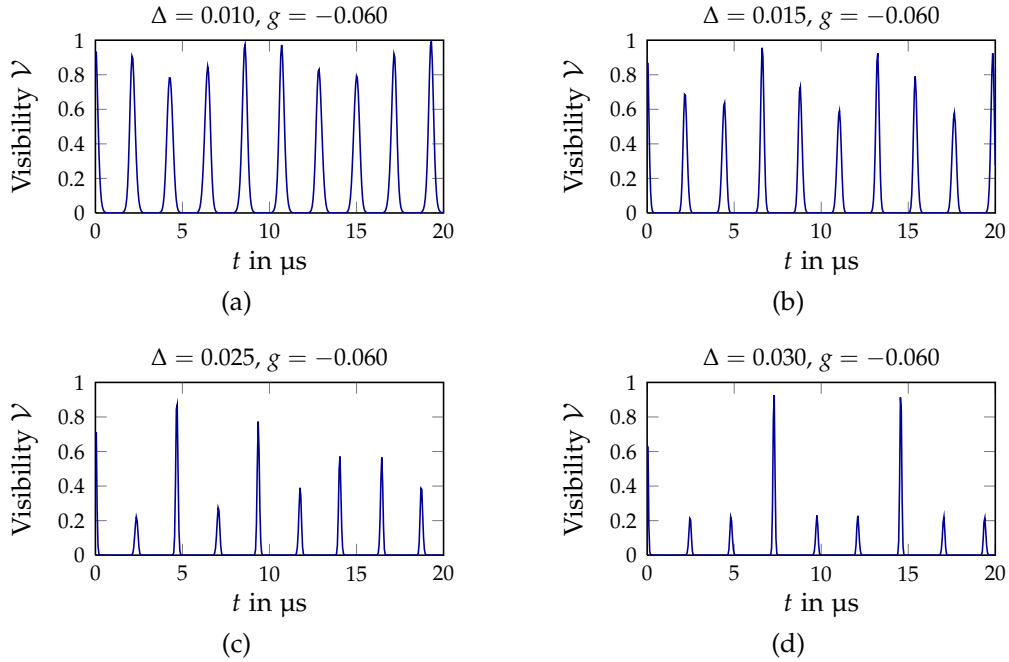

Figure 5.8: Visibility between the Ramsey pulses for varied dipole strength Δ as in Figure 5.6 but in the zigzag regime at a fixed value of $g = -0.060$.

Indeed, the calculated visibility as a function of the time between the two Ramsey pulses can be explained by such a dynamical evolution, as we can see in Figure 5.5. In all plots, the visibility is always close to unity with some sinus-like oscillation on top. The origin of this oscillating modulation comes from the sudden tightening of the confining potential: The wavefunction before the quench was described by the ground state wavefunction with a definite spread in the positions and momenta; in the sudden approximation (cf. Chapter 4) the wavefunction remains unchanged in its initial form. Yet, this state has now a considerably higher spread in the positions and a lower spread in the momenta compared to the new ground state wave function; this state turns out to be a multi-mode (momentum-)squeezed state. Such a state has an evolution for which the spread in the positions is oscillating around the value of the spread of the new ground state. We shall see in the following pages that this squeezing is, for the parameters and constraints considered, dominated by the single-mode squeezing of one specific mode, the zigzag mode.

In the subplots of Figure 5.5 we show the visibility for different values of the trapping strength g. By increasing the trapping strength, the amplitude of the oscillation decreases but its frequency increases. For higher trapping strengths, the relative effect of the dipole potential becomes smaller such that the amount of squeezing immediately after the quench is reduced, thus explaining the decreasing amplitude.

Next, in Figure 5.6, we examine the dependence of the visibility on the strength of the dipole potential. Here we see an increase of both the amplitude and the frequency of the modulating visibility for higher Δ. The amplitude is rising for a stronger quench as the wavefunction gets increasingly squeezed through the change of the confinement. The frequency is increasing as a stronger quench with larger Δ puts the final state farther away from the transition boundary shown in Figure 5.2. If the new state is farther away from the transition boundary its zigzag eigenfrequency will increase, and with it the frequency of the oscillating modulation of the visibility.

Zigzag Regime

When the crystal is prepared in a zigzag configuration before the quench, the visibility has a seemingly different behaviour. In Figure 5.7 the visibility as a function of time between the Ramsey pulses is shown for various values of g. The visibility is quickly decaying (on a time scale shorter than 1 µs) to a value practically indistinguishable from zero on the plot scale, while at definite and periodic times a series of revivals appears. The height of these revivals is in general clearly below unity and varies from peak to peal, depending on the parameters. We see further that in some cases the height of the revivals

apparently follows some rule, as in Figure 5.7b, while at other values of g no regularity is obvious. As the value of g moves toward 0, the time between the revivals grows and the peaks get slightly wider. We shall see later that as the trapping strength comes even closer the critical value g_c, these revivals become double-peaked; we discuss this case in Figure 5.9 and in the next section together with quenches across the transition.

In Figure 5.8 we examine the properties of the visibility for varied dipole strength Δ. For weak quenches, i. e. small values of the dipole strength Δ, the variation in the height of the revivals is less than for larger quenches. The width of the revivals becomes narrower as the strength of the dipole potential is increased, and the distance between the peaks also increases slightly.

The main functional behaviour of the visibility in the zigzag regime can be explained by the oscillatory dynamics resulting from the sudden change of equilibrium positions for all the ions, which is following the classical dynamics. This oscillatory dynamics is governed by the interplay of different normal modes, by which we can also explain the specific properties of the details of the visibility: For these parameters, the total overlap is dominated by the contribution from the terms (5.18), which can be regarded as the product of the individual overlapping wavefunctions of coherent states for each of the normal modes. As we shall show later, the dominant contribution comes from a single mode, the zigzag mode, which determines the appearance of the main peaks. The height of the peaks and the degree of regularity of the height of the peaks can be explained by the interplay of different modes. The separate overlap factors for each of the normal modes in Eqs. (5.18) exhibit revivals at the respective eigenfrequency, therefore the total overlap will be governed by the interplay of all these revivals. Therefore, the total overlap and thus the visibility will be larger for the cases in which revivals of separate modes are closer together. In the case of weaker quenches the wavepackets do not become so far separated from each other during the evolution, so that the peaks of the visibility become wider.

Quenches Close to the Linear–Zigzag Instability

Figure 5.9 displays the visibility when the final state of the quench moves closer to the linear–zigzag instability and when it finally crosses it, taking the restrictions of the previous section into account. In Figure 5.9a the peaks of the visibility already show small subpeaks, which turn into double peaks for Figures 5.9b, 5.9c and 5.9d. These double peaks can become separate as in Figure 5.9d, in which minor tertiary and even quaternary peaks become recognizable as well. The distance between the (double) peaks is also increasing for g moving

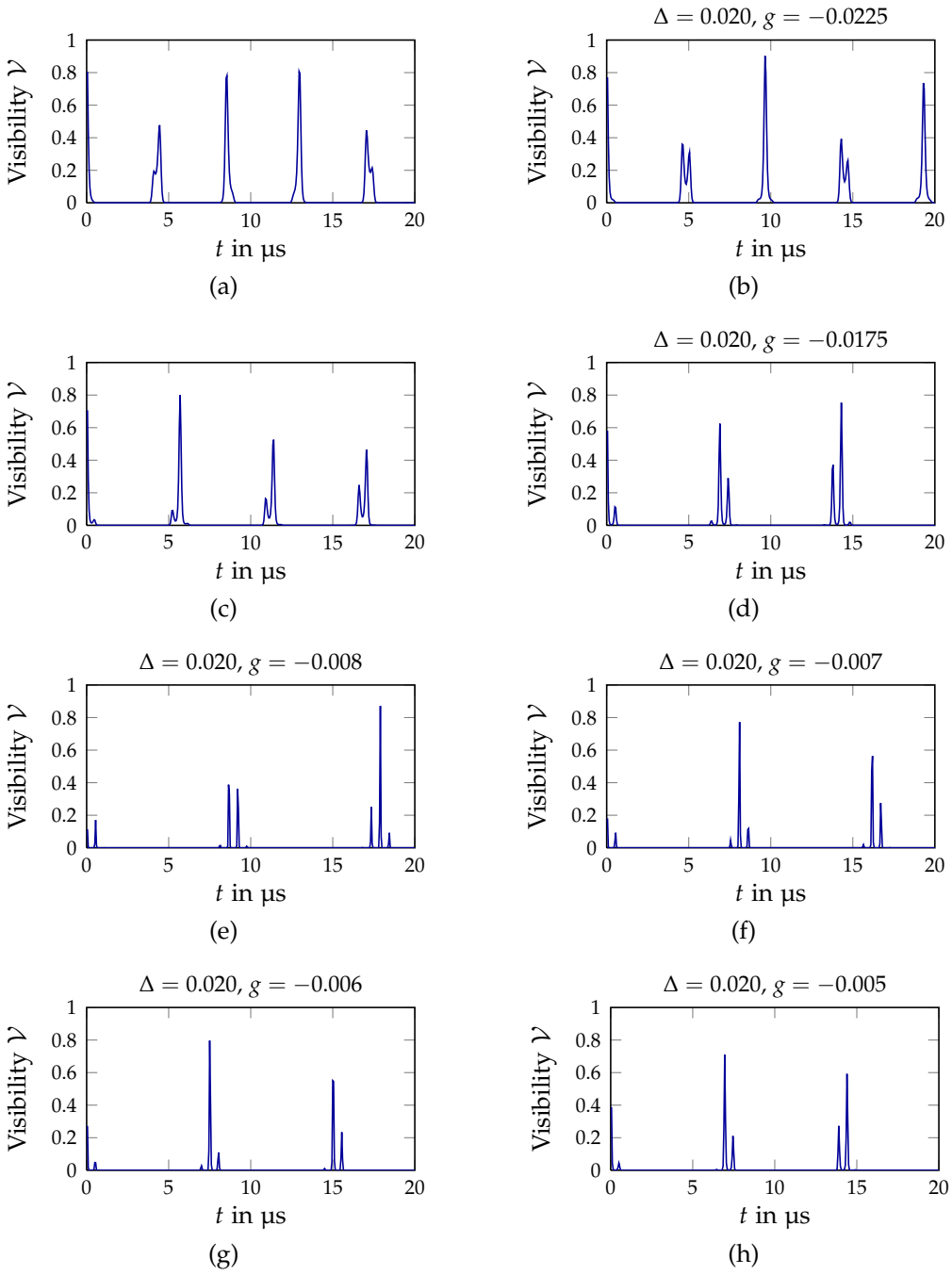

Figure 5.9: Visibility as in the previous figures in the regime where the quench is close to the linear–zigzag instability. In (a) to (a), the quench for both initial and final configurations remains in the zigzag regime. For (e) to (h), the structure before the quench is a zigzag configuration, while after the quench the ions are oscillating around the equilibrium positions of the linear chain.

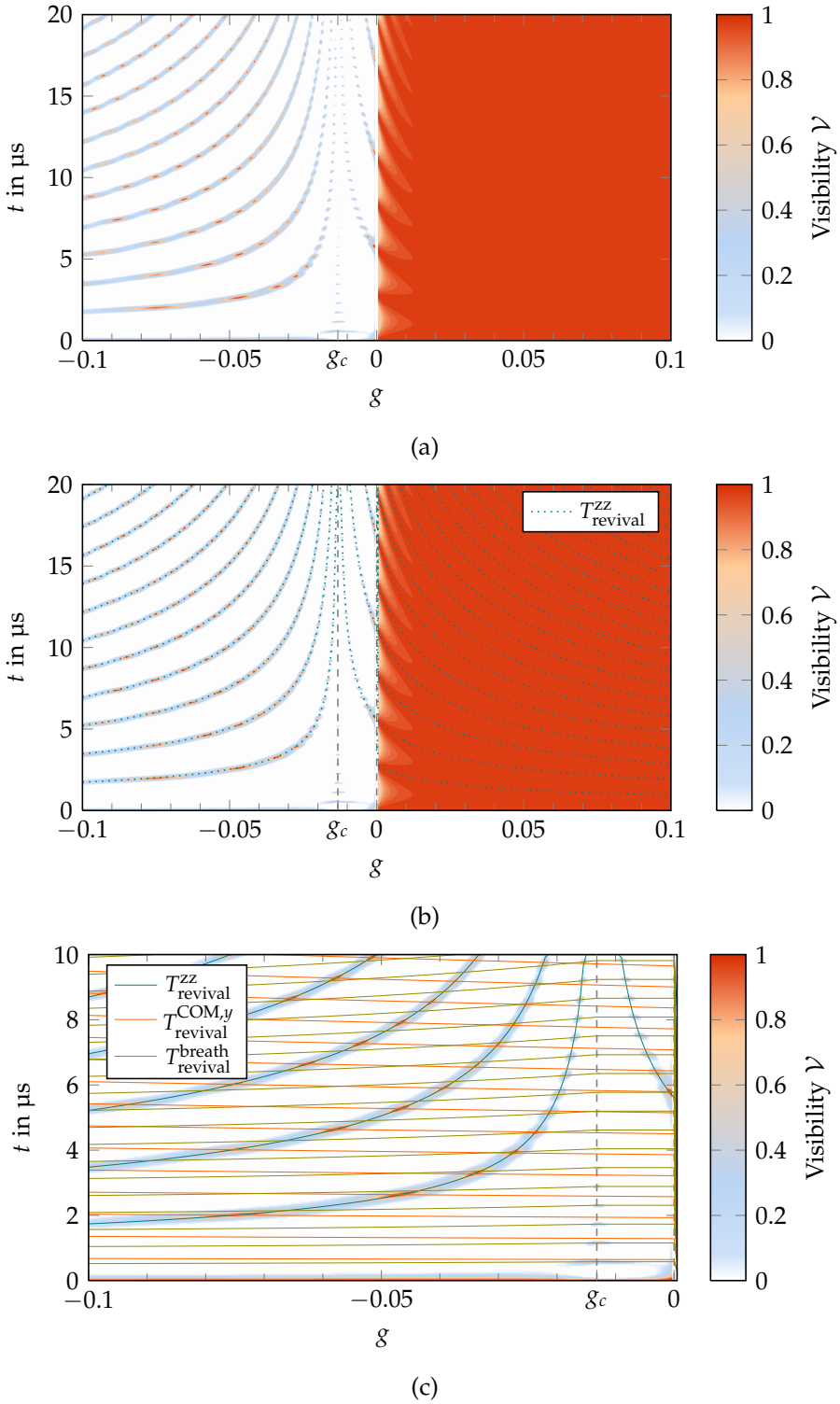

Figure 5.10: (a) Density plot of the visibility as a function of the trapping strength g and the time t (in μsec) evolved in between the two Ramsey pulses for $\Delta = 0.020$. The other parameters are the same as in Figure 5.2. (b) compares the revival times of the zigzag mode overlaid onto the visibility. (c) also shows the revival times of other modes in the zigzag regime. The crossing points coincide with the local maxima along the main peaks of the visibility.

towards g_c. For values of g closer to g_c, we are approaching the regime where the harmonic approximation fails to provide a correct description of the dynamics.

Next, Figures 5.9e–5.9h show plots of the visibility when the initial equilibrium configuration before the quench is still in the zigzag regime, while the final state will be oscillating around a linear equilibrium configuration, in accordance with the discussion of Section 5.1.3. In this regime, we see that the visibility shows fast decay and periodic revivals which are composed of a series of peaks. So in this regime the functional behaviour of the visibility is very similar to the one in which the equilibrium positions of the final parameters of the quench are in the zigzag regime. But this comes as no surprise when recognizing that both cases induce an oscillatory behaviour around some new equilibrium positions; it is not of importance that they belong to different types of crystal structures. In both cases, the main contribution comes from the oscillation of the COM motion, while the squeezing contributes to a much smaller degree.

Comparison of the Different Regimes of the Visibility

For a more systematic analysis of the visibility we compare the form of the visibility as a function of the time elapsed between the pulses and of the trapping strength, while keeping the dipole strength constant. In order to make this comparison, we display the data in a density plot, shown in Figure 5.10a, where the value of the visibility is colour-coded, the time evolved is plotted along the y-axis, and the values of the trapping strength g are along the x-axis. The previous plots for the same value of the dipole strength Δ in Figures 5.5, 5.7, and 5.9 would correspond here to vertical cuts in the figure at the corresponding value of g.

In this plot we also include values of g which are too close to the linear–zigzag instability for the harmonic approximation to be valid; therefore, the plot does not show the actual visibility of a quench with an ion Coulomb crystal but rather that of a multidimensional harmonic oscillator model with the normal mode frequencies as oscillator frequencies. In an experiment we therefore expect a deviant behaviour for the parameter domain where the harmonic approximation is invalid.

In the density plot of Figure 5.10a we can clearly distinguish two different regions which are separated at $g = 0$ vertically. In the first region, for $g < 0$, where the initial configuration is a zigzag structure, the visibility is most of the time close to zero with several revivals. The revivals are continuously appearing at later times as g increases up to the value g_c, the point at which the revival time diverges. Later revivals always occur on approximately multiples of the first one.

To further investigate the properties of the revivals, we show in Figure 5.10b the same plot with the revival times of the zigzag mode of the final configuration overlaid. By the revival time we mean the time when the overlap of the quantum state of the zigzag mode is regaining its original distribution in phase space. For instance, for an oscillation of a coherent state, this time will be the period time of the corresponding classical oscillation, while a squeezed state returns to its initial state within half of a period of the classical oscillation. Therefore, we define the revival times by

$$T^{\mathrm{zz}}_{\mathrm{revival}} = \begin{cases} 2n\pi/\omega_{zz} & \text{for } g < 0\,, \\ n\pi/\omega_{\mathrm{zz}} & \text{for } g > 0\,, \end{cases} \quad \text{with } n = 1,2,3,\ldots \tag{5.36}$$

Here we take half the period time for the linear regime in which we expect squeezing dynamics.

In comparing these times with the visibility in Figure 5.10b, we see that for all values of n they are located exactly on top of the local maxima of the visibility along the time dimension. This is a strong indication that the main revivals' appearance is governed by the zigzag mode.

While the curves of the occurrence of the revivals appear to be continuous as a function of g, the height of the revivals varies along these curves. The cause for this is rooted in the interplay of the zigzag mode with other modes; while the zigzag mode has completed a full period, or multiples thereof, the other relevant modes usually have not completed an integer number of periods. Thus we expect the visibility along these curves to peak only at coincidental resonances with the other modes.

To check this assertion we have replotted the relevant region of the zigzag regime in Figure 5.10c and have overlaid this with the revival times of two other relevant modes. These are the COM-mode in y-direction and the breathing mode, see Figure 2.3 for an illustration. For these modes, we define $T^{\mathrm{COM},y}_{\mathrm{revival}}$ and $T^{\mathrm{breath}}_{\mathrm{revival}}$ analogously to Eq. (5.36) with ω_{zz} replaced by $\omega_{\mathrm{COM},y}$ and by ω_{breath}, respectively (only for $g < 0$). The other modes do not contribute because of the symmetry of the excitation created by the state-dependent potential.

In the plot the revivals closely follow the zigzag revival time, as shown before. The main revivals display local maxima exactly at the crossing points of the zigzag revival time with the revival times of other modes. For the ion crystal deep in the zigzag regime, these maxima regularly occur at the points where the revivals of the zigzag and the COM-mode in y-direction coincide; closer to the linear–zigzag instability the local maxima of the revivals are located at the crossing points of the zigzag and the breathing mode revival times (there may be coincidences of all three revival times falling together, too). At the

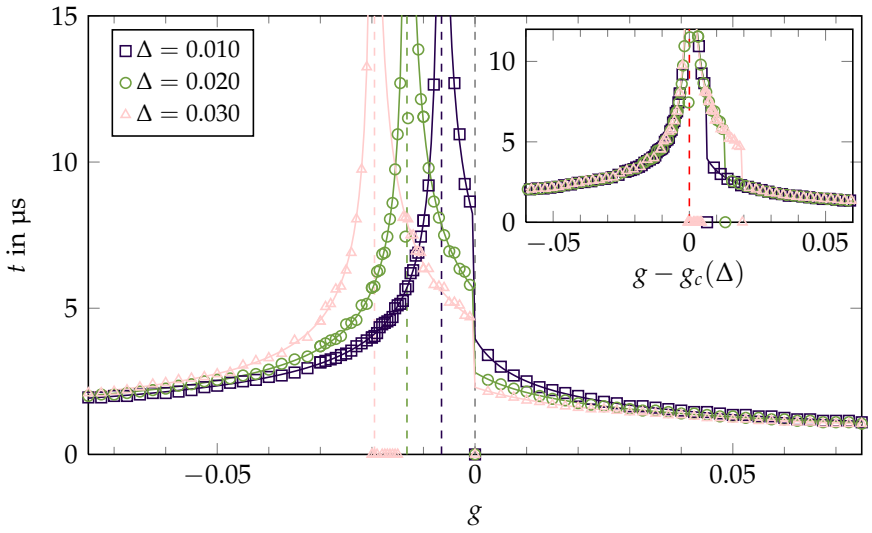

Figure 5.11: Comparison of the revival times for $g < 0$ and the periods of the modulation for $g > 0$ for different values of the dipole strength Δ. The other parameters are chosen identically to those in the previous figures. The symbols are the peak times determined by a numerical routine, and the lines determine the time of the period of the zigzag eigenfrequencies for $g < 0$ and half that time for $g > 0$. The values of $g_c(\Delta)$ are displayed as vertical dashed lines. In the inset, the same plot is shown with the origin of the x-axis shifted to $g_c(\Delta)$.

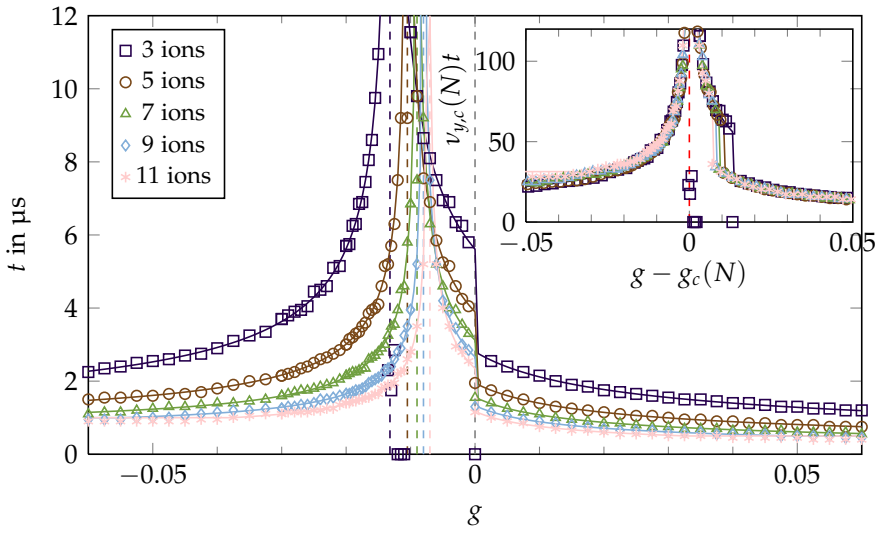

Figure 5.12: Comparison of the revival times for $g < 0$ and the periods of the modulation for $g > 0$ for different ion numbers. For all curves, the dipole strength is $\Delta = 0.020$, while the remaining parameters are chosen as before. The symbols are the peak times determined by a numerical routine, and the lines determine the time of the period of the zigzag eigenfrequencies for $g < 0$ and half the time for $g > 0$. The values of $g_c(N)$ are displayed as vertical dashed lines. In the inset, the same plot is shown with the origin of the x-axis shifted to $g_c(N)$ and the time axis rescaled by $\nu_c(N)$.

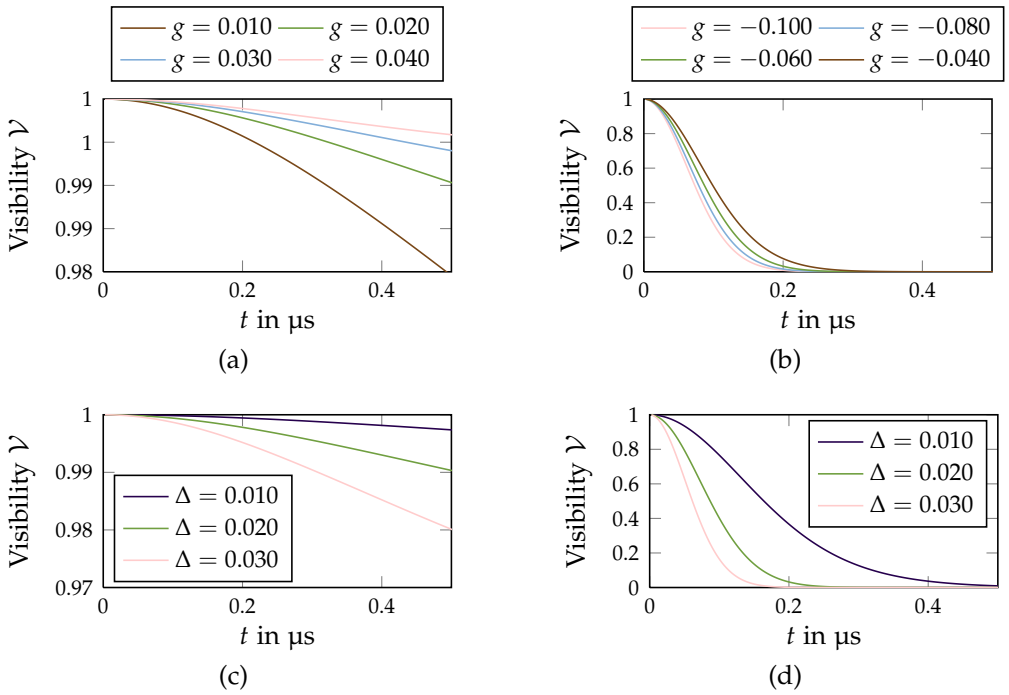

Figure 5.13: Short-time behaviour of visibility. The visibility is plotted for the fixed value of $\Delta = 0.020$ for different values of the transverse trapping g in the linear (a) and the zigzag regime (b). The visibility is plotted for various values of Δ for a fixed value of $g = 0.020$ in the linear (c), and for $g = -0.060$ in the zigzag regime (d).

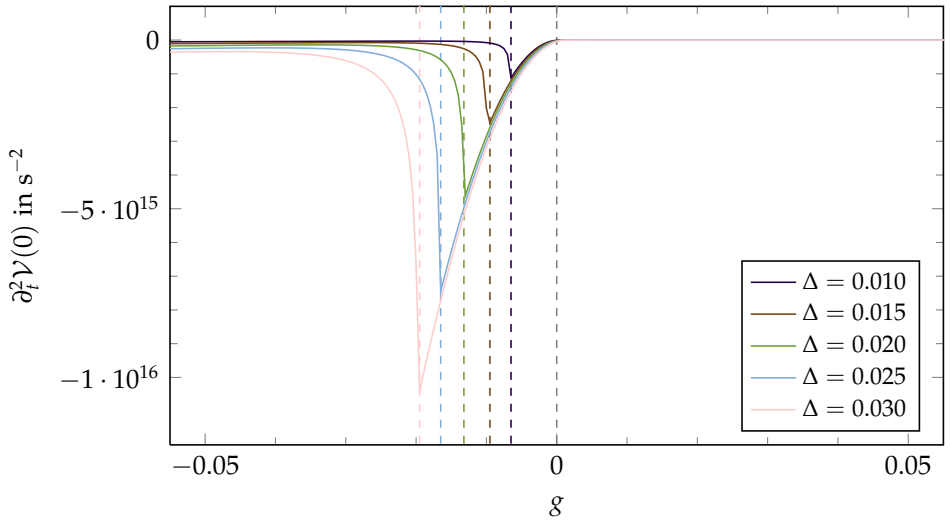

Figure 5.14: Numerically calculated approximate second derivative of the visibility at $t = 0$ for varied values of Δ as a function of the transverse trapping g . All curves are for three $^9Be^+$ ions with 1 MHz axial trapping frequency.

regime close to the instability we can also identify the cause for the appearance of double peaks: A vertical cut in this diagram crosses several peaks resulting from the crossing of revival times of different modes and different order.

The second region in Figure 5.10a is identified for $g > 0$ with the initial configuration being a linear chain. Here, the visibility is for the main part close to unity. Close to $g = 0$ there are modulations showing up which become more pronounced as they approach the boundary. Also, their frequency of modulation is decreasing as $g \to 0$. Again, we can overlay the time period of the zigzag eigenmode on this graph as before. Yet, we choose here to overlay it with only half of the period, as the revival times are half the oscillation periods for pure squeezing dynamics. And indeed, in Figure 5.10a the time of the first local maximum of the visibility coincides with the plotted overlay. Here, the influence of the other modes is negligible as no features at other time scales are distinguishable in the plot.

Next we examine the times of the first revivals for $g < 0$ and the first maximum for $g > 0$ for different values of the dipole strength Δ. In the main plot, the times of the first peaks for both regions are determined by a numerical routine (O'Haver 2011) and plotted as symbols for different values of Δ. These data points are then compared for $g < 0$ to the period time of the zigzag eigenmode and for $g > 0$ to half the period time of the zigzag eigenmode, with the curves matching the data points. For the decreasing values of the dipole strength Δ, the value of the critical trapping strength $g_c(\Delta)$ is shifted closer to zero, and with it the divergences of the various curves. In the inset of the figure, we have replotted the same graphs with the origin of the x-axis shifted to the respective value of $g_c(\Delta)$; in this graph the three curves all fall closely together, as the dependence of the zigzag eigenfrequency is approximately identical for all values of Δ.

5.3.2 *Short-Time Behaviour of the Visibility*

We now analyse the short-time behaviour of the visibility. For this, we first look at the expansion of the modulus of the overlap for times around $t = 0$, where t is the time between the Ramsey pulses. First, we expand the overlap as

$$\mathcal{O}(t) \approx 1 - \mathrm{i}\mathcal{O}_1 t - \frac{1}{2}\mathcal{O}_2 t^2 , \tag{5.37}$$

where the quantities $\mathcal{O}_1 = \mathrm{d}\mathcal{O}(0)/\mathrm{d}t$ and $\mathcal{O}_2 = \mathrm{d}^2\mathcal{O}(0)/\mathrm{d}t^2$ are the first two time derivatives of $\mathcal{O}(t)$ evaluated at $t = 0$. Then the expansion of the visibility is directly calculated to be

$$\mathcal{V}(t) \approx 1 + \eta t^2/2 , \tag{5.38}$$

where we identified the curvature $\eta < 0$ as $\eta = -(\mathcal{O}_2 - \mathcal{O}_1^2)$.

As it turns out, the curvature of the decay of the visibility at very short time intervals already allows us to infer information about how close to the linear–zigzag transition the system is. This can be seen by taking the formula for the overlap, Eq. (4.24), by expanding the unitary time-evolution operator in powers of t,

$$\mathcal{O} = {}_{\downarrow}\langle 0|\, \mathrm{e}^{-\mathrm{i}\hat{\mathrm{H}}_{\uparrow} t/\hbar} |0\rangle_{\downarrow} \approx {}_{\downarrow}\langle 0| \Big(1 - \mathrm{i}\hat{\mathrm{H}}_{\uparrow} t/\hbar - \hat{\mathrm{H}}_{\uparrow}^2 t^2/2\hbar^2 + \cdots\Big) |0\rangle_{\downarrow}\,, \tag{5.39}$$

and evaluating the time-derivatives at $t = 0$ for the ground state $|0\rangle_{\downarrow}$. We have then that the term $\mathcal{O}_1$ is just proportional to the expectation value of the Hamiltonian of the new configuration, $\hat{\mathrm{H}}_{\uparrow}$, evaluated with respect to the ground state of the initial configuration:

$$\mathcal{O}_1 = \frac{\mathrm{d}\mathcal{O}(0)}{\mathrm{d}t} = \frac{1}{\hbar}\, {}_{\downarrow}\langle 0|\hat{\mathrm{H}}_{\uparrow}|0\rangle_{\downarrow}\,. \tag{5.40}$$

Evaluating in the same way the term $\mathcal{O}_2$,

$$\mathcal{O}_2 = \frac{\mathrm{d}\mathcal{O}(0)}{\mathrm{d}t} = \frac{1}{\hbar^2}\, {}_{\downarrow}\langle 0|\hat{\mathrm{H}}_{\uparrow}^2|0\rangle_{\downarrow}\,. \tag{5.41}$$

we find that the curvature is proportional to the variance of the Hamilton operator of the new structure evaluated in the initial ground state:

$$\eta = -\frac{1}{\hbar^2}\Big[{}_{\downarrow}\langle 0|\hat{\mathrm{H}}_{\uparrow}^2|0\rangle_{\downarrow} - \big({}_{\downarrow}\langle 0|\hat{\mathrm{H}}_{\uparrow}|0\rangle_{\downarrow}\big)^2\Big]\,. \tag{5.42}$$

In order to facilitate the calculation of the curvature, it is advantageous to reformulate the matrix Ω for calculation of its inverse and determinant. First, for simplifying the notation, we introduce the definitions

$$\Xi = 1 + \Lambda^+\,, \qquad\qquad \mathrm{Y} = 1 - \Lambda^+\,. \tag{5.43}$$

Then, the identities for the determinant and the inverse for a partitioned matrix (Henderson and Searle 1981) involve the Schur complement Θ of Ξ, defined by

$$\Theta = \mathrm{Y} + \Lambda^- \Xi^{-1} \Lambda^-\,. \tag{5.44}$$

With that, provided that Ξ and Θ are non-singular, the inverse and the determinant are given by

$$\Omega^{-1} = \begin{pmatrix} \Theta^{-1} & \mathrm{i}\Theta^{-1}\Lambda^-\Xi^{-1} \\ \mathrm{i}\Xi^{-1}\Lambda^-\Theta^{-1} & \Xi^{-1} - \Xi^{-1}\Lambda^-\Theta^{-1}\Lambda^-\Xi^{-1} \end{pmatrix}\,, \tag{5.45}$$

and

$$\det \Omega = \det \Xi \cdot \det \Theta \,. \tag{5.46}$$

The non-singularity of Ξ and Θ is warranted by the results of Appendix C.

In Figure 5.14, the curvature is plotted for three $^9Be^+$ ions for varying values of g and Δ. On the plot scale, the curvature far away from the linear–zigzag transition is practically indistinguishable from 0. When the parameters are approaching the critical line, the curvature shows a sudden decrease. This means that the visibility decays much stronger when the final parameters are close to the linear–zigzag instability. Thus, by just observing the curvature of the visibility decay it is possible to infer the position at which the final state crosses the linear–zigzag instability.

An interesting feature of the short-time dependence of the visibility is the independence of the curvature on the strength of the dipole potential for a fixed value of the trapping strength g (as long as $g > g_c(\Delta)$ is valid). We refer to similar results obtained in the context of the Loschmidt echo or fidelity approach, where the so-called *fidelity susceptibility* (You et al. 2007) is a quantity related to the curvature used here. For instance, Mukherjee et al. (2012) show that the short-time scaling of the decay rate of the Loschmidt echo close to the quantum critical point of a central spin model (Quan et al. 2006) is independent of the quenching.

Fourier Spectra of Logarithmic Visibility

Alternatively, we may study the Fourier spectra of the visibility. The Fourier transform of the visibility is given by

$$\mathcal{F}_{\mathcal{V}}(\omega) = \frac{1}{2\pi} \int_0^\infty \mathrm{d}t \, \mathcal{V}(t) \, \mathrm{e}^{-\mathrm{i}\omega t} \,. \tag{5.47}$$

For the following evaluation, however, we do not calculate the spectra analytically but evaluate the visibility for sufficiently long times, typically 1000 µs, and with a high sampling rate such that all features are still resolved. As the obtained visibility is already discretized by the numerical evaluation, we apply the common fast Fourier transform (FFT) algorithm implemented within MATLAB, which is based on a discrete Fourier transform (Frigo and Johnson 2005). Some exemplary Fourier spectra are displayed on the left panel of Figure 5.15. Except for the linear case, there is a multitude of peaks which makes it difficult to extract the relevant information. To gain more insight, we might take the logarithm of the visibility before performing the Fourier transform; this step is motivated by the functional form of

the visibility, cf. Eq. (5.28). The Fourier spectrum of the logarithmic visibility is defined as

$$\mathcal{F}_{\ln \mathcal{V}}(\omega) = \frac{1}{2\pi} \int_0^\infty \mathrm{d}t \ln[\mathcal{V}(t)] \, \mathrm{e}^{-\mathrm{i}\omega t} \,. \tag{5.48}$$

Indeed, as we look at the right panels of Figure 5.15, the spectra of the logarithmic visibility now show clear distinct peaks at specific frequencies.

The spectrum of the logarithmic visibility in the linear case in Figure 5.15b displays one clear peak. The location of the peak coincides with twice the frequency of the zigzag mode, confirming the previous argument about the squeezing origin of the dynamics in this case. The next peak is considerably smaller, hardly observable in Figure 5.15b, located at the inverse of a sum of two of the eigenfrequencies. This means the small modulation in the Figure 5.5 originates from the squeezing of two modes. As this effect becomes more apparent in the other regimes, we shall discuss it there in detail, neglecting it here as it is only a small correction.

In the zigzag regime, plotted in Figure 5.15d, we identify the major peak located at the zigzag eigenfrequency. In this case, the quench predominantly excites an oscillatory motion around the new equilibrium positions. Here we see some other peaks, again considerably smaller: One is located at twice the zigzag eigenfrequency, thus showing also the presence of single-mode squeezing. The other two are located at eigenfrequencies of other modes which are excited by the quench. These other peaks are much smaller than the main peak, so our intuitive interpretation of the motion to be dominated by an oscillatory dynamics similar to that of coherent states is justified.

Finally, the visibility is displayed in Figures 5.15f and 5.15h for the regime close to the linear–zigzag instability. There, the spectrum is similar to the one in Figure 5.15d, with the main peak again located at the zigzag eigenfrequency and a minor peak at twice the zigzag eigenfrequency, hinting at oscillation and single-mode squeezing in the dynamics after the quench. But there are also two minor peaks, more visible than in the linear case of Figure 5.15b, originating from two-mode squeezing of two involved eigenmodes. The peak of the zigzag mode has shifted more toward the low-frequency region (as the zigzag mode has a lower frequency in this region), which explains the less regular behaviour of the visibility on longer time scales. We can identify the modes of the most important minor peaks to be the zigzag mode and the COM-mode in y-direction, which become two-mode squeezed.

Before concluding, we want to discuss the feasibility of performing the Fourier transformation of the logarithmic visibility in an experi-

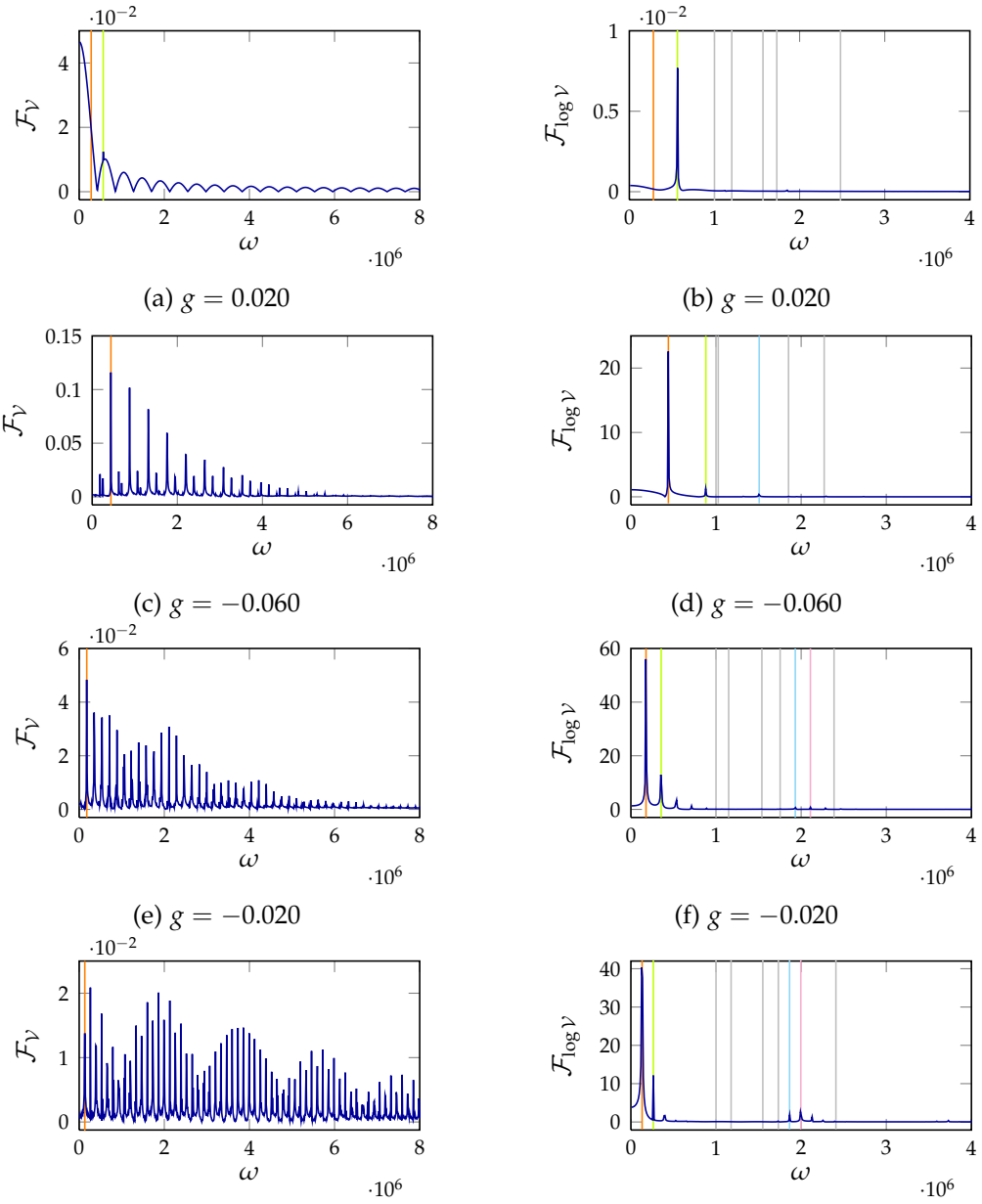

(a) $g = 0.020$ (b) $g = 0.020$

(c) $g = -0.060$ (d) $g = -0.060$

(e) $g = -0.020$ (f) $g = -0.020$

(g) $g = -0.006$ (h) $g = -0.006$

Figure 5.15: Spectra (left) and logarithmic spectra (right) for different regimes. All spectra have been calculated from visibility signals with sampling time 50 ns and total time 100 µs.

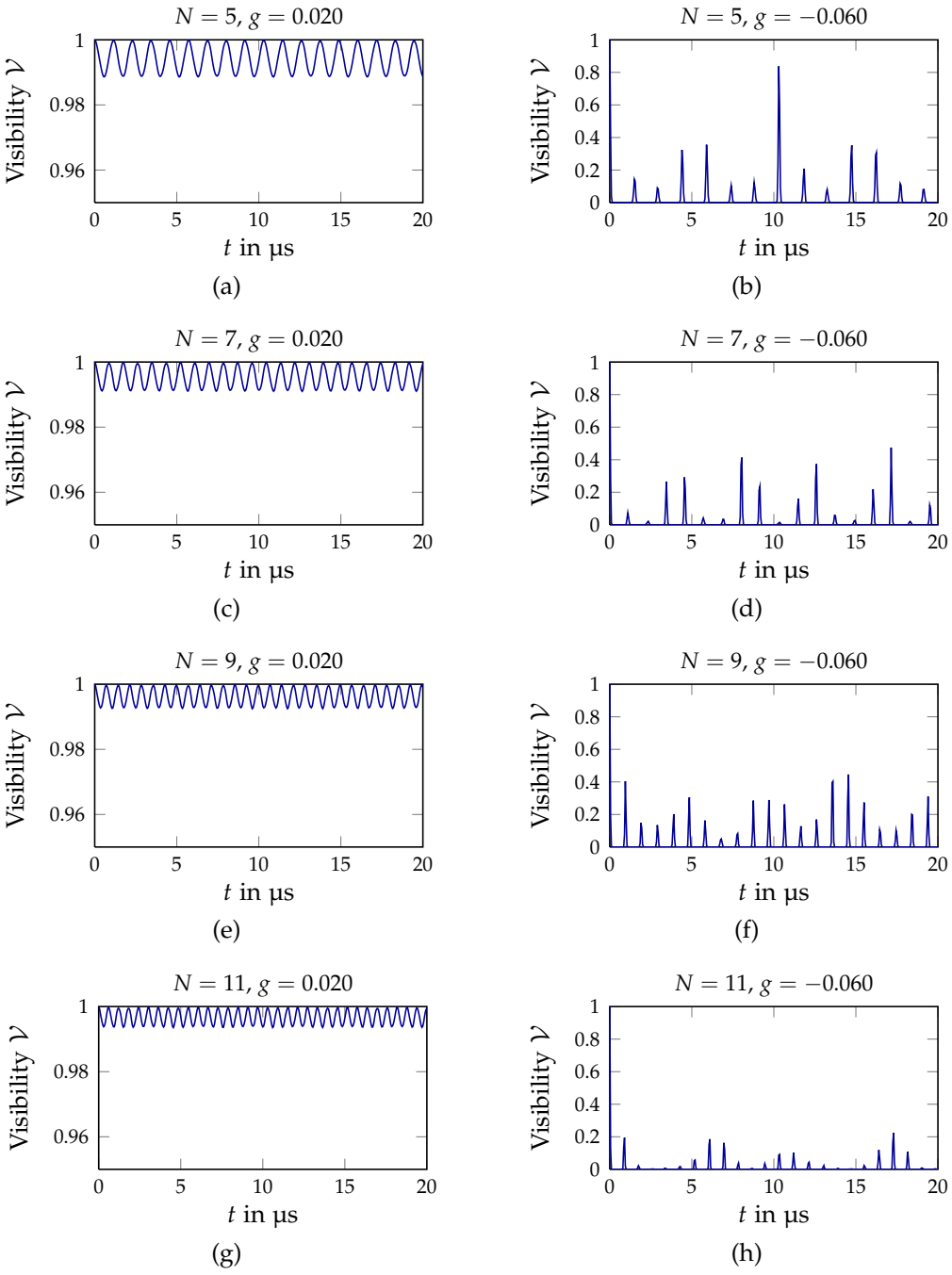

Figure 5.16: Comparison of the visibility in the linear and zigzag regimes for different ion numbers for $\Delta = 0.02$. On the left, the crystals are all prepared in the linear chain before the quench with $g = 0.02$, while on the right the crystals are prepared in the zigzag regime at $g = -0.060$.

ment in which the data taken will be discretized. Yet, there are two reasons why the logarithmic spectra of the visibility as shown in the plots on the right side of Figure 5.15 might not be something one might hope to measure in an actual experiment. First, the need for longer time windows to capture all the long-time features of the visibility conflicts with the requirement to have the time between the pulses sufficiently short as to avoid the effects of coupling to the environment to come in. Also, it might be quite wearisome to take the necessary amount of data points for a long-time record of the visibility with a sufficiently high sampling rate in an experiment, where every data point is determined by some hundred single measurements. Second, taking the logarithm of the visibility requires to have a low noise in the visibility measurement. The plots shown here take advantage of the fact that the numerical algorithm for the FFT can evaluate the temporal behaviour for the visibility being close to zero; in fact, on a logarithmic scale the seemingly constant parts between the peaks, for instance in Figure 5.7c, have a strong oscillatory dependence which is accounted for when performing the theoretical Fourier analysis.

Yet, despite these short-comings for an actual experimental verification, these plots give us more insight into the spectral properties of the calculated signals and into their dependence on the different parameters.

5.3.3 *Scaling with the Number of Ions*

Finally, we might ask ourselves how the visibility changes when the number of ions in the crystal increases. For this, we compare the visibility signals for small ion crystals containing an odd number of up to 11 ions, which are plotted in Figure 5.16 for the zigzag and the linear regime.

In the linear regime, here with a chosen value of $g = 0.020$, there are two variations appearing as the number of ions increases. First, the amplitude of the modulation shrinks. The reason is that even though the dipole strength is scaled to the critical transverse trapping frequency, the impact of a change in confinement for a single ion becomes less important. Second, the frequency of the modulation increases, since the eigenfrequency of the zigzag mode is increasing.

For the plots in the zigzag regime, shown on the right side, the dipole strength is chosen to be $g = -0.060$, so that we can compare it with Figure 5.7c as well. For an increasing number of ions in the crystal, the peaks of the revivals become smaller in height, on average. Some of the peaks, in particular, become so weak that they vanish on the plot scale. Then again, the time between the peaks becomes shorter as the zigzag eigenfrequency increases for larger ion crystals.

Additionally, we might compare the scaling of the first peaks for the crystals with different ion numbers. In the main figure, the times of the first peaks are plotted, similar to Figure 5.12 but with a different number of ions. The values of other symbols are again determined by `findpeaks.m` (O'Haver 2011), and the lines show the times of the full period for $g < 0$ or the half period for $g > 0$ of the zigzag mode. The data points and curves coincide, and they diverge at the critical trapping strength $g_c(N)$, which depends on the ion number. In the inset, we plotted the same graphs but with the origins of the x-axis shifted to $g_c(N)$ and the time on the y-axis rescaled in units of the critical transverse trapping frequency, i. e. in units of $1/\nu_c$. Again, the curves and data are all approximately located on top of each other, as they all depend only on the form of the zigzag eigenmode.

Comparison of Masses and Trapping Frequencies

In this section we compare the visibility for different masses and different axial trapping frequencies while keeping all the other parameters fixed. Essentially, this means varying the parameter ζ_0 between the minimum and maximum values it attains in Table 5.1, which means we can change the quantumness of the quench. It suffices thus to compare the following combinations to qualitatively understand the behaviour:

i) a light ion with a high axial trapping frequency,

ii) a light ion with a medium axial trapping frequency,

iii) a heavy ion with a medium axial trapping frequency,

iv) a heavy ion with a low axial trapping frequency.

The results of these comparisons are plotted in Figures 5.17 and 5.18. In Figure 5.17, the comparison is drawn for the fixed parameters $g = -0.050$ and $\Delta = 0.010$. In the zigzag regime, smaller mass and higher axial trapping frequency result in revival peaks that are wider, higher, and more regular.

In Figure 5.18, all the plots for different mass and axial trapping frequency but with fixed parameters $g = 0.020$ and $\Delta = 0.010$ are merged into a single plot. This plot, which is in the linear regime, shows all curves lying exactly on top of each other, so that there is no effect whatsoever of mass and axial trapping frequency on the form of the visibility. This at first quite surprising result can be explained by recalling that the change of the visibility is induced purely by the squeezing dynamics of the quantum quench. Although the ground state wavefunction depends on the mass and the initial steepness of

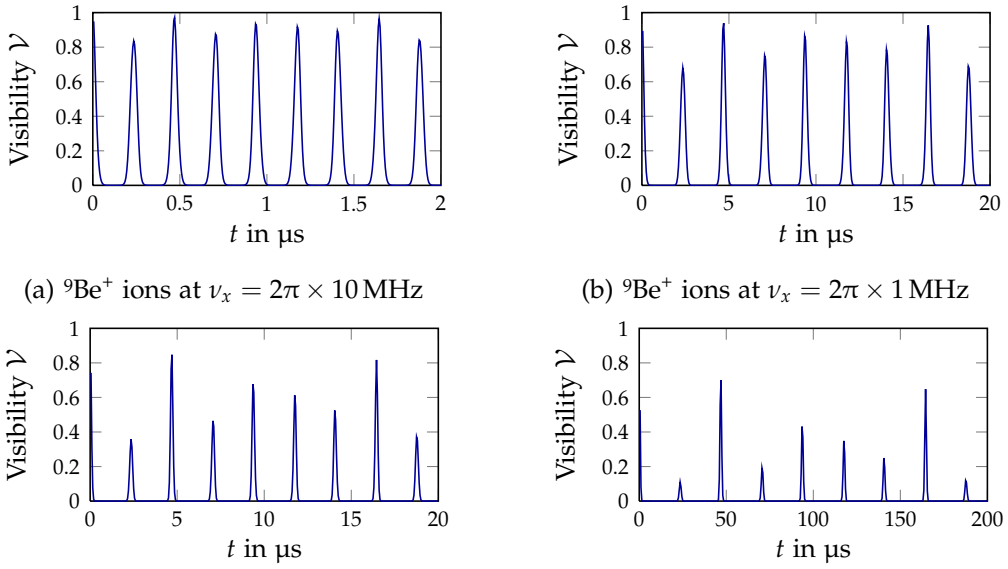

(a) $^{9}Be^{+}$ ions at $\nu_x = 2\pi \times 10\,\mathrm{MHz}$

(b) $^{9}Be^{+}$ ions at $\nu_x = 2\pi \times 1\,\mathrm{MHz}$

(c) $^{171}Yb^{+}$ ions at $\nu_x = 2\pi \times 1\,\mathrm{MHz}$

(d) $^{171}Yb^{+}$ ions at $\nu_x = 2\pi \times 100\,\mathrm{kHz}$

Figure 5.17: Comparison of visibility for different masses and trapping frequencies for fixed $\Delta = 0.01$ and $g = -0.05$ for a three-ion crystal.

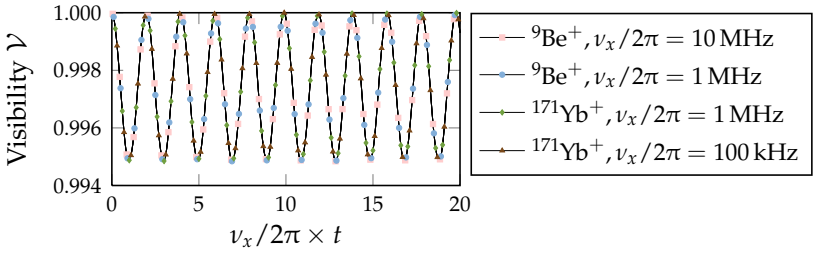

Figure 5.18: Comparison of visibility for fixed $\Delta = 0.01$ and $g = 0.02$ for a three-ion crystal with varied mass of the ion species and varied trapping frequency. The curves exactly overlap each other.

the potential, the relative squeezing induced is identical in all cases because the relative change of the potential is also identical in all cases.

From another perspective, the quench in the linear regime is already a pure quantum quench and the parameter ζ_0 therefore not important (as long as quantum degeneracy can be neglected). In the zigzag regime, the quantumness parameter ζ_0 allows us to change the form of the visibility, in particular to adjust the width of the revival peaks.

With this, we conclude the discussion of the ground state quenches, and turn to thermal effects and imperfections, the topic of the next chapter.

6

QUANTUM QUENCHES OF THERMALLY EXCITED ION COULOMB CRYSTALS

In this chapter we investigate the visibility of the Ramsey interferometry scheme under more realistic conditions than for those of the results presented in Chapter 5. In particular, in Section 6.2, we take into account the effect of a possible momentum kick transferred to the ions by recoil of the absorption and emission of photons accompanying the $\pi/2$-pulses. We find that the recoil of the photons is decreasing the visibility of the Ramsey interferometry. The effect of the photon recoil is much stronger in the linear regime, in which the quench does not lead to an oscillation of the ions.

Then, in Section 6.3, we analyse the visibility for quenches when for which the initial state of the crystal is not perfectly in the motional ground state in all modes but rather has some thermal excitation. As a result the visibility for higher temperatures is in general lower than the one for the ground state cooled crystal, but a new revival time scale emerges that is *absent* at $T = 0\,\mathrm{K}$, and that occurs at times that are *independent* of the temperature. In the next section we derive the expression of the visibility that takes into account the effect of the finite temperature and the mechanical effects of the Ramsey pulses.

6.1 EVALUATION OF THE VISIBILITY FOR THERMAL STATES

We now evaluate the visibility of the Ramsey interferometer with an ion Coulomb crystal prepared initially in a thermal state, Eq. (4.60). Besides taking a finite thermal occupation into account, we are also including the effect of the photon recoil of the Ramsey pulses in the calculation.

The operators that describe the recoil which the photon exchanges with the absorbing or emitting ion are given by

$$\hat{\mathrm{R}}_{\mathbf{k}}(\hat{\mathbf{r}}_{n_0}) = \exp(\mathrm{i}\mathbf{k}\cdot\hat{\mathbf{r}}_{n_0})\,, \tag{6.1}$$

where $\mathbf{k}$ is the wave vector of the laser beam and $\hat{\mathbf{r}}_{n_0}$ is the position operator of the central ion. The recoil operator can be written in

the form of a displacement operator acting on all normal modes. In particular, we have

$$\hat{\mathrm{R}}_{\mathbf{k}}(\hat{\mathbf{x}}) = \hat{\mathrm{D}}_{\uparrow}(\kappa)\,, \tag{6.2}$$

with

$$\hat{\mathrm{D}}_{\uparrow}(\kappa) = \hat{\mathrm{D}}_{\uparrow}(\kappa_1) \otimes \cdots \otimes \hat{\mathrm{D}}_{\uparrow}(\kappa_{3N}) = \exp\Big\{\sum_j (\kappa_j \hat{\mathrm{b}}_j^{\uparrow\dagger} - \kappa_j^* \hat{\mathrm{b}}_j^{\uparrow})\Big\}\,, \tag{6.3}$$

where the displacements in the modes are given by

$$\kappa_j = \mathrm{i}\sqrt{\frac{\hbar}{2m\omega_j^{\uparrow}}} K_j\,. \tag{6.4}$$

Here we have expanded the wave vector $\mathbf{k}$ of the photon, which is absorbed or emitted by the ion labelled by n_0, into the basis spanned by the normal modes, such that

$$K_j = k_x \mathrm{M}^{\uparrow}_{j_{0x},j} + k_y \mathrm{M}^{\uparrow}_{j_{0y},j} + k_z \mathrm{M}^{\uparrow}_{j_{0z},j} \tag{6.5}$$

is the projection onto the normal mode labelled by j ($j_{0\alpha}$ labels the coordinate describing the $\alpha = x, y, z$ displacement of the n_0th ion, i. e. $j_{0x} = n_0$, $j_{0y} = N + n_0$ and $j_{0z} = 2N + n_0$ in the convention of Table 2.1).

Second, we consider the case in which the initial motional state is in thermal equilibrium at some finite temperature. For describing this thermal state we use the density matrix as introduced in Chapter 4. The overlap, as derived in Section 4.4, is determined by the formula Eq. (4.60),

$$\mathcal{O}(t) = \mathrm{Tr}\{\hat{\mathrm{R}}^{\dagger}_{\mathbf{k}'} \hat{\mathrm{U}}_{\uparrow} \hat{\mathrm{R}}_{\mathbf{k}} \rho_0 \hat{\mathrm{U}}^{\dagger}_{\downarrow}\}\,. \tag{6.6}$$

Then, we can evaluate the trace in any basis that is convenient for the calculation – which here turns out to be the overcomplete coherent state basis with respect to the equilibrium positions of the crystal when the central ion is in the state $|{\uparrow}\rangle$. In this basis, the trace operator explicitly reads as

$$\mathrm{Tr}\{\,\cdot\,\} = \frac{1}{\pi^{3N}} \int \mathrm{d}^{6N}\alpha \; {}_{\uparrow}\langle\alpha| \cdot |\alpha\rangle_{\uparrow}\,, \tag{6.7}$$

where $|\alpha\rangle_{\uparrow} = \bigotimes_j |\alpha_j\rangle_{\uparrow}$ describes a multi-mode coherent state as it is generated by application of the multi-mode displacement operator onto the ground state,

$$\bigotimes_j \hat{\mathrm{D}}_{\uparrow}(\alpha_j)\,|0\rangle_{\uparrow} = \bigotimes_j |\alpha_j\rangle_{\uparrow}\,. \tag{6.8}$$

Before we turn to the evaluation of this matrix element and the integral, we first make use of the cyclic property of the trace operation, that is, we write the overlap as

$$\mathcal{O}(t) = \int \frac{\mathrm{d}^{6N}\alpha}{\pi^{3N}} \,{}_{\uparrow}\langle\alpha|\hat{\mathrm{R}}_{\mathbf{k}}\rho_0\hat{\mathrm{U}}_{\downarrow}^{\dagger}\hat{\mathrm{R}}_{\mathbf{k}'}^{\dagger}\hat{\mathrm{U}}_{\uparrow}|\alpha\rangle_{\uparrow}\,. \tag{6.9}$$

In this way, the time evolution operator $\hat{\mathrm{U}}_{\uparrow}$ is applied directly to the coherent state, which simplifies the evaluation.

For the next step in the evaluation, we need to insert the explicit form of ρ_0, which may be represented in an arbitrary basis. A convenient choice is a basis in which the initial density matrix is expressed in terms of coherent states, and in which it is *diagonal* no matter the form of the initial state. Such a basis representation exists, called the *Glauber-Sudarshan-P distribution* (Carmichael 1998, Ch. 3, pp. 75f.). With the help of this distribution any arbitrary initial density matrix can be written in the following form,

$$\rho_0 = \int \frac{\mathrm{d}^{6N}\lambda^{\downarrow}}{\pi^{3N}} \, P_0(\lambda^{\downarrow})|\lambda^{\downarrow}\rangle_{\downarrow}\langle\lambda^{\downarrow}|\,, \tag{6.10}$$

where $|\lambda^{\downarrow}\rangle_{\downarrow} = \otimes_j |\lambda_j^{\downarrow}\rangle_{\downarrow}$ is the basis of coherent states when the central ion is in state $|\downarrow\rangle$, with $\lambda^{\downarrow} = (\lambda_1^{\downarrow}, \ldots, \lambda_{3N}^{\downarrow})$, of course.

6.1.1 *Calculation of the Overlap*

Inserting Eq. (6.10), the equation for the overlap, Eq. (6.9), is written as a double integral in the coherent states,

$$\mathcal{O}(t) = \int \frac{\mathrm{d}^{6N}\alpha}{\pi^{3N}} \int \frac{\mathrm{d}^{6N}\lambda^{\downarrow}}{\pi^{3N}} P_0(\lambda^{\downarrow}) \,{}_{\uparrow}\langle\alpha|\hat{\mathrm{R}}_{\mathbf{k}}|\lambda^{\downarrow}\rangle_{\downarrow}\,{}_{\downarrow}\langle\lambda^{\downarrow}|\hat{\mathrm{U}}_{\downarrow}^{\dagger}\hat{\mathrm{R}}_{\mathbf{k}'}^{\dagger}\hat{\mathrm{U}}_{\uparrow}|\alpha\rangle_{\uparrow}\,. \tag{6.11}$$

The integrand is composed of two matrix elements which need to be evaluated first. In the first matrix element, we replace the coherent state $|\lambda^{\downarrow}\rangle_{\downarrow}$ by the corresponding identity involving the multimode displacement operator applied on the ground state, $|\lambda^{\downarrow}\rangle_{\downarrow} = \hat{\mathrm{D}}_{\downarrow}(\lambda^{\downarrow})\,|0\rangle_{\downarrow}$. In the definition of the displacement operator, Eq. (6.3), we change the basis of the operators by means of the Bogoliubov transformation, Eqs. (3.25), such that we can write the displacement operator in the changed basis as

$$\hat{\mathrm{D}}_{\downarrow}(\lambda^{\downarrow}) = \mathrm{e}^{\mathrm{i}\varphi_{\lambda^{\downarrow}}}\hat{\mathrm{D}}_{\uparrow}(\lambda^{\uparrow})\,, \tag{6.12}$$

where the displacements in the changed basis are given by

$$\lambda_j^{\uparrow} = \sum_k (\lambda_k^{\downarrow} u_{kj} + \lambda_k^{\downarrow *} v_{kj})\,. \tag{6.13}$$

When applying this transformation the following phase factor needs to be included,

$$\varphi_{\lambda^\downarrow} = 2\,\mathrm{Im}\Big[\sum_j \lambda_j^\downarrow \beta_j^\downarrow\Big]\,, \tag{6.14}$$

where $\beta^\downarrow$ is the displacement between the ground states of the two different configurations, Eq. (3.30).

Putting in the transformation between the ground states, Eq. (3.42), we can write the coherent state $|\lambda^\downarrow\rangle_\downarrow$ as

$$|\lambda^\downarrow\rangle_\downarrow = Z\hat{\mathrm{D}}_\uparrow(\lambda^\uparrow)\hat{\mathrm{D}}_\uparrow(\beta^\uparrow)\,\mathrm{e}^{\hat{\mathrm{A}}}\,|0\rangle_\uparrow\,. \tag{6.15}$$

Using this result and replacing the recoil operator via Eqs. (6.2), (6.4) and (6.5), we arrive at the following expression for the first matrix element,

$${}_\uparrow\langle\alpha|\hat{\mathrm{R}}_{\mathbf{k}}|\lambda^\downarrow\rangle_\downarrow = Z\,\mathrm{e}^{\mathrm{i}\varphi_{\lambda^\downarrow}}\,{}_\uparrow\langle\alpha|\hat{\mathrm{D}}_\uparrow(\kappa)\hat{\mathrm{D}}_\uparrow(\lambda^\uparrow)\hat{\mathrm{D}}_\uparrow(\beta^\uparrow)\,\mathrm{e}^{\hat{\mathrm{A}}}|0\rangle_\uparrow\,. \tag{6.16}$$

To evaluate this matrix element, we first combine the three displacement operators, using the BCH formula, into a single operator,

$$\hat{\mathrm{D}}_\uparrow(\kappa)\hat{\mathrm{D}}_\uparrow(\lambda^\uparrow)\hat{\mathrm{D}}_\uparrow(\beta^\uparrow) = \mathrm{e}^{\mathrm{i}\varphi_\theta}\hat{\mathrm{D}}_\uparrow(\theta)\,, \tag{6.17}$$

where the new combined displacement θ is given by

$$\theta_j = \kappa_j + \beta_j^\uparrow + \lambda_j^\uparrow\,, \tag{6.18}$$

with a phase factor

$$\varphi_\theta = \mathrm{Im}\Big[\sum_j (\kappa_j(\lambda_j^{\uparrow *} + \beta_j^\uparrow) + \lambda_j^\uparrow\beta_j^\uparrow)\Big]\,. \tag{6.19}$$

In the step, we exchange the displacement with the exponential operator, as in Eqs. (5.8), obtaining again a generalized or displaced $\hat{\mathrm{A}}$-operator in the exponent. Summing up, we have simplified the first matrix element to be

$${}_\uparrow\langle\alpha|\hat{\mathrm{R}}_{\mathbf{k}}|\lambda^\downarrow\rangle_\downarrow = Z\,\mathrm{e}^{\mathrm{i}\varphi_{\lambda^\downarrow}}\,\mathrm{e}^{\mathrm{i}\varphi_\theta}\,{}_\uparrow\langle\alpha|\,\mathrm{e}^{\hat{\mathrm{A}}(\theta)}|\theta\rangle_\uparrow\,. \tag{6.20}$$

In the same way, we can simplify the second matrix element in Eq. (6.11) by transforming the operators and ground states. But before we do so, we first apply the evolution operator $\hat{\mathrm{U}}_\downarrow^\dagger$ from the left to the coherent state $\langle\lambda^\downarrow|_\downarrow$, resulting in the time-dependent coherent state $\langle\lambda^\downarrow|_\downarrow\,\hat{\mathrm{U}}_\downarrow^\dagger = \langle\lambda^\downarrow(t)|_\downarrow$. When this coherent state is rewritten as the ground state with a displacement operator applied to it, as before, and when we transform all quantities into the other basis, the transformed displacements are now time-dependent,

$$\lambda_j^\uparrow(t) = \sum_k \Big(\lambda_k^\downarrow\,\mathrm{e}^{-\mathrm{i}\omega_k^\downarrow t}u_{kj} + \lambda_k^{\downarrow *}\,\mathrm{e}^{+\mathrm{i}\omega_k^\downarrow t}v_{kj}\Big)\,. \tag{6.21}$$

Again, we have to accompany this displacement operator in the transformed basis with a phase factor, $\exp\{-\mathrm{i}\varphi_{\lambda^\downarrow(t)}\}$,

$$\varphi_{\lambda^\downarrow(t)} = 2\,\mathrm{Im}\Big[\sum_j \mathrm{e}^{-\mathrm{i}\omega_j^\downarrow t}\lambda_j^\downarrow \beta_j^\downarrow\Big]\,, \tag{6.22}$$

which is time-dependent in this case. Comparing the complex conjugate of the second matrix element with the first one in Eq. (6.11), we figure out that the displacement operators appear in the same order as before, with $\lambda^\downarrow$ replaced by $\lambda^\downarrow(t)$ and κ replaced by κ'. Thus they can be merged just as before in Eq. (6.17), thereby defining the combined displacement

$$\theta_j' = \kappa_j' + \beta_j^\uparrow + \lambda_j^\uparrow(t)\,, \tag{6.23}$$

with the phase factor $\exp\{\varphi_{\theta'}\}$, where

$$\varphi_{\theta'} = \mathrm{Im}\Big[\sum_j \big(\kappa_j'(\lambda_j^{\uparrow *}(t) + \beta_j^\uparrow) + \lambda_j^{\uparrow *}(t)\beta_j^\uparrow\big)\Big]\,. \tag{6.24}$$

Hence, the second matrix element reads in its simplified version as

$${}_\downarrow\langle\lambda^\downarrow|\hat{\mathrm{U}}_\downarrow^\dagger \hat{\mathrm{R}}_{\mathbf{k}'}^\dagger \hat{\mathrm{U}}_\uparrow|\alpha\rangle_\uparrow = Z\,\mathrm{e}^{-\mathrm{i}\varphi_{\lambda^\downarrow(t)}}\,\mathrm{e}^{-\mathrm{i}\varphi_{\theta'}}\,{}_\uparrow\langle\theta'|\,\mathrm{e}^{\hat{\mathrm{A}}^\dagger(\theta')}|\alpha(t)\rangle_\uparrow\,. \tag{6.25}$$

Combining all of the steps above, the overlap, Eq. (6.11), is written as

$$\begin{aligned}\mathcal{O}(t) = \int \frac{\mathrm{d}^{6N}\alpha}{\pi^{3N}} \int \frac{\mathrm{d}^{6N}\lambda^\downarrow}{\pi^{3N}}\, Z^2\,\mathrm{e}^{\mathrm{i}\varphi} P_0(\lambda^\downarrow) \\ \times\ {}_\uparrow\langle\alpha|\,\mathrm{e}^{\hat{\mathrm{A}}(\theta)}|\theta\rangle_\uparrow\,{}_\uparrow\langle\theta'|\,\mathrm{e}^{\hat{\mathrm{A}}^\dagger(\theta')}|\alpha(t)\rangle_\uparrow\,,\end{aligned} \tag{6.26}$$

where we merged all the phase factors into a single one,

$$\varphi = \varphi_{\lambda^\downarrow} - \varphi_{\lambda^\downarrow(t)} + \varphi_\theta - \varphi_{\theta'}\,. \tag{6.27}$$

In order to proceed with the evaluation, we first exchange the order of the integrations,

$$\mathcal{O}(t) = Z^2 \int \frac{\mathrm{d}^{6N}\lambda^\downarrow}{\pi^{3N}}\,\mathrm{e}^{\mathrm{i}\varphi} P_0(\lambda^\downarrow)\,\mathcal{I}_\alpha(\lambda^\downarrow)\,, \tag{6.28}$$

where we defined the inner integral by

$$\mathcal{I}_\alpha(\lambda^\downarrow) = \int \frac{\mathrm{d}^{6N}\alpha}{\pi^{3N}}\,{}_\uparrow\langle\alpha|\,\mathrm{e}^{\hat{\mathrm{A}}(\theta)}|\theta\rangle_\uparrow\,{}_\uparrow\langle\theta'|\,\mathrm{e}^{\hat{\mathrm{A}}^\dagger(\theta')}|\alpha(t)\rangle_\uparrow\,. \tag{6.29}$$

Exchanging the two matrix elements, we arrive at the following form for the inner integral,

$$\mathcal{I}_\alpha(\lambda^\downarrow) = \int \frac{\mathrm{d}^{6N}\alpha}{\pi^{3N}}\,{}_\uparrow\langle\theta'|\,\mathrm{e}^{\hat{\mathrm{A}}^\dagger(\theta')}|\alpha(t)\rangle_\uparrow\,{}_\uparrow\langle\alpha|\,\mathrm{e}^{\hat{\mathrm{A}}(\theta)}|\theta\rangle_\uparrow\,, \tag{6.30}$$

where we can evaluate the matrix elements by using the same methods as presented in the previous chapter, see the evaluation following Eq. (5.12), giving us the result

$$\mathfrak{I}_\alpha(\lambda^\downarrow) = \int \frac{\mathrm{d}^{6N}\alpha}{\pi^{3N}} \left\langle \mathrm{e}^{\hat{\mathrm{A}}(\theta')} \right\rangle^*_{\alpha(t)} {}_\uparrow\!\left\langle \alpha(t) \middle| \theta' \right\rangle^*_\uparrow \left\langle \mathrm{e}^{\hat{\mathrm{A}}(\theta)} \right\rangle_\alpha {}_\uparrow\!\langle \alpha | \theta \rangle_\uparrow \,. \quad (6.31)$$

A comparison with Eq. (5.17) shows that both integrals are almost identical, with $\beta^\uparrow$ replaced by θ in the scalar product on the right and by θ' in the scalar product on the left. Indeed, performing the calculation in the same way, i. e. merging all terms into a common exponent and grouping them by their order in the α variables, we see that only the linear and constant terms are different to Eq. (5.21). The integral takes the following form,

$$\mathfrak{I}_\alpha(\lambda^\downarrow) = Z^2 \mathrm{e}^{\mathrm{i}\varphi} \mathrm{e}^{G^*(\theta')} \mathrm{e}^{G(\theta)} \int \frac{\mathrm{d}\mathbf{w}}{\pi^{3N}} \mathrm{e}^{-\mathbf{w}^T.\mathbf{s} - \mathbf{w}^T \Omega \mathbf{w}} \,, \quad (6.32)$$

with a result similar to before:

$$\mathfrak{I}_\alpha(\lambda^\downarrow) = \frac{Z^2}{\sqrt{\det \Omega}} \mathrm{e}^{\mathrm{i}\varphi} \mathrm{e}^{G^*(\theta')} \mathrm{e}^{G(\theta)} \mathrm{e}^{\frac{1}{4}\mathbf{s}^T \Omega^{-1} \mathbf{s}} \,. \quad (6.33)$$

In this equation we introduced the following abbreviations:

$$G(\gamma) = \sum_{jk} \frac{A_{jk}}{2} \gamma_j^* \gamma_k^* - \sum_j \frac{|\gamma_j|^2}{2} \,, \quad (6.34)$$

with $\gamma_j = \theta_j, \theta'_j$; Ω is a complex symmetric $6N$-by-$6N$ matrix, which is defined by

$$\Omega = \begin{pmatrix} \Omega^{++} & \Omega^{+-} \\ \Omega^{-+} & \Omega^{--} \end{pmatrix} = \begin{pmatrix} 1 - \mathrm{A}^+ & -\mathrm{i}\mathrm{A}^- \\ -\mathrm{i}\mathrm{A}^- & 1 + \mathrm{A}^+ \end{pmatrix} \quad (6.35)$$

with

$$\mathrm{A}^\pm_{jk} = \frac{1}{2}\left[A_{jk} \left(\mathrm{e}^{-\mathrm{i}(\omega_j^\uparrow + \omega_k^\uparrow)t} \pm 1 \right) \right] ; \quad (6.36)$$

$\mathbf{s}$ is a $6N$-dimensional vector given by

$$\mathbf{s} = \begin{pmatrix} S^+ \\ -\mathrm{i}S^- \end{pmatrix} , \quad (6.37)$$

with

$$S_j^\pm[\theta, \theta'] = S_j[\theta] \pm S_j^*[\theta'] \mathrm{e}^{-\mathrm{i}\omega_j^\uparrow t} \,, \quad (6.38a)$$

$$S_j[\gamma] = \sum_k A_{jk} \gamma_k^* - \gamma_j \,. \quad (6.38b)$$

The discussion of the convergence of the integration in Eq. (6.32) applies in exactly the same way as in Chapter 5, so there is no need to repeat it here.

In summary, the double integral Eq. (6.11) is reduced to a single integral over the variables λ,

$$\mathcal{O}(t) = \int \frac{\mathrm{d}^{6N}\lambda^{\downarrow}}{\pi^{3N}} P_0(\lambda^{\downarrow}) \frac{Z^2 \mathrm{e}^{\mathrm{i}\varphi}}{\sqrt{\det \Omega}} \mathrm{e}^{G^*(\theta')} \mathrm{e}^{G(\theta)} \mathrm{e}^{\frac{1}{4}\mathbf{s}^T \Omega^{-1} \mathbf{s}}, \quad (6.39)$$

where we need to insert the corresponding Glauber-Sudarshan-P distribution $P_0(\lambda^{\downarrow})$ of the initial density matrix.

Equation (6.39) gives the visibility as a function of an arbitrary initial state for an arbitrary number of ions N while also accounting for the mechanical effect associated with the absorption of a photon out of and emission of a photon into the laser pulse. We evaluate the visibility for different initial states in the next sections.

6.1.2 *Initial Preparation of Coherent States*

The Glauber-Sudarshan-P distribution for the single-mode coherent state $|\alpha_0\rangle$ is given by

$$P(\alpha) = \delta^{(2)}(\alpha - \alpha_0). \quad (6.40)$$

If the initial motional state of an ion Coulomb crystal is prepared in a coherent state $|\alpha\rangle_{\downarrow} = \bigotimes_j |\alpha_j\rangle_{\downarrow}$, with $|\alpha_j\rangle_{\downarrow}$ being a coherent state in the normal mode labelled by j, the corresponding Glauber-Sudarshan-P distribution is given by

$$P_0(\lambda^{\downarrow}) = \prod_j \delta^{(2)}(\lambda_j^{\downarrow} - \alpha_j). \quad (6.41)$$

The visibility of an ion Coulomb crystal initially prepared in a coherent state can be calculated with the formulae derived in the previous section. The expected behaviour of the visibility for a coherent state would depend strongly on the exact point of time of the first Ramsey pulse, as the coherent states are following the trajectories of classical harmonic oscillators. To correctly predict the visibility for an experiment, we would first need to determine the phases of all the coherent states. There exists an abundance of possible choices for these initial phases, which would obfuscate a clear analysis. For this reason, we chose not to include a discussion of the coherent state case in this thesis, even if it might be useful for measuring the motional state of an ion Coulomb crystal.

To conclude this section we would like to check if we regain the formula for ground state as a special case of the derived formula.

The ground state is the coherent state $|0\rangle_\downarrow = \bigotimes_j |0_j\rangle_\downarrow$, so that the Glauber-Sudarshan-P distribution is simply given by

$$P_0(\lambda^\downarrow) = \prod_j \delta^{(2)}(\lambda_j^\downarrow)\,. \tag{6.42}$$

The overlap is then given by inserting the P-distribution into Eq. (6.39), yielding

$$\mathcal{O}(t) = \frac{Z^2\,\mathrm{e}^{\mathrm{i}\varphi}}{\sqrt{\det\Omega}}\,\mathrm{e}^{G^*(\theta')}\,\mathrm{e}^{G(\theta)}\,\mathrm{e}^{\frac{1}{4}\mathbf{s}^T\Omega^{-1}\mathbf{s}}\,, \tag{6.43}$$

which is a generalisation of Eq. (5.28), which allows for the inclusion of the effect of the photon recoil. By setting κ and κ' to zero we recover the result of Eq. (5.28).

6.1.3 *Initial Thermal State*

We now consider the case of the initial motional state being a thermal state. A particular instance of such a state is the steady state of a laser cooling process of an ion Coulomb crystal. A thermal state of a mode of a harmonic oscillator, as given by Eq. (4.39), has the following Glauber-Sudarshan-P-distribution (Carmichael 1998, Ch. 3, p. 85),

$$P_0(\lambda_j^\downarrow) = \frac{1}{\pi\,\langle\hat{\mathrm{n}}_j^\downarrow\rangle}\exp\left[-\frac{|\lambda_j^\downarrow|^2}{\langle\hat{\mathrm{n}}_j^\downarrow\rangle}\right], \tag{6.44}$$

where the expectation value of the occupation number $\langle n_j^\downarrow\rangle$ fulfils the following relation (Carmichael 1998),

$$\langle\hat{\mathrm{n}}_j^\downarrow\rangle = \langle\hat{\mathrm{b}}_j^{\downarrow\dagger}\hat{\mathrm{b}}_j^\downarrow\rangle = \frac{\mathrm{e}^{-\hbar\omega_j^\downarrow/k_\mathrm{B}T}}{1-\mathrm{e}^{-\hbar\omega_j^\downarrow/k_\mathrm{B}T}}\,, \tag{6.45}$$

where k_B is the Boltzmann constant, T the temperature and $\langle n_j^\downarrow\rangle$ the mean vibrational number of mode j.

By integrating Eq. (6.39) over the variables $\lambda^\downarrow$ taking the distribution $P_0(\lambda^\downarrow) = \prod_j P_0(\lambda_j^\downarrow)$, we obtain the overlap for the thermal state. The integral in the variable $\lambda^\downarrow$ is a Gaussian integral and the resulting visibility reads:

$$\mathcal{O}(t) = \frac{Z^2\,\mathrm{e}^{\mathrm{i}\tilde{\varphi}}\,\mathrm{e}^{\mathcal{G}}}{\langle\hat{\mathrm{n}}_1^\downarrow\rangle\cdots\langle\hat{\mathrm{n}}_{3N}^\downarrow\rangle}\frac{\exp\left\{\frac{1}{4}\mathcal{L}^T\mathcal{X}^{-1}\mathcal{L}\right\}}{\sqrt{\det\Omega\det\mathcal{X}}}\,. \tag{6.46}$$

This is the main result for the overlap for any initial temperature T and any number of ions; it is valid as long as the harmonic approximation

is feasible (cf. the discussion in Chapter 5). The visibility is then simply the absolute value of the overlap. In Eq. (6.46) we have defined a set of new expressions that allowed us to write the result in such a compact form. The rest of this section is devoted to expanding these expressions and relating them to the terms established in the previous chapters. The derivation of these expressions is simply lengthy arithmetic of no considerable difficulty whatsoever; for this reason we have moved it to Appendix E. The derivation of these expressions is not difficult but just lengthy arithmetic, so we leave it here but include it in Appendix E for completeness.

The prefactors in Eq. (6.46) contain two exponentials, whose exponents take the form

$$\tilde{\varphi} = (\varphi[\kappa] - \varphi[\kappa'])/2\,, \tag{6.47}$$

and

$$\mathcal{G} = G(\zeta) + G^*(\zeta') + \sum_{j,k=1}^{3N} \sum_{\alpha,\beta=\pm} \frac{S_j^\alpha[\kappa,\kappa'][\Omega^{-1}]_{jk}^{\alpha\beta} S_k^\beta[\kappa,\kappa']}{4}\,, \tag{6.48}$$

where

$$\zeta_j = \kappa_j + \beta_j^\uparrow\,, \qquad\qquad \zeta_j' = \kappa_j' + \beta_j^\uparrow\,. \tag{6.49}$$

The $6N$-dimensional vector $\mathcal{L}$ is conveniently split into three parts,

$$\mathcal{L} = \mathcal{I} + \mathcal{J} + \mathcal{K}\,. \tag{6.50}$$

The first term on the right-hand side is given by

$$\begin{pmatrix} \mathcal{I}_j^1 \\ \mathcal{I}_j^2 \end{pmatrix} = \begin{pmatrix} I_j^1(\zeta^*) + I_j^2(\zeta')\,\mathrm{e}^{-\mathrm{i}\omega_j^\downarrow t} \\ I_j^2(\zeta^*) + I_j^1(\zeta')\,\mathrm{e}^{+\mathrm{i}\omega_j^\downarrow t} \end{pmatrix} \tag{6.51}$$

where the $3N$-dimensional vectors are

$$I_l^1(\zeta^*) = \sum_{jk} v_{lj} A_{jk} \zeta_k^* - \frac{1}{2} \sum_j \left(v_{lj}\zeta_j + u_{lj}\zeta_j^* \right)\,, \tag{6.52a}$$

$$I_l^2(\zeta^*) = \sum_{jk} u_{lj} A_{jk} \zeta_k^* - \frac{1}{2} \sum_j \left(u_{lj}\zeta_j + v_{lj}\zeta_j^* \right)\,. \tag{6.52b}$$

The second term can be written as

$$\begin{pmatrix} \mathcal{J}_k^1 \\ \mathcal{J}_k^2 \end{pmatrix} = \begin{pmatrix} \beta_j^\downarrow(1 - \mathrm{e}^{-\mathrm{i}\omega_j^\downarrow t}) + \frac{1}{2}\left(J_k^+(\kappa) - J_k^+(\kappa')\,\mathrm{e}^{-\mathrm{i}\omega_k^\downarrow t}\right) \\ \beta_j^\downarrow(\mathrm{e}^{+\mathrm{i}\omega_j^\downarrow t} - 1) + \frac{1}{2}\left(J_k^-(\kappa) - J_k^-(\kappa')\,\mathrm{e}^{+\mathrm{i}\omega_k^\downarrow t}\right) \end{pmatrix}\,, \tag{6.53}$$

with

$$J_k^\pm(\kappa) = \sum_j \Big(\kappa_j(u_{kj} + v_{kj}) \pm \beta_j^\uparrow(u_{kj} - v_{kj}) \Big) \tag{6.54}$$

The third term reads

$$\begin{pmatrix} \mathcal{K}_k^1 \\ \mathcal{K}_k^2 \end{pmatrix} = \sum_{\alpha\beta}\sum_{jk}\left[\begin{pmatrix} \Upsilon_{jl}[\Omega^{-1}]_{jk}^{\alpha\beta} S_k^\beta[\kappa,\kappa'] \\ \Upsilon_{jl}^\alpha[\Omega^{-1}]_{jk}^{\alpha\beta} S_k^\beta[\kappa,\kappa'] \end{pmatrix} + \begin{pmatrix} S_j^\alpha[\kappa,\kappa'][\Omega^{-1}]_{jk}^{\alpha\beta}\Upsilon_{kl} \\ S_j^\alpha[\kappa,\kappa'][\Omega^{-1}]_{jk}^{\alpha\beta}\Upsilon_{kl}^\beta \end{pmatrix}\right], \tag{6.55}$$

where

$$\Upsilon_{jl} = \sum_k A_{jk} v_{lk} - u_{lj}\,, \tag{6.56a}$$

$$\Upsilon_{jl}^{\pm} = \pm\Upsilon_{jl}\,\mathrm{e}^{-\mathrm{i}(\omega_j^\uparrow - \omega_l^\downarrow)t}\,. \tag{6.56b}$$

The matrix $\mathcal{X}$ in Eq. (6.46) is given by the following expression,

$$\begin{pmatrix} \mathcal{X}_{lm}^{11} & \mathcal{X}_{lm}^{12} \\ \mathcal{X}_{lm}^{21} & \mathcal{X}_{lm}^{22} \end{pmatrix} = \begin{pmatrix} 0 & 0 \\ \mathcal{T}_{lm} & 0 \end{pmatrix} + \begin{pmatrix} \Upsilon_{lm}^0 & -\frac{1}{2}\,\mathrm{e}^{-\mathrm{i}(\omega_l^\downarrow - \omega_m^\downarrow)t} \\ -\frac{1}{2} & \Upsilon_{lm}^0\,\mathrm{e}^{+i(\omega_l^\downarrow + \omega_m^\downarrow)t} \end{pmatrix}$$
$$+\sum_{\alpha\beta}\sum_{jk}\begin{pmatrix} \Upsilon_{jl} & 0 \\ 0 & \Upsilon_{jl}^\alpha \end{pmatrix}\begin{pmatrix} [\Omega^{-1}]_{jk}^{\alpha\beta} & [\Omega^{-1}]_{jk}^{\alpha\beta} \\ [\Omega^{-1}]_{jk}^{\alpha\beta} & [\Omega^{-1}]_{jk}^{\alpha\beta} \end{pmatrix}\begin{pmatrix} \Upsilon_{km} & 0 \\ 0 & \Upsilon_{km}^\beta \end{pmatrix}, \tag{6.57}$$

with

$$\Upsilon_{lm}^0 = \frac{1}{2}\sum_j v_{lj}\Upsilon_{jm}\,, \tag{6.58}$$

and the thermal excitation,

$$\mathcal{T}_{lm} = \delta_{lm}\left\langle n_l^\downarrow \right\rangle^{-1}\,. \tag{6.59}$$

The integration in $\lambda^\downarrow$ is facilitated by changing to real and imaginary parts of $\lambda_j^\downarrow = x_j + \mathrm{i}y_j$, thereby introducing

$$\begin{pmatrix} \mathcal{X}_{lm}^{xx} & \mathcal{X}_{lm}^{xy} \\ \mathcal{X}_{lm}^{yx} & \mathcal{X}_{lm}^{yy} \end{pmatrix} = \begin{pmatrix} 1 & 1 \\ \mathrm{i} & -\mathrm{i} \end{pmatrix}\begin{pmatrix} \mathcal{X}_{lm}^{11} & \mathcal{X}_{lm}^{12} \\ \mathcal{X}_{lm}^{21} & \mathcal{Y}_{lm}^{22} \end{pmatrix}\begin{pmatrix} 1 & \mathrm{i} \\ 1 & -\mathrm{i} \end{pmatrix} \tag{6.60}$$

and

$$\begin{pmatrix} \mathcal{L}_j^x \\ \mathcal{L}_j^y \end{pmatrix} = \begin{pmatrix} \mathcal{L}_j^1 + \mathcal{L}_j^2 \\ \mathcal{L}_j^1 - \mathcal{L}_j^2 \end{pmatrix}\,. \tag{6.61}$$

Equations (6.47) to (6.61) allow the calculation of the visibility of any thermal state.

6.2 ANALYSIS OF QUENCHES INCLUDING THE PHOTON RECOIL

First we shall examine the influence of the photon recoil of the Ramsey pulses on the form of the visibility. A previous study (De Chiara et al. 2008) has already analysed the effect of the recoil on the visibility for ion chains in the linear configuration without any state-dependent potential. Here, we shall extend this approach to the quench scenarios examined in Chapter 5. The relevant formulae of Section 6.1 are included into the numerical MATLAB code to account for the effect of the photon recoil.

For this analysis we focus on one particular experimental setup for which we expect the maximal effect of the photon recoil. It turns out that the best suited choice is an ion crystal composed of $^9Be^+$ ions. First, by virtue of Eq. (6.4) the low mass of the $^9Be^+$ ions gives the biggest displacement in phase space for the typical ion species considered in experiments. Second, the relatively short wavelength of the transition between the $S_{1/2}$ and the $P_{1/2}$ levels, which is approximately 313 nm and thus no longer in the visible, but in the UV spectrum, results in large absolute values of the wave vector $\mathbf{k}$. Third, the two metastable states for $^9Be^+$ ions are usually two different hyperfine states of the ground state domain, which are connected via a Raman transition employing the $S_{1/2}$ to $P_{1/2}$ transition. Such a Raman transition is achieved by two laser pulses, each with a wavelength of approximately 313 nm but sufficiently tuned out of resonance to avoid unwanted transition to the $P_{1/2}$ level. The total recoil transferred from the light fields to the ion is then given by the *effective wave vector*, which is given by the difference between the individual wave vectors,

$$\mathbf{k}_{\text{eff}} = \mathbf{k}_{\text{Raman},1} - \mathbf{k}_{\text{Raman},2} \tag{6.62}$$

This allows us to tune the effective wave vector from having double the length of the wave vector of a single photon at 313 nm to virtually zero by just changing the angle ϕ_R between the two Raman pulses.

Here, we shall consider three different values for the angle:

i) $\phi_R = 0$, for no effect of the recoil,

ii) $\phi_R = \pi/2$, for medium effect of the recoil,

iii) $\phi_R = \pi$, for maximum effect of the recoil.

In Figure 6.1 we compare the effect of the recoil for these three values on the visibility. In Figure 6.1a, the signals are in the linear regime we see that the recoil has quite a strong effect compared to the change resulting from the state-dependent potential. This is, however, not a big surprise as the kick obtained by the absorbed and the re-emitted photons leads to a centre-of-mass oscillation of the wavepacket

of the central ion and, by virtue of the Coulomb interaction, of the other ions in the crystal. Therefore, the other normal modes are more excited than in the case of no recoil, and the visibility shows a much more irregular behaviour than in the case without a recoil. The quench inside the state-dependent potential leads here only to an evolution of the spread of the wavefunctions. The visibility including the recoil is always below the visibility with no recoil, and the visibility with a stronger recoil always below the visibility with a medium recoil.

Figure 6.1b shows the analogous plots in the zigzag regime. Here, the visibility including the recoil is always below the visibility without. As the ions are already oscillating around new equilibrium positions due to the quench in the state-dependent potential, the recoil does not have such a large effect as in the linear regime. The only visible effect on this plot scale is therefore a decreased peak height for higher recoil.

A similar behaviour is apparent in the regime close to linear–zigzag instability in Figure 6.1c. The only effect is, again, a decreasing height of the double peaks for stronger recoil.

To show that the recoil has a bigger effect on the visibility in the linear regime than the quench dynamics, we can compare the behaviour of the visibility for fixed recoil and different values of the trapping strength g in Figure 6.2a and of the dipole strength Δ in Figure 6.2c. Although the trapping strength ranges from $g = 0.01$ to $\Delta = 0.10$ there is hardly a difference visible on the plot scale in Figure 6.2a.

The same is true for the dipole whose strength is varied from $\Delta = 0$ to $\Delta = 0.030$, although there is no big difference between the plots in Figure 6.2c. Again, this is rooted in the fact that the photon recoil induces a motion of the centre-of-mass of the wavepackets of the ions while the quench in the state-dependent potential does not. In Figure 6.2d we compare the visibilities for varied Δ in the zigzag regime. The visibility for $\Delta = 0$, i. e. for no quench at all, has a remarkable similarity to visibilities of the linear regime. All other plots are mostly well below the plot for $\Delta = 0$ so that the effect of the quench is more important than that of the photon recoil.

6.3 ANALYSIS OF QUENCHES FOR THERMAL STATES

In this section we analyse the Ramsey interferometer visibility for quenches of an ion Coulomb crystal in a state-dependent potential with the initial motional state of the crystal being a thermal state. The results of Section 6.1 are all integrated into the MATLAB algorithm to enable the calculation of the visibility for thermal states. In this section, we are interested in the effect of the initial thermal occupation of the motional state on the visibility of the Ramsey interferometer, thus we shall restrict ourselves to the case of no photon recoil here.

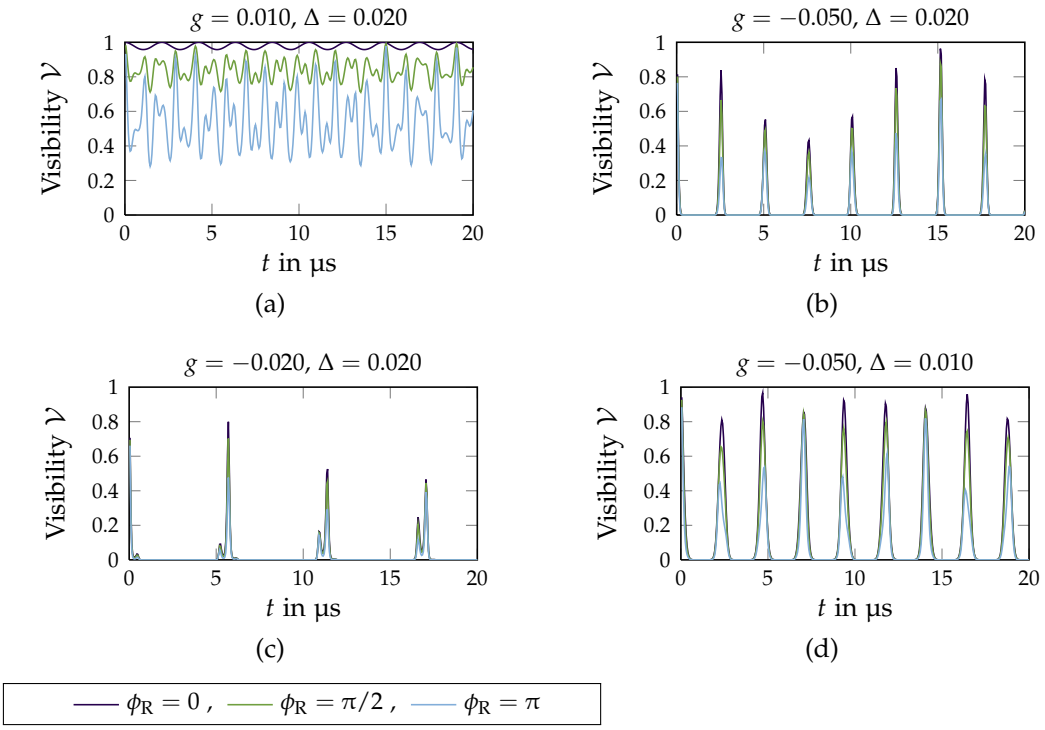

Figure 6.1: Visibility with the photon recoil of the Ramsey pulses included for different effective wave vectors depending on the Raman angle ϕ_R. The plots show (a) the linear regime, (b) and (d) the zigzag regime, (c) the regime close to the instability.

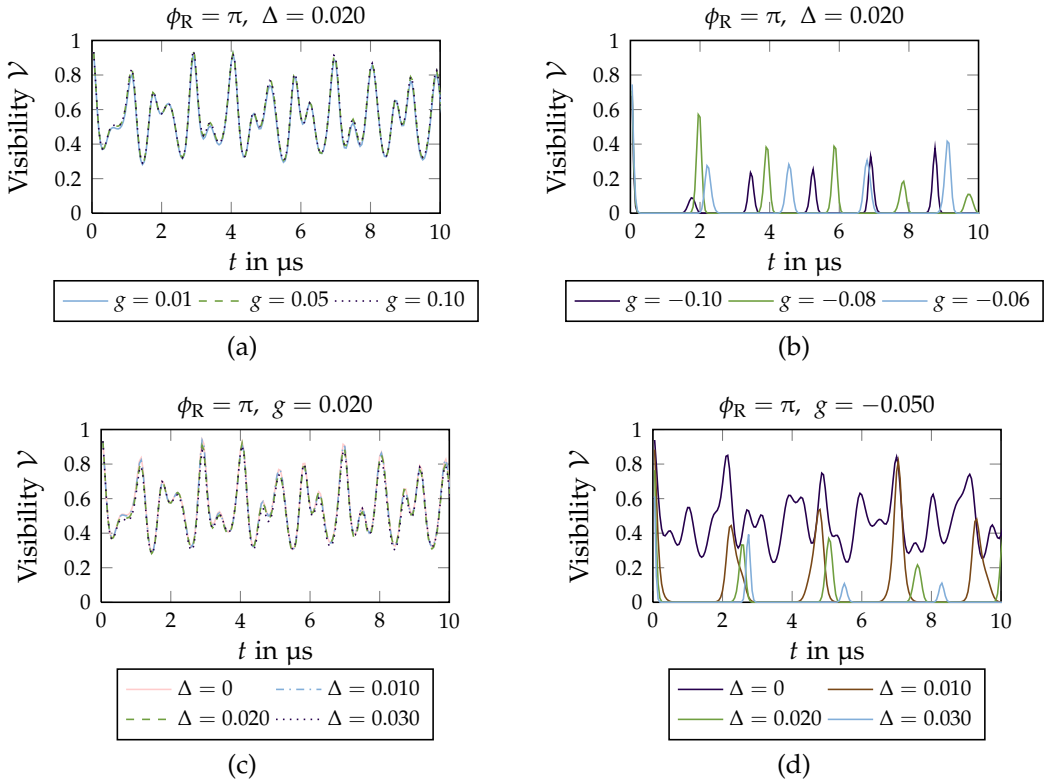

Figure 6.2: Visibility for fixed photon recoil for varied trapping strength g in (a) and (b), and for varied dipole strength Δ in (c) and (d).

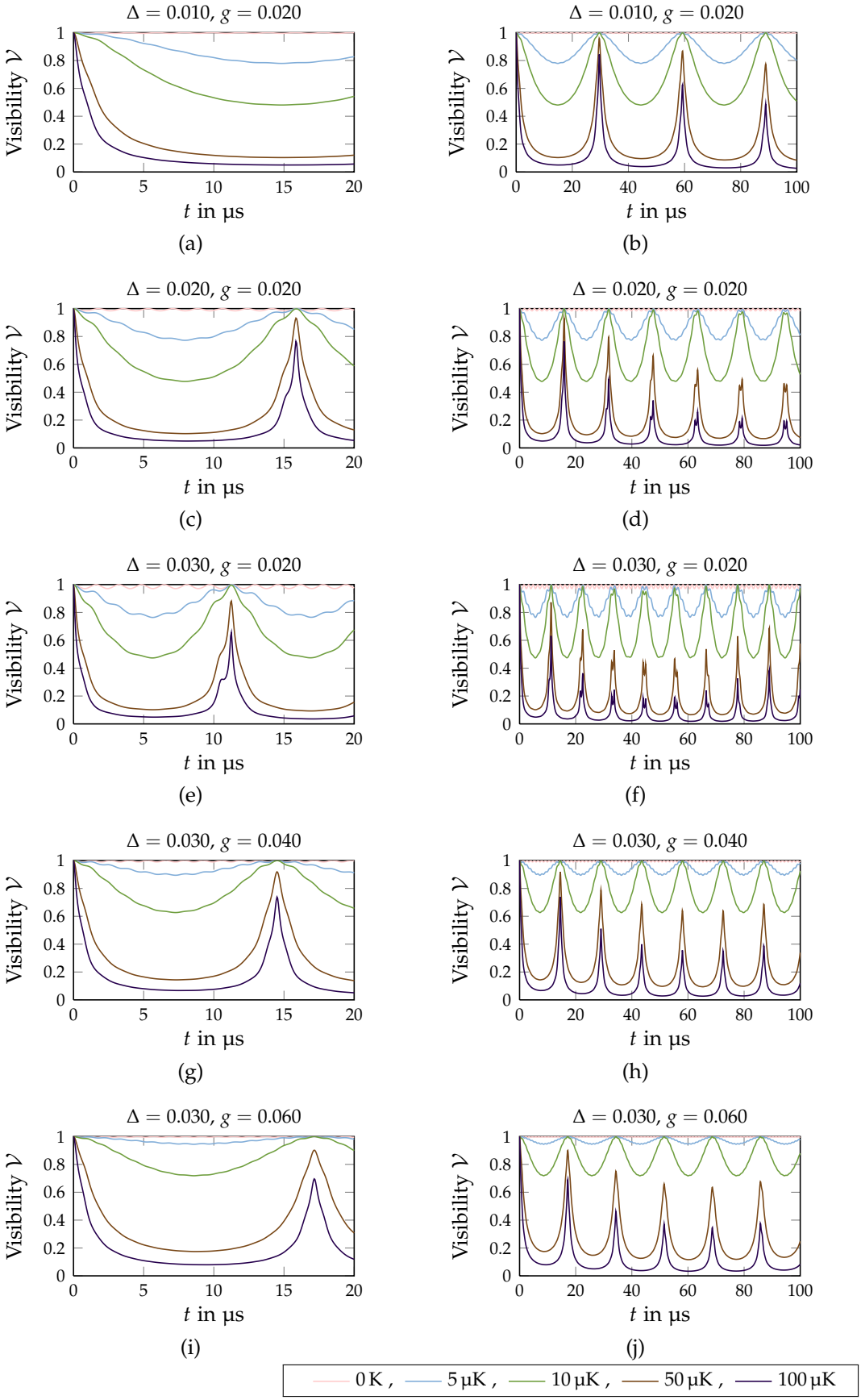

Figure 6.3: Visibility for thermal states in the linear regime for varied trapping strength g and dipole strength Δ, shown for 20 µs on the left and 100 µs on the right side.

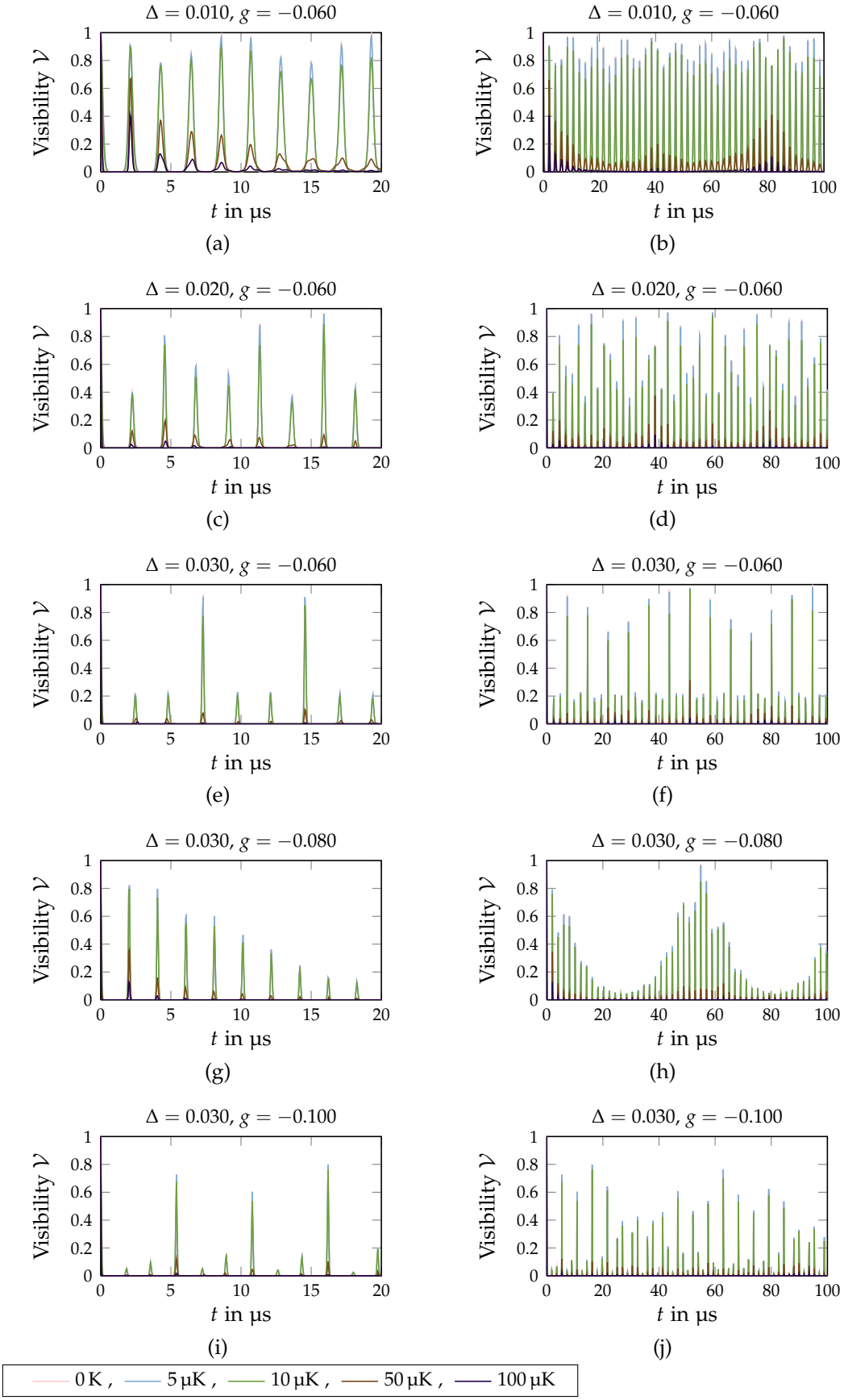

Figure 6.4: Visibility for thermal states in the zigzag regime for varied trapping strength g and dipole strength Δ, shown for 20 µs on the left and 100 µs on the right side.

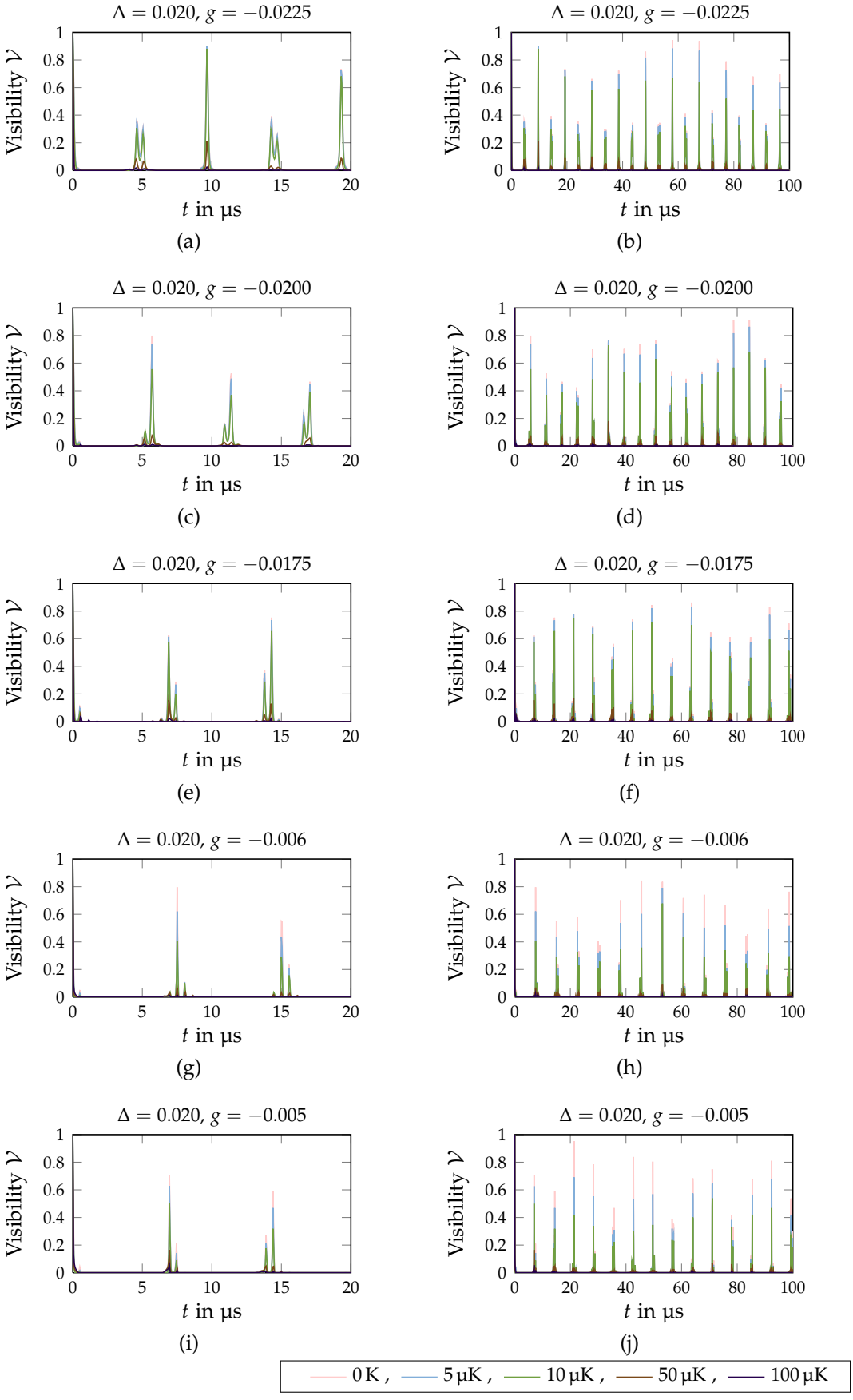

Figure 6.5: Visibility for thermal states in the regime close to the transition for varied trapping strength g and fixed dipole strength $\Delta = 0.020$, shown for 20 µs on the left and 100 µs on the right side.

LINEAR REGIME In Figure 6.3 the visibility is shown for three $^9Be^+$ ions and for various values for the dipole and the trapping strength in the linear regime. In each of the different subplots we compare the visibility for several different initial temperatures. First, we realize that the visibility drops much lower for higher temperatures than for $T = 0\,\mathrm{K}$; at $10\,\mu\mathrm{K}$ the minimum of the visibility decreases down to about 0.5 or less for most of the chosen parameters. The visibility no longer shows the quasi-periodicity of an oscillation-like behaviour that it had for 0 K, but a quasi-periodicity in the form of decay and revivals with a much longer period time. The second observation is that these periodically occurring revivals are *absent* at zero temperature. An ultra-cold temperature of $5\,\mu\mathrm{K}$ already leads to a significant decrease of the minimum value of the visibility. Even for $100\,\mu\mathrm{K}$ these revivals are significantly above zero.

The revival time decreases for increasing dipole strength Δ while keeping the trapping strength fixed, and it increases for increasing trapping strength g while keeping the dipole strength fixed. The drop in the visibility shows not much dependence on the dipole strength Δ, as the minimum value of the visibility at $10\,\mu\mathrm{K}$ is roughly the same in Figures 6.3b, 6.3d and 6.3f. The minimum value of the visibility does depend on the trapping strength, however; see the signal at $10\,\mu\mathrm{K}$ in Figures 6.3f, 6.3h and 6.3j, where this minimum increases for increasing trapping strength g.

In addition, the height of the revival peaks changes from peak to peak for temperatures higher than $10\,\mu\mathrm{K}$; first the height decreases with a minimum attained at around several ten to hundred µs, after which the height of the revival peaks increases again. This change is not visible for $10\,\mu\mathrm{K}$ and lower temperatures.

ZIGZAG REGIME The zigzag regime for the same ion Coulomb crystal is shown in Figure 6.4, again comparing the results for different parameters in the various subfigures and for different temperatures within each subplot. For most of the time the visibility for non-zero temperatures is well below the visibility for 0 K. Yet, the difference between the visibility for 0 K and the visibility for $5\,\mu\mathrm{K}$ is hardly visible on any of the plots. Also for $10\,\mu\mathrm{K}$ the visibility shows only a small decrease compared to the 0 K visibility.

For $50\,\mu\mathrm{K}$, however, the visibility drops to a value below 0.1 for most of the parameters considered here. This drop is generally stronger for higher values of the dipole strength Δ and for lower (more negative) values of the trapping strength g. Yet, from time to time there are occasional revivals higher than 0.1. For lower values of the dipole potential considered here, Figure 6.4b and 6.4d, it appears as if the peak height also follows a quite regular behaviour. The peak height

is changing smoothly from peak to peak and it exhibits a maximum with a revival of the visibility of about 0.4 at around 80 µs for both and around 40 µs for $\Delta = 0.020$. For the other values considered here, such a local peak in the revival height is either not as significant as in the cases before, as in Figure 6.4f where the spike in the peak height is rather abrupt, or it is not visible at all.

For 100 µK the peaks of the visibility remain close to 0 and they rarely reach a height significantly above 0 which would allow us to distinguish them from statistical noise in a measurement. For the lowest value of the dipole strength Δ and for 100 µK these peaks increase before 80 µs and decline afterwards with a maximum peak height of about 0.1, see Figure 6.4b. It is worth emphasizing that each of these maxima in the peak height for 50 µK and 100 µK in Figure 6.4b coincides with a minimum of the peak height for lower temperatures. Thus, for higher temperatures the visibility does not decrease homogeneously over the time domain, but rather it exhibits certain time intervals during which it does not diminish as strong as in other intervals. This corresponds to the thermal revivals we have observed in the linear regime in Figure 6.3.

Regime close to the transition The visibility close to the linear–zigzag instability shows a similar behaviour for finite temperatures to the zigzag case. In Figure 6.5 the peak height decreases for increasing temperatures just as before; however, now the decrease for 5 µK and 10 µK is much stronger than in the zigzag case. In particular, for the case when the quench is across the transition, see Figures 6.5h and 6.5j, the visibility for 5 µK already shows a significant drop compared to the one for 0 K.

Furthermore, we can look at the behaviour of the multiple peaks that are appearing close to the transition. The side peaks do not decrease proportionally to the decrease of the major peak, but rather all peaks attain about the same level in height, as one can see in the plots for 50 µK.

Interpretation of the Results

The occurrence of thermal revivals may be explained in the following way: At higher temperatures the wavefunction experiences an additional thermal dephasing that is absent at $T = 0$ K. This dephasing depends on the energy difference between the two parts of the superposition. To be more specific, the initial state can be rewritten in a

diagonal form in the energy eigenstate basis of the quantum harmonic oscillator for each of the normal modes:

$$\rho_0 = \sum_{n_1,\ldots,n_{3N}=0}^{\infty} c_{n_1,\ldots,n_{3N}} |n_1,\ldots,n_{3N}\rangle_\downarrow \langle n_1,\ldots,n_{3N}| \,. \tag{6.63}$$

We first turn to a simplified discussion for a single mode, which allows us to write the initial density matrix as

$$\rho_0 = \sum_{n=0}^{\infty} c_n |n\rangle_\downarrow \langle n| \,. \tag{6.64}$$

The time evolution operator for the state-dependent potential in the ground state leads to time-dependent phase factors that cancel out each other:

$$\hat{U}_\downarrow(t)\rho_0\hat{U}_\downarrow^\dagger(t) = \sum_{n=0}^{\infty} c_n \, \mathrm{e}^{-\mathrm{i}n\omega^\downarrow t} |n\rangle_\downarrow \langle n| \, \mathrm{e}^{+\mathrm{i}n\omega^\downarrow t} = \sum_{n=0}^{\infty} c_n |n\rangle_\downarrow \langle n| \overset{(6.64)}{=} \rho_0 \,. \tag{6.65}$$

Here we need to keep in mind that the second equality sign has the meaning of an equivalence relation modulo the global phases of the eigenstates $|n\rangle_g$. A pure state written as a state vector would exhibit these phases that cannot be measured directly, while the same state written as a density matrix does not attain these phases. As we have seen, the density matrix does not keep track of these phases originating from the time evolution. This is probably the origin of the widespread but wrong claim that a thermal state does not have a phase.

The calculation for the multi-mode case shows a similar result, the only difference being that $3N$ pairs of exponentials cancelling each other now:

$$\begin{aligned}
&\hat{U}_\downarrow(t)\rho_0\hat{U}_\downarrow^\dagger(t) \\
&= \sum_{n_1,\ldots,n_{3N}=0}^{\infty} c_{n_1,\ldots,n_{3N}} \, \mathrm{e}^{-\mathrm{i}n_1\omega_1^\downarrow t} \cdots \mathrm{e}^{-\mathrm{i}n_{3N}\omega_{3N}^\downarrow t} \times \\
&\qquad\qquad \times |n_1,\ldots,n_{3N}\rangle_\downarrow \langle n_1,\ldots,n_{3N}| \, \mathrm{e}^{+\mathrm{i}n_1\omega_1^\downarrow t} \cdots \mathrm{e}^{+\mathrm{i}n_{3N}\omega_{3N}^\downarrow t} \\
&= \sum_{n=0}^{\infty} c_n |n\rangle_\downarrow \langle n| \overset{(6.63)}{=} \rho_0 \,.
\end{aligned} \tag{6.66}$$

The visibility of the Ramsey interferometer as discussed in Chapter 4 does in fact measure the interference between two different time evolutions of the same initial state. The corresponding term in the result for the visibility in Section 4.4 is the absolute value of the overlap given by Eq. (4.60), which contains the term

$$\hat{U}_\uparrow(t)\rho_0\hat{U}_\downarrow^\dagger(t) \,,$$

where we dropped the photon recoil operators.

Evaluating this term, starting with the single-mode case, we need to first change the basis of the state vector onto which the unitary $\hat{U}_{\uparrow}(t)$ is applied on,

$$|n\rangle_g = \sum_{m=0}^{\infty} S_{nm} |m\rangle_e \,, \tag{6.67}$$

where the factors S_{nm} can be calculated by the procedure outlined in Section 3.3.2. The initial state may be rewritten as

$$\rho_0 = \sum_{n=0}^{\infty} \sum_{m=0}^{\infty} c_n S_{nm} |m\rangle_{\uparrow\downarrow}\langle n| \,. \tag{6.68}$$

For the term relevant for the visibility we get

$$\hat{U}_{\uparrow}(t)\rho_0\hat{U}_{\downarrow}^{\dagger}(t) = \sum_{n=0}^{\infty} \sum_{m=0}^{\infty} c_n S_{nm} \, \mathrm{e}^{-\mathrm{i}m\omega^{\uparrow}t} |m\rangle_{\uparrow\downarrow}\langle n| \, \mathrm{e}^{+\mathrm{i}n\omega^{\downarrow}t} \,, \tag{6.69}$$

we find that there is no cancellation of phases in general, and that the expression $\hat{U}_{\uparrow}(t)\rho_0\hat{U}_{\downarrow}^{\dagger}(t)$ is not the same as ρ_0. The difference is in the phase factors $\exp\{\mathrm{i}(n\omega^{\downarrow} - m\omega^{\uparrow})t\}$ for the term containing $|m\rangle_{\uparrow\downarrow}\langle n|$, which would need to be all equal to 1 at the same time. These exponentials are equal to 1 for the times

$$\tau_{mn}^{\text{thermal}} = 2\pi(n\omega^{\downarrow} - m\omega^{\uparrow})^{-1} \text{ for all } m, n = 0, 1, 2, \ldots \tag{6.70}$$

Now, for all possible pairs (m, n) these times are generally incommensurable, yet for certain values it is possible to identify common times for which a group of terms equals 1 at the same time. Take for instance the two cases $2\pi(\omega^{\downarrow} - \omega^{\uparrow})^{-1}$ and $2\pi(2\omega^{\downarrow} - 2\omega^{\uparrow})^{-1}$. The second term is just half the first one, so every second revival of the second term coincides with a revival of the first term. A similar reasoning holds for higher values of $m = n$, so all such factors have a revival at the same time, given by $2\pi(\omega^{\downarrow} - \omega^{\uparrow})^{-1}$. However, this does not hold for terms with $m \neq n$ in general. If those terms are important or not depends on the form of the factor S_{nm}, in particular whether the off-diagonal parts of S_{nm} are comparable to the diagonal ones or not. In the case of quenches between two similar states, the diagonal terms have much bigger absolute values than the off-diagonal, so we can expect to observe a revival of the visibility at the time given by $2\pi(\omega^{\downarrow} - \omega^{\uparrow})^{-1}$.

In the multimode case, we need to extend these considerations to all the normal modes, so that we obtain revival times for all normal mode frequencies, $2\pi(\omega_1^{\downarrow} - \omega_1^{\uparrow})^{-1}, \ldots, 2\pi(\omega_{3N}^{\downarrow} - \omega_{3N}^{\uparrow})^{-1}$. For quenching an ion Coulomb crystal in the particular setting considered in this thesis, the differences between the normal mode frequencies are all

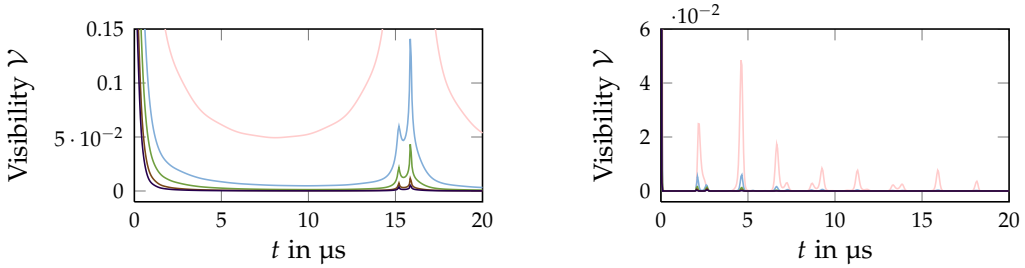

(a) $\Delta = 0.020$, $g = 0.020$ (b) $\Delta = 0.030$, $g = 0.060$

Figure 6.6 Visibility as a function of the time t between the two Ramsey pulses for three $^9Be^+$ ions, with the axial trapping frequency given by $2\pi \times 1\,\text{MHz}$. In all plots the crystal is prepared in a linear chain configuration before the quench, and the dipole strength is chosen to be $\Delta = 0.020$ while the transverse trapping strength g is varied.

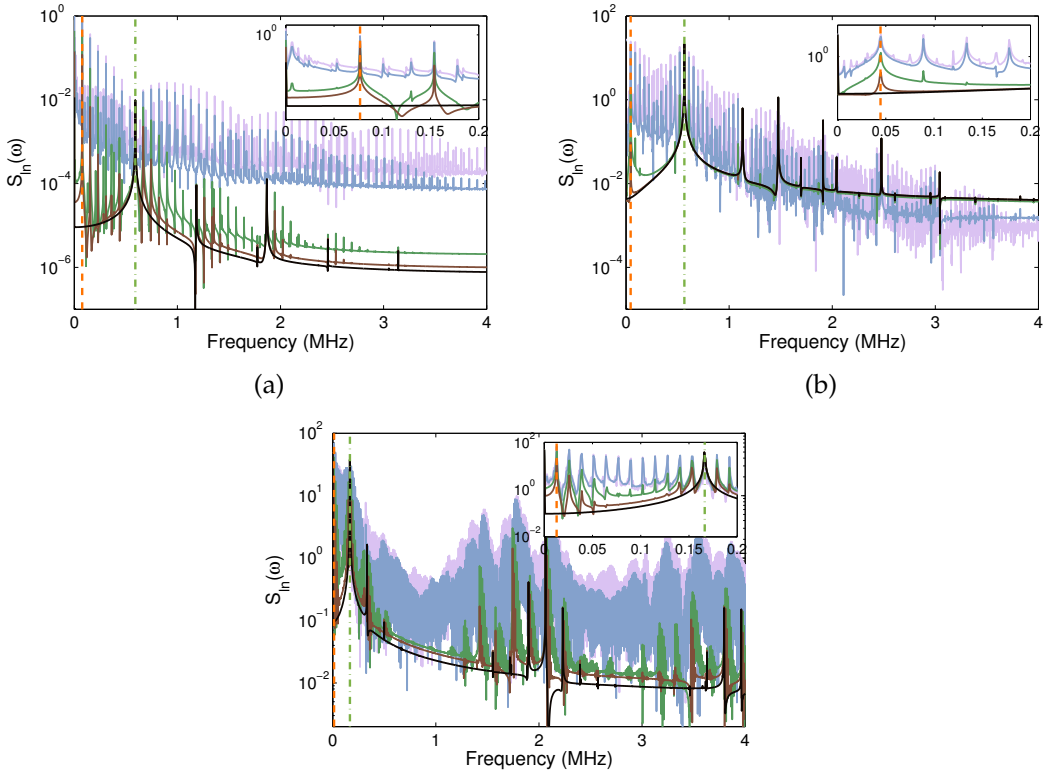

(a) (b)

(c)

Figure 6.7 Semilog plot of the logarithmic spectra of the visibility for thermal states for a dipole strength of $\Delta = 0.025$. These are evaluated in (a) the linear regime for $g = 0.020$, (b) the zigzag regime for $g = -0.100$, and (c) for $g = -0.050$ for the regime close to the transition. The insets show a zoom of the low frequency domain. The vertical green dashed lines mark the frequency of the zigzag eigenmode (or double the frequency for the linear case), and the orange dashed line gives the beating frequency. (Figures taken from Baltrusch, Cormick and Morigi (2013) © held by American Physical Society)

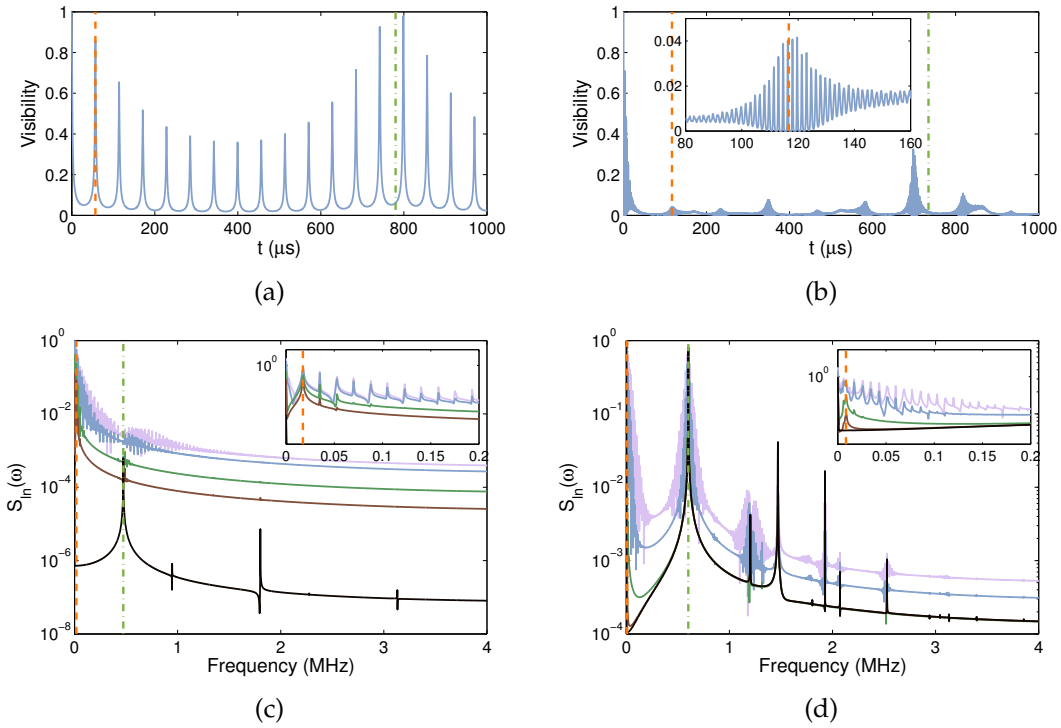

Figure 6.8 Long time behaviour of the visibility for weak quenches for $\Delta = 0.005$ (a) in the linear regime for $g = 0.020$, and (b) in the zigzag regime for $g = -0.100$. The orange dashed line marks the revival time caused by the beating between the zigzag eigenfrequencies, the green dashed line the beating between the transverse centre of mass frequencies. (c) and (d) show the corresponding logarithmic spectra with the beating frequencies highlighted by the vertical dashed lines. (Figures taken from Baltrusch, Cormick and Morigi (2013) © held by American Physical Society)

quite small with the exception of the difference of the zigzag mode frequencies. Additionally the ground states before and after the quench in the linear regime are different from each other only in two normal modes, the zigzag mode and the COM-mode in y-direction. Therefore, we expect the visibility to exhibit partial revivals at about the times $2\pi(\omega_{zz}^{\downarrow} - \omega_{zz}^{\uparrow})^{-1}$, with a slower modulation of the revival height at the times $2\pi(\omega_{\mathrm{COM},y}^{\downarrow} - \omega_{\mathrm{COM},y}^{\uparrow})^{-1}$.

The appearance of these thermal revivals can also be analysed in the frequency domain. The frequency differences or *beat frequencies* should turn up as certain peaks in the spectrum of the visibility or the spectra of the logarithmic visibility, whichever is more suitable, see the discussion in Chapter 5.

In Figure 6.7 the spectra for the logarithmic visibility are plotted for different temperatures. The spectra at $T = 0\,\mathrm{K}$ have a few peaks, but as the temperature rises more and more peaks become visible. These additional peaks are integer multiples of the beat frequency $\omega_{\mathrm{beat,zz}} = \omega_{zz}^{\downarrow} - \omega_{zz}^{\uparrow}$, which is highlighted by the orange dashed verical line. At 50 µK and 100 µK these peaks are well distributed over a wide frequency range.

In Figure 6.8 the thermal revivals show an additional dependence on longer times. To analyse this dependence we take the case of a very weak dipole potential by choosing $\Delta = 0.005$, and examine the visibility for 100 µK for a longer time, here $T_f = 1\,\mathrm{ms}$ in Figure 6.8. We observe in Figure 6.8a that the peak height of the thermal revivals first decreases to something around 0.4 but then increases again to a value very close to 1 at around 800 µs. This maximum peak height is close to the revival time of the COM-mode in y-direction, $2\pi(\omega_{\mathrm{COM,y}}^{\downarrow} - \omega_{\mathrm{COM,y}}^{\uparrow})$; however, it does not coincide exactly. When comparing the heights of the observed revival peaks and drawing an envelope to them, it looks as if this revival time were at the centre of this envelope.

For the signal in the zigzag case, shown in Figure 6.4, the visibility first seems to be decaying, with thermal revivals very close to zero. However, it is not a complete loss of coherence as the minimum visibility is rising from time to time (and falling again shortly after). Still one might ask if this decay is irreversible. The coherence of the Ramsey interferometer has become deteriorated due to the dephasing of the eigenmodes with incommensurable eigenfrequencies, so a full revival is not possible. But revivals close to a full revival are possible. Here, at around 700 µs, there is a partial revival of about 0.35. Again, the revival time associated with the beat frequency of the transverse COM modes is located close by. The reason for the revival not being as strong as in the linear case might stem from the fact that for the zigzag quench there are many more modes involved. Thus, for a full revival the revival times of the beat frequencies of all these modes

should be integer multiples of each other, which will eventually be the case at some, much later, point in time.

DISCUSSION AND CONCLUSIONS

In this thesis, we discussed the visibility of a Ramsey interferometer kind of experiment with a small trapped ion Coulomb crystal that is subjected to a state-dependent potential. In the first part, we examined the properties of ion Coulomb crystals in state-dependent potentials, while in the second part we analysed the scheme of Ramsey interferometry to extract information about the motional state of an ion Coulomb crystal in a state-dependent potential.

After reviewing the physics of trapped ion Coulomb crystals in Chapter 1, we have shown in Chapter 2 that one possible way to realize such a state-dependent potential is to combine a dipole trap with the ion trap apparatus such that a meta-stable excited state of an ion experiences a position-dependent ac-Stark shift. The excitation of a single ion into this meta-stable state by a coherent laser pulse changes the spectrum of the normal modes, and given a suitable choice of the involved parameters, even the equilibrium positions of all ions of a small ion crystal can be changed. When the ion Coulomb crystal is close to the structural transition between a linear chain and a zigzag chain configuration, the state-dependent potential can also induce this transition even though only the electronic state of a single ion is excited. We have characterized the possible structural configurations for a three-ion crystal as well as the transition between these configurations in dependence on the dipole trap and ion trap parameters.

For each of the different state-dependent structures the motional state can be equivalently described by eigenstates of a harmonic oscillator in a second-order approximation of the potential around the corresponding equilibrium positions. In Chapter 3, we derived the transformation between these different harmonic oscillator bases; the obtained formulae are applicable in the region of parameter space where the quadratic approximation is feasible for both basis expansions simultaneously. On the basis of this transformation, we were then able to analytically calculate the dynamics of the motional states following a local rapid change of the potential energy which can be induced by an excitation of the electronic state of an ion that is exposed to a state-dependent potential.

In Chapter 4 we reviewed the scheme of a Ramsey interferometer type of experiment with the aim of analysing the dynamics by an experimental technique. There, two branches of the total wavefunction

evolve via state-dependent dynamics after the central ion is put into a quantum superposition state. After interfering the two differently evolved branches again, the probabilities for measuring the central ion in one or the other electronic state vary in dependence on an experimentally controllable phase shift introduced for one evolution path only. The amount by which these probabilities can depart from the indeterministic result of $1/2$ for varied phase shifts is characterized by the visibility of the interferometer, which depends on the distinguishability of the motional states of the two branches. Therefore, the time-dependence of the visibility of a state-measurement repeated with varied phases between the two evolution paths yields an indirect probe of the motional state dynamics that we examined in the following chapters.

In Chapter 5 we analysed the properties of the visibility in dependence on the dynamics induced by the first Ramsey pulse, leading to a dynamical evolution that can be regarded as a local quantum quench. After this quench the motional state of the crystal is in a superposition of two branches with different motional states; that superposition may even evolve around different equilibrium positions. For this, we calculated an analytical expression for the visibility of a Ramsey interferometer setup as a function of the time between the two Ramsey pulses. We then investigated the dependence on the trap anisotropy, on the strength of the dipole potential, and in Chapter 6, on the strength of the photon recoil of the Ramsey pulses and on the temperature.

The theoretically calculated visibility curves yielded the following observations: The visibility shows a fundamentally different behaviour depending on whether the ion Coulomb crystal is initially prepared in the linear or the zigzag configuration. Starting from the zigzag regime, the visibility shows a series of regularly occurring revivals whose appearance is completely dominated by the zigzag normal mode, the mode that is excited the most by the quench. We have analysed the properties of the revival peaks like height, width, and separation as a function of the parameters. Variations in the height of the revivals are rooted in coincidences (or the absence thereof) of full periods with other modes. In the linear regime, the visibility stays almost close to unity with small oscillations, which again are mainly caused by the dynamics of the zigzag mode. We further compared the visibility for different ion masses and trapping frequencies to identify the ideal specifications for an experimental realization.

The effect of the photon recoil on the visibility is mainly detrimental, and larger in the linear regime for the considered parameters than in the zigzag regime, where the oscillation induced by the quench dominates the behaviour of the visibility. Allowing for an initially

thermally excited motional state of the crystal, we observed a large drop of the visibility even for fractions of a mK. We discovered a new time scale totally absent in the $T = 0\,\mathrm{K}$ case that is induced by an interplay of the dynamical phases of the thermal state. This interplay can lead to thermal revivals, which are more pronounced in the linear regime.

Probably the most significant finding of this thesis is that, even with a three-ion crystal and at temperatures as low as $100\,\mu\mathrm{K}$, coherence between the electronic states of the central ion is remarkably reduced, as is evident in the drop in visibility at these temperature. This is even true for a quench where the equilibrium positions do not change at all, as is the case for local quenches in the linear regime. We would like to emphasize that the model analysed here only takes into consideration harmonic oscillator dynamics without anharmonic corrections; it regards the ion Coulomb crystal as a closed system without interaction with the environment and without any perturbation by external noise. The cause of the reduction in visibility is a dephasing process that is solely induced by the dynamical phases of the initial thermal state. It is therefore necessary to further investigate the importance of this drop in visibility in relation to other decoherence and noise sources; it might well turn out that the dephasing at such low temperatures of fractions of mK, which are in the range of temperatures that are achieved regularly in experiments with trapped ions, may reduce the coherence properties of quantum systems to a greater extent than previously considered.

Another important finding is the possibility of obtaining the motional frequency spectrum from the Fourier transform of the visibility. This provides an independent way of measuring the eigenfrequencies of the normal modes, complementing the established method of resolved-sideband spectroscopy (Kaufmann et al. 2012) even outside the Lamb-Dicke regime. The method involving Ramsey interferometry can be calibrated by local quenches with specific chosen symmetries that excite only certain normal modes of the ion Coulomb crystal, and it can then be applied to measuring the normal modes of an arbitrary motional state. Moreover, calculating the visibility for an initial motional state of the ion Coulomb crystal prepared in coherent states or energy eigenstates in the normal modes could provide an independent tool to verify the creation of certain quantum states in an experiment.

Since ultrafast Ramsey pulses (Campbell et al. 2010; Mizrahi, Senko et al. 2013), as required for the setup discussed here, can be created with a much shorter duration than a micromotion period, one possible application could involve a direct measurement of the micromotion by the Ramsey interferometer scheme suggested here – provided the

phase of the micromotion drive is synchronized with the timing of the Ramsey pulses (otherwise one would get an averaged measurement over the different phases of the micromotion). In fact, any modifications of the overlap originating from the micromotion should be directly observable in the visibility as a modulation with the frequency of the rf-field. An extension of the calculations presented here, using the approach of Landa et al. (2012b,a) for linearising the micromotion, should be feasible.

A further extension to the presented work would be to allow for slow Ramsey pulses as currently employed in the majority of trapped ion experiments. The sudden approximation would then, of course, no longer hold and we would need to calculate the state-dependent evolution of the total wavefunction during the Ramsey pulses. If a full calculation should prove infeasible, an approximative solution might be found by replacing the $\pi/2$-pulses with two $\pi/4$ pulses in the sudden approximation; those again with two $\pi/8$-pulses, and so on, taking the limit to infinite pulses – similarly to the approach discussed by Ramsey (1980). One possible application would be the simulation of Franck-Condon transitions just as discussed by Hu et al. (2011).

A further possible application might be found in measuring the nonlinearities in the potential energy by comparing the measurement of the visibility with the calculated results presented here for quenches exploring the excluded regimes in Figure 5.3. Additionally, one could extend the calculation presented in Section 5.2 by adding nonlinear terms to the unitary evolution operator and applying time-dependent perturbation theory for the evaluation of the matrix elements in the calculation of the overlap.

In this context, it is interesting to consider to what kind of states the ion Coulomb crystal evolves in the long-time limit after the local quantum quench. Without nonlinear corrections, the initial state of the evolving branch is a Gaussian state and remains so for all times; any initial excitation in one normal mode can never be transferred to another normal mode by the Hamiltonian of the free evolution alone. So by including the nonlinear terms in the interaction energy, the system might be able to exhibit a kind of equilibration to some quasi-stationary state such that the system remains close to this state nearly all the time.

Observing the long-time behaviour of the visibility after weaker quenches as per Figure 6.8, we have found that the visibility is able to exhibit strong (in the linear regime almost perfect) revivals at longer time scales; analysing ion Coulomb crystals with more ions would just shift these revivals to much longer times (necessarily larger than the inverse of the smallest gap in the frequency spectrum), thereby only mimicking an equilibration that does not actually takes place.

Therefore, it seems more promising to analyse the effect of a nonlinear interaction on the constructive interference at the revival times for a rather small ion Coulomb crystal instead. The nonlinearities can become important even for weak quenches that are close to the linear–zigzag transition. However, as the zigzag mode frequency changes dramatically when close to the transition and therefore dominates the behaviour of the visibility, one could consider restricting the proposed scheme to quenches that are not exciting the zigzag mode; one possible realization would be aligning the dipole trap axis perpendicularly to the trap axis, which would then excite mainly the Egyptian mode instead.

Other approaches applied the Loschmidt echo or quantum fidelity approach to the equilibration after quantum quenches (Campos Venuti and Zanardi 2010a,b; Campos Venuti, Jacobson et al. 2011; Jacobson et al. 2011). In particular, there the values of the Loschmidt echo (which closely corresponds to the visibility in our work) were analysed as if they were random variables; the behaviour of the distribution function of the values so obtained showed a double-peaked behaviour close to a critical point of the model considered, while the distribution approached a Gaussian normal distribution for regular parameters. This was interpreted as a probabilistic approach to an equilibrium state justified by the universal behaviour of the functional dependence of the distribution. For quenches with ion Coulomb crystals, a preliminary analysis of the long-time captured visibility in various regimes confirms the observation of the two regimes, with the Gaussian far away and the double-peak close to the linear–zigzag transition. What is still missing, however, is the confirmation that the equilibration is independent on the choice of the initial state, which could be obtained by analysing e. g. the long-time behaviour of the visibility for coherent states with different phases and amplitudes. However, further analysis is necessary to put this preliminary numerical observation onto a firm theoretical basis like in the publications cited above, for instance by establishing a better understanding of the relation of the visibility to various correlation functions.

Other theoretical approaches managed to find relations that connect the visibility of such a Ramsey interferometer scheme to the work distribution for non-equilibrium quenches (Dorner et al. 2013; Mazzola et al. 2013; Batalhão et al. 2014), and for a non-Markovianity measure of open quantum systems (Haikka et al. 2012; Borrelli et al. 2013).[1]

1 Some of the publications cited here reported results in the regime extremly close to the linear–zigzag transition, so that their model departs from a faithful description of an ion Coulomb crystal since they are neglecting the restrictions imposed by the harmonic approximation.

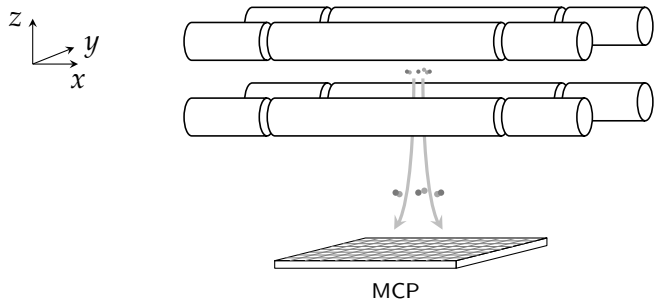

Figure 1: Sketch of a possible setup for measuring the superposition of crystalline structures via a free fall expansion, where the spatial positions of the ions are recorded on an MCP. For the verification of the superposition of different crystalline structures one needs to ensure that the wavepackets of the two branches overlap at the position of impact on the MCP.

A legitimate objection is whether the setup analysed in this thesis is feasible in an experiment, and whether one can expect an implementation in the near future. The Ramsey interferometry scheme has already been implemented for interferometry with a single trapped ion in the experiment of Mizrahi, Senko et al. (2013), using ultrafast Ramsey pulses that have the additional merit of also enabling entangling operations on much faster time scales than the currently predominantly employed slower manipulation techniques for quantum computation.

Trapping of ions in a dipole trap has been successfully demonstrated by Schneider, Enderlein et al. (2010), although with the restriction of a high excitation probability to the upper state of the dipole trapping owing to technical reasons resulting from the isotope involved. Yet this is likely not a lasting problem for the implementation of a state-dependent potential with low excitation probability via an optical dipole trap, as these are presumably useful for many interesting applications, in particular for quantum simulation.

Basically, all the requirements for the experimental actualization of the scheme presented in this thesis have been successfully demonstrated, and we expect the required techniques to spread further, making an actual implementation in the next years quite probable.

A more speculative potential expansion is the independent measurement of the superposition of the different crystal structures. Here, we might draw on a similar technique as applied for BECs, namely the time-of-flight measurement. In our case, outlined in Figure 1, we would also switch off the trapping potential and let the ions fall onto a multi-channel plate (MCP) (or use an electric field to accelerate them toward the plate) where their spatial positions are registered – just as in the experiment of Schellekens et al. (2005), where an MCP was used to measure two-body correlation functions of a BEC. For spatial regions where the wavepackets overlap we should see a spatial

interference pattern when we record their impact coordinates on the MCP indiscriminately of the electronic state they are in. There are two technical difficulties that need to be overcome: First, to ensure that the wavepackets of the two branches of the total ion Coulomb crystal wavefunction overlap with each other at the MCP; and second, that the wavepackets expand wide enough for the interference fringes to become resolvable on the MCP. This, of course, requires that the COM-position of the ions for the two wavepackets depart from each other slower than their spreads widen during the expansion. Here, it could also be advantageous to employ the ion implantation technique of Schnitzler et al. (2009) and draw on the various established techniques for focussing used in charged-particle beams (Pierce 1954). Of course, at this stage the theoretical and experimental feasibility of such a setup is still highly speculative.

APPENDIX

A

CALCULATION OF THE NORMAL MODES

A.1 TAYLOR EXPANSION OF THE POTENTIAL ENERGY

The potential energy given by Eqs. (1.13), (1.22b) and (1.22c) can be rewritten as

$$V = \sum_n \left[x_n^2 + \alpha_n y_n^2 + \beta_n z_n^2 \right] + \sum_{n,l} |1 - \delta_{nl}| \frac{1}{d_{nl}} , \tag{A.1}$$

where the shorthand

$$d_{nl} = \|\mathbf{r}_n - \mathbf{r}_l\| = \sqrt{(x_n - x_l)^2 + (y_n - y_l)^2 + (z_n - z_l)^2} , \tag{A.2}$$

is the distance between ions n and l, respectively. The expression $\sum_{n,l} |1 - \delta_{nl}|$ is a shorthand to replace the restricted sum $\sum_{n,l;n\neq l}$, facilitating the following calculations of the derivatives.

A.1.1 *First order*

The first derivatives are given by

$$\frac{\partial V}{\partial x_n} = \quad x_n - \sum_l |1 - \delta_{nl}| \frac{x_n - x_l}{d_{nl}^3} , \tag{A.3a}$$

$$\frac{\partial V}{\partial y_n} = \alpha_n y_n - \sum_l |1 - \delta_{nl}| \frac{y_n - y_l}{d_{nl}^3} , \tag{A.3b}$$

$$\frac{\partial V}{\partial z_n} = \beta_n z_n - \sum_l |1 - \delta_{nl}| \frac{z_n - z_l}{d_{nl}^3} . \tag{A.3c}$$

A.1.2 *Second order*

The second derivatives read

$$\frac{\partial^2 V}{\partial x_n \partial x_l} = \delta_{nl} \left[1 \ - \sum_k |1 - \delta_{nk}| S_{nk}^{xx} \right] + |1 - \delta_{nl}| S_{nl}^{xx} , \tag{A.4a}$$

$$\frac{\partial^2 V}{\partial y_n \partial y_l} = \delta_{nl} \left[\alpha_n - \sum_k |1 - \delta_{nk}| S_{nk}^{yy} \right] + |1 - \delta_{nl}| S_{nl}^{yy} , \tag{A.4b}$$

$$\frac{\partial^2 V}{\partial z_n \partial z_l} = \delta_{nl}\left[\beta_n - \sum_k |1-\delta_{nk}| S^{zz}_{nk}\right] + |1-\delta_{nl}| S^{zz}_{nl}\,, \tag{A.4c}$$

and

$$\frac{\partial^2 V}{\partial x_n \partial y_l} = \delta_{nl}\sum_k |1-\delta_{nk}| S^{xy}_{nk} - |1-\delta_{nl}| S^{xy}_{nl}\,, \tag{A.4d}$$

$$\frac{\partial^2 V}{\partial x_n \partial z_l} = \delta_{nl}\sum_k |1-\delta_{nk}| S^{xz}_{nk} - |1-\delta_{nl}| S^{xz}_{nl}\,, \tag{A.4e}$$

$$\frac{\partial^2 V}{\partial y_n \partial z_l} = \delta_{nl}\sum_k |1-\delta_{nk}| S^{yz}_{nk} - |1-\delta_{nl}| S^{yz}_{nl}\,. \tag{A.4f}$$

We introduced here the shorthands

$$S^{xx}_{nl} = \frac{1}{d^3_{nl}} - 3\frac{(x_n - x_l)^2}{d^5_{nl}}\,, \tag{A.5a}$$

$$S^{yy}_{nl} = \frac{1}{d^3_{nl}} - 3\frac{(y_n - y_l)^2}{d^5_{nl}}\,, \tag{A.5b}$$

$$S^{zz}_{nl} = \frac{1}{d^3_{nl}} - 3\frac{(z_n - z_l)^2}{d^5_{nl}}\,, \tag{A.5c}$$

$$S^{xy}_{nl} = 3\frac{(x_n - x_l)(y_n - y_l)}{d^5_{nl}}\,, \tag{A.5d}$$

$$S^{xz}_{nl} = 3\frac{(x_n - x_l)(z_n - z_l)}{d^5_{nl}}\,, \tag{A.5e}$$

$$S^{yz}_{nl} = 3\frac{(y_n - y_l)(z_n - z_l)}{d^5_{nl}}\,. \tag{A.5f}$$

A.1.3 *Third order*

The third order derivatives are given in the following from,

$$\begin{aligned}\frac{\partial}{\partial \chi_n}\frac{\partial}{\partial v_l}\frac{\partial}{\partial \zeta_m} V = \delta_{nl}\delta_{nm}\sum_k |1-\delta_{nk}| R^{\chi v \zeta}_{nk} - \delta_{nl}|1-\delta_{nm}| R^{\chi v\zeta}_{nm} \\ - |1-\delta_{nl}|(\delta_{nm} - \delta_{lm}) R^{\chi v\zeta}_{nl}\end{aligned}\,, \tag{A.6}$$

where $\chi, v, \zeta \in \{x, y, z\}$ and the following shorthands have been introduced:

$$R^{xxx}_{nl} = 9\frac{x_n - x_l}{d^5_{nl}} - 15\frac{(x_n - x_l)^3}{d^7_{nl}}\,, \tag{A.7a}$$

$$R^{yyy}_{nl} = 9\frac{y_n - y_l}{d^5_{nl}} - 15\frac{(y_n - y_l)^3}{d^7_{nl}}\,, \tag{A.7b}$$

$$R^{zzz}_{nl} = 9\frac{z_n - z_l}{d^5_{nl}} - 15\frac{(z_n - z_l)^3}{d^7_{nl}}\,, \tag{A.7c}$$

$$R_{nl}^{xxy} = 3\frac{y_n - y_l}{d_{nl}^5} - 15\frac{(x_n - x_l)^2(y_n - y_l)}{d_{nl}^7}, \tag{A.7d}$$

$$R_{nl}^{xxz} = 3\frac{z_n - z_l}{d_{nl}^5} - 15\frac{(x_n - x_l)^2(z_n - z_l)}{d_{nl}^7}, \tag{A.7e}$$

$$R_{nl}^{xyy} = 3\frac{x_n - x_l}{d_{nl}^5} - 15\frac{(x_n - x_l)(y_n - y_l)^2}{d_{nl}^7}, \tag{A.7f}$$

$$R_{nl}^{xzz} = 3\frac{x_n - x_l}{d_{nl}^5} - 15\frac{(x_n - x_l)(z_n - z_l)^2}{d_{nl}^7}, \tag{A.7g}$$

$$R_{nl}^{yyz} = 3\frac{z_n - z_l}{d_{nl}^5} - 15\frac{(y_n - y_l)^2(z_n - z_l)}{d_{nl}^7}, \tag{A.7h}$$

$$R_{nl}^{yzz} = 3\frac{y_n - y_l}{d_{nl}^5} - 15\frac{(y_n - y_l)(z_n - z_l)^2}{d_{nl}^7}, \tag{A.7i}$$

$$R_{nl}^{xyz} = -15\frac{(x_n - x_l)(y_n - y_l)(z_n - z_l)}{d_{nl}^7}. \tag{A.7j}$$

B

EQUILIBRIUM CONFIGURATIONS FOR THREE IONS

B.1 NOTATIONS

In this thesis we use a different convention for the anisotropy parameter α than in Baltrusch, Cormick, De Chiara et al. (2011). There, the anisotropy parameter is defined as the ratio

$$\overline{\alpha} = \frac{\nu_y}{\nu_x}\,, \tag{B.1}$$

while here we have defined it in Eq. (1.23) as

$$\alpha = \left(\frac{\nu_y}{\nu_x}\right)^2 = \overline{\alpha}^2\,. \tag{B.2}$$

Similarly, we have defined the effect of the dipole potential in a different way. There, we introduced it as a shift of the angular frequency of the harmonic potential,

$$V_e(\mathbf{r}_n) = \frac{1}{2}m\nu_x^2\left[x_n^2 + \frac{(\nu_y+\delta\nu_y)^2}{\nu_x^2}y_n^2\right] = \frac{1}{2}m\nu_x^2\left[x_n^2 + (\overline{\alpha}+\delta\overline{\alpha})^2 y_n^2\right], \tag{B.3}$$

that is denoted by $\delta\overline{\alpha}$. In Section 2.3 we expressed the effect of the dipole potential by

$$V_e(\mathbf{r}_n) = \frac{1}{2}m\nu_x^2\left[x_n^2 + \left(\frac{\nu_y^2}{\nu_x^2} + \frac{\nu_{\mathrm{dip}}^2}{\nu_x^2}\right)y_n^2\right] = \frac{1}{2}m\nu_x^2\left[x_n^2 + (\alpha^2+\delta\alpha^2)y_n^2\right]. \tag{B.4}$$

Here, we provide the formulae for interchanging the two notations. The starting point, obviously, is then to set the two expressions in the potential equal. However, care has to be taken for the sign of the expression; as we see in the following, we also need to take the case into account for which the total potential becomes anti-trapping

$$(\overline{\alpha}+\delta\overline{\alpha})^2 = \quad \alpha+\delta\alpha \quad \text{for } \alpha+\delta\alpha > 0\,, \tag{B.5a}$$

$$(\overline{\alpha}+\delta\overline{\alpha})^2 = -\alpha-\delta\alpha \quad \text{for } \alpha+\delta\alpha < 0\,, \tag{B.5b}$$

from which we obtain

$$\delta\bar{\alpha} = \sqrt{\alpha+\delta\alpha} - \sqrt{\alpha} \quad \text{for } \alpha+\delta\alpha > 0\,, \tag{B.6a}$$

$$\delta\bar{\alpha} = \mathrm{i}\sqrt{\alpha+\delta\alpha} - \sqrt{\alpha} \quad \text{for } \alpha+\delta\alpha < 0\,, \tag{B.6b}$$

and the inverse formulae

$$\delta\alpha = \delta\bar{\alpha}^2 + 2\bar{\alpha}\delta\bar{\alpha} \quad \text{for } \alpha+\delta\alpha > 0\,, \tag{B.7a}$$

$$\delta\alpha = -\delta\bar{\alpha}^2 - 2\bar{\alpha}\delta\bar{\alpha} - 2\bar{\alpha}^2 \quad \text{for } \alpha+\delta\alpha < 0\,. \tag{B.7b}$$

B.2 EQUILIBRIUM POSITIONS

Here, we summarize and extend the discussion of the equilibrium positions made in Sections 2.1.4 and 2.3. Additionally, we provide details for other solutions not discussed within the scope of this thesis.

x-LINEAR The equilibrium positions for the linear chain aligned along the x-axis are given by Eq. (2.29),

$$X_1 = -\sqrt[3]{5/4}\,, \qquad Y_1 = 0\,, \tag{B.8a}$$

$$X_2 = 0\,, \qquad Y_2 = 0\,, \tag{B.8b}$$

$$X_3 = \sqrt[3]{5/4}\,, \qquad Y_3 = 0\,. \tag{B.8c}$$

x-ZIGZAG The equilibrium positions for the zigzag chain aligned along the x-axis are given by Eq. (2.30),

$$X_1 = -\bar{X}\,, \qquad Y_1 = -\bar{Y}\,, \tag{B.9a}$$

$$X_2 = 0\,, \qquad Y_2 = 2\bar{Y}\,, \tag{B.9b}$$

$$X_3 = \bar{X}\,, \qquad Y_3 = -\bar{Y}\,, \tag{B.9c}$$

where

$$\bar{X} = \left[4\left(1-\frac{\alpha}{3}\right)\right]^{-1/3}, \tag{B.10a}$$

$$\bar{Y} = \pm\frac{1}{3}\left[\left(\frac{3}{\alpha}\right)^{2/3} - \bar{X}^2\right]^{1/2}. \tag{B.10b}$$

y-LINEAR The equilibrium positions for a linear chain aligned along the y-direction now depend on the anisotropy parameter. They are given by

$$X_1 = 0\,, \qquad Y_1 = -\sqrt[3]{5/(4\alpha)}\,, \tag{B.11a}$$

$$X_2 = 0\,, \qquad Y_2 = 0\,, \tag{B.11b}$$

$$X_3 = 0\,, \qquad Y_3 = \sqrt[3]{5/(4\alpha)}\,. \tag{B.11c}$$

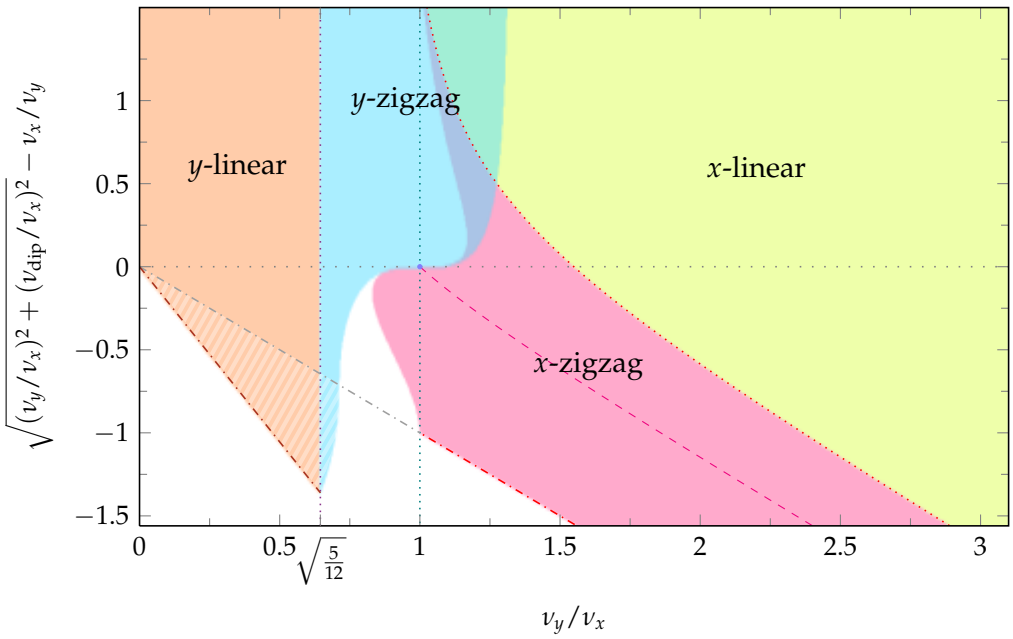

Figure B.1: Structural diagram for three ions, where the excited ion is located at the symmetry axis of the configuration. The red dotted line marks the transition between the x-linear and the x-zigzag configuration. The violet dotted vertical line located at $\sqrt{5/12}$ marks the transition between the y-linear and the y-zigzag configuration. The dash-dotted line marks the stability boundary for the crystal where it coincides with the stability boundary for a single ion (red). The brown dash-dotted line marks the stability boundary for the crystal where it extends below the stability boundary for a single ion. The hatched area labels the parameter domain where meta-stable trapping is possible due to the Coulomb forces of the outer ions. The red dashed line refers to x-zigzag structures where the zigzag forms an equilateral triangle. Between the x-zigzag and the y-zigzag, and between the x-linear and the y-zigzag regions of coexisting configurations are possible. In the white area bordered by the x-zigzag, the y-zigzag, and the single-ion stability boundary, no symmetric structure is stable; there, only asymmetric configurations are stable, see Figure B.2.

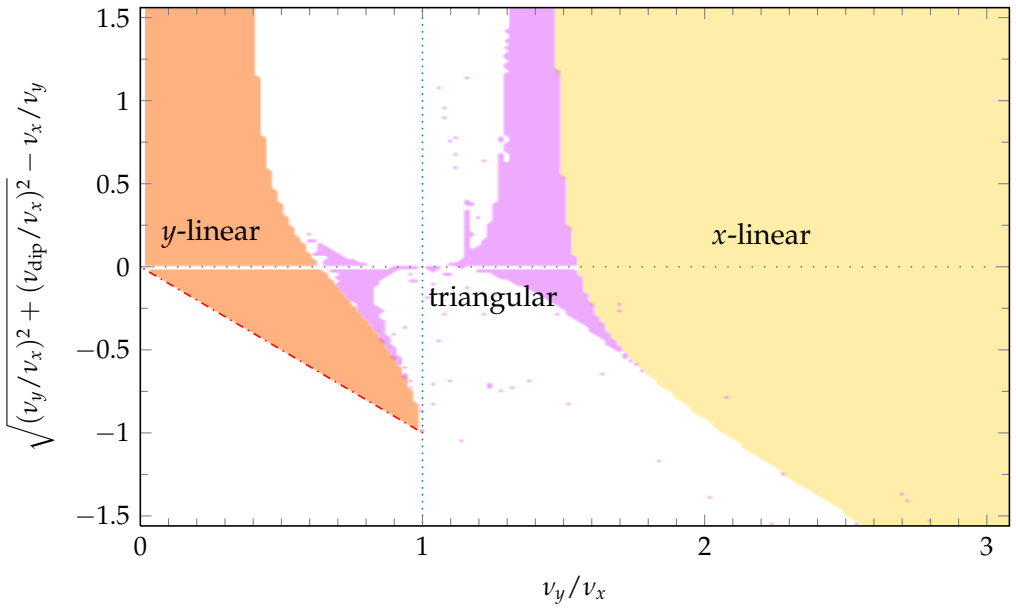

Figure B.2: Structural diagram for three ions where the excited ion is not located at the symmetry axis of the configuration. The data points in this figure have been obtained by numerical calculations with limited ability to distinguish sharply between the different configurations (hence the frayed boundaries and scattered stray points). The dash-dotted red line marks the stability boundary for the crystal where it coincides with the stability boundary for a single ion. No meta-stable configuration below the single-ion stability boundary exist.

This is actually the dependence on the transverse trapping angular frequency, just as the x-linear depends on the axial trapping angular frequency, which is one in our units.

The normal mode frequencies are

$$\omega_1 = 1\,, \tag{B.12a}$$
$$\omega_2 = \sqrt{1-\alpha}\,, \tag{B.12b}$$
$$\omega_3 = \sqrt{1-12\alpha/5}\,, \tag{B.12c}$$
$$\omega_4 = \sqrt{3\alpha}\,, \tag{B.12d}$$
$$\omega_5 = \sqrt{17\alpha/5+\delta\alpha/2-\eta_0}\,, \tag{B.12e}$$
$$\omega_6 = \sqrt{17\alpha/5+\delta\alpha/2+\eta_0}\,, \tag{B.12f}$$

where

$$\eta_0 = \sqrt{\delta\alpha^2/4+4\alpha\delta\alpha/5+144\alpha^2/25}\,. \tag{B.13}$$

y-ZIGZAG For the zigzag aligned along the y-direction we find the following equilibrium positions,

$$X_1 = -\bar{x}\,, \qquad Y_1 = -\bar{Y}\,, \tag{B.14a}$$
$$X_2 = \;2\bar{Y}\,, \qquad Y_2 = \;\;0\,, \tag{B.14b}$$
$$X_3 = -\bar{X}\,, \qquad Y_3 = \;\;\bar{Y}\,, \tag{B.14c}$$

where

$$\bar{X} = \pm\frac{1}{3}\left[3^{2/3}-\bar{Y}^2\right]^{1/2}, \tag{B.15a}$$
$$\bar{Y} = \left[4\left(\alpha-\frac{1}{3}\right)\right]^{-1/3}. \tag{B.15b}$$

B.3 STRUCTURAL DIAGRAM

The x-linear and the y-zigzag are separated by the curves given by

$$\alpha_{\mathrm{dip},c} = \left(\frac{8}{5\alpha-4}-1\right)\alpha \tag{B.16a}$$

or[1]

$$\delta\overline{\alpha}_c = \left(\sqrt{\frac{8}{5\overline{\alpha}^2-4}}-1\right)\overline{\alpha}\,. \tag{B.16b}$$

1 These formulae resemble each other to a large degree, but each can be obtained from the other by Eqs. (B.6) and (B.7).

The line delimiting the x-linear structure has a pole for $\alpha = 4/5$ or rather $\overline{\alpha} = \nu_y/\nu_x = \sqrt{4/5}$. When lowering the anisotropy parameter for $\delta\alpha \geq 7$, the mode with frequency $\sqrt{1-\alpha}$ becomes unstable for $\alpha = 1$ before reaching the boundary given by Eq. (B.16). In any case, below the value of $\alpha = 1$ the x-linear chain is unstable, no matter how strong the dipole potential.

y-LINEAR We obtain the following stability boundary for the linear chain aligned along the y-axis,

$$\alpha_{\text{crit}} = 5/12\,, \tag{B.17}$$

which is independent of the dipole potential. A second stability boundary, determined by the roots of the normal mode frequencies, is given by

$$\delta\alpha_{\text{crit}} = -\frac{29\alpha}{13}\,, \tag{B.18a}$$

or

$$\delta\overline{\alpha}_{\text{crit}} = \Big(-1 - \frac{4}{\sqrt{13}}\Big)\overline{\alpha}\,. \tag{B.18b}$$

Thus the regime for the y-linear reaches below the boundary for stable trapping of a single ion, given by $\delta\alpha = -\alpha$. Yet, quite remarkably, there is a metastable configuration possible, where the middle ion in the chain is trapped by the Coulomb potential of the two outer ions.

C

THE DISENTANGLING THEOREM

C.1 INTRODUCTION

One of the difficulties that arise regularly in theoretical quantum optics is to have an exponential operator with a sum of non-commuting operators in the exponent. If in a *sum* of two operators the operators by themselves are commuting both with their mutual commutator, the well-known Baker-Campbell-Hausdorff identity (BCH)-identity (Mandel and Wolf 1995, pp. 519–520) can be applied to obtain a *product* of exponentials containing the summand operators and a factor stemming from their commutator.

However, if this condition is not fulfilled, it becomes much more difficult to transform a sum of operators in the exponential into a product of exponentials containing only simpler expressions. In fact, the nested commutation relations may not vanish after the first order and might even continue infinitely. Yet, when the operators involved form a closed algebra, a closed solution is feasible. We are going to illustrate this for the case of the spin algebra in the next section.

But first, we will review the general considerations of the disentangling theorem. Feynman (1951) introduced a method for disentangling exponentials of sums of two operators into the product of the expontentials of the individual operators without making assumptions on the commutator between the operators. However, since he used a somewhat unusual notation, we will not discuss his approach here. We rather follow the path of Bogoliubov and Shirkov (1982). Other treatments are presented e. g. in Arecchi et al. (1972) and Collett (1988).

The idea is as follows: Let us consider the operator $\exp(\hat{A}+\hat{B})$ with $[\hat{A},\hat{B}] \neq 0$ in general. This operator may be written generally in the form $e^{\hat{A}} F e^{\hat{B}}$, where F is dependent on $\hat{A}$ and $\hat{B}$ and their nested commutators in all orders. Introducing a continuous real auxiliary parameter λ, we write $e^{\lambda(\hat{A}+\hat{B})} = e^{\lambda\hat{A}} F(\lambda;\hat{A},\hat{B},[\hat{A},\hat{B}],\dots)\, e^{\lambda\hat{B}}$, and differentiate this equation with respect to λ,

$$(\hat{A}+\hat{B})\, e^{\lambda(\hat{A}+\hat{B})} = \hat{A}\, e^{\lambda\hat{A}} F e^{\lambda\hat{B}} + e^{\lambda\hat{A}} F' e^{-\lambda\hat{A}}\, e^{\lambda(\hat{A}+\hat{B})} + e^{\lambda\hat{A}} F \hat{B} F^{-1} e^{-\lambda\hat{A}}\, e^{\lambda(\hat{A}+\hat{B})}. \quad \text{(C.1)}$$

Multiplying the result by $\mathrm{e}^{-\lambda(\hat{\mathrm{A}}+\hat{\mathrm{B}})}$ from the right, we obtain:

$$(\hat{\mathrm{A}}+\hat{\mathrm{B}}) = \hat{\mathrm{A}} + \mathrm{e}^{\lambda\hat{\mathrm{A}}} F' \mathrm{e}^{-\lambda\hat{\mathrm{A}}} + \mathrm{e}^{\lambda\hat{\mathrm{A}}} F \hat{\mathrm{B}} F^{-1} \mathrm{e}^{-\lambda\hat{\mathrm{A}}} \,. \tag{C.2}$$

After reordering and multiplying by $\mathrm{e}^{-\lambda A}$ from the left and $\mathrm{e}^{\lambda A}$ from the right, we obtain a differential equation for F ,

$$F' = \mathrm{e}^{-\lambda\hat{\mathrm{A}}} \hat{\mathrm{B}}\, \mathrm{e}^{\lambda\hat{\mathrm{A}}} - F\hat{\mathrm{B}}F^{-1} \,, \tag{C.3}$$

which we need to solve.

In the case of $\hat{\mathrm{A}}$ and $\hat{\mathrm{B}}$ being elements of a closed algebra, the nested commutators can be grouped in terms that are proportional to elements of the algebra, but not to products of elements of the operator algebra. In that case, the ansatz for the function F can be simplified.

C.2 A PARADIGMATIC EXAMPLE – THE SPIN ALGEBRA

As an illustration we shall now apply the approach of Bogoliubov and Shirkov (1982) for disentangling the operator $\exp(\hat{\sigma}_+ + \hat{\sigma}_-)$, where the operators $\hat{\sigma}_+$ and $\hat{\sigma}_-$ are given by

$$\hat{\sigma}_+ = \frac{1}{2}\Big(\hat{\sigma}_x + \mathrm{i}\hat{\sigma}_y\Big) \,, \qquad\qquad \hat{\sigma}_- = \frac{1}{2}\Big(\hat{\sigma}_x - \mathrm{i}\hat{\sigma}_y\Big) \,. \tag{C.4}$$

Here, $\hat{\sigma}_x$, $\hat{\sigma}_y$, and $\hat{\sigma}_z$ are the common Pauli spin matrices. The commutator of $\hat{\sigma}_+$ with $\hat{\sigma}_-$ is given by

$$[\hat{\sigma}_+, \hat{\sigma}_-] = \hat{\sigma}_z \,, \tag{C.5a}$$

and the commutators of $\hat{\sigma}_+$ and $\hat{\sigma}_-$ with $\hat{\sigma}_z$ (their mutual commutator) are given by

$$[\hat{\sigma}_z, \hat{\sigma}_+] = 2\hat{\sigma}_+ \,, \qquad\qquad [\hat{\sigma}_z, \hat{\sigma}_-] = -2\hat{\sigma}_- \,. \tag{C.5b}$$

Hence, the operators $\{\hat{\sigma}_+, \hat{\sigma}_-, \hat{\sigma}_z\}$ form a closed algebra called spin algebra. Although the nested mutual commutators of $\hat{\sigma}_+$ and $\hat{\sigma}_-$ never vanish at any order, they always yield terms that are proportional to any operator in the algebra.

Recapitulating the approach of Bogoliubov and Shirkov (1982), we thus take the following ansatz:[1]

$$\mathrm{e}^{\lambda(\hat{\sigma}_+ + \hat{\sigma}_-)} = \mathrm{e}^{f(\lambda)\hat{\sigma}_+} F(\lambda; \hat{\sigma}_+, \hat{\sigma}_-, \hat{\sigma}_z)\, \mathrm{e}^{g(\lambda)\hat{\sigma}_-} \tag{C.6}$$

where $f(\lambda), g(\lambda)$ are continous functions in λ with boundary values $f(0) = 0$ and $g(0) = 0$, and $F(\lambda; \hat{\sigma}_+, \hat{\sigma}_-, \hat{\sigma}_z)$ is a functional of all the

1 This ansatz is well defined, as we always have the trivial solution for $f(\lambda) = 0$ and $g(\lambda) = 0$, and $F = \exp\{\lambda(\hat{\sigma}_+ + \hat{\sigma}_-)\}$.

operators and a function in λ with boundary value $F(\lambda = 0) = 1$. Inverting Eq. (C.6) yields

$$F(\lambda; \hat{\sigma}_+, \hat{\sigma}_-, \hat{\sigma}_z) = \mathrm{e}^{-f(\lambda)\hat{\sigma}_+} \mathrm{e}^{\lambda(\hat{\sigma}_+ + \hat{\sigma}_-)} \mathrm{e}^{-g(\lambda)\hat{\sigma}_-} . \tag{C.7}$$

Taking the derivative with respect to λ, we obtain the following first-order differential equation for F (where $F' = \partial F/\partial\lambda$ etc.):

$$\begin{aligned} F' = \Big\{ &-f'\hat{\sigma}_+ + \mathrm{e}^{-f\hat{\sigma}_+}(\hat{\sigma}_+ + \hat{\sigma}_-)\mathrm{e}^{f\hat{\sigma}_+} \\ &- g' \mathrm{e}^{-f\hat{\sigma}_+} \mathrm{e}^{\lambda(\hat{\sigma}_+ + \hat{\sigma}_-)} \hat{\sigma}_- \mathrm{e}^{\lambda(\hat{\sigma}_+ + \hat{\sigma}_-)} \mathrm{e}^{f\hat{\sigma}_+} \Big\} F . \end{aligned} \tag{C.8}$$

In order to evaluate this expression we use the following identities,

$$\mathrm{e}^{-f\hat{\sigma}_+} \hat{\sigma}_- \mathrm{e}^{f\hat{\sigma}_+} = \hat{\sigma}_- - f\hat{\sigma}_z - f^2\hat{\sigma}_+ \tag{C.9a}$$

$$\begin{aligned} \mathrm{e}^{\lambda(\hat{\sigma}_+ + \hat{\sigma}_-)} \hat{\sigma}_- \mathrm{e}^{-\lambda(\hat{\sigma}_+ + \hat{\sigma}_-)} &= \hat{\sigma}_- \cosh^2(\lambda) - \hat{\sigma}_+ \sinh^2(\lambda) \\ &\quad + \hat{\sigma}_z \sinh(\lambda)\cosh(\lambda) \end{aligned} \tag{C.9b}$$

$$\mathrm{e}^{-f\hat{\sigma}_+} \hat{\sigma}_z \mathrm{e}^{f\hat{\sigma}_+} = \hat{\sigma}_z + 2f\hat{\sigma}_+ , \tag{C.9c}$$

and insert them into Eq. (C.8). We arrive at the following differential equation:

$$\begin{aligned} F' = \Big\{ &\hat{\sigma}_+ \Big[1 - f' - f^2 + \cosh^2(\lambda) g' f^2 + \sinh^2(\lambda) g' \\ &- 2\sinh(\lambda)\cosh(\lambda) g' f \Big] + \hat{\sigma}_- \Big[1 - \cosh^2(\lambda) g' \Big] \\ &+ \hat{\sigma}_z \Big[-f + \cosh^2(\lambda) g' f - \sinh(\lambda)\cosh(\lambda) g' \Big] \Big\} . \end{aligned} \tag{C.10}$$

In order to disentangle the operators, we want $F(\lambda; \hat{\sigma}_+, \hat{\sigma}_-, \hat{\sigma}_z)$ to be neither a function of $\hat{\sigma}_+$ nor of $\hat{\sigma}_-$. We try to choose appropriate functions $f(\lambda)$ and $g(\lambda)$ such that the first two squared brackets in the equation above are identical to zero for all values of λ chosen. This ansatz leads to the following two equations:

$$\Big[1 - \cosh^2(\lambda) g' \Big] = 0 \tag{C.11a}$$

$$\begin{aligned} \Big[1 - f' - f^2 + \cosh^2(\lambda) g' f^2 + \sinh^2(\lambda) g' \\ - 2\sinh(\lambda)\cosh(\lambda) g' f \Big] = 0 . \end{aligned} \tag{C.11b}$$

From the first one, we find that

$$g'(\lambda) = \frac{1}{\cosh^2(\lambda)}, \qquad \text{and} \qquad g(\lambda) = \tanh(\lambda). \tag{C.12}$$

Inserting this result in the second equation reduces it to

$$f'(\lambda) + 2\tanh(\lambda) f(\lambda) - \tanh^2(\lambda) - 1 = 0 , \tag{C.13}$$

which we can integrate. The general solution is given by

$$\begin{aligned} f(\lambda) &= \exp\{-2\ln(\cosh(\lambda))\} \\ &\qquad \left[\int (\tanh^2(\lambda)+1)\exp\Big\{2\ln(\cosh(\lambda))\Big\}d\lambda + C_f\right] \\ &= \frac{\int \cosh(2\lambda)d\lambda + C_f}{\cosh^2(\lambda)} = \tanh(\lambda) + \frac{C_f}{\cosh^2(\lambda)}\,. \end{aligned} \tag{C.14}$$

We require that $f = 0$ for $\lambda = 0$, which is the case for $C_f = 0$, and thus

$$f(\lambda) = \tanh(\lambda)\,. \tag{C.15}$$

Inserting the result in the differential equation (C.8), we obtain finally

$$F'(\lambda) = -\hat{\sigma}_z \tanh(\lambda) F(\lambda)\,, \tag{C.16}$$

which gives the general solution

$$F(\lambda) = C\exp\Big\{-\ln(\cosh(\lambda))\hat{\sigma}_z\Big\}\,, \tag{C.17}$$

with C a constant coming from the integration. For $\lambda = 0$, we find that $C\exp(0) = 1$, thus $C = 1$ and we obtain for

$$F(\lambda) = \mathrm{e}^{-\hat{\sigma}_z \ln(\cosh(\lambda))}\,. \tag{C.18}$$

Inserting the result into Eq. (C.6), the disentangling formula reads (Collett 1988; Carmichael 1998)

$$\mathrm{e}^{\lambda(\hat{\sigma}_+ + \hat{\sigma}_-)} = \mathrm{e}^{\hat{\sigma}_+ \tanh(\lambda)}\,\mathrm{e}^{-\hat{\sigma}_z \ln[\cosh(\lambda)]}\,\mathrm{e}^{\hat{\sigma}_- \tanh(\lambda)}\,. \tag{C.19}$$

C.3 THE SINGLE-MODE HARMONIC OSCILLATOR ALGEBRA

We want now to use the same approach in order to disentangle the so-called squeezing operator, which is given by

$$\hat{\mathrm{S}}(\lambda) = \exp\left\{\frac{\lambda}{2}\left(\hat{\mathrm{a}}^{\dagger 2} - \hat{\mathrm{a}}^2\right)\right\}. \tag{C.20}$$

For this, we first determine the commutators between the operators:

$$[\hat{\mathrm{a}}^2, \hat{\mathrm{a}}^{\dagger 2}] = 4\hat{\mathrm{a}}^\dagger\hat{\mathrm{a}} + 2\,, \tag{C.21a}$$

$$[\hat{\mathrm{a}}^2, [\hat{\mathrm{a}}^2, \hat{\mathrm{a}}^{\dagger 2}]\,] = [\hat{\mathrm{a}}^2, 4\hat{\mathrm{a}}^\dagger\hat{\mathrm{a}} + 2] = 8\hat{\mathrm{a}}^2\,, \tag{C.21b}$$

$$[\hat{\mathrm{a}}^{\dagger 2}, [\hat{\mathrm{a}}^{\dagger 2}, \hat{\mathrm{a}}^2]\,] = [\hat{\mathrm{a}}^{\dagger 2}, 4\hat{\mathrm{a}}^\dagger\hat{\mathrm{a}}^\dagger + 2] = -8\hat{\mathrm{a}}^{\dagger 2}\,, \tag{C.21c}$$

$$\vdots$$

The commutators yield therefore only operators that are multiples of $\hat{a}, \hat{a}^\dagger$ and $\hat{a}^\dagger\hat{a}$. This can be easily turned into a closed algebra by multiplying the operators by an appropriate numerical factor. In fact, the set $\{\frac{1}{2}\hat{a}^2, \frac{1}{2}\hat{a}^{\dagger 2}, \hat{a}^\dagger\hat{a} + \frac{1}{2}\}$ has the same commutation relations as the spin operators in Eq. (C.5b), so that we can identify the operators as follows:

$$\hat{a}^\dagger\hat{a} + \frac{1}{2} \sim \hat{\sigma}_z\,, \qquad \frac{1}{2}\hat{a} \sim \hat{\sigma}_+\,, \qquad \frac{1}{2}\hat{a}^\dagger \sim \hat{\sigma}_-\,, \tag{C.22}$$

Since only the properties of the commutators are used in the previous section – and not other special properties of the spin operators like e. g. $\hat{\sigma}_z^2 = 1$ – we can immediately apply the previously obtained result to these operators:

$$\mathrm{e}^{\frac{\lambda}{2}(\hat{a}^{\dagger 2} - \hat{a}^2)} = \mathrm{e}^{\frac{\tanh\lambda}{2}\hat{a}^{\dagger 2}}\,\mathrm{e}^{-(\hat{a}^\dagger\hat{a} + \frac{1}{2})\ln[\cosh\lambda]}\,\mathrm{e}^{-\frac{\tanh\lambda}{2}\hat{a}^2}. \tag{C.23}$$

C.4 THE MULTI-MODE HARMONIC OSCILLATOR ALGEBRA

The multimode squeezing operator is given by

$$\hat{S} = \exp\left\{\frac{1}{2}\sum_{jk}\xi_{jk}\left(\hat{a}_j^\dagger\hat{a}_k^\dagger - \xi_{jk}^*\hat{a}_j\hat{a}_k\right)\right\}, \tag{C.24}$$

where the matrix ξ can always be chosen to be complex symmetric since $[\hat{a}_j, \hat{a}_k] = [\hat{a}_j^\dagger, \hat{a}_k^\dagger] = 0$. Commutators between operators of the same mode have the form of the spin algebra in Eq. (C.5b). However, as ξ is not diagonal in general, the commutators between operators of different modes span over the different sets such that the closed algebra involves all possible combinations.

We could try to bring the multimode squeezing operator into a diagonal form by introducing new collective operators, which we then can try to solve for each of these new modes independently. As ξ is complex symmetric, we can apply Takagi's factorization (Horn and Johnson 1985, Theorem 4.4.4, pp. 204f.), i. e.

$$\xi = \Lambda\chi\Lambda^T\,, \tag{C.25}$$

where the matrix $\chi = \mathrm{diag}(\{\chi_1, \chi_2, \dots\})$ is diagonal with $\chi_j \geq 0$ real and non-negative entries, and the transformation matrix Λ is unitary.[2] This allows us to define new creation and annihilation operators

2 Such a factorization exists for any complex symmetric matrix, whereas not every complex symmetric matrix can be diagonalized by a similarity transformation. But if it is possible to diagonalize a complex symmetric matrix, it will be diagonalized by a complex orthogonal matrix and have complex eigenvalues in general (Horn and Johnson 1985, Theorem 4.4.13, pp. 211f.).

$\{\hat{b}_j^\dagger, \hat{b}_j\}$, which are connected to our initial ones by the following Bogoliubov transformation:

$$\hat{b}_j^\dagger = \sum_k \Lambda_{kj} \hat{a}_k^\dagger, \qquad \hat{b}_j = \sum_k \Lambda_{kj}^* \hat{a}_k \,. \tag{C.26}$$

These new operators obey the same bosonic commutator relations, as follows directly from the general properties of Bogoliubov transformations. It can also be checked easily, $[\hat{b}_j, \hat{b}_k] = [\hat{b}_j^\dagger, \hat{b}_k^\dagger] = 0$, and $[\hat{b}_j, \hat{b}_k^\dagger] = \sum_l \Lambda_{lk} \Lambda_{lj}^* = \delta_{jk}$, since Λ is a unitary matrix. With these new operators, the squeezing operator (C.24) is written in diagonal form,

$$\hat{S} = \exp\left\{ \frac{1}{2} \sum_j \chi_j \left(\hat{b}_j^{\dagger 2} - \hat{b}_j{}^2 \right) \right\} = \prod_j \exp\left\{ \frac{\chi_j}{2} \left(\hat{b}_j^{\dagger 2} - \hat{b}_j{}^2 \right) \right\}. \tag{C.27}$$

The different modes factorize as their mutual commutators are zero. For each mode the set of operators $\{\frac{1}{2}\hat{b}_j{}^2, \frac{1}{2}\hat{b}_j^{\dagger 2}, \hat{b}_j^\dagger \hat{b}_j + \frac{1}{2}\}$ is a closed algebra as in the previous section. Thus we can generalize the result from the single mode case to obtain the following disentangled form:

$$\begin{aligned} \hat{S} &= \prod_j \exp\left\{ \frac{\chi_j}{2} \left(\hat{b}_j^{\dagger 2} - \hat{b}_j{}^2 \right) \right\} \\ &= \prod_j \mathrm{e}^{\frac{1}{2}\tanh(\chi_j)\hat{b}_j^{\dagger 2}} \, \mathrm{e}^{-(\hat{b}_j^\dagger \hat{b}_j + \frac{1}{2})\ln(\cosh\chi_j)} \, \mathrm{e}^{-\frac{1}{2}\tanh(\chi_j)\hat{b}_j{}^2} . \end{aligned} \tag{C.28}$$

The exponentials for different modes commute such that we can rearrange the exponentials in such a way that a product of exponentials containing only creation operators is put to the left, the ones containing number operators is in the middle and the ones containing only annihilation operators is on the right side,

$$\hat{S} = \prod_j \mathrm{e}^{\frac{1}{2}\tanh(\chi_j)\hat{b}_j^{\dagger 2}} \prod_j \mathrm{e}^{-(\hat{b}_j^\dagger \hat{b}_j + \frac{1}{2})\ln(\cosh\chi_j)} \prod_j \mathrm{e}^{-\frac{1}{2}\tanh(\chi_j)\hat{b}_j{}^2} .$$

In the exponents, we transform the products into sums again and apply the inverse transformation of Eq. (C.26), obtaining the final result

$$\hat{S} = Z \, \mathrm{e}^{\frac{1}{2}\sum_{jk} A_{jk} \hat{a}_j^\dagger \hat{a}_k^\dagger} \, \mathrm{e}^{-\sum_{jk} B_{jk} \hat{a}_j^\dagger \hat{a}_k} \, \mathrm{e}^{-\frac{1}{2}\sum_{jk} C_{jk} \hat{a}_j \hat{a}_k} , \tag{C.29}$$

where the factors are given by

$$A_{jk} = \sum_l \tanh(\chi_l) \Lambda_{jl} \Lambda_{kl} \,, \tag{C.29a}$$

$$B_{jk} = \sum_l \ln\big(\cosh\chi_l\big) \Lambda_{jl} \Lambda_{kl}^* \,, \tag{C.29b}$$

$$C_{jk} = \sum_l \tanh(\chi_l) \Lambda_{jl}^* \Lambda_{kl}^* = A_{jk}^* \,, \tag{C.29c}$$

$$Z \;\; = \exp\left\{ -\sum_j \frac{1}{2} \ln\big(\cosh\chi_j\big) \right\}. \tag{C.29d}$$

D

GAUSSIAN INTEGRALS

In this appendix, we proof the multidimensional Gaussian integral for a quadratic form in several real variables, but described by a complex symmetric matrix as applied in Chapters 5 and 6. For completeness' sake, we also discuss the theorems for the one-dimensional case and the real multi-dimensional case, but omit the proofs as they can be found in the literature.

The one-dimensional Gaussian integral along the real axis with the complex prefactor $a \in \mathbb{C}, \operatorname{Re} a > 0$ is given by

$$\int_{-\infty}^{+\infty} \mathrm{d}x \, \mathrm{e}^{-ax^2} = \sqrt{\frac{\pi}{a}}. \tag{D.1}$$

This has the following immediate generalizations,

$$\int_{-\infty}^{+\infty} \mathrm{d}x \, \mathrm{e}^{-a(x+c)^2} = \sqrt{\frac{\pi}{a}} \tag{D.1a}$$

for arbitrary $x \in \mathbb{C}$, and

$$\int_{-\infty}^{+\infty} \mathrm{d}x \, \mathrm{e}^{-ax^2+bx} = \sqrt{\frac{\pi}{a}} \, \mathrm{e}^{b^2/4a} \tag{D.1b}$$

for arbritrary $b \in \mathbb{C}$.

The first is shown by shifting the integration variable, $x \mapsto x + c$, and taking the complex contour integral along a parallelogram composed of the shifted integration path, the real axis, and the two connection lines located at $\pm\infty$. The identity in Eq. (D.1b) is obtained by completing the square in the exponent by adding and subtracting $b^2/4a$, such that the integral then is reduced to Eq. (D.1a) with $c = -b/2a$.

The multi-dimensional real Gaussian integral of a quadratic form involving a real symmetric matrix A is given by

$$\int_{\mathbb{R}^n} \mathrm{d}^n x \, \mathrm{e}^{-x^T \mathrm{A} x} = \sqrt{\frac{\pi^n}{\det \mathrm{A}}}. \tag{D.2}$$

The proof of Eq. (D.2) proceeds via diagonalization of A by real orthogonal matrices, which induce a coordinate change in the integration

variables; this can be executed easily as the Jacobian of the orthogonal transformation is just unity. In the new variables, each integral can be evaluated completely independently of all the others by Eq. (D.1), where in each integration an eigenvalue of A is taking the role of the parameter a, here real-valued. So we get for each variable a factor of $\sqrt{\pi}$ divided by the square root of product of all the eigenvalues, i. e. the square root of the determinant of A.

Despite the fact that a quadratic form can in general be described by an arbitrary, not necessarily symmetric matrix, this identity applies only to symmetric matrices. This becomes clear when one considers a quadratic form described by an upper (or lower) triagonal matrix U. The same quadratic form is described by the symmetrized version, obtained by $\mathrm{A} = (\mathrm{U} + \mathrm{U}^T)/2$ with the *same* diagonal entries as U; however, as is readily apparent when considering the case of a two-dimensional quadratic form, the determinants of U and A are unequal in general.

We can now state the main theorem, which is applied in Chapters 5 and 6 in the calculation of the visibility of the Ramsey signal.

THEOREM 1. *Let* $\mathrm{A} = \mathrm{A}^T$ *be a complex symmetric matrix,* $a_{jk} \in \mathbb{C}$*, with positive definite Hermitian part. Then the n-dimensional complex Gaussian integral is evaluated with the following value:*

$$\int_{\mathbb{R}^n} \mathrm{d}^n x \, \mathrm{e}^{-x^T \mathrm{A} x} = \sqrt{\frac{\pi^n}{\det \mathrm{A}}} \,.$$

We have the following Corollaries:

COROLLARY 1. *Let* $\mathrm{A} = \mathrm{A}^T$ *be a complex symmetric matrix,* $a_{jk} \in \mathbb{C}$*, with positive definite Hermitian part, and* $r \in \mathbb{C}^n$ *an arbitrary vector. Then the n-dimensional complex Gaussian integral is evaluated with the following value:*

$$\int_{\mathbb{R}^n} \mathrm{d}^n x \, \mathrm{e}^{-(x+c)^T \mathrm{A} (x+c)} = \sqrt{\frac{\pi^n}{\det \mathrm{A}}} \,.$$

COROLLARY 2. *Let* $\mathrm{A} = \mathrm{A}^T$ *be a complex symmetric matrix,* $a_{jk} \in \mathbb{C}$*, with positive definite Hermitian part, and* $b \in \mathbb{C}^n$ *an arbitrary vector. Then the n-dimensional complex Gaussian integral is evaluated with the following value:*

$$\int_{\mathbb{R}^n} \mathrm{d}^n x \, \mathrm{e}^{-x^T \mathrm{A} x + b^T x} = \sqrt{\frac{\pi^n}{\det \mathrm{A}}} \, \mathrm{e}^{\frac{1}{4} b^T \mathrm{A}^{-1} b} \,.$$

Remark. The proof of Theorem 1 presented here does not rely on any coordinate transformation in the same way as the proof of the corresponding statement for real symmetric matrices proceeds. Despite an extensive search of the relevant literature, I have not found any references carrying out the proof without relying on a coordinate transformation. It is not clear – at least to me – if the coordinate transformation rule used in the real version of the proof actually applies to the complex case. In Altland and Simons (2010, Ch. 3.2, pp. 104f.), a corresponding theorem is given for complex matrices with real Hermitian part, where the authors merely sketch the proof by the hint that any matrix can be decomposed into a Hermitian and a skew-Hermitian part. The Hermitian case is traced back to the real case via a unitary transformation, thereby relying on the correct use of the Jacobian for the transformation, but without showing this explicitly. For the skew-Hermitian part they claim the proof to be "more elaborate, if unedifying" and they "refer to the literature for details" (Altland and Simons 2010, p. 105), unfortunately without giving any actual reference.

Therefore, we will here carry out another, quite intricate version of the proof without making use of a coordinate transformation. But before we come to the proof on p. 212, we need to show some preparatory lemmas and propositions. We start with the following definition.

DEFINITION 1. A complex symmetric matrix A is said to be *positive definite* if

$$\mathrm{Re}(x^\dagger \mathrm{A} x) > 0 \quad \forall \quad x \in \mathbb{C}^n : x \neq 0\,.$$

Remark. Not all of the properties of positive definiteness for Hermitian matrices carry over to this extended definition for complex symmetric matrices. However, we find the following lemmas useful in the proof of Theorem 1. These proofs are oriented along the proofs for the properties of Hermitian positive definite matrices as described in Horn and Johnson (1985, Ch. 7, pp. 396–404).

LEMMA 1. *A complex symmetric $n \times n$ matrix* A *is positive definite if and only if its Hermitian part,* $\frac{1}{2}(\mathrm{A} + \mathrm{A}^\dagger)$*, is positive definite.*

Proof. The matrix A can be decomposed as $\mathrm{A} = \frac{1}{2}(\mathrm{A} + \mathrm{A}^\dagger) - \frac{1}{2}(\mathrm{A} - \mathrm{A}^\dagger)$. The first expression is Hermitian and real, while the second expression is skew-Hermitian, thus $\frac{1}{2\mathrm{i}}(\mathrm{A} - \mathrm{A}^\dagger)$ is Hermitian and real. As $\mathrm{A}^\dagger = \mathrm{A}^*$, we can write $\mathrm{A} = \frac{1}{2}(\mathrm{A} + \mathrm{A}^*) + \mathrm{i}\frac{1}{2\mathrm{i}}(\mathrm{A} - \mathrm{A}^*)$. Hermitian quadratic forms are real-valued, so that we can identify $\mathrm{Re}\{x^\dagger \mathrm{A} x\} = x^\dagger \frac{1}{2}(\mathrm{A} + \mathrm{A}^\dagger)x$ for arbitrary $x \in \mathbb{C}^n$, from which the equivalence of the two statements follows. □

LEMMA 2. *A complex symmetric matrix* $\mathrm{A} \in M(n)$ *is positive definite if and only if all eigenvalues of* A *have positive real parts.*

Remark. Please note that this does not imply that $\mathrm{Re}\{\det \mathrm{A}\} > 0$, since the product of two (or more) complex numbers with positive real parts does not necessarily need to have a positive real part! If this were the case, the proof of Theorem 1 would be much easier.

Before we prove Lemma 2, we first demonstrate the following proposition:

PROPOSITION 1. *The quadratic form $x^\dagger \mathrm{A} x$ for an arbitrary vector $x \in \mathbb{C}^n$ and a complex symmetric matrix* A *can be rewritten as $x^\dagger A x = y^T \mathrm{A} y$ with $y = (\mathrm{Re}\, x + \mathrm{Im}\, x) \in \mathbb{R}^n$.*

Proof. Let $u = \frac{1}{2}(x + x^*)$ and $v = \frac{1}{2\mathrm{i}}(x - x^*)$ be the real and imaginary parts of x. Then the quadratic form can be written as

$$x^\dagger \mathrm{A} x = (u + \mathrm{i}v)^\dagger \mathrm{A}(u + \mathrm{i}v) = (u + v)^T \mathrm{A}(u + v) + \mathrm{i}(u^T \mathrm{A} v - v^T \mathrm{A} u)\,.$$

The term in the second bracket is

$$u^T \mathrm{A} v - v^T \mathrm{A} u = \Big(\sum_{j,k=1}^{n} u_j a_{jk} v_k\Big) - \Big(\sum_{j,k=1}^{n} v_j a_{jk} u_k\Big)\,.$$

Interchanging the summation indices in the second sum and using the symmetry of A, $a_{kj} = a_{jk}$, the imaginary part vanishes. □

Proof of Lemma 2. Let A be complex symmetric and positive definite. Further let λ be an eigenvalue of the A, and x the corresponding eigenvector. Then

$$\mathrm{A}x = \lambda x \qquad \Leftrightarrow \qquad x^\dagger \mathrm{A} x = \lambda x^\dagger x\,,$$

and, as $x^\dagger x > 0 \;\forall\; x \in \mathbb{C}^n, x \neq 0$ (this is just the squared norm of x),

$$\Leftrightarrow \qquad \lambda = \frac{x^\dagger \mathrm{A} x}{x^\dagger x} \qquad \Rightarrow \qquad \mathrm{Re}\,\lambda = \frac{\mathrm{Re}\{x^\dagger \mathrm{A} x\}}{x^\dagger x} > 0\,,$$

since A is positive definite.

For the converse direction, assume all eigenvalues of A have positive real parts. Because of Proposition 1, it suffices to restrict the proof to vectors $x \in \mathbb{R}^n$. The complex symmetric matrix A (non-singular since no eigenvalue is zero) is diagonalized by a complex orthogonal matrix Q (Horn and Johnson 1985, Theorem 4.4.13, pp. 211–212), $\mathrm{A} = \mathrm{Q}\Lambda\mathrm{Q}^T$, where $\Lambda = \mathrm{diag}(\lambda_1, \ldots, \lambda_n)$ is diagonal with the eigenvalues $\{\lambda_j\}$ as entries. Thus we have for any vector $x \in \mathbb{R}^n$

$$x^T \mathrm{A} x = x^T \mathrm{Q}\Lambda\mathrm{Q}^T x = y^T \Lambda y\,,$$

with $y = \mathrm{Q}^T x \in \mathbb{C}^n$. Further $y^T y = x^T \mathrm{Q}\mathrm{Q}^T x = x^T x > 0$, as Q is orthogonal. For arbitrary $x \in \mathbb{R}^n, x \neq 0$, we choose $\tilde{x} = \mathrm{Q}(0, \ldots, y_j, \ldots, 0)$ for $y = \mathrm{Q}^T x$. so that $y_j^2 = \tilde{x}^T \tilde{x} > 0$. Then

$$\mathrm{Re}\{x^T \mathrm{A} x\} = \mathrm{Re}\{y^T \Lambda y\} = \mathrm{Re}\Big\{\sum_{j=1}^{n} \lambda_j y_j y_j\Big\} = \sum_{j=1}^{n} \mathrm{Re}\{\lambda_j\} {y_j}^2 > 0\,.$$

□

LEMMA 3. *Let* $A \in M(n)$ *be complex symmetric and positive definite. Then any principal submatrix of* A *is positive definite.*

Proof. Let $S \subset \{1, \ldots, n\}$, and let $x \in \mathbb{C}^n$ be equal to zero for all x_j with $j \notin S$ and arbitrary otherwise. Then $\mathrm{Re}\{x^\dagger A x\} > 0$, since A is positive definite. Let $A(S)$ be the matrix A where all rows and columns that are not contained in S are deleted; $A(S)$ is complex symmetric again. Let likewise be $x(S)$ the vector x where all (zero-valued) entries that are not contained in S are deleted. Then $x(S)^\dagger A(S) x(S) = x^\dagger A x$. Since $\mathrm{Re}\{x^\dagger A x\} > 0$ it follows that $\mathrm{Re}\{x(S)^\dagger A(S) x(S)\} > 0$. But as $x(S)$ is arbitrary, it follows that $A(S)$ is positive definite. □

COROLLARY 3. *Let* $A \in M(n)$ *be complex symmetric and positive definite. Then all diagonal entries have positive real parts.*

PROPOSITION 2. *Let* x_{11}, x_{12} *and* $x_{22} \in \mathbb{R}$ *and* $x_{11} > 0$. *Further let* $x_{11}x_{22} - x_{12}^2 > 0$. *Then*

$$x_{22} > 0 \qquad \text{and} \qquad \frac{x_{11} + x_{22}}{2} > |x_{12}| \,.$$

Proof. The left property follows simply from the second inequality and $x_{11} > 0$, so that $x_{22} > x_{22} - x_{12}^2/x_{11} > 0$.

For the right property, we demonstrate $x_{11} + x_{22} - 2|x_{12}^2| > 0$, for which we check the different cases. The case $x_{11} < |x_{12}|$ and $x_{22} < |x_{12}|$ is excluded due to the second inequality in the assumptions, and the case $x_{11} > |x_{12}|$ and $x_{22} > |x_{12}|$ is trivial. The case in which $x_{11} > |x_{12}|$ and $x_{22} < |x_{12}|$ (or equivalently $x_{11} < |x_{12}|$ and $x_{22} > |x_{12}|$) can be treated as follows:

$$\begin{aligned} x_{11} + x_{22} - 2|x_{12}|^2 &= \big(x_{11} - |x_{12}|\big) + \big(x_{22} - |x_{12}|\big) \\ &> \big(x_{11} - |x_{12}|\big) + \left(\frac{x_{12}^2}{x_{11}} - |x_{12}|\right), \end{aligned}$$

where we used $x_{22} > x_{12}^2/x_{11}$,

$$\begin{aligned} &= \big(x_{11} - |x_{12}|\big) + |x_{12}|\left(\frac{|x_{12}| - x_{11}}{x_{11}}\right) \\ &= \big(x_{11} - |x_{12}|\big) - \frac{|x_{12}|}{x_{11}}\big(x_{11} - |x_{12}|\big) \\ &= \big(x_{11} - |x_{12}|\big)\left(1 - \frac{|x_{12}|}{x_{11}}\right) > 0 \,, \end{aligned}$$

since each of the brackets is bigger than zero by itself. The remaining case follows from $x_{22} > x_{12}^2/x_{11} \Leftrightarrow x_{11} > x_{12}^2/x_{22}$. □

PROPOSITION 3. *Let the* 2×2 *matrix* A *be complex symmetric with positive definite Hermitian part. Then the real part of the determinant of* A *divided by the element* a_{11} *is positive.*

Proof. Let $X = \frac{1}{2}(A + A^\dagger)$, $Y = \frac{1}{2i}(A + A^\dagger)$, so that $A = X + iY$. Since X is positive definite, we have $x_{11} > 0$ and $x_{11}x_{22} - x_{12}^2 > 0$. From Proposition 2 follows $x_{22} > 0$.

The real part of the determinant of A divided by a_{11} is

$$\begin{aligned}\mathrm{Re}\{a_{22} - a_{12}^2/a_{11}\} &= x_{22} - \frac{\mathrm{Re}\{a_{12}^2 a_{11}^*\}}{|a_{11}|^2} \\ &= x_{22} - \frac{\mathrm{Re}\{(x_{12} + iy_{12})^2(x_{11} - iy_{11})^*\}}{|a_{11}|^2},\end{aligned}$$

which gives, after multiplying out and keeping only the real part,

$$\begin{aligned}&= x_{22} - \frac{x_{11}(x_{12}^2 - y_{12}^2) + 2x_{12}y_{12}y_{11}}{|a_{11}|^2} \\ &= \frac{|a_{11}|^2 x_{22} - x_{11}(x_{12}^2 - y_{12}^2) - 2x_{12}y_{12}y_{11}}{|a_{11}|^2} \\ &= \frac{({x_{11}}^2 + y_{11}^2)x_{22} - x_{11}^2\frac{x_{12}^2}{x_{11}} + x_{11}y_{12}^2 - 2x_{12}y_{12}y_{11}}{|a_{11}|^2},\end{aligned}$$

which can be reordered as

$$= \frac{{x_{11}}^2(x_{22} - \frac{x_{12}^2}{x_{11}}) + [x_{11}y_{12}^2 + x_{22}y_{11}^2 - 2x_{12}y_{12}y_{11}]}{|a_{11}|^2}.$$

We have already showed that the first part of this expression is greater than zero. The first part of the term in the bracket, $x_{11}y_{12}^2 + x_{22}y_{11}^2$, is greater than zero. The remaining expression is greater than zero in the cases for which $x_{12} < 0$ and y_{11}, y_{12} have the same sign, and for which $x_{12} > 0$ and y_{11}, y_{12} have different sign.

Thus we have to analyse the full bracket for the remaining cases. First assume that $x_{12} > 0$. Then, by Proposition 2

$$\begin{aligned}&x_{11}y_{12}^2 + x_{22}y_{11}^2 - 2x_{12}y_{12}y_{11} > x_{11}y_{12}^2 + x_{22}y_{11}^2 - 2\frac{x_{11} + x_{22}}{2}y_{12}y_{11} \\ &= (y_{11}^2 - y_{11}y_{12})x_{22} + (y_{12}^2 - y_{11}y_{12})x_{11} \\ &> (y_{11}^2 - y_{11}y_{12})\min(x_{11}, x_{22}) + (y_{12}^2 - y_{11}y_{12})\min(x_{11}, x_{22}) \\ &> \min(x_{11}, x_{22})(y_{11}^2 + y_{12}^2 - 2y_{11}y_{12}) = \min(x_{11}, x_{22})(y_{11} - y_{12})^2 > 0.\end{aligned}$$

The remaining case can be proved in the same way by tracing it back to this result by the inequality $-2x_{12}y_{11}y_{12} > -2|x_{12}|\,|y_{11}|\,|y_{12}|$. □

Now we have all the necessary ingredients for the proof of Theorem 1.

Proof of Theorem 1. The proof uses complete induction and *Chiò's pivotal condensation process* (Eves 1980, pp. 129–133), a special case of Sylvester's identity (Horn and Johnson 1985, p. 22).

Induction start. We start with $n = 2$, as for $n = 1$ the determinant is just a trivial factor. From Lemma 3 it follows that the entry a_{11} regarded as a

principal submatrix of A is positive definite, i. e. $\operatorname{Re} a_{11} > 0$. Thus $a_{11} \neq 0$, such that we can complete the square in x_1,

$$\begin{aligned}
&\int_{\mathbb{R}^2} \mathrm{d}x_1\, \mathrm{d}x_2 \exp\Big\{-a_{11}x_1^2 - a_{22}x_2^2 - 2a_{12}x_1x_2\Big\} \\
&= \int_{\mathbb{R}^2} \mathrm{d}x_1\, \mathrm{d}x_2 \exp\Big\{-a_{22}x_2^2 - a_{11}\Big(x_1 + \frac{a_{12}x_2}{a_{11}}\Big)^2 + \frac{(a_{12}x_2)^2}{a_{11}}\Big\},
\end{aligned}$$

and pull the part that depends not on x_1 out of the integral,

$$\begin{aligned}
&= \Bigg[\int_{-\infty}^{+\infty} \mathrm{d}x_2 \exp\Big\{-\Big(a_{22} - \frac{a_{12}^2}{a_{11}}\Big)x_2^2\Big\} \\
&\qquad \int_{-\infty}^{+\infty} \mathrm{d}x_1 \exp\Big\{-a_{11}\Big(x_1 + \frac{a_{12}x_2}{a_{11}}\Big)^2\Big\}\Bigg].
\end{aligned}$$

Since $\operatorname{Re} a_{11} > 0$, the second integral can be evaluated using Eq. (D.1a), with the result being independent of x_2,

$$= \sqrt{\frac{\pi}{a_{11}}} \int_{-\infty}^{+\infty} \mathrm{d}x_2 \exp\Big\{-\Big(a_{22} - \frac{a_{12}^2}{a_{11}}\Big)x_2^2\Big\}.$$

The complex factor in the parentheses in front of x_2 has a positive real part, see Proposition 3, so that we can evaluate this integral with the help of Eq. (D.1a) again. The result can be rewritten using $\det \mathrm{A} = a_{11}a_{22} - a_{12}^2$,

$$= \sqrt{\frac{\pi}{a_{11}}}\, \sqrt{\frac{\pi}{a_{22} - a_{12}^2/a_{11}}} = \sqrt{\frac{\pi^2}{a_{11}a_{22} - a_{12}^2}} = \sqrt{\frac{\pi^2}{\det \mathrm{A}}},$$

so that the statement is true for $n = 2$.

Induction statement. We assume the following identity to be true for $n - 1$,

$$\int_{\mathbb{R}^{n-1}} \mathrm{d}^{n-1}x\, \mathrm{e}^{-x^T \mathrm{A} x} = \sqrt{\frac{\pi^{n-1}}{\det \mathrm{A}}}, \tag{D.3}$$

where A is a complex symmetric $(n-1) \times (n-1)$ matrix, $\mathrm{A}^T = \mathrm{A}$, $a_{jk} \in \mathbb{C}$ with positive definite Hermitian part.

Induction step. Again, we start by separating the terms dependent on x_1,

$$\begin{aligned}
&\int_{\mathbb{R}^n} \mathrm{d}^n x\, \mathrm{e}^{-x^T \mathrm{A} x} = \int_{\mathbb{R}^n} \mathrm{d}^n x \exp\Big\{-\sum_{j,k=1}^{n} x_j a_{jk} x_k\Big\} \\
&= \Bigg[\int_{\mathbb{R}^{n-1}} \mathrm{d}^{n-1}x \exp\Big\{-\sum_{j,k=2}^{n} x_j a_{jk} x_k\Big\} \\
&\qquad\qquad \int_{-\infty}^{+\infty} \mathrm{d}x_1 \exp\Big\{-a_{11}x_1^2 - 2\sum_{k=2}^{n} a_{1k}x_k x_1\Big\}\Bigg].
\end{aligned} \tag{D.4}$$

Since $a_{11} \neq 0$, the integral in x_1 can be split as

$$\begin{aligned}
&\int_{-\infty}^{+\infty} \mathrm{d}x_1 \exp\Big\{-a_{11}x_1^2 - 2\sum_{k=2}^{n} a_{1k}x_k x_1\Big\} \\
&\quad = \int_{-\infty}^{+\infty} \mathrm{d}x_1 \exp\Big\{-a_{11}\Big(x_1 + \frac{1}{a_{11}}\sum_{k=2}^{n} a_{1k}x_k\Big)^2 + \frac{1}{a_{11}}\Big(\sum_{k=2}^{n} a_{1k}x_k\Big)^2\Big\}.
\end{aligned} \tag{D.5}$$

The last term is not dependent on x_1, so it can be pulled out of the integral in x_1 and merged into the exponent in the integral in x_2 in Eq. (D.4). The integral in x_1 can be evaluated by Eq. (D.1a), as $\operatorname{Re} a_{11} > 0$ because of Lemma 3,

$$\int_{-\infty}^{+\infty} \mathrm{d}x_1 \exp\Big\{-a_{11}\Big(x_1 + \frac{1}{a_{11}}\sum_{k=2}^{n} a_{1k}x_k\Big)^2\Big\} = \sqrt{\frac{\pi}{a_{11}}}\,. \tag{D.6}$$

Inserting the term pulled out and the result of this integral into Eq. (D.4), we obtain

$$\int \mathrm{d}^n x\, \mathrm{e}^{-x^T \mathrm{A} x} = \sqrt{\frac{\pi}{a_{11}}} \int \mathrm{d}^{n-1} x \exp\Big\{-\sum_{j,k=2}^{n} x_j a_{jk} x_k + \frac{1}{a_{11}}\Big(\sum_{k=2}^{n} a_{1k}x_k\Big)^2\Big\}\,. \tag{D.7}$$

Multiplying out the squared sum in the exponent yields

$$\begin{aligned}\Big(\sum_{k=2}^{n} a_{1k}x_k\Big)^2 =& a_{12}^2x_2^2 + a_{12}a_{23}x_2x_3 + \cdots + a_{12}a_{1n}x_1x_n + \cdots \\ &\cdots + a_{1n}a_{12}x_nx_2 + \cdots + a_{1n}a_{1\,n-1}x_nx_{n-1} + a_{1n}^2x_n^2\,,\end{aligned} \tag{D.8a}$$

which can be rewritten as a quadratic form,

$$= x_{(1)}^T \begin{pmatrix} a_{12}^2 & a_{12}a_{13} & \dots & a_{12}a_{1n} \\ a_{12}a_{13} & a_{13}^2 & \dots & a_{13}a_{1n} \\ \vdots & \vdots & \ddots & \vdots \\ a_{12}a_{1n} & a_{13}a_{1n} & \dots & a_{1n}^2 \end{pmatrix} x_{(1)}\,, \tag{D.8b}$$

where $x_{(1)}$ denotes the $n-1$-dimensional vector obtained from x by deleting the first element x_1. Thus, Eq. (D.7) can be written compactly using a quadratic form with the $(n-1)\times(n-1)$ matrix B, given by

$$\mathrm{B} = \begin{pmatrix} a_{22} - a_{12}^2/a_{11} & a_{23} - a_{12}a_{13}/a_{11} & \dots & a_{2n} - a_{12}a_{1n}/a_{11} \\ a_{23} - a_{12}a_{13}/a_{11} & a_{33} - a_{13}^2/a_{11} & \dots & a_{23} - a_{13}a_{1n}/a_{11} \\ \vdots & \vdots & \ddots & \vdots \\ a_{2n} - a_{12}a_{1n}/a_{11} & a_{2n} - a_{13}a_{1n}/a_{11} & \dots & a_{nn} - a_{1n}^2/a_{11} \end{pmatrix}. \tag{D.9}$$

Equation (D.7) reads then

$$\int \mathrm{d}^n x\, \mathrm{e}^{-x^T \mathrm{A} x} = \sqrt{\frac{\pi}{a_{11}}} \int \mathrm{d}^{n-1} x \exp\Big\{-\sum_{j,k=2}^{n} x_j b_{jk} x_k\Big\}\,, \tag{D.10}$$

where the b_{jk} are the entries of B, given by

$$b_{jk} = a_{j+1\,k+1} - a_{1\,j+1}a_{1\,k+1}/a_{11}\,. \tag{D.11}$$

Since $a_{jk} = a_{kj}$, the matrix B is complex symmetric, obviously, but in order to be able to apply the induction statement, we also need to account for positive definiteness. To this end, we rewrite the quadratic form $x^T\mathrm{A}x$ as

$$x^T\mathrm{A}x = \begin{pmatrix} x_1 & x_{(1)}^T \end{pmatrix} \begin{pmatrix} a_{11} & a_1^T \\ a_1 & \mathrm{A}_{(1)(1)} \end{pmatrix} \begin{pmatrix} x_1 \\ x_{(1)} \end{pmatrix}\,, \tag{D.12}$$

where $A_{(1)(1)}$ denotes the $(n-1)\times(n-1)$ submatrix of A obtained after deleting the first row and column, and a_1 is the first column of A. By multiplying out the quadratic form blockwise, we obtain

$$x^T A x = x_1 a_{11} x_1 + x_{(1)}^T a_1 x_1 + x_1 a_1^T x_{(1)} + x_{(1)}^T A_{(1)(1)} x_{(1)} \,. \tag{D.13a}$$

Then, we complete the square by inserting the appropriate term,

$$\begin{aligned} &= a_{11}\left(x_1 x_1 + \frac{x_{(1)}^T a_1}{a_{11}} x_1 + x_1 \frac{a_1^T x_{(1)}}{a_{11}} + \frac{(x_{(1)}^T a_1)(a_1^T x_{(1)})}{a_{11}^2} \right) \\ &\quad - \frac{(x_{(1)}^T a_1)(a_1^T x_{(1)})}{a_{11}} + x_{(1)}^T A_{(1)(1)} x_{(1)} \qquad \text{(D.13b)} \\ &= a_{11}\Big(x_1 + a_1^T x_{(1)}/a_{11} \Big)\Big(x_1 + a_1^T x_{(1)}/a_{11} \Big)^T \\ &\quad + x_{(1)}^T \Big(A_{(1)(1)} - a_1 a_1^T/a_{11} \Big) x_{(1)} \,. \qquad \text{(D.13c)} \end{aligned}$$

By introducing the n-dimensional vector $y = (y_1 \; x_{(1)}^T)^T$, where $y_1 = x_1 + a_1^T x_{(1)}/a_{11} \in \mathbb{C}$ is now complex, the quadratic form can be put into the following form:

$$x^T A x = y^T \tilde{A} y = y^T \begin{pmatrix} a_{11} & 0 \\ 0 & B \end{pmatrix} y \,. \tag{D.13d}$$

The positive definiteness of B now follows from the positive definiteness of A by choosing the element x_1 to be equal to $x_1 = -a_1^T x_{(1)}/a_{11}$ for $x_{(1)} \in \mathbb{R}^{n-1}$, $x_{(1)} \neq 0$ arbitrary, such that $y_1 = 0$ and $y \in \mathbb{R}^n$. Then, $\mathrm{Re}\{x^T A x\} > 0$ implies $\mathrm{Re}\{y^T \tilde{A} y\} > 0$, so by Lemma 3 we conclude $\mathrm{Re}\{x_{(1)}^T B x_{(1)}\} > 0$ for any vector $x_{(1)} \in \mathbb{R}^{n-1}$ with $x_{(1)} \neq 0$.

Thus for the remaining integral in Eq. (D.10), all requirements for applying the induction statement, Eq. (D.3), are fulfilled. We obtain

$$\sqrt{\frac{\pi}{a_{11}}} \int \mathrm{d}^{n-1}x \exp\Big\{ -\sum_{j,k=2}^{n} x_j b_{jk} x_k \Big\} = \sqrt{\frac{\pi^{n-1}}{\det B}} \,, \tag{D.14}$$

which gives for the integral

$$\int \mathrm{d}^n x \; \mathrm{e}^{-x^T A x} = \sqrt{\frac{\pi}{a_{11}}} \sqrt{\frac{\pi^{n-1}}{\det B}} \,. \tag{D.15}$$

It remains to show that $a_{11} \det B = \det A$. Since we can write the elements of the matrix B as

$$b_{jk} = \frac{1}{a_{11}}(a_{11}a_{j+1\,k+1} - a_{1\,j+1}a_{1\,k+1}) = \frac{1}{a_{11}} \begin{vmatrix} a_{11} & a_{1\,j+1} \\ a_{1\,k+1} & a_{j+1\,k+1} \end{vmatrix} \,, \tag{D.16}$$

we can calculate the determinant of B by pulling out the $n-1$ factors a_{11} in each row, resulting in

$$|\mathrm{B}| = \frac{1}{a_{11}^{n-1}} \begin{vmatrix} \begin{vmatrix} a_{11} & a_{12} \\ a_{21} & a_{22} \end{vmatrix} & \begin{vmatrix} a_{11} & a_{13} \\ a_{21} & a_{23} \end{vmatrix} & \cdots & \begin{vmatrix} a_{11} & a_{1n} \\ a_{21} & a_{2n} \end{vmatrix} \\ \begin{vmatrix} a_{11} & a_{12} \\ a_{31} & a_{32} \end{vmatrix} & \begin{vmatrix} a_{11} & a_{13} \\ a_{31} & a_{33} \end{vmatrix} & \cdots & \begin{vmatrix} a_{11} & a_{1n} \\ a_{31} & a_{3n} \end{vmatrix} \\ \vdots & \vdots & \ddots & \vdots \\ \begin{vmatrix} a_{11} & a_{12} \\ a_{n1} & a_{n2} \end{vmatrix} & \begin{vmatrix} a_{11} & a_{13} \\ a_{n1} & a_{n3} \end{vmatrix} & \cdots & \begin{vmatrix} a_{11} & a_{1n} \\ a_{n1} & a_{nn} \end{vmatrix} \end{vmatrix} . \tag{D.17}$$

We can compare this determinant with the one obtained in Chiò's pivotal condensation process (Eves 1980, p. 129) applied to the matrix A. The core of Chiò's pivotal condensation process is a theorem which states that the determinant of any $n \times n$ matrix A with $a_{11} \neq 0$ is given by

$$|\mathrm{A}| = \frac{1}{a_{11}^{n-2}} \begin{vmatrix} \begin{vmatrix} a_{11} & a_{12} \\ a_{21} & a_{22} \end{vmatrix} & \begin{vmatrix} a_{11} & a_{13} \\ a_{21} & a_{23} \end{vmatrix} & \cdots & \begin{vmatrix} a_{11} & a_{1n} \\ a_{21} & a_{2n} \end{vmatrix} \\ \begin{vmatrix} a_{11} & a_{12} \\ a_{31} & a_{32} \end{vmatrix} & \begin{vmatrix} a_{11} & a_{13} \\ a_{31} & a_{33} \end{vmatrix} & \cdots & \begin{vmatrix} a_{11} & a_{1n} \\ a_{31} & a_{3n} \end{vmatrix} \\ \vdots & \vdots & \ddots & \vdots \\ \begin{vmatrix} a_{11} & a_{12} \\ a_{n1} & a_{n2} \end{vmatrix} & \begin{vmatrix} a_{11} & a_{13} \\ a_{n1} & a_{n3} \end{vmatrix} & \cdots & \begin{vmatrix} a_{11} & a_{1n} \\ a_{n1} & a_{nn} \end{vmatrix} \end{vmatrix} . \tag{D.18}$$

Thus, $a_{11} \det \mathrm{B}$ just yields the form of determinant of A obtained in the first step of Chiò's condensation process. □

The proof of Corollary 1 follows directly from the separate application of Eq. (D.1a) for each variable, while the corresponding integration is carried out during the proof. Corollary 2 follows from completing the square and from rewriting the quadratic form in terms of a new coordinate vector given by $(x + \mathrm{A}^{-1}b/2)$, which than can be handled via Eq. (D.1b) separately for each variable.

E

DERIVATION OF THE VISIBILITY FOR THERMAL STATES

Here we present a detailed derivation of the visibility for an ion Coulomb crystal initially prepared in a thermal state, the result of Eq. (6.46).

The starting point is Eq. (6.39),

$$\mathcal{O}(t) = \int \frac{\mathrm{d}^{6N}\lambda^{\downarrow}}{\pi^{3N}}\, P_0(\lambda^{\downarrow}) \frac{Z^2\, \mathrm{e}^{\mathrm{i}\varphi}}{\sqrt{\det \Omega}}\, \mathrm{e}^{G^*(\theta')}\, \mathrm{e}^{G(\theta)}\, \mathrm{e}^{\frac{1}{4}\mathbf{s}^T\Omega^{-1}\mathbf{s}}\,, \tag{E.1}$$

where the Glauber-Sudarshan-P distribution for the thermal state, Eq. (6.44),

$$P_0(\lambda_j^{\downarrow}) = \frac{1}{\pi \langle \hat{\mathrm{n}}_j^{\downarrow} \rangle} \exp\left[-\frac{\left|\lambda_j^{\downarrow}\right|^2}{\langle \hat{\mathrm{n}}_j^{\downarrow} \rangle} \right], \tag{E.2}$$

is inserted. The mode occupation $\langle n_j^{\downarrow} \rangle$ is given by Eq. (6.45) for a thermal state,

$$\langle \hat{\mathrm{n}}_j^{\downarrow} \rangle = \langle \hat{\mathrm{b}}_j^{\downarrow\dagger} \hat{\mathrm{b}}_j^{\downarrow} \rangle = \frac{\mathrm{e}^{-\hbar\omega_j^{\downarrow}/k_{\mathrm{B}}T}}{1 - \mathrm{e}^{-\hbar\omega_j^{\downarrow}/k_{\mathrm{B}}T}}\,, \tag{E.3}$$

where k_{B} is the Boltzmann constant and $\langle n_j^{\downarrow} \rangle$ is the mean vibrational number of mode j.

In order to calculate the integral in $\lambda^{\downarrow}$, we rephrase all of the above defined quantities, making their dependence on $\lambda^{\downarrow}$ apparent. We will do this in the following by looking at each term of the integrand.

E.1 THE TERM $\mathbf{s}^T\Omega^{-1}\mathbf{s}$

We first express all quantities in terms of $\lambda_j^{\downarrow}$'s, by defining the total displacements ζ_j's,

$$\zeta_j = \kappa_j + \beta_j^{\uparrow}\,, \qquad\qquad \zeta_j' = \kappa_j' + \beta_j^{\uparrow}\,. \tag{E.4}$$

$$S_j[\theta] = C_j^S(\zeta) + \sum_k P_{jk}\lambda_k^{\downarrow} + \sum_l R_{jk}\lambda_k^{\downarrow *}\,, \tag{E.5a}$$

$$S_j[\theta'] = C_j^S(\zeta') + \sum_k P_{jk}\,\mathrm{e}^{-\mathrm{i}\omega_k^{\downarrow}t}\lambda_k^{\downarrow} + \sum_k R_{jk}\,\mathrm{e}^{+\mathrm{i}\omega_k^{\downarrow}t}\lambda_k^{\downarrow *}\,, \tag{E.5b}$$

where

$$C_j^S(\zeta) = \sum_k A_{jk}\zeta_k^* - \zeta_j\,, \tag{E.6a}$$

$$C_j^{S*}(\zeta') = \sum_k A_{jk}\zeta_k' - \zeta_j'^*\,, \tag{E.6b}$$

$$P_{jl} = \sum_k A_{jk}v_{lk} - u_{lj}\,, \tag{E.6c}$$

$$R_{jl} = \sum_k A_{jk}u_{lk} - v_{lj} = 0\,, \tag{E.6d}$$

where the last equation, $R_{jk} = 0$ for all values of j and k, follows from Eq. (3.51). With Eqs. (E.5) simplified and taking the complex conjugate of the second one,

$$S_j[\theta] = C_j^S(\zeta) + \sum_k P_{jk}\lambda_k^{\downarrow}\,, \tag{E.7a}$$

$$S_j^*[\theta'] = C_j^{S*}(\zeta') + \sum_k P_{jk}\,\mathrm{e}^{+\mathrm{i}\omega_k^{\downarrow}t}\lambda_k^{\downarrow *}\,, \tag{E.7b}$$

we can define

$$S_j^{\pm} = S_j[\theta] \pm S_j^*[\theta']\,\mathrm{e}^{-\mathrm{i}\omega_j^e t} = C_j^{\pm} + \sum_k P_{jk}\lambda_k^{\downarrow} + \sum_k P_{jk}^{\pm}\lambda_k^{\downarrow *}\,, \tag{E.8}$$

with

$$C_j^{\pm} = C_j^S(\kappa) \pm C_j^{S*}(\kappa')\,\mathrm{e}^{-\mathrm{i}\omega_j^e t}\,, \tag{E.9a}$$

$$P_{jk}^{\pm} = \pm P_{jk}\,\mathrm{e}^{-\mathrm{i}(\omega_j^e - \omega_k^{\downarrow})t}\,. \tag{E.9b}$$

Let us denote $\mho \equiv \Omega^{-1}$. Since Ω is symmetric, $\mho$ is symmetric as well. By taking the blockwise inverse of Ω, we can calculate the blocks of $\mho$.

$$\begin{aligned}\mho &= \begin{pmatrix} \mho^{++} & \mho^{+-} \\ \mho^{-+} & \mho^{--} \end{pmatrix} = \Omega^{-1} = \begin{pmatrix} \Lambda & -\mathrm{i}\Gamma \\ -i\Gamma & \Xi \end{pmatrix}^{-1} \\ &= \begin{pmatrix} \Lambda^{-1} - \Lambda^{-1}\Gamma\Theta^{-1}\Gamma\Lambda^{-1} & i\Lambda^{-1}\Gamma\Theta^{-1} \\ i\Theta^{-1}\Gamma\Lambda^{-1} & \Theta^{-1} \end{pmatrix}\,,\end{aligned} \tag{E.10}$$

where

$$\Theta = (\Xi + \Gamma\Lambda^{-1}\Gamma) \tag{E.11}$$

is called the Schur complement of Λ.

We have to evaluate

$$\mathbf{s}^T\Omega^{-1}\mathbf{s} = \sum_{jk}\Big[S_j^+ \mho_{jk}^{++} S_k^+ - \mathrm{i}S_j^+ \mho_{jk}^{+-} S_k^- - \mathrm{i}S_j^- \mho_{jk}^{-+} S_k^+ - S_j^- \mho_{jk}^{--} S_k^-\Big]. \tag{E.12}$$

The sums in j and k can be evaluated as

$$\sum_{jk} S_j^\alpha \mho_{jk}^{\alpha\beta} S_k^\beta = C^{\alpha\beta} + \sum_l \left(g_l^{\alpha\beta}\lambda_l + h_l^{\alpha\beta}\lambda_l^*\right) + \sum_{lm}\begin{pmatrix}\lambda_l\\ \lambda_l^*\end{pmatrix}^T \Gamma_{lm}^{\alpha\beta}\begin{pmatrix}\lambda_m\\ \lambda_m^*\end{pmatrix}, \tag{E.13}$$

with

$$C^{\alpha\beta} = \sum_{jk} C_j^\alpha \mho_{jk}^{\alpha\beta} C_k^\beta, \tag{E.14}$$

and the vectors

$$g_l^{\alpha\beta} = \sum_{jk}\left(P_{jl}\mho_{jk}^{\alpha\beta}C_k^\beta + C_j^\alpha \mho_{jk}^{\alpha\beta}P_{kl}\right), \tag{E.15a}$$

$$h_l^{\alpha\beta} = \sum_{jk}\left(P_{jl}^\alpha \mho_{jk}^{\alpha\beta}C_k^\beta + C_j^\alpha \mho_{jk}^{\alpha\beta}P_{kl}^\beta\right). \tag{E.15b}$$

The 2-by-2 matrices $\Gamma_{lm}^{\alpha\beta}$ are given by

$$\Gamma_{lm}^{\alpha\beta} = \sum_{jk}\begin{pmatrix}P_{jl} & 0\\ 0 & P_{jl}^\alpha\end{pmatrix}\begin{pmatrix}\mho_{jk}^{\alpha\beta} & \mho_{jk}^{\alpha\beta}\\ \mho_{jk}^{\alpha\beta} & \mho_{jk}^{\alpha\beta}\end{pmatrix}\begin{pmatrix}P_{km} & 0\\ 0 & P_{km}^\beta\end{pmatrix}. \tag{E.16}$$

Summing over α, β, we obtain

$$\mathbf{s}^T\Omega^{-1}\mathbf{s} = \mathcal{G}^\Omega + \sum_l\left(\mathcal{K}_l^1\lambda_l + \mathcal{K}_l^2\lambda_l^*\right) + \sum_{lm}\begin{pmatrix}\lambda_l\\ \lambda_l^*\end{pmatrix}^T\begin{pmatrix}\mathcal{G}_{lm}^{11} & \mathcal{G}_{lm}^{12}\\ \mathcal{G}_{lm}^{21} & \mathcal{G}_{lm}^{22}\end{pmatrix}\begin{pmatrix}\lambda_m\\ \lambda_m^*\end{pmatrix}, \tag{E.17}$$

where

$$\mathcal{G}^\Omega = \sum_{\alpha\beta} C^{\alpha\beta}, \qquad \mathcal{K}_l^1 = \sum_{\alpha\beta} g_l^{\alpha\beta}, \qquad \mathcal{K}_l^2 = \sum_{\alpha\beta} h_l^{\alpha\beta}, \tag{E.18}$$

and

$$\mathcal{G}_{lm} = \begin{pmatrix}\mathcal{G}_{lm}^{11} & \mathcal{G}_{lm}^{12}\\ \mathcal{G}_{lm}^{21} & \mathcal{G}_{lm}^{22}\end{pmatrix} = \sum_{\alpha\beta}\Gamma_{lm}^{\alpha\beta}. \tag{E.19}$$

Changing to real and imaginary parts of $\lambda_j^{\downarrow} = x_j + iy_j$, we have

$$\mathbf{s}^T\Omega^{-1}\mathbf{s} = \mathcal{G}^{\Omega} + \sum_l \left(\mathcal{K}_l^x x_l + i\mathcal{K}_l^y y_l\right) + \sum_{lm} \begin{pmatrix} x_l \\ y_l \end{pmatrix}^T \begin{pmatrix} \mathcal{G}_{lm}^{xx} & \mathcal{G}_{lm}^{xy} \\ \mathcal{G}_{lm}^{yx} & \mathcal{G}_{lm}^{yy} \end{pmatrix} \begin{pmatrix} x_m \\ y_m \end{pmatrix}, \tag{E.20}$$

with

$$\mathcal{K}_j^x = \mathcal{K}_j^1 + \mathcal{K}_j^2 \tag{E.21a}$$

$$\mathcal{K}_j^y = \mathcal{K}_j^1 - \mathcal{K}_j^2 \tag{E.21b}$$

and

$$\begin{pmatrix} \mathcal{G}_{lm}^{xx} & \mathcal{G}_{lm}^{xy} \\ \mathcal{G}_{lm}^{yx} & \mathcal{G}_{lm}^{yy} \end{pmatrix} = \begin{pmatrix} 1 & 1 \\ i & -\mathrm{i} \end{pmatrix} \begin{pmatrix} \mathcal{G}_{lm}^{11} & \mathcal{G}_{lm}^{12} \\ \mathcal{G}_{lm}^{21} & \mathcal{G}_{lm}^{22} \end{pmatrix} \begin{pmatrix} 1 & i \\ 1 & -\mathrm{i} \end{pmatrix} \tag{E.22}$$

E.2 THE TERMS $G(\theta), G^*(\theta')$

$G(\theta)$ is given by Eq. (6.34), repeated here as

$$G(\theta) = \sum_{jk} \frac{A_{jk}}{2}\theta_j^*\theta_k^* - \sum_j \frac{|\theta_j|^2}{2}, \tag{E.23}$$

Introducing the quantities

$$C^G(\zeta^*) = \frac{1}{2}\sum_{jk}\left(\zeta_j^* A_{jk}\zeta_k^*\right) - \frac{1}{2}\sum_j |\zeta_j|^2, \tag{E.24}$$

and

$$I_l^1(\zeta^*) = \sum_{jk} v_{lj}A_{jk}\zeta_k^* - \frac{1}{2}\sum_j \left(v_{lj}\zeta_j + u_{lj}\zeta_j^*\right), \tag{E.25a}$$

$$I_l^2(\zeta^*) = \sum_{jk} u_{lj}A_{jk}\zeta_k^* - \frac{1}{2}\sum_j \left(u_{lj}\zeta_j + v_{lj}\zeta_j^*\right). \tag{E.25b}$$

and

$$\Upsilon_{lm}^{11} = \frac{1}{2}\sum_j v_{lj}\Big(\sum_k A_{jk}v_{mk} - u_{mj}\Big), \tag{E.26a}$$

$$\Upsilon_{lm}^{12} = \frac{1}{2}\sum_j v_{lj}\Big(\sum_k A_{jk}u_{mk} - v_{mj}\Big) = 0, \tag{E.26b}$$

$$\Upsilon_{lm}^{21} = \frac{1}{2}\sum_j u_{lj}\Big(\sum_k A_{jk}v_{mk} - u_{mj}\Big) = -\frac{1}{2}, \tag{E.26c}$$

$$\Upsilon_{lm}^{22} = \frac{1}{2}\sum_j u_{lj}\Big(\sum_k A_{jk}u_{mk} - v_{mj}\Big) = 0. \tag{E.26d}$$

where only Υ^{11}_{lm} is non-trivial, and the other relations follow from Eq. (3.51), explicitly given by

$$\sum_k u_{jk} A_{kl} - v_{jl} = 0\,, \tag{E.27}$$

respectively by the derived relation $A_{jk} = \sum_l (u^{-1})_{jl} v_{lk}$. We can write the constant $G(\theta)$ as

$$\begin{aligned} G(\theta) &= C^G(\zeta^*) + \sum_{lm} \begin{pmatrix} \lambda_l \\ \lambda_l^* \end{pmatrix}^T \begin{pmatrix} \Upsilon^{11}_{lm} & \Upsilon^{12}_{lm} \\ \Upsilon^{21}_{lm} & \Upsilon^{22}_{lm} \end{pmatrix} \begin{pmatrix} \lambda_m \\ \lambda_m^* \end{pmatrix} \\ &\qquad + \sum_l \left(I^1_l(\zeta^*)\lambda_l + I^2_l(\zeta^*){\lambda_l}^* \right) \qquad \text{(E.28)} \\ &= C^G(\zeta^*) + \sum_{lm} \begin{pmatrix} \lambda_l \\ \lambda_l^* \end{pmatrix}^T \begin{pmatrix} \Upsilon^{11}_{lm} & 0 \\ -\frac{1}{2} & 0 \end{pmatrix} \begin{pmatrix} \lambda_m \\ \lambda_m^* \end{pmatrix} \\ &\qquad + \sum_l \left(I^1_l(\zeta^*)\lambda_l + I^2_l(\zeta^*){\lambda_l}^* \right)\,. \qquad \text{(E.29)} \end{aligned}$$

Correspondingly for $G^*(\theta')$,

$$\begin{aligned} G^*(\theta') &= C^G(\zeta') + \sum_{lm} \begin{pmatrix} \lambda_l \\ \lambda_l^* \end{pmatrix}^T \begin{pmatrix} \bar{\Upsilon}^{11}_{lm} & \bar{\Upsilon}^{12}_{lm} \\ \bar{\Upsilon}^{21}_{lm} & \bar{\Upsilon}^{22}_{lm} \end{pmatrix} \begin{pmatrix} \lambda_m \\ \lambda_m^* \end{pmatrix} \\ &\qquad + \sum_l \left(I^2_l(\zeta')\,\mathrm{e}^{-\mathrm{i}\omega_l^{\downarrow} t}\lambda_l + I^1_l(\zeta')\,\mathrm{e}^{+\mathrm{i}\omega_l^{\downarrow} t}\lambda_l^* \right)\,, \end{aligned} \tag{E.30}$$

with

$$\bar{\Upsilon}^{11}_{lm} = \mathrm{e}^{-\mathrm{i}\omega_l^{\downarrow} t}\Upsilon^{22}_{lm}\,\mathrm{e}^{-\mathrm{i}\omega_m^{\downarrow} t} = 0\,, \tag{E.31a}$$

$$\bar{\Upsilon}^{12}_{lm} = \mathrm{e}^{-\mathrm{i}\omega_l^{\downarrow} t}\Upsilon^{21}_{lm}\,\mathrm{e}^{+\mathrm{i}\omega_m^{\downarrow} t} = -\frac{1}{2}\,\mathrm{e}^{-\mathrm{i}(\omega_l^{\downarrow} - \omega_m^{\downarrow})t}\,, \tag{E.31b}$$

$$\bar{\Upsilon}^{21}_{lm} = \mathrm{e}^{+\mathrm{i}\omega_l^{\downarrow} t}\Upsilon^{12}_{lm}\,\mathrm{e}^{-\mathrm{i}\omega_m^{\downarrow} t} = 0\,, \tag{E.31c}$$

$$\bar{\Upsilon}^{22}_{lm} = \mathrm{e}^{+\mathrm{i}\omega_l^{\downarrow} t}\Upsilon^{11}_{lm}\,\mathrm{e}^{+\mathrm{i}\omega_m^{\downarrow} t}\,, \tag{E.31d}$$

and the other quantities given above.

Summing both terms up, we have

$$\begin{aligned} G(\theta) + G(\theta') &= \mathcal{G}^G + \sum_j \left(\mathcal{I}^1_j \lambda_j + \mathcal{I}^2_j \lambda_j^* \right) \\ &\qquad + \sum_{lm} \begin{pmatrix} \lambda_l \\ \lambda_l^* \end{pmatrix}^T \begin{pmatrix} \mathcal{Y}^{11}_{lm} & \mathcal{Y}^{12}_{lm} \\ \mathcal{Y}^{21}_{lm} & \mathcal{Y}^{22}_{lm} \end{pmatrix} \begin{pmatrix} \lambda_m \\ \lambda_m^* \end{pmatrix}\,, \end{aligned} \tag{E.32}$$

with

$$\mathcal{G}^G = C^G(\zeta^*) + C^G(\zeta')\,, \tag{E.33}$$

and

$$\mathcal{I}_j^1 = I_j^1(\zeta^*) + I_j^2(\zeta')\,\mathrm{e}^{-\mathrm{i}\omega_j^{\downarrow}t}\,, \tag{E.34a}$$

$$\mathcal{I}_j^2 = I_j^2(\zeta^*) + I_j^1(\zeta')\,\mathrm{e}^{+\mathrm{i}\omega_j^{\downarrow}t}\,, \tag{E.34b}$$

and

$$\begin{aligned}\begin{pmatrix}\mathcal{Y}_{lm}^{11} & \mathcal{Y}_{lm}^{12}\\ \mathcal{Y}_{lm}^{21} & \mathcal{Y}_{lm}^{22}\end{pmatrix} &= \begin{pmatrix}\Upsilon_{lm}^{11} & \Upsilon_{lm}^{12}\\ \Upsilon_{lm}^{21} & \Upsilon_{lm}^{22}\end{pmatrix} + \begin{pmatrix}\bar{\Upsilon}_{lm}^{11} & \bar{\Upsilon}_{lm}^{12}\\ \bar{\Upsilon}_{lm}^{21} & \bar{\Upsilon}_{lm}^{22}\end{pmatrix}\\ &= \begin{pmatrix}\mathcal{Y}_{lm}^{11} & -\frac{1}{2}\,\mathrm{e}^{-\mathrm{i}(\omega_l^{\downarrow}-\omega_m^{\downarrow})t}\\ -\frac{1}{2} & \mathrm{e}^{+\mathrm{i}\omega_l^{\downarrow}t}\Upsilon_{lm}^{11}\,\mathrm{e}^{+\mathrm{i}\omega_m^{\downarrow}t}\end{pmatrix}\,.\end{aligned} \tag{E.35}$$

Changing to real and imaginary parts of $\lambda_j^{\downarrow} = x_j + iy_j$, we have

$$\begin{aligned}G(\theta) + G(\theta') = \mathcal{G}^G &+ \sum_l \left(\mathcal{I}_l^x x_l + i\mathcal{I}_l^y y_l\right)\\ &+ \sum_{lm}\begin{pmatrix}x_l\\ y_l\end{pmatrix}^T\begin{pmatrix}\mathcal{Y}_{lm}^{xx} & \mathcal{Y}_{lm}^{xy}\\ \mathcal{Y}_{lm}^{yx} & \mathcal{Y}_{lm}^{yy}\end{pmatrix}\begin{pmatrix}x_m\\ y_m\end{pmatrix}\,,\end{aligned} \tag{E.36}$$

with

$$\mathcal{I}_j^x = \mathcal{I}_j^1 + \mathcal{I}_j^2\,, \tag{E.37a}$$

$$\mathcal{I}_j^y = \mathcal{I}_j^1 - \mathcal{I}_j^2\,, \tag{E.37b}$$

and

$$\begin{pmatrix}\mathcal{Y}_{lm}^{xx} & \mathcal{Y}_{lm}^{xy}\\ \mathcal{Y}_{lm}^{yx} & \mathcal{Y}_{lm}^{yy}\end{pmatrix} = \begin{pmatrix}1 & 1\\ i & -\mathrm{i}\end{pmatrix}\begin{pmatrix}\mathcal{Y}_{lm}^{11} & \mathcal{Y}_{lm}^{12}\\ \mathcal{Y}_{lm}^{21} & \mathcal{Y}_{lm}^{22}\end{pmatrix}\begin{pmatrix}1 & i\\ 1 & -\mathrm{i}\end{pmatrix}\,. \tag{E.38}$$

E.3 THE TERM $\mathrm{e}^{\mathrm{i}\varphi}$

We have

$$\mathrm{i}\varphi_\lambda = \sum_j \beta_j^{\downarrow}\lambda_j^{\downarrow} - \sum_j \beta_j^{\downarrow}\lambda_j^{\downarrow *}\,, \tag{E.39a}$$

$$\mathrm{i}\varphi_{\lambda(t)} = \sum_j \beta_j^{\downarrow}\,\mathrm{e}^{-\mathrm{i}\omega_j^{\downarrow}t}\lambda_j^{\downarrow} - \sum_j \beta_j^{\downarrow}\,\mathrm{e}^{i\omega_j^{\downarrow}t}\lambda_j^{\downarrow *}\,, \tag{E.39b}$$

and

$$\varphi_\theta = \mathrm{Im}\Big[\sum_j \kappa_j\beta_j^{\uparrow}\Big] + \frac{1}{2\mathrm{i}}\sum_k\Big[J_k^+(\kappa)\lambda_k^{\downarrow} + J_k^-(\kappa)\lambda_k^{\downarrow *}\Big]\,, \tag{E.40a}$$

$$\begin{aligned}\varphi_{\theta'} = \mathrm{Im}&\Big[\sum_j \kappa_j'\beta_j^{\uparrow}\Big]\\ &+ \frac{1}{2\mathrm{i}}\sum_k\Big[J_k^+(\kappa')\,\mathrm{e}^{-\mathrm{i}\omega_k^{\downarrow}t}\lambda_k^{\downarrow} + J_k^-(\kappa')\,\mathrm{e}^{i\omega_k^{\downarrow}t}\lambda_k^{\downarrow *}\Big]\,,\end{aligned} \tag{E.40b}$$

where we defined

$$J_k^{\pm}(\kappa) = \sum_j \Big(\kappa_j (u_{kj} + v_{kj}) \pm \beta_j^{\uparrow} (u_{kj} - v_{kj}) \Big) \,. \tag{E.41}$$

Summing up, we have

$$\mathrm{i}\varphi = \mathrm{i}\tilde{\varphi} + \sum_k \left(\mathcal{J}_k^1 \lambda_k^{\downarrow} + \mathcal{J}_k^2 \lambda_k^{\downarrow *} \right) \,, \tag{E.42}$$

with

$$\tilde{\varphi} = \mathrm{Im}\Big[\sum_j \kappa_j \beta_j^{\uparrow} \Big] - \mathrm{Im}\Big[\sum_j \kappa'_j \beta_j^{\uparrow} \Big] \,, \tag{E.43}$$

and

$$\mathcal{J}_k^1 = \beta_j^{\downarrow} (1 - \mathrm{e}^{-\mathrm{i}\omega_j^{\downarrow} t}) + \frac{1}{2} \left(J_k^+(\kappa) - J_k^+(\kappa') \, \mathrm{e}^{-\mathrm{i}\omega_k^{\downarrow} t} \right) \,, \tag{E.44a}$$

$$\mathcal{J}_k^2 = \beta_j^{\downarrow} (\mathrm{e}^{+\mathrm{i}\omega_j^{\downarrow} t} - 1) + \frac{1}{2} \left(J_k^-(\kappa) - J_k^-(\kappa') \, \mathrm{e}^{+\mathrm{i}\omega_k^{\downarrow} t} \right) \,, \tag{E.44b}$$

Changing to real and imaginary parts again, we have

$$\mathrm{i}\varphi = \mathrm{i}\tilde{\varphi} + \sum_k \left(\mathcal{J}_k^x x_k + \mathrm{i} \mathcal{J}_k^y y_k \right) \,, \tag{E.45}$$

with

E.4 THE TERM $P_i(\lambda)$

Finally, the thermal state with mean values $\langle \hat{\mathrm{n}}_l \rangle$ is written as

$$P_i(\lambda) = \frac{1}{\pi^{3N} \langle \hat{\mathrm{n}}_1 \rangle \cdots \langle \hat{\mathrm{n}}_{3N} \rangle} \exp \left[- \sum_l \frac{\lambda_l^* \lambda_l}{\langle \hat{\mathrm{n}}_l \rangle} \right] \,. \tag{E.46}$$

The exponent is written as a quadratic form,

$$- \sum_{lm} \lambda_l^* \frac{\delta_{lm}}{\langle \hat{\mathrm{n}}_l \rangle} \lambda_m = - \sum_l \frac{(x_l^2 + y_l^2)}{\langle \hat{\mathrm{n}}_l \rangle} \,. \tag{E.47}$$

That is, the exponent is

$$- \sum_{lm} \begin{pmatrix} x_l \\ y_l \end{pmatrix}^T \begin{pmatrix} \mathcal{T}_{lm} & 0 \\ 0 & \mathcal{T}_{lm} \end{pmatrix} \begin{pmatrix} x_m \\ y_m \end{pmatrix} \,, \tag{E.48}$$

with

$$\mathcal{T}_{lm} = \langle \hat{\mathrm{n}}_l \rangle^{-1} \, \delta_{lm} \,. \tag{E.49}$$

E.5 SUMMING UP THE TERMS

Summing up, we have a prefactor

$$\frac{1}{\pi^{3N}\langle \hat{n}_1\rangle \cdots \langle \hat{n}_{3N}\rangle}\,, \tag{E.50}$$

and are left with a phase and constant terms

$$i\tilde{\varphi} + \frac{1}{4}\mathcal{G}^{\Omega} + \mathcal{G}^{G}\,, \tag{E.51}$$

linear terms

$$\sum_j \left[\mathcal{L}_j^x x_j + i\mathcal{L}_j^x y_j\right], \tag{E.52}$$

with

$$\mathcal{L}_j^x = \mathcal{I}_j^x + \mathcal{J}_j^x + \mathcal{K}_j^x \tag{E.53a}$$

$$,\mathcal{L}_j^y = \mathcal{I}_j^y + \mathcal{J}_j^y + \mathcal{K}_j^y\,. \tag{E.53b}$$

Finally, the quadratic terms read

$$\sum_{lm} \begin{pmatrix} x_l \\ y_l \end{pmatrix}^T \begin{pmatrix} \mathcal{X}_{lm}^{xx} & \mathcal{X}_{lm}^{xy} \\ \mathcal{X}_{lm}^{yx} & \mathcal{X}_{lm}^{yx} \end{pmatrix} \begin{pmatrix} x_m \\ y_m \end{pmatrix} \tag{E.54}$$

with

$$\begin{pmatrix} \mathcal{X}_{lm}^{xx} & \mathcal{X}_{lm}^{xy} \\ \mathcal{X}_{lm}^{yx} & \mathcal{X}_{lm}^{yy} \end{pmatrix} = \begin{pmatrix} \mathcal{Y}_{lm}^{xx} & \mathcal{Y}_{lm}^{xy} \\ \mathcal{Y}_{lm}^{yx} & \mathcal{Y}_{lm}^{yy} \end{pmatrix} + \frac{1}{4}\begin{pmatrix} \mathcal{G}_{lm}^{xx} & \mathcal{G}_{lm}^{xy} \\ \mathcal{G}_{lm}^{yx} & \mathcal{G}_{lm}^{yy} \end{pmatrix} - \begin{pmatrix} \mathcal{T}_{lm} & 0 \\ 0 & \mathcal{T}_{lm} \end{pmatrix}. \tag{E.55}$$

LIST OF PUBLICATIONS

This thesis is mainly based on the following publications:

Baltrusch, Jens D., Cecilia Cormick, Gabriele De Chiara, Tommaso Calarco and Giovanna Morigi, 'Quantum superpositions of crystalline structures', Phys. Rev. A **84** (6), 063821 (2011).

Baltrusch, Jens D., Cecilia Cormick and Giovanna Morigi, 'Quantum quenches of ion Coulomb crystals across structural instabilities', Phys. Rev. A **86** (3), 32104 (2012).

Baltrusch, Jens D., Cecilia Cormick and Giovanna Morigi, 'Quantum quenches of ion Coulomb crystals across structural instabilities. II. Thermal effects', Phys. Rev. A **87** (3), 32116 (2013).

Additionally, the following publication has been completed during the graduation; it is only marginally relevant to the work presented here:

Baltrusch, Jens D., Antonio Negretti, Jake M. Taylor and Tommaso Calarco, 'Fast and robust quantum computation with ionic Wigner crystals', Phys. Rev. A **83** (4), 042319 (2011).

LIST OF REFERENCES

Abrikosov, A. A., L. P. Gor'kov and I. Ye. Dzyaloshinkii, *Quantum Field Theoretical Methods in Statistical Physics*, ed. by D. ter Haar, trans. from Russian by D. E. Brown, second, revised and enlarged edition, Vol. 4, International series of monographs in natural philosophy (Pergamon Press, Oxford) (cit. on p. 68).

Afshar, Shahriar S., 'Violation of the principle of complementarity, and its implications', in Proc. SPIE, Vol. 5866, pp. 229–244, *The Nature of Light: What Is a Photon?*, ed. by Chandrasekhar Roychoudhuri and Katherine Creath (SPIE) (cit. on p. 107).

Afshar, Shahriar S., Eduardo Flores, Keith F. McDonald and Ernst Knoesel, 'Paradox in Wave-Particle Duality', Found. Phys. **37** (2), 295–305 (2007) (cit. on p. 107).

Aharonov, Yakir, David Z. Albert and Lev Vaidman, 'How the result of a measurement of a component of the spin of a spin-1/2 particle can turn out to be 100', Phys. Rev. Lett. **60** (14), 1351–1354 (1988) (cit. on p. 106).

Allen, L. and J. H. Eberly, *Optical Resonance and Two-Level Atoms*, unabr., corr. ed. (Dover Publications, New York) (cit. on pp. 7, 44, 90, 108, 110f.).

Altland, Alexander and Ben Simons, *Condensed Matter Field Theory*, 2nd ed. (Cambridge University Press, Cambridge et al.) (cit. on p. 209).

Arecchi, F. T., Eric Courtens, Robert Gilmore and Harry Thomas, 'Atomic Coherent States in Quantum Optics', Phys. Rev. A **6** (6), 2211–2237 (1972) (cit. on p. 201).

Arnol'd, Vladimir Igorevich, *Mathematical Methods of Classical Mechanics*, trans. from Russian by K. Vogtmann and A. Weinstein, 1st ed., Graduate Texts in Mathematics (Springer-Verlag, New York et al.) (cit. on pp. 34f.).

Audenaert, K., J. Eisert, M. B. Plenio and R. F. Werner, 'Entanglement properties of the harmonic chain', Phys. Rev. A **66** (4), 042327 (2002) (cit. on p. 2).

Baltrusch, Jens D., Cecilia Cormick, Gabriele De Chiara, Tommaso Calarco and Giovanna Morigi, 'Quantum superpositions of crystalline structures', Phys. Rev. A **84** (6), 063821 (2011) (cit. on p. 195).

Baltrusch, Jens D., Cecilia Cormick and Giovanna Morigi, 'Quantum quenches of ion Coulomb crystals across structural instabilities', Phys. Rev. A **86** (3), 32104 (2012).

Baltrusch, Jens D., Cecilia Cormick and Giovanna Morigi, 'Quantum quenches of ion Coulomb crystals across structural instabilities. II. Thermal effects', Phys. Rev. A **87** (3), 32116 (2013) (cit. on p. 112).

Baltrusch, Jens D., Antonio Negretti, Jake M. Taylor and Tommaso Calarco, 'Fast and robust quantum computation with ionic Wigner crystals', Phys. Rev. A **83** (4), 042319 (2011) (cit. on p. 18).

Banaszek, K., P. Horodecki, M. Karpiński and C. Radzewicz, 'Quantum mechanical which-way experiment with an internal degree of freedom', Nat. Commun. **4** (2013) 10.1038/ncomms3594 (cit. on p. 107).

Barbieri, M, M E Goggin, M P Almeida, B P Lanyon and A G White, 'Complementarity in variable strength quantum non-demolition measurements', New J. Phys. **11** (9), 093012 (2009) (cit. on p. 107).

Bartell, L. S., 'Complementarity in the double-slit experiment: On simple realizable systems for observing intermediate particle-wave behavior', Phys. Rev. D **21** (6), 1698–1699 (1980) (cit. on p. 105).

Bassani, Roberto, 'Earnshaw (1805–1888) and Passive Magnetic Levitation', Meccanica **41** (4), 375–389 (2006) (cit. on p. 9).

Batalhão, Tiago B., Alexandre M. Souza, Laura Mazzola, Ruben Auccaise, Roberto S. Sarthour, Ivan S. Oliveira, John Goold, Gabriele De Chiara, Mauro Paternostro and Roberto M. Serra, 'Experimental Reconstruction of Work Distribution and Study of Fluctuation Relations in a Closed Quantum System', Phys. Rev. Lett. **113** (14), 140601 (2014) (cit. on p. 185).

Beaty, Earl C., 'Simple electrodes for quadrupole ion traps', J. Appl. Phys. **61** (6), 2118–2122 (1987) (cit. on p. 13).

Bender, Carl M. and Steven A. Orszag, *Advanced Mathematical Methods for Scientists and Engineers*, 1st ed. (McGraw-Hill, Inc., New York) (cit. on p. 29).

Berkeland, D. J., J. D. Miller, J. C. Bergquist, W. M. Itano and D. J. Wineland, 'Minimization of ion micromotion in a Paul trap', J. Appl. Phys. **83** (10), 5025–5033 (1998) (cit. on p. 16).

Bermudez, A. and M. B. Plenio, 'Spin Peierls Quantum Phase Transitions in Coulomb Crystals', Phys. Rev. Lett. **109**, 010501 (2012) (cit. on p. 8).

Berry, MV and AK Geim, 'Of flying frogs and levitrons', Eur. J. Phys. **18** (4), 307 (1997) (cit. on p. 9).

Bertet, P., S. Osnaghi, A. Rauschenbeutel, G. Nogues, A. Auffeves, M. Brune, J. M. Raimond and S. Haroche, 'A complementarity experiment with an interferometer at the quantum-classical boundary', Nature **411** (6834), 166–170 (2001) (cit. on p. 107).

Bethge, Klaus, Gerhard Kraft, Peter Kreisler and Gertrud Walter, *Medical applications of nuclear physics*, Biological and medical physics, biomedical engineering (Springer-Verlag, Berlin et al.) (cit. on pp. 90, 95).

Birkl, G., S. Kassner and H. Walther, 'Multiple-Shell Structures of Laser-Cooled $^{24}Mg^{+}$ Ions in a Quadrupole Storage Ring', Nature **357** (6376), 310–313 (1992) (cit. on pp. 24, 26).

Björk, Gunnar, Jonas Söderholm, Alexei Trifonov, Tedros Tsegaye and Anders Karlsson, 'Complementarity and the uncertainty relations', Phys. Rev. A **60** (3), 1874–1882 (1999) (cit. on p. 106).

Blatt, R. and D. J. Wineland, 'Entangled states of trapped atomic ions', Nature **453**, 1008–1015 (2008) (cit. on pp. 2, 8, 46).

Blatt, Rainer and Christian F. Roos, 'Quantum simulations with trapped ions', Nat. Phys. **8** (4), 277–284 (2012) (cit. on p. 8).

Bloch, F., 'Nuclear Induction', Phys. Rev. **70**, 460–474 (1946) (cit. on p. 95).

Bloch, F., W. W. Hansen and Martin Packard, 'Nuclear Induction', Phys. Rev. **69**, 127–127 (1946) (cit. on p. 89).

Bloch, F. and A. Siegert, 'Magnetic Resonance for Nonrotating Fields', Phys. Rev. **57** (6), 522–527 (1940) (cit. on pp. 48, 90).

Bogoliubov, Nikolai Nikolaevich and Dimitrii Vasil'evich Shirkov, *Quantum Fields*, 1st ed. (Benjamin/Cummings, Reading, Massachusetts) (cit. on pp. 201f.).

Bogoliubov, Nikolai Nikolayevich and Nikolai Nikolayevich Bogoliubov Jr., *Introduction to Quantum Statistical Mechanics*, 2nd ed. (World Scientific, New Jersey et al.) (cit. on p. 68).

Bollinger, J. J., D. J. Wineland and Daniel H. E. Dubin, 'Non-Neutral Ion Plasmas and Crystals, Laser Cooling, and Atomic Clocks', Phys. Plasmas **1** (5), 1403–1414 (1994) (cit. on p. 23).

Borrelli, Massimo, Pinja Haikka, Gabriele De Chiara and Sabrina Maniscalco, 'Non-Markovian qubit dynamics induced by Coulomb crystals', Phys. Rev. A **88** (1), 010101 (2013) (cit. on p. 185).

Braig, C., P. Zarda, C. Kurtsiefer and H. Weinfurter, 'Experimental demonstration of complementarity with single photons', Appl. Phys. B **76** (2), 113–116 (2003) (cit. on p. 107).

Brookfield, Gary, 'Factoring Quartic Polynomials: A Lost Art', Mathematics Magazine **80** (1), 67–70 (2007) (cit. on p. 43).

Brown, Lowell S., 'Quantum motion in a Paul trap', Phys. Rev. Lett. **66**, 527–529 (1991) (cit. on p. 16).

Brown, Lowell and Gerald Gabrielse, 'Geonium theory: Physics of a single electron or ion in a Penning trap', Rev. Mod. Phys. **58** (1), 233–311 (1986) (cit. on pp. 2, 10).

Buks, E., R. Schuster, M. Heiblum, D. Mahalu and V. Umansky, 'Dephasing in electron interference by a 'which-path' detector', Nature **391** (6670), 871–874 (1998) (cit. on p. 107).

Busch, Paul and Christopher Shilladay, 'Complementarity and uncertainty in Mach–Zehnder interferometry and beyond ', Phys. Rep. **435** (1), 1–31 (2006) (cit. on pp. 106f.).

Calabrese, Pasquale, Fabian H. L. Essler and Maurizio Fagotti, 'Quantum Quench in the Transverse-Field Ising Chain', Phys. Rev. Lett. **106** (22), 227203 (2011) (cit. on p. 2).

Caldeira, A.O and A.J Leggett, 'Quantum tunnelling in a dissipative system', Ann. Physics **149** (2), 374–456 (1983) (cit. on p. 2).

Campbell, W. C., J. Mizrahi, Q. Quraishi, C. Senko, D. Hayes, D. Hucul, D. N. Matsukevich, P. Maunz and C. Monroe, 'Ultrafast Gates for Single Atomic Qubits', Phys. Rev. Lett. **105** (9), 090502 (2010) (cit. on pp. 112, 183).

Campos Venuti, Lorenzo, N. Tobias Jacobson, Siddhartha Santra and Paolo Zanardi, 'Exact Infinite-Time Statistics of the Loschmidt Echo for a Quantum Quench', Phys. Rev. Lett. **107** (1), 010403 (2011) (cit. on p. 185).

Campos Venuti, Lorenzo and Paolo Zanardi, 'Unitary equilibrations: Probability distribution of the Loschmidt echo', Phys. Rev. A **81** (2), 022113 (2010) (cit. on p. 185).

Campos Venuti, Lorenzo and Paolo Zanardi, 'Universality in the equilibration of quantum systems after a small quench', Phys. Rev. A **81** (3), 032113 (2010) (cit. on p. 185).

Carmichael, Howard, *Statistical Methods in Quantum Optics 1: Master Equations and Fokker-Planck Equations*, Physics and Astronomy Online Library (Springer) (cit. on pp. 159, 164, 204).

Carr, H. Y. and E. M. Purcell, 'Effects of Diffusion on Free Precession in Nuclear Magnetic Resonance Experiments', Phys. Rev. **94** (3), 630–638 (1954) (cit. on p. 95).

Casabone, B., I. García-Mata and D. A. Wisniacki, 'Discrepancies between decoherence and the Loschmidt echo', EPL **89** (5), 50009 (2010) (cit. on p. 101).

Chapman, Michael S, Troy D Hammond, Alan Lenef, Jörg Jorg Schmiedmayer, Richard A Rubenstein, Edward Smith and David E Pritchard, 'Photon Scattering from Atoms in an Atom Interferometer: Coherence Lost and Regained', Phys. Rev. Lett. **75** (21), 3783–3787 (1995) (cit. on p. 107).

Chou, C. W., D. B. Hume, J. C. J. Koelemeij, D. J. Wineland and T. Rosenband, 'Frequency comparison of two high-accuracy Al^+ optical clocks', Phys. Rev. Lett. **104** (7), 070802 (2010) (cit. on p. 8).

Chu, Steven, 'The manipulation of neutral particles', Rev. Mod. Phys. **70** (3), 685–706 (1998) (cit. on p. 9).

Chu, Steven, L. Hollberg, J. E. Bjorkholm, Alex Cable and A. Ashkin, 'Three-dimensional viscous confinement and cooling of atoms by resonance radiation pressure', Phys. Rev. Lett. **55** (1), 48–51 (1985) (cit. on p. 16).

Church, D. A., 'Storage-Ring Ion Trap Derived from the Linear Quadrupole Radio-Frequency Mass Filter', J. Appl. Phys. **40** (8), 3127–3134 (1969) (cit. on pp. 13, 26).

Cirac, J. I. and P. Zoller, 'Quantum Computations with Cold Trapped Ions', Phys. Rev. Lett. **74** (20), 4091–4094 (1995) (cit. on p. 8).

Cochran, W., 'Crystal stability and the theory of ferroelectricity', Advan. Phys. **9** (36), 387–423 (1960) (cit. on p. 28).

Cochran, W., 'Crystal stability and the theory of ferroelectricity part II. Piezoelectric crystals', Advan. Phys. **10** (40), 401–420 (1961) (cit. on p. 28).

Cohen-Tannoudji, C, J Dupont-Roc and G Grynberg, *Atom-photon interactions: basic processes and applications*, Wiley-Interscience publication (J. Wiley) (cit. on p. 47).

Cohen-Tannoudji, Claude, 'Manipulating Atoms with Photons', en, Phys. Scr. **T76** (1), 33 (1998) (cit. on pp. 47, 51f.).

Cohen-Tannoudji, Claude, Bernard Diu and Franck Laloë, *Quantum mechanics*, trans. from French by Patricia de Forcrand-Millard, Vol. Vol.1, A Wiley-Interscience Publication (Wiley, New York, NY et al.), pp. XV, 898 (cit. on pp. 90, 114).

Cohen-Tannoudji, Claude and David Guéry-Odelin, *Advances in Atomic Physics: An Overview* (World Scientific, New Jersey et al.) (cit. on p. 103).

Coleman, Sidney, 'There are no Goldstone bosons in two dimensions', Comm. Math. Phys. **31** (4), 259–264 (1973) (cit. on p. 30).

Coleman, Sidney, 'The Uses of Instantons', in *The Whys of Subnuclear Physics*, Vol. 15, pp. 805–941, ed. by Antonino Zichichi, Vol. 15, The Subnuclear Series (Springer US), pp. 805–941 (cit. on p. 29).

Collett, M. J., 'Exact density-matrix calculations for simple open systems', Phys. Rev. A **38** (5), 2233–2247 (1988) (cit. on pp. 201, 204).

Combescure, M., 'A quantum particle in a quadrupole radio-frequency trap', eng, Annales de l'institut Henri Poincaré (A) Physique théorique **44** (3), 293–314 (1986) (cit. on p. 16).

Cook, Richard J., Donn G. Shankland and Ann L. Wells, 'Quantum theory of particle motion in a rapidly oscillating field', Phys. Rev. A **31**, 564–567 (1985) (cit. on p. 16).

Cormick, Cecilia and Giovanna Morigi, 'Structural Transitions of Ion Strings in Quantum Potentials', Phys. Rev. Lett. **109** (5), 053003 (2012) (cit. on p. 36).

Cucchietti, F. M., D. A. R. Dalvit, J. P. Paz and W. H. Zurek, 'Decoherence and the Loschmidt Echo', Phys. Rev. Lett. **91** (21), 210403 (2003) (cit. on p. 101).

Dalibard, J. and C. Cohen-Tannoudji, 'Dressed-atom approach to atomic motion in laser light: the dipole force revisited', J. Opt. Soc. Am. B. **2** (11), 1707–1720 (1985) (cit. on pp. 49–51).

Davidson, *Physics of Nonneutral Plasmas*, 2nd ed. (Imperial College Press et al.) (cit. on p. 10).

De Chiara, Gabriele, Tommaso Calarco, Shmuel Fishman and Giovanna Morigi, 'Ramsey interferometry with a spin embedded in a Coulomb chain', Phys. Rev. A **78** (4), 43414 (2008) (cit. on pp. 3, 89, 115, 167).

De Zela, F., 'Comment on "Fringe Visibility and Which-Way Information: An Inequality"', ArXiv e-prints (2013) (cit. on p. 233).

Dehmelt, Hans, 'Proposed $10^{14}\Delta\nu/\nu$ laser fluorescence spectroscopy on Tl+ mono-ion oscillator', in Bulletin of the American Physical Society, Vol. 20, p. 60, Vol. 20 () (cit. on p. 113).

Dehmelt, H.G., 'Radiofrequency Spectroscopy of Stored Ions I: Storage ', in , Vol. 3, pp. 53–72, ed. by D.R. Bates and Immanuel Estermann, Vol. 3, Advances in Atomic and Molecular Physics (Academic Press, New York, London), pp. 53–72 (cit. on pp. 9, 15).

Dehmelt, H.G., 'Mono-Ion Oscillator as Potential Ultimate Laser Frequency Standard', in , pp. 596–601 () (cit. on p. 8). 'Monoion oscillator as potential ultimate laser frequency standard', in Instrumentation and Measurement, IEEE Transactions on **IM-31** (2), June 1982, 83–87.

Dehmelt, H.G., 'Monoion oscillator as potential ultimate laser frequency standard', Instrumentation and Measurement, IEEE Transactions on **IM-31** (2), 83–87 (1982). 'Mono-Ion Oscillator as Potential Ultimate Laser Frequency Standard', in , pp. 596–601, Thirty Fifth Annual Frequency Control Symposium. 1981 (Marriott Hotel, Philadelphia, Pennsylvania, 27th–29th May 1981), May 1981, pp. 596–601.

Del Campo, A., Ga De Chiara, Giovanna Morigi, M. B. Plenio and A. Retzker, 'Structural Defects in Ion Chains by Quenching the External Potential: The Inhomogeneous Kibble-Zurek Mechanism', Phys. Rev. Lett. **105** (7), 075701 (2010) (cit. on pp. 28, 122).

Del Campo, Adolfo and Wojciech H. Zurek, 'Universality of phase transition dynamics: Topological defects from symmetry breaking', Int. J. Mod. Phys. A **29** (08), 1430018 (2014) (cit. on p. 28).

Diddams, S A, J C Bergquist, S R Jefferts and C W Oates, 'Standards of time and frequency at the outset of the 21st century.', Science **306** (5700), 1318–24 (2004) (cit. on p. 90).

Diedrich, F., J. C. Bergquist, Wayne M. Itano and D. J. Wineland, 'Laser Cooling to the Zero-Point Energy of Motion', Phys. Rev. Lett. **62**, 403–406 (1989) (cit. on pp. 8, 114).

Diedrich, F., E. Peik, J. M. Chen, W. Quint and H. Walther, 'Observation of a Phase Transition of Stored Laser-Cooled Ions', Phys. Rev. Lett. **59** (26), 2931–2934 (1987) (cit. on p. 23).

DiVincenzo, David P., 'The Physical Implementation of Quantum Computation', Fortschr. Phys. **48** (9-11), 771–783 (2000) (cit. on p. 8).

Domb, Cyril, 'Graph Theory and Embeddings', in *Series Expansions for Lattice Models*, Vol. 3, ed. by Cyril Domb and Melville S. Green, 1st ed., Vol. 3, 20 vols., Phase transitions and critical phenomena (Academic Press, London et al.) (cit. on p. 76).

Dorner, R., S. R. Clark, L. Heaney, R. Fazio, J. Goold and V. Vedral, 'Extracting Quantum Work Statistics and Fluctuation Theorems by Single-Qubit Interferometry', Phys. Rev. Lett. **110** (23), 230601 (2013) (cit. on pp. 8, 185).

Drewsen, M. and A. Brøner, 'Harmonic linear Paul trap: Stability diagram and effective potentials', Phys. Rev. A **62** (4), 045401 (2000) (cit. on p. 15).

Drezet, Aurélien, Andreas Hohenau and Joachim R. Krenn, 'Momentum transfer for momentum transfer-free which-path experiments', Phys. Rev. A **73** (6), 062112 (2006) (cit. on p. 106).

Dubin, Daniel H. E., 'Theory of structural phase transitions in a trapped Coulomb crystal', Phys. Rev. Lett. **71**, 2753–2756 (1993) (cit. on pp. 24, 44).

Dubin, Daniel H. E., 'Minimum Energy State of the One-Dimensional Coulomb Chain', Phys. Rev. E **55** (4), 4017–4028 (1997) (cit. on p. 27).

Dubin, Daniel H. E. and T. M. O'Neil, 'Trapped nonneutral plasmas, liquids, and crystals (the thermal equilibrium states)', Rev. Mod. Phys. **71** (1), 87–172 (1999) (cit. on pp. 8, 10, 18, 22–25, 27).

Dürr, S., T. Nonn and G. Rempe, 'Fringe Visibility and Which-Way Information in an Atom Interferometer', Phys. Rev. Lett. **81** (26), 5705–5709 (1998) (cit. on p. 107).

Dürr, S., T. Nonn and G. Rempe, 'Origin of quantum-mechanical complementarity probed by a 'which-way'experiment in an atom interferometer', Nature **395** (6697), 33–37 (1998) (cit. on p. 107).

Dürr, Stephan and Gerhard Rempe, 'Can wave–particle duality be based on the uncertainty relation?', Am. J. Phys. **68** (11), 1021–1024 (2000) (cit. on p. 106).

Dziarmaga, Jacek, Wojciech H. Zurek and Michael Zwolak, 'Non-local quantum superpositions of topological defects', Nat. Phys. **8** (1), 49–53 (2011) (cit. on p. 28).

Earnshaw, Samuel, 'Transactions of the Cambridge Philosophical Society', Transactions of the Cambridge Philosophical Society **7**, 97–112 (1842) (cit. on p. 9).

Eichmann, U., J. C. Bergquist, J. J. Bollinger, J. M. Gilligan, W. M. Itano, D. J. Wineland and M. G. Raizen, 'Young's interference experiment with

light scattered from two atoms', Phys. Rev. Lett. **70** (16), 2359–2362 (1993) (cit. on p. 107).
Eisert, J., M. Friesdorf and C. Gogolin, 'Quantum many-body systems out of equilibrium', Nat. Phys. **11**, 124–130 (2015) (cit. on p. 2).
Englert, Berthold-Georg, 'Fringe Visibility and Which-Way Information: An Inequality', Phys. Rev. Lett. **77** (11), 2154–2157 (1996), see also (De Zela 2013) (cit. on pp. 100, 106).
Englert, Berthold-Georg and Giovanna Morigi, 'Five Lectures on Dissipative Master Equations', in *Coherent Evolution in Noisy Environments*, Vol. 611, pp. 55–106, ed. by Andreas Buchleitner and Klaus Hornberger, Vol. 611, Lecture Notes in Physics (Springer Berlin Heidelberg), pp. 55–106 (cit. on p. 1).
Englert, Berthold-Georg, Marian O. Scully and Herbert Walther, 'Complementarity and uncertainty', Nature **375** (6530), 367–368 (1995) (cit. on p. 106).
Englert, Berthold-Georg, Marlan O. Scully and Herbert Walther, 'Quantum erasure in double-slit interferometers with which-way detectors', Am. J. Phys. **67** (4), 325–329 (1999) (cit. on p. 106).
Englert, Berthold-Georg, Marlan O. Scully and Herbert Walther, 'On mechanisms that enforce complementarity', J. Mod. Opt. **47** (12), 2213–2220 (2000) (cit. on p. 106).
Eschner, Jürgen, Giovanna Morigi, Ferdinand Schmidt-Kaler and Rainer Blatt, 'Laser cooling of trapped ions', J. Opt. Soc. Am. B. **20** (5), 1003–1015 (2003) (cit. on p. 114).
Eves, Howard, *Elementary Matrix Theory*, unabridged and corrected (Dover Publications, New York) (cit. on pp. 212, 216).
Fasano, Antonio and Stefano Marmi, *Analytical Mechanics*, trans. from Italian by Beatrice Pelloni, 1st ed. (Oxford University Press, Oxford) (cit. on p. 38).
Feldker, T., P. Bachor, M. Stappel, D. Kolbe, R. Gerritsma, J. Walz and F. Schmidt-Kaler, 'Rydberg Excitation of a Single Trapped Ion', Phys. Rev. Lett. **115** (17), 173001 (2015) (cit. on p. 46).
Feldker, T., L. Pelzer, M. Stappel, P. Bachor, R. Steinborn, D. Kolbe, J. Walz and F. Schmidt-Kaler, 'Mode Shaping in Mixed Ion Crystals of $^{40}Ca^{+}$ and $^{40}Ca^{+}$', Appl. Phys. B (2013) 10.1007/s00340-013-5673-1 (cit. on p. 32).
Ferrari, Lodovico (cit. on p. 43).
Ferraro, Alessandro, Stefano Olivares and Matteo G. A. Paris, *Gaussian States in Quantum Information* (Bibliopolis, Napoli), p. 100 (cit. on p. 71).
Fetter, Alexander L., 'Nonuniform states of an imperfect bose gas ', Ann. Physics **70** (1), 67–101 (1972) (cit. on pp. 70f., 73).
Fetter, Alexander L. and John Dirk Walecka, *Quantum Theory of Many-Particle Systems*, 1st ed., International series in pure and applied physics (McGraw-Hill, New York) (cit. on p. 68).
Feynman, Richard P., 'An Operator Calculus Having Applications in Quantum Electrodynamics', Phys. Rev. **84** (1), 108–128 (1951) (cit. on p. 201).
Feynman, Richard P., *Statistical Mechanics: A Set of Lectures*, ed., with a forew., by David Pines, 1st ed., Vol. 36, Frontiers in Physics (Addison Wesley Publishing, Reading, Massachusetts et al.) (cit. on p. 75).

Feynman, Richard P., Robert B. Leighton and Matthew Sands, *The Feynman Lectures on Physics* (Addison-Wesley, Reading, Ma.) (cit. on p. 105).

Feynman, Richard P., Robert B. Leighton and Matthew Sands, *The Feynman Lectures on Physics*, Vol. 3: *Quantum Mechanics* (Addison-Wesley, Reading, Ma.) (cit. on p. 105).

Fishman, Shmuel, Gabriele De Chiara, Tommaso Calarco and Giovanna Morigi, 'Structural Phase Transitions in Low-Dimensional Ion Crystals', Phys. Rev. B **77** (6), 64111 (2008) (cit. on pp. 27, 42, 124, 126, 129).

Flores, E. V. and J. M. Tata, 'Complementarity Paradox Solved: Surprising Consequences', Foundations of Physics **40** (11), 1731–1743 (2010) (cit. on p. 107).

Flores, Eduardo V., 'Reply to Comments of Steuernagel on the Afshar's Experiment', Foundations of Physics **38** (8), 778–781 (2008) (cit. on p. 107).

Fogarty, T., E. Kajari, B. G. Taketani, A. Wolf, Th. Busch and Giovanna Morigi, 'Entangling two defects via a surrounding crystal', Phys. Rev. A **87** (5), 050304 (2013) (cit. on p. 2).

Ford, G. W., M. Kac and P. Mazur, 'Statistical Mechanics of Assemblies of Coupled Oscillators', J. Math. Phys. **6** (4), 504–515 (1965) (cit. on p. 2).

Frigo, Matteo and Steven G. Johnson, 'The design and implementation of FFTW3', Proceedings of the IEEE **93** (2), Special issue on "Program Generation, Optimization, and Platform Adaptation", 216–231 (2005) (cit. on p. 149).

Furry, W. H. and N. F. Ramsey, 'Significance of Potentials in Quantum Theory', Phys. Rev. **118** (3), 623–626 (1960) (cit. on p. 105).

Gardiner, C. P and P. Zoller, *Quantum Noise: A Handbook of Markovian and Non-Markovian Quantum Stochastic Methods with Applications to Quantum Optics*, Second enlarged edition (Springer, Berlin et al.) (cit. on p. 1).

Garg, Anupam, 'Tunnel splittings for one-dimensional potential wells revisited', Am. J. Phys. **68** (5), 430–437 (2000) (cit. on p. 29).

Garretson, J. L., H. M. Wiseman, D. T. Pope and D. T. Pegg, 'The uncertainty relation in 'which-way' experiments: how to observe directly the momentum transfer using weak values', Journal of Optics B: Quantum and Semiclassical Optics **6** (6), S506 (2004) (cit. on p. 106).

Geim, Andrey, 'Everyone's Magnetism', en, Physics Today **51** (9), 36 (1998) (cit. on p. 9).

Georgescu, I. M., S. Ashhab and Franco Nori, 'Quantum simulation', Rev. Mod. Phys. **86** (1), 153–185 (2014) (cit. on p. 8).

Ghosh, Pradip K., *Ion Traps*, Vol. 90, International Series of Monographs on Physics (Clarendon Press) (cit. on pp. 17, 23).

Gilmore, Robert, *Lie Groups, Physics, and Geometry: An Introduction for Physicists, Engineers, and Chemists*, 1st ed. (Cambridge University Press, Cambridge et al.) (cit. on p. 71).

Ginzburg, V. L., 'Some remarks on ferroelectricity, soft modes and related problems', Ferroelectrics **76** (1), 3–22 (1987) (cit. on p. 28).

Glauber, Roy J., 'The Quantum Mechanics of Trapped Wavepackets', in *Quantum Theory of Optical Coherence: Selected Papers and Lectures*, pp. 577–594 (Wiley-VCH Verlag), pp. 577–594 (cit. on p. 16).

Goldstein, H., *Classical Mechanics*, Addison-Wesley Series in Advanced Physics (Addison-Wesley Publishing Company) (cit. on pp. 19, 38).
Goldstone, J., 'Field theories with « Superconductor » solutions', Il Nuovo Cimento **19** (1), 154–164 (1961) (cit. on p. 30).
Goldstone, Jeffrey, Abdus Salam, Steven Weinberg and Broken Symmetries, 'Broken Symmetries', Phys. Rev. **127** (3), 965–970 (1962) (cit. on p. 30).
Gorin, Thomas, Tomaž Prosen, Thomas H. Seligman and Marko Žnidarič, 'Dynamics of Loschmidt echoes and fidelity decay', Phys. Rep. **435** (2–5), 33–156 (2006) (cit. on p. 101).
Gottfried, K and T Yan, *Quantum mechanics: fundamentals*, Graduate texts in contemporary physics (Springer) (cit. on p. 111).
Greenberger, Daniel M. and Allaine Yasin, 'Simultaneous wave and particle knowledge in a neutron interferometer', Phys. Lett. A **128** (8), 391–394 (1988) (cit. on p. 105).
Grimm, Rudolf, Matthias Weidemüller and Yurii B Ovchinnikov, 'Optical Dipole Traps for Neutral Atoms', in Vol. 42, pp. 95–170, ed. by Benjamin Bederson and Herbert Walther, Vol. 42, Advances In Atomic, Molecular, and Optical Physics (Academic Press), pp. 95–170 (cit. on pp. 46f., 50).
Häffner, Hartmut, Christian F. Roos and Rainer Blatt, 'Quantum computing with trapped ions ', Phys. Rep. **469** (4), 155–203 (2008) (cit. on pp. 2, 8, 13, 18).
Hahn, E. L., 'Spin Echoes', Phys. Rev. **80** (4), 580–594 (1950) (cit. on p. 95).
Haikka, P., J. Goold, S. McEndoo, F. Plastina and S. Maniscalco, 'Non-Markovianity, Loschmidt echo, and criticality: A unified picture', Phys. Rev. A **85** (6), 060101 (2012) (cit. on p. 185).
Hayes, D., D. N. Matsukevich, P. Maunz, D. Hucul, Q. Quraishi, S. Olmschenk, W. Campbell, J. Mizrahi, C. Senko and C. Monroe, 'Entanglement of Atomic Qubits Using an Optical Frequency Comb', Phys. Rev. Lett. **104** (14), 140501 (2010) (cit. on p. 112).
Heisenberg, Werner, 'Zur Theorie des Ferromagnetismus', Zeitschrift für Physik **49** (9-10), 619–636 (1928) (cit. on p. 30).
Hempel, C., B. P. Lanyon, P. Jurcevic, R. Gerritsma, R. Blatt and C. F. Roos, 'Entanglement-enhanced detection of single-photon scattering events', Nat. Phot. **7** (8), 630–633 (2013) (cit. on p. 109).
Henderson, H. and S. Searle, 'On Deriving the Inverse of a Sum of Matrices', SIAM Review **23** (1), 53–60 (1981) (cit. on p. 148).
Hohenberg, PC, 'Existence of long-range order in one and two dimensions', Phys. Rev. **158** (2), 383–386 (1967) (cit. on p. 30).
Holzscheiter, Michael H., 'A brief history in time of ion traps and their achievements in science', Phys. Scr. **1995** (T59), 69 (1995) (cit. on p. 9).
Home, Jonathon P., 'Quantum Science and Metrology with Mixed-Species Ion Chains ', in *Advances in Atomic, Molecular, and Optical Physics*, Vol. 62, pp. 231–277, ed. by Ennio Arimondo, Paul R. Berman and Chun C. Lin, Vol. 62, Advances In Atomic, Molecular, and Optical Physics (Academic Press) Chap. 4, pp. 231–277 (cit. on pp. 32, 109).
Horn, Roger A. and Charles R. Johnson, *Matrix Analysis*, reprinted with corrections (Cambridge University Press, Cambridge et al.) (cit. on pp. 39, 85, 134f., 205, 209f., 212).

Hu, Y M, W L Yang, Y Y Xu, F Zhou, L Chen, K L Gao, M Feng and C Lee, 'Franck–Condon physics in a single trapped ion', New J. Phys. **13** (5), 053037 (2011) (cit. on p. 184).

Huang, Kerson, *Statistical Mechanics*, 2nd ed. (John Wiley & Sons, New York et al.) (cit. on pp. 27, 75, 79, 114).

Huber, Gerhard, Ferdinand Schmidt-Kaler, Sebastian Deffner and Eric Lutz, 'Employing Trapped Cold Ions to Verify the Quantum Jarzynski Equality', Phys. Rev. Lett. **101**, 070403 (2008) (cit. on p. 8).

Huntemann, N., M. Okhapkin, B. Lipphardt, S. Weyers, Chr. Tamm and E. Peik, 'High-accuracy optical clock based on the octupole transition in $^{171}Yb^{+}$', Phys. Rev. Lett. **108** (9), 090801 (2012) (cit. on p. 8).

Iglói, Ferenc and Heiko Rieger, 'Quantum Relaxation after a Quench in Systems with Boundaries', Phys. Rev. Lett. **106** (3), 035701 (2011) (cit. on p. 1).

Islam, R. et al., 'Onset of a quantum phase transition with a trapped ion quantum simulator', Nat. Commun. **2**, 377 (2011) (cit. on p. 8).

Itano, Wayne M, J C Bergquist, J J Bollinger and D J Wineland, 'Cooling methods in ion traps', Phys. Scr. **1995** (T59), 106 (1995) (cit. on pp. 17, 114).

Itano, Wayne M. and Norman F. Ramsey, 'Accurate Measurement of Time', Scientific American **269** (1), 56–65 (1993) (cit. on p. 90).

Jackson, John David, *Classical Electrodynamics*, 3rd ed. (John Wiley & Sons, New York et al.) (cit. on pp. 10, 90).

Jacobson, N. Tobias, Lorenzo Campos Venuti and Paolo Zanardi, 'Unitary equilibration after a quantum quench of a thermal state', Phys. Rev. A **84** (2), 022115 (2011) (cit. on p. 185).

Jacques, V, N D Lai, a Dréau, D Zheng, D Chauvat, F Treussart, P Grangier and J-F Roch, 'Illustration of quantum complementarity using single photons interfering on a grating', New J. Phys. **10** (12), 123009 (2008) (cit. on p. 107).

Jacques, Vincent, E Wu, Frédéric Grosshans, François Treussart, Philippe Grangier, Alain Aspect and Jean-François Roch, 'Delayed-Choice Test of Quantum Complementarity with Interfering Single Photons', Phys. Rev. Lett. **100** (22), 220402 (2008) (cit. on p. 107).

Jacquod, Ph., P.G. Silvestrov and C.W.J. Beenakker, 'Golden rule decay versus Lyapunov decay of the quantum Loschmidt echo', Phys. Rev. E **64** (5), 055203 (2001) (cit. on p. 101).

Jaeger, Gregg, Abner Shimony and Lev Vaidman, 'Two interferometric complementarities', Phys. Rev. A **51** (1), 54–67 (1995) (cit. on p. 105).

Jalabert, Rodolfo A. and Horacio M. Pastawski, 'Environment-Independent Decoherence Rate in Classically Chaotic Systems', Phys. Rev. Lett. **86** (12), 2490–2493 (2001) (cit. on p. 101).

James, D.F.V., 'Quantum Dynamics of Cold Trapped Ions with Application to Quantum Computation', Appl. Phys. B **66** (2), 181–190 (1998) (cit. on p. 41).

Johanning, M., A. Braun, N. Timoney, V. Elman, W. Neuhauser and Chr. Wunderlich, 'Individual Addressing of Trapped Ions and Coupling of Motional and Spin States Using rf Radiation', Phys. Rev. Lett. **102** (7), 073004 (2009) (cit. on pp. 2, 8, 109).

Joos, Erich, H. Dieter Zeh, Claus Kiefer, Domenico J. W. Giulini, Joachim Kupsch and Ion-Olimpiu Stamatescu, *Decoherence and the Appearance of a Classical World in Quantum Theory*, 2nd ed. (Berlin et al.) (cit. on p. 1).

Jost, J. D., J. P. Home, J. M. Amini, D. Hanneke, R. Ozeri, C. Langer, J. J. Bollinger, D. Leibfried and D. J. Wineland, 'Entangled mechanical oscillators', Nature **459** (7247), 683–685 (2009) (cit. on p. 109).

Kaiser, Florian, Thomas Coudreau, Pérola Milman, Daniel B. Ostrowsky and Sébastien Tanzilli, 'Entanglement-Enabled Delayed-Choice Experiment', Science **338** (6107), 637–640 (2012) (cit. on p. 107).

Kapitza, Pyotr Leonidovich, 'Pendulum with a vibrating suspension', in *Collected papers of Kapitza*, pp. 726–737 () Chap. 46, pp. 726–737, originally published as Kapitza (1951b) (cit. on p. 14).

Kapitza, Pyotr Leonidovich, 'Dynamic stability of a pendulum when its point of suspension vibrates', Russian, Zhur. Eksp. i Teoret. Fiz. **21**, 588 (1951) (cit. on p. 237).

Kapitza, Pyotr Leonidovich, 'Pendulum with a vibrating suspension', Usp. Fiz. Nauk **44**, 7–15 (1951) (cit. on p. 237).

Kapitza, Pyotr Leonidovich, 'Dynamical stability of a pendulum when its point of suspension vibrates', in *Collected papers of Kapitza*, Vol. II, pp. 714–725, Vol. II () Chap. 45, pp. 714–725, originally published as Kapitza (1951c) (cit. on p. 14).

Kastler, Alfred, 'Quelques suggestions concernant la production optique et la détection optique d'une inégalité de population des niveaux de quantifigation spatiale des atomes. Application à l'expérience de Stern et Gerlach et à la résonance magnétique', J. Phys. Radium **11** (6), 255–265 (1950) (cit. on p. 108).

Kastler, Alfred, 'Optical Methods for Studying Hertzian Resonances', Science **158** (3798), 214–221 (1967) (cit. on p. 108).

Kastner, R. E., 'On Visibility in the Afshar Two-Slit Experiment', Found. Phys. **39** (10), 1139–1144 (2009) (cit. on p. 107).

Kaufmann, H., S. Ulm, G. Jacob, U. Poschinger, H. Landa, A. Retzker, M. B. Plenio and F. Schmidt-Kaler, 'Precise Experimental Investigation of Eigenmodes in a Planar Ion Crystal', Phys. Rev. Lett. **109** (26), 263003 (2012) (cit. on p. 183).

Keller, J et al., 'Topological defect formation and spontaneous symmetry breaking in ion Coulomb crystals.', en, Nat. Commun. **4**, 2291 (2013) (cit. on p. 28).

Khaetskii, Alexander V., Daniel Loss and Leonid Glazman, 'Electron Spin Decoherence in Quantum Dots due to Interaction with Nuclei', Phys. Rev. Lett. **88** (18), 186802 (2002) (cit. on p. 1).

Kibble, Tom, 'Phase-Transition Dynamics in the Lab and the Universe', Physics Today **60** (9), 47 (2007) (cit. on p. 122).

King, S. A., R. M. Godun, S. A. Webster, H. S. Margolis, L. A. M. Johnson, K. Szymaniec, P. E. G. Baird and P. Gill, 'Absolute frequency measurement of the $^2S_{1/2} - {}^2F_{7/2}$ electric octupole transition in a single ion of $^{171}Yb^+$ with 10^{-15} fractional uncertainty', New J. Phys. **14** (1), 013045 (2012) (cit. on p. 8).

Kittel, Charles, *Introduction to Solid State Physics*, 8th ed. (John Wiley & Sons, New Jersey) (cit. on p. 90).

Kramida, A., Yu. Ralchenko, J. Reader and NIST ASD Team, *NIST Atomic Spectra Database*, version 5.1, `http://physics.nist.gov/asd` (visited on 12/05/2014) (cit. on p. 108).

Kwapień, T., U. Eichmann and W. Sandner, 'Sympathetic Cooling of Laser-Produced Doubly Charged Ions in a Few-Ion Crystal', Phys. Rev. A **75** (6), 063418 (2007) (cit. on p. 32).

Kwiat, Paul G., Aephraim M. Steinberg and Raymond Y. Chiao, 'Observation of a "quantum eraser": A revival of coherence in a two-photon interference experiment', Phys. Rev. A **45** (11), 7729–7739 (1992) (cit. on p. 107).

Landa, H., M. Drewsen, B. Reznik and A. Retzker, 'Modes of Oscillation in Radiofrequency Paul Traps', New J. Phys. **14** (9), 093023 (2012) (cit. on pp. 34, 184).

Landa, H., M. Drewsen, B. Reznik and A. Retzker, 'Classical and Quantum Modes of Coupled Mathieu Equations', en, J. Phys. A **45** (45), 455305 (2012) (cit. on pp. 34, 184).

Landa, H., S. Marcovitch, A. Retzker, M. B. Plenio and B. Reznik, 'Quantum Coherence of Discrete Kink Solitons in Ion Traps', Phys. Rev. Lett. **104** (4), 043004 (2010) (cit. on pp. 28, 122).

Landau, Lev Davidovich, *Collected Papers of L.D. Landau.* Ed., with an introd., by D. Ter Haar, 1st ed. (Pergamon Press et al., Oxford et al.) (cit. on p. 27).

Landau, Lev Davidovich and Evgenii Mikhailovich Lifschitz, *Quantum Mechanics: Non-relativistic Theory*, trans. from Russian by J. B. Sykes and J. S. Bell, 2nd ed., Vol. 3, Course of Theoretical Physics (Pergamon Press, Oxford et al.) (cit. on p. 29).

Landau, Lev Davidovich and Evgenii Mikhailovich Lifschitz, *Mechanics*, trans. from Russian by J. B. Sykes and J. S. Bell, 2nd ed., Vol. 1, Course of Theoretical Physics (Pergamon Press, Oxford et al.) (cit. on pp. 14f., 18–20, 38).

Landau, Lev Davidovich and Evgenii Mikhailovich Lifschitz, *Statistical Physics*, trans. from Russian by J. B. Sykes and M. J. Kearsley, 2nd ed., Vol. 5, Course of Theoretical Physics (Pergamon Press, Oxford et al.) (cit. on p. 27).

Landau, Lev Davidovich and Evgenii Mikhailovich Lifschitz, *The Classical Theory of Fields*, trans. from Russian by Morton Hamermesh, 3rd ed., Vol. 2, Course of Theoretical Physics (Pergamon Press, Oxford et al.) (cit. on p. 9).

Le Bellac, Michel, *Quantum Physics*, trans. from French by Patricia de Forcrand-Millard (Cambridge University Press, Cambridge et al.), p. 585 (cit. on p. 97).

Leggett, A. J., S. Chakravarty, A. T. Dorsey, Matthew P. A. Fisher, Anupam Garg and W. Zwerger, 'Dynamics of the dissipative two-state system', Rev. Mod. Phys. **59** (1), 1–85 (1987) (cit. on pp. 2, 29).

Leibfried, D, R Blatt, C Monroe and D Wineland, 'Quantum dynamics of single trapped ions', Rev. Mod. Phys. **75** (1), 281–324 (2003) (cit. on pp. 8, 14f., 110).

Li, Weibin and Igor Lesanovsky, 'Electronically Excited Cold Ion Crystals', Phys. Rev. Lett. **108** (2), 023003 (2012) (cit. on p. 46).

Lin, G-D and L-M Duan, 'Equilibration and temperature distribution in a driven ion chain', New Journal of Physics **13** (7), 075015 (2011) (cit. on p. 9).

Lin, Y., J. P. Gaebler, T. R. Tan, R. Bowler, J. D. Jost, D. Leibfried and D. J. Wineland, 'Sympathetic Electromagnetically-Induced-Transparency Laser Cooling of Motional Modes in an Ion Chain', Phys. Rev. Lett. **110** (15), 153002 (2013) (cit. on p. 114).

Liu, Hong-Yu, Jie-Hui Huang, Jiang-Rui Gao, M. Suhail Zubairy and Shi-Yao Zhu, 'Relation between wave-particle duality and quantum uncertainty', Phys. Rev. A **85** (2), 022106 (2012) (cit. on p. 107).

Luis, A. and L. L. Sánchez-Soto, 'Complementarity Enforced by Random Classical Phase Kicks', Phys. Rev. Lett. **81** (19), 4031–4035 (1998) (cit. on p. 106).

Ma, Xiao-Song et al., 'Quantum erasure with causally disconnected choice', PNAS **110** (4), 1221–1226 (2013) (cit. on p. 107).

Madej, Alan A. and John E. Bernard, 'Single-Ion Optical Frequency Standards and Measurement of their Absolute Optical Frequency', in *Frequency Measurement and Control*, Advanced Techniques and Future TrendsVol. 79, pp. 153–195, ed. by Andre N. Luiten, Vol. 79, Topics in Applied Physics (Springer, Berlin, Heidelberg), pp. 153–195 (cit. on p. 8).

Madej, Alan A., Pierre Dubé, Zichao Zhou, John E. Bernard and Marina Gertsvolf, '$^{88}Sr^{+}$ 445 THz single-ion reference at the 10^{-17} level via control and cancellation of systematic uncertainties and its measurement against the si second', Phys. Rev. Lett. **109** (20), 203002 (2012) (cit. on p. 8).

Major, Fouad G., Viorica N. Gheorghe and Günther Werth, *Charged particle traps: Physics and Techniques of Charged Particle Field Confinement*, Vol. 37, Springer Series on Atomic, Optical and Plasma Physics (Springer, Berlin et al.) (cit. on pp. 17f., 23).

Mandel, Leonard and Emil Wolf, *Optical coherence and quantum optics* (Cambridge University Press, Cambridge) (cit. on pp. 74, 201).

March, Raymond E., 'Quadrupole ion traps', Mass Spectrometry Reviews **28** (6), 961–989 (2009) (cit. on p. 10).

Marquet, C., F. Schmidt-Kaler and D. F. V. James, 'Phonon-phonon interactions due to non-linear effects in a linear ion trap', Appl. Phys. B **76**, 199 (2003) (cit. on p. 37).

Mazzola, L., G. De Chiara and M. Paternostro, 'Measuring the Characteristic Function of the Work Distribution', Phys. Rev. Lett. **110** (23), 230602 (2013) (cit. on pp. 9, 185).

McLachlan, N. W., *Theory and application of Mathieu functions*, 1st ed. (Clarendon Press, London et al.) (cit. on pp. 14f.).

Meekhof, D M, C Monroe, B E King, W M Itano and D J Wineland, 'Generation of Nonclassical Motional States of a Trapped Atom', Phys. Rev. Lett. **77** (11), 2346 (1996) (cit. on p. 8).

Merkulov, I. A., Al. L. Efros and M. Rosen, 'Electron spin relaxation by nuclei in semiconductor quantum dots', Phys. Rev. B **65** (20), 205309 (2002) (cit. on p. 1).

Mermin, N. and H. Wagner, 'Absence of Ferromagnetism or Antiferromagnetism in One- or Two-Dimensional Isotropic Heisenberg Models', Phys. Rev. Lett. **17** (26), 1307–1307 (1966) (cit. on p. 30).

Mielenz, M., J. Brox, S. Kahra, G. Leschhorn, M. Albert, T. Schaetz, H. Landa and B. Reznik, 'Trapping of Topological-Structural Defects in Coulomb Crystals', Phys. Rev. Lett. **110** (13), 133004 (2013) (cit. on pp. 28, 122).

Mintert, Florian and Christof Wunderlich, 'Ion-Trap Quantum Logic Using Long-Wavelength Radiation', Phys. Rev. Lett. **87** (25), 257904 (2001) (cit. on p. 46).

Mir, R., J. S. Lundeen, M. W. Mitchell, A. M. Steinberg, J. L. Garretson and H. M. Wiseman, 'A double-slit 'which-way' experiment on the complementarity–uncertainty debate', New J. Phys. **9** (8), 287–287 (2007) (cit. on p. 106).

Mittelstaedt, P., A. Prieur and R. Schieder, 'Unsharp particle-wave duality in a photon split-beam experiment', Found. Phys. **17** (9), 891–903 (1987) (cit. on p. 107).

Mizrahi, J., B. Neyenhuis, K.G. Johnson, W.C. Campbell, C. Senko, D. Hayes and C. Monroe, 'Quantum control of qubits and atomic motion using ultrafast laser pulses', Appl. Phys. B **114** (1-2), 45–61 (2014) (cit. on p. 112).

Mizrahi, J., C. Senko, B. Neyenhuis, K. G. Johnson, W. C. Campbell, C. W. S. Conover and C. Monroe, 'Ultrafast Spin-Motion Entanglement and Interferometry with a Single Atom', Phys. Rev. Lett. **110** (20), 203001 (2013) (cit. on pp. 112, 183, 186).

Mohrhoff, Ulrich, 'Restoration of interference and the fallacy of delayed choice: concerning an experiment proposed by Englert, Scully, and Walther', Am. J. Phys. **64** (12), 1468–1475 (1996) (cit. on p. 106).

Mohrhoff, Ulrich, 'Objectivity, retrocausation, and the experiment of Englert, Scully, and Walther', Am. J. Phys. **67** (4), 330–335 (1999) (cit. on p. 106).

Monroe, C., D. M. Meekhof, B. E. King, S. R. Jefferts, W. M. Itano, D. J. Wineland and P. Gould, 'Resolved-Sideband Raman Cooling of a Bound Atom to the 3D Zero-Point Energy', Phys. Rev. Lett. **75** (22), 4011–4014 (1995) (cit. on pp. 8, 114).

Monroe, C, Dm Meekhof, Be King and Dj Wineland, 'A "Schrodinger Cat"Superposition State of an Atom', Science (New York, N.Y.) **272** (5265), 1131–6 (1996) (cit. on p. 2).

Monz, Thomas, Philipp Schindler, Julio T. Barreiro, Michael Chwalla, Daniel Nigg, William A. Coish, Maximilian Harlander, Wolfgang Hänsel, Markus Hennrich and Rainer Blatt, '14-Qubit Entanglement: Creation and Coherence', Phys. Rev. Lett. **106** (13), 130506 (2011) (cit. on p. 8).

Morigi, G., J. Eschner, J. I. Cirac and P. Zoller, 'Laser cooling of two trapped ions: Sideband cooling beyond the Lamb-Dicke limit', Phys. Rev. A **59** (5), 3797–3808 (1999) (cit. on p. 37).

Morigi, Giovanna, Jürgen Eschner and Christoph H. Keitel, 'Ground State Laser Cooling Using Electromagnetically Induced Transparency', Phys. Rev. Lett. **85** (21), 4458–4461 (2000) (cit. on p. 114).

Morigi, Giovanna and Shmuel Fishman, 'Dynamics of an Ion Chain in a Harmonic Potential', Phys. Rev. E **70** (6), 066141 (2004) (cit. on pp. 26, 44, 123).

Mukherjee, Victor, Shraddha Sharma and Amit Dutta, 'Loschmidt echo with a nonequilibrium initial state: Early-time scaling and enhanced decoherence', Phys. Rev. B **86** (2), 020301 (2012) (cit. on p. 149).

Myatt, C. J., B. E. King, Q. A. Turchette, C. A. Sackett, D. Kielpinski, W. M. Itano, C. Monroe and D. J. Wineland, 'Decoherence of quantum superpositions through coupling to engineered reservoirs', Nature **403** (6767), 269–273 (2000) (cit. on p. 2).

Nagourney, Warren, Jon Sandberg and Hans Dehmelt, 'Shelved optical electron amplifier: Observation of quantum jumps', Phys. Rev. Lett. **56** (26), 2797–2799 (1986) (cit. on p. 113).

Neuhauser, W., M. Hohenstatt, P. E. Toschek and H. Dehmelt, 'Localized visible Ba^+ mono-ion oscillator', Phys. Rev. A **22**, 1137–1140 (1980) (cit. on p. 8).

Neuhauser, W., M. Hohenstatt, P. Toschek and H. Dehmelt, 'Optical-Sideband Cooling of Visible Atom Cloud Confined in Parabolic Well', Phys. Rev. Lett. **41**, 233–236 (1978) (cit. on pp. 7, 114).

O'Haver, Tom, *findpeaks.m*, version 3, `http://terpconnect.umd.edu/~toh/spectrum/PeakFindingandMeasurement.htm` (visited on 16/08/2011) (cit. on pp. 147, 154).

Olivares, S., 'Quantum optics in the phase space', The European Physical Journal Special Topics **203** (1), 3–24 (2012) (cit. on p. 71).

Paul, W. and M. Raether, 'Das elektrische Massenfilter', German, Zeitschrift für Physik **140** (3), 262–273 (1955) (cit. on p. 10).

Paul, W., H.P. Reinhard and U. Zahn, 'Das elektrische Massenfilter als Massenspektrometer und Isotopentrenner', German, Zeitschrift für Physik **152** (2), 143–182 (1958) (cit. on p. 10).

Paul, Wolfgang, 'Electromagnetic traps for charged and neutral particles', Rev. Mod. Phys. **62** (3), 531–540 (1990) (cit. on pp. 7, 10, 14f.).

Paul, Wolfgang and Helmut Steinwedel, 'Verfahren zur Trennung bzw. zum getrennten Nachweis von Ionen verschiedener spezifischer Ladung', german Patent DE 944 900 B (), filed December 24, 1953 and issued June 07, 1956 (cit. on p. 10).

Paz, Juan Pablo and Augusto J. Roncaglia, 'Dynamics of the Entanglement between Two Oscillators in the Same Environment', Phys. Rev. Lett. **100** (22), 220401 (2008) (cit. on p. 2).

Paz, Juan Pablo and Wojciech Hubert Zurek, 'Environment-Induced Decoherence and the Transition from Quantum to Classical', in *Fundamentals of Quantum Information*, Vol. 587, pp. 77–148, ed. by Dieter Heiss, Vol. 587, Lecture Notes in Physics (Springer Berlin Heidelberg), pp. 77–148 (cit. on p. 1).

Penning, F. M., 'Ein neues manometer für niedrige gasdrucke, insbesondere zwischen lo $^{-3}$ und 10 $^{-5}$ mm', Physica **4**, 71–75 (1937) (cit. on p. 9).

Penrose, Roger, *The Road to Reality: A complete Guide to the Laws of the Universe*, 1st ed., First published in 2004 by Cape, London (Vintage Books, London et al.) (cit. on p. 1).

Peres, Asher, 'Stability of quantum motion in chaotic and regular systems', Phys. Rev. A **30** (4), 1610–1615 (1984) (cit. on p. 101).

Pfau, T., S. Spälter, Ch. Kurtsiefer, C. R. Ekstrom and J. Mlynek, 'Loss of Spatial Coherence by a Single Spontaneous Emission', Phys. Rev. Lett. **73** (9), 1223–1226 (1994) (cit. on p. 107).

Phillips, WD, 'Laser cooling and trapping of neutral atoms', Rev. Mod. Phys. **70** (3), 721–741 (1998) (cit. on p. 9).

Piacente, G., I. V. Schweigert, J. J. Betouras and F. M. Peeters, 'Generic Properties of a Quasi-One-Dimensional Classical Wigner Crystal', Phys. Rev. B **69** (4), 045324 (2004) (cit. on p. 27).

Pierce, John Robinson, *Theory and design of electron beams*, 2nd ed., The Bell Telephone Laboratories series (Van Nostrand, Princeton, N.J. et al.) (cit. on pp. 9, 187).

Pitaevskii, L.P. and S. Stringari, *Bose-Einstein Condensation*, Vol. 116, International Series of Monographs on Physics (Oxford University Press, Oxford) (cit. on p. 68).

Polkovnikov, Anatoli, Krishnendu Sengupta, Alessandro Silva and Mukund Vengalattore, '*Colloquium* : nonequilibrium dynamics of closed interacting quantum systems', Rev. Mod. Phys. **83** (3), 863–883 (2011) (cit. on p. 2).

Porras, D. and J. I. Cirac, 'Effective Quantum Spin Systems with Trapped Ions', Phys. Rev. Lett. **92** (20), 207901 (2004) (cit. on p. 2).

Porras, D., F. Marquardt, J. von Delft and J. I. Cirac, 'Mesoscopic spin-boson models of trapped ions', Phys. Rev. A **78** (1), 010101 (2008) (cit. on p. 2).

Poyatos, J. F., J. I. Cirac, R. Blatt and P. Zoller, 'Trapped ions in the strong-excitation regime: Ion interferometry and nonclassical states', Phys. Rev. A **54** (2), 1532–1540 (1996) (cit. on pp. 3, 89, 111).

Poyatos, J. F., J. I. Cirac and P. Zoller, 'Quantum Reservoir Engineering with Laser Cooled Trapped Ions', Phys. Rev. Lett. **77** (23), 4728–4731 (1996) (cit. on p. 8).

Prestage, J. D., G. J. Dick and L. Maleki, 'New ion trap for frequency standard applications', J. Appl. Phys. **66** (3), 1013–1017 (1989) (cit. on p. 13).

Purcell, E. M., H. C. Torrey and R. V. Pound, 'Resonance Absorption by Nuclear Magnetic Moments in a Solid', Phys. Rev. **69**, 37–38 (1946) (cit. on p. 89).

Quan, H. T., Z. Song, X. F. Liu, P. Zanardi and C. P. Sun, 'Decay of Loschmidt Echo Enhanced by Quantum Criticality', Phys. Rev. Lett. **96** (14), 140604 (2006) (cit. on pp. 101, 122, 149).

Rabi, I. I., N. F. Ramsey and J. Schwinger, 'Use of Rotating Coordinates in Magnetic Resonance Problems', Rev. Mod. Phys. **26** (2), 167–171 (1954) (cit. on p. 93).

Rabi, I., S. Millman, P. Kusch and J. Zacharias, 'The Molecular Beam Resonance Method for Measuring Nuclear Magnetic Moments. The Magnetic Moments of Li63, Li73 and F199', Phys. Rev. **55** (6), 526–535 (1939) (cit. on p. 89).

Rabi, I., J. Zacharias, S. Millman and P. Kusch, 'A New Method of Measuring Nuclear Magnetic Moment', Phys. Rev. **53** (4), 318–318 (1938) (cit. on pp. 89, 93).

Rafac, R., J. P. Schiffer, J. S. Hangst, D. H. Dubin and D. J. Wales, 'Stable Configurations of Confined Cold Ionic Systems', PNAS **88** (2), 483–486 (1991) (cit. on pp. 40f.).

Raizen, M. G., J. M. Gilligan, J. C. Bergquist, W. M. Itano and D. J. Wineland, 'Ionic Crystals in a Linear Paul Trap', Phys. Rev. A **45** (9), 6493–6501 (1992) (cit. on p. 13).

Ramsey, N.F., 'History of Atomic Clocks', Journal of Research of the National Bureau of Standards **88** (5), 301 (1983) (cit. on p. 90).
Ramsey, Norman, 'A New Molecular Beam Resonance Method', Phys. Rev. **76** (7), 996–996 (1949) (cit. on pp. 89f., 95).
Ramsey, Norman, 'A Molecular Beam Resonance Method with Separated Oscillating Fields', Phys. Rev. **78** (6), 695–699 (1950) (cit. on pp. 90, 96).
Ramsey, Norman F., *Molecular Beams*, The International Series of Monographs on Physics (Oxford University Press, London et al.) (cit. on pp. 89f.).
Ramsey, Norman F., 'The method of successive oscillatory fields', Physics Today **33** (7), 25–30 (1980) (cit. on p. 184).
Retzker, A., R. C. Thompson, D. M. Segal and M. B. Plenio, 'Double Well Potentials and Quantum Phase Transitions in Ion Traps', Phys. Rev. Lett. **101** (26), 260504 (2008) (cit. on p. 126).
Riehle, Fritz, *Frequency Standards: Basics and Applications* (Wiley, Weinheim) (cit. on pp. 2, 8, 23).
Roos, C. F., D. Leibfried, A. Mundt, F. Schmidt-Kaler, J. Eschner and R. Blatt, 'Experimental Demonstration of Ground State Laser Cooling with Electromagnetically Induced Transparency', Phys. Rev. Lett. **85** (26), 5547–5550 (2000) (cit. on p. 114).
Rosenband, T. et al., 'Frequency ratio of Al^+ and Hg^+ single-ion optical clocks; metrology at the 17th decimal place', Science **319** (5871), 1808–1812 (2008) (cit. on p. 8).
Saleh, Bahaa E.A. and Malvin Carl Teich, *Fundamentals of Photonics*, ed. by Bahaa E.A. Saleh, 2nd ed., Wiley Series in Pure and Applied Optics (John Wiley & Sons, Hoboken, New Jersey) (cit. on p. 53).
Schätz, T., U. Schramm and D. Habs, 'Crystalline Ion Beams', Nature **412** (6848), 717–720 (2001) (cit. on p. 26).
Schellekens, M., R. Hoppeler, A. Perrin, J. Viana Gomes, D. Boiron, A. Aspect and C. I. Westbrook, 'Hanbury Brown Twiss Effect for Ultracold Quantum Gases', Science **310** (5748), 648–651 (2005) (cit. on p. 186).
Schiffer, J., 'Phase Transitions in Anisotropically Confined Ionic Crystals', Phys. Rev. Lett. **70** (6), 818–821 (1993) (cit. on pp. 27, 44).
Schlosshauer, Maximilian, 'Decoherence, the Measurement Problem, and Interpretations of Quantum Mechanics', Rev. Mod. Phys. **76** (4), 1267–1305 (2005) (cit. on p. 1).
Schmidt-Kaler, Ferdinand, Hartmut Häffner, Mark Riebe, Stephan Gulde, Gavin P. T. Lancaster, Thomas Deuschle, Christoph Becher, Christian F. Roos, Jürgen Eschner and Rainer Blatt, 'Realization of the cirac–zoller controlled-NOT quantum gate', Nature **422** (6930), 408–411 (2003) (cit. on p. 8).
Schneider, Ch., M. Enderlein, T. Huber and T. Schaetz, 'Optical trapping of an ion', Nat. Phot. **4** (October) (2010) 10.1038/nphoton.2010.236 (cit. on pp. 51, 54, 186).
Schneider, Christian, Diego Porras and Tobias Schaetz, 'Experimental quantum simulations of many-body physics with trapped ions', Reports on progress in physics **75** (2), 024401 (2012) (cit. on pp. 2, 8).

Schnitzler, W., N. M. Linke, R. Fickler, J. Meijer, F. Schmidt-Kaler and K. Singer, 'Deterministic Ultracold Ion Source Targeting the Heisenberg Limit', Phys. Rev. Lett. **102** (7), 070501 (2009) (cit. on p. 187).

Schwindt, Peter D. D., Paul G. Kwiat and Berthold-Georg Englert, 'Quantitative wave-particle duality and nonerasing quantum erasure', Phys. Rev. A **60** (6), 4285–4290 (1999) (cit. on p. 107).

Scott, William T., 'Who Was Earnshaw?', Am. J. Phys. **27** (6), 418 (1959) (cit. on p. 9).

Scully, Marian O., Berthold-Georg Englert and Herbert Walther, 'Quantum optical tests of complementarity', Nature **351** (6322), 111–116 (1991) (cit. on p. 106).

Scully, Marlan O., Berthold-Georg Englert and Julian Schwinger, 'Spin coherence and Humpty-Dumpty. III. The effects of observation', Phys. Rev. A **40** (4), 1775–1784 (1989) (cit. on p. 106).

Scully, Marlan and Kai Drühl, 'Quantum eraser: A proposed photon correlation experiment concerning observation and "delayed choice"in quantum mechanics', Phys. Rev. A **25** (4), 2208–2213 (1982) (cit. on p. 106).

Shimshoni, Efrat, Giovanna Morigi and Shmuel Fishman, 'Quantum Structural Phase Transition in Chains of Interacting Atoms', Phys. Rev. A **83** (3), 32308 (2011) (cit. on p. 27).

Shimshoni, Efrat, Giovanna Morigi and Shmuel Fishman, 'Quantum Zigzag Transition in Ion Chains', Phys. Rev. Lett. **106** (1), 10401 (2011) (cit. on pp. 8, 27).

Silvi, Pietro, Gabriele De Chiara, Tommaso Calarco, Giovanna Morigi and Simone Montangero, 'Full Characterization of the Quantum Linear-Zigzag Transition in Atomic Chains', Annalen der Physik **6**, 827–832 (2013) (cit. on p. 27).

Simonius, Markus, 'Spontaneous Symmetry Breaking and Blocking of Metastable States', Phys. Rev. Lett. **40** (15), 980–983 (1978) (cit. on p. 30).

Slichter, Charles P., *Principles of Magnetic Resonance*, 2nd ed., Vol. 1, Springer Series in Solid-State Sciences (Springer-Verlag, Berlin et al.) (cit. on p. 95).

Stenholm, S., 'Quantum Motion in a Paul Trap', J. Mod. Opt. **39** (2), 279–290 (1992) (cit. on p. 16).

Stephenson, Andrew, 'On induced stability', Philosophical Magazine Series 6 **15** (86), 233–236 (1908) (cit. on p. 14).

Steuernagel, Ole, 'Afshar's Experiment Does Not Show a Violation of Complementarity', Found. Phys. **37** (9), 1370–1385 (2007) (cit. on p. 107).

Storey, E. Pippa, Sze M. Tan, Matthew J. Collett and Daniel F. Walls, 'Complementarity and uncertainty', Nature **375** (6530), 368 (1995) (cit. on p. 106).

Storey, Pippa, Sze Tan, Matthew Collett and Daniel Walls, 'Path detection and the uncertainty principle', Nature **367** (6464), 626–628 (1994) (cit. on p. 106).

Summhammer, J., H. Rauch and D. Tuppinger, 'Stochastic and deterministic absorption in neutron-interference experiments', Phys. Rev. A **36** (9), 4447–4455 (1987) (cit. on p. 107).

Taketani, B. G., T. Fogarty, E. Kajari, Th. Busch and Giovanna Morigi, 'Quantum reservoirs with ion chains', Phys. Rev. A **90** (1), 012312 (2014) (cit. on p. 2).

Tan, S. M. and D. F. Walls, 'Loss of coherence in interferometry', Phys. Rev. A **47** (6), 4663–4676 (1993) (cit. on p. 105).

Tang, Jian-Shun, Yu-Long Li, Chuan-Feng Li and Guang-Can Guo, 'Revisiting Bohr's principle of complementarity with a quantum device', Phys. Rev. A **88** (1), 014103 (2013) (cit. on p. 107).

Thomson, William, 'The Kinetic Theory of the Dissipation of Energy', Proceedings of the Royal Society of Edinburgh **8**, 325–334 (1875) (cit. on p. 101).

Turchette, Q. A., C. J. Myatt, B. E. King, C. A. Sackett, D. Kielpinski, W. M. Itano, C. Monroe and D. J. Wineland, 'Decoherence and decay of motional quantum states of a trapped atom coupled to engineered reservoirs', Phys. Rev. A **62** (5), 053807 (2000) (cit. on p. 2).

Turnbull, Herbert Westren, *Theory of equations*, 4., revised (Oliver et al., Edinburgh, London, New York) (cit. on p. 43).

Ulm, S et al., 'Observation of the Kibble-Zurek scaling law for defect formation in ion crystals.', en, Nat. Commun. **4**, 2290 (2013) (cit. on p. 28).

Wagner, Herbert, 'Long-wavelength excitations and the Goldstone theorem in many-particle systems with "broken symmetries"', Zeitschrift für Physik **195** (3), 273–299 (1966) (cit. on p. 30).

Waki, I., S. Kassner, G. Birkl and H. Walther, 'Observation of Ordered Structures of Laser-Cooled Ions in a Quadrupole Storage Ring', Phys. Rev. Lett. **68** (13), 2007–2010 (1992) (cit. on p. 26).

Wang, C.-C. Joseph, Adam C. Keith and J. K. Freericks, 'Phonon-Mediated Quantum Spin Simulator Employing a Planar Ionic Crystal in a Penning Trap', Phys. Rev. A **87** (1), 013422 (2013) (cit. on p. 18).

Warren, W. S., H. Rabitz and M. Dahleh, 'Coherent control of quantum dynamics - The dream is alive', Science **259**, 1581–1589 (1993) (cit. on p. 90).

Weiss, Ulrich, Hermann Grabert, Peter Hänggi and Peter Riseborough, 'Incoherent tunneling in a double well', Phys. Rev. B **35** (18), 9535–9551 (1987) (cit. on p. 2).

Wheeler, John Archibald, 'Law without law', in *Quantum Theory and Measurement*, pp. 182–213, ed. by John Archibald Wheeler and Wojciech Hubert Zurek, Princton Series in Physics (Princton University Press, New Jersey), pp. 182–213 (cit. on p. 106).

Wheeler, John Archibald and Wojciech Hubert Zurek, eds. (1983), *Quantum Theory and Measurement*, Princeton Series in Physics (Princeton University Press, New Jersey) (cit. on pp. 1, 105).

Williamson, John, 'On the algebraic problem concerning the normal forms of linear dynamical systems', American Journal of Mathematics, 141–163 (1936) (cit. on p. 38).

Wineland, D. J., J. C. Bergquist, Wayne M. Itano, J. J. Bollinger and C. H. Manney, 'Atomic-Ion Coulomb Clusters in an Ion Trap', Phys. Rev. Lett. **59** (26), 2935–2938 (1987) (cit. on p. 23).

Wineland, D. J., R. E. Drullinger and F. L. Walls, 'Radiation-Pressure Cooling of Bound Resonant Absorbers', Phys. Rev. Lett. **40**, 1639–1642 (1978) (cit. on pp. 7, 114).

Wineland, D. J. and D. Leibfried, 'Quantum information processing and metrology with trapped ions', Laser Physics Letters **8** (3), 175 (2011) (cit. on p. 13).

Wineland, D. J., C. Monroe, W. M. Itano, B. E. King, D. Leibfried, D. M. Meekhof, C. Myatt and C. Wood, Fortschr. Phys. **46** (4-5), 363–390 (1998) (cit. on p. 46).

Wineland, D., P. Ekstrom and H. Dehmelt, 'Monoelectron Oscillator', Phys. Rev. Lett. **31**, 1279–1282 (1973) (cit. on p. 8).

Wiseman, H., F. Harrison, M. Collett, S. Tan, D. Walls and R. Killip, 'Nonlocal momentum transfer in welcher Weg measurements', Phys. Rev. A **56** (1), 55–75 (1997) (cit. on p. 106).

Wiseman, H.M., 'Directly observing momentum transfer in twin-slit "which-way" experiments ', Phys. Lett. A **311** (4–5), 285–291 (2003) (cit. on p. 106).

Wiseman, Howard and Fiona Harrison, 'Uncertainty over complementarity?', Nature **377** (6550), 584–584 (1995) (cit. on p. 106).

Wolf, A., G. De Chiara, E. Kajari, E. Lutz and G. Morigi, 'Entangling two distant oscillators with a quantum reservoir', EPL **95** (6), 60008 (2011) (cit. on p. 2).

Wootters, William and Wojciech Zurek, 'Complementarity in the double-slit experiment: Quantum nonseparability and a quantitative statement of Bohr's principle', Phys. Rev. D **19** (2), 473–484 (1979) (cit. on p. 105).

Wunderlich, Christof, 'Conditional Spin Resonance with Trapped Ions', in *Laser Physics at the Limits*, ed. by Dieter Figger, Hartmut Meschede and Claus Zimmermann (Springer, Berlin et al.) (cit. on p. 46).

You, Wen-Long, Ying-Wai Li and Shi-Jian Gu, 'Fidelity, dynamic structure factor, and susceptibility in critical phenomena', Phys. Rev. E **76** (2), 022101 (2007) (cit. on p. 149).

Zanardi, Paolo and Nikola Paunković, 'Ground state overlap and quantum phase transitions', Phys. Rev. E **74** (3), 031123 (2006) (cit. on p. 101).

Zou, X. Y., L. J. Wang and L. Mandel, 'Induced coherence and indistinguishability in optical interference', Phys. Rev. Lett. **67** (3), 318–321 (1991) (cit. on p. 107).

Zurek, W. H., 'Pointer Basis of Quantum Apparatus: Into What Mixture does the Wave Packet Collapse?', Phys. Rev. D **24** (6), 1516–1525 (1981) (cit. on p. 30).

Zurek, W.H., 'Cosmological experiments in condensed matter systems ', Phys. Rep. **276** (4), 177–221 (1996) (cit. on p. 122).

Zurek, Wojciech Hubert, 'Decoherence, Einselection, and the Quantum Origins of the Classical', Rev. Mod. Phys. **75** (3), 715–775 (2003) (cit. on p. 1).

JOURNAL ABBREVIATIONS

Advan. Phys.	Advances in Physics
Am. J. Phys.	American Journal of Physics
Ann. Physics	Annals of Physics
Appl. Phys. B	Applied Physics B
Comm. Math. Phys.	Communications in Mathematical Physics
EPL	Europhysics Letters
Eur. J. Phys.	European Journal of Physics
Fortschr. Phys.	Fortschritte der Physik
Found. Phys.	Foundations of Physics
Int. J. Mod. Phys. A	International Journal of Modern Physics A
Int. J. Mod. Phys. C	International Journal of Modern Physics C
J. Appl. Phys.	Journal of Applied Physics
J. Mod. Opt.	Journal of Modern Optics
J. Opt. Soc. Am. B	Journal of the Optical Society of America B
J. Phys. A	Journal of Physics A: Mathematical and Theoretical
J. Phys. Radium	Journal de Physique et le Radium
Nat. Commun.	Nature Communications
Nat. Phot.	Nature Photonics
Nat. Phys.	Nature Physics
New J. Phys.	New Journal of Physics
Phys. Plasmas	Physics of Plasmas
Phys. Rep.	Physics Reports
Phys. Rev.	Physical Review
Phys. Rev. A	Physical Review A
Phys. Rev. B	Physical Review B
Phys. Rev. C	Physical Review C
Phys. Rev. D	Physical Review D
Phys. Rev. E	Physical Review E
Phys. Rev. Lett.	Physical Review Letters
Phys. Scr.	Physica Scripta
Phys. Lett. A	Physics Letters A
PNAS	Proceedings of the National Academy of Sciences of the United States of America
Proc. SPIE	Proceedings of SPIE
Rev. Mod. Phys.	Reviews of Modern Physics

ACRONYMS

ac	Alternating current
bcc	Body-centered cubic
BCH	Baker-Campbell-Hausdorff identity
BEC	Bose-Einstein-condensate
CCD	Charge-coupled device
COM	Centre of mass
dc	Direct current
FFT	Fast Fourier transform
MCP	Multi-channel plate
MRI	Magnetic resonance imaging
NMR	Nuclear magnetic resonance
rf	Radio-frequency
RWA	Rotating-wave approximation
SI	International system of units
UV	Ultra-violet
WKB	Wentzel-Kramers-Brillouin approximation